Valence bond approach to the low-energy physics of antiferromagnets

David Schwandt

▶ **To cite this version:**

David Schwandt. Valence bond approach to the low-energy physics of antiferromagnets. Strongly Correlated Electrons [cond-mat.str-el]. Université Paul Sabatier - Toulouse III, 2011. English. NNT : . tel-00783224

HAL Id: tel-00783224
https://theses.hal.science/tel-00783224

Submitted on 31 Jan 2013

HAL is a multi-disciplinary open access archive for the deposit and dissemination of scientific research documents, whether they are published or not. The documents may come from teaching and research institutions in France or abroad, or from public or private research centers.

L'archive ouverte pluridisciplinaire **HAL**, est destinée au dépôt et à la diffusion de documents scientifiques de niveau recherche, publiés ou non, émanant des établissements d'enseignement et de recherche français ou étrangers, des laboratoires publics ou privés.

THÈSE

En vue de l'obtention du

DOCTORAT DE L'UNIVERSITÉ DE TOULOUSE

Délivré par l'Université Toulouse III – Paul Sabatier
Discipline ou spécialité : Physique de la matière

Présentée et soutenue par David SCHWANDT
Le 13 juillet 2011

Titre : Approche *liens de valence* de la physique de basse énergie des systèmes antiferromagnétiques

---

JURY

Fabien ALET	(Directeur de thèse)
Bernard BERNU	(Rapporteur)
Daniel BRAUN	(Examinateur)
Michel CAFFAREL	(Président)
Benjamin CANALS	(Rapporteur)
Matthieu MAMBRINI	(Directeur de thèse)
Roderich MOESSNER	(Examinateur)
Anders W. SANDVIK	(Examinateur)

Ecole doctorale : Sciences de la matière
Unité de recherche : Laboratoire de Physique Théorique
Directeurs de Thèse : Fabien ALET & Matthieu MAMBRINI

DISSERTATION

submitted in fullfillment of the requirements for the degree of

DOCTORAT DE L'UNIVERSITÉ DE TOULOUSE

Delivered by l'Université Toulouse III – Paul Sabatier
Discipline: Physique de la matière

Presented and defended by David SCHWANDT
13 July 2011

Title : *Valence bond* approach to the low–energy physics of antiferromagnets

---

JURY

Fabien ALET	(Advisor)
Bernard BERNU	(Examiner)
Daniel BRAUN	(Jury member)
Michel CAFFAREL	(President)
Benjamin CANALS	(Examiner)
Matthieu MAMBRINI	(Advisor)
Roderich MOESSNER	(Jury member)
Anders W. SANDVIK	(Jury member)

Remerciements

Cette thèse a été réalisée au sein du Laboratoire de Physique Théorique où son directeur Clément Sire a gentiment accepté de m'accueillir. Merci a tous les membres du laboratoire et plus particulièrement à l'équipe des fermions fortement corrélés pour m'avoir chaleureusement accompagné durant ces dernières années.

Je tiens tout particulièrement à remercier Fabien Alet et Matthieu Mambrini, pour qui j'ai été le premier doctorant. J'ai pris beaucoup de plaisir à travailler sur le sujet de thèse qu'ils m'ont proposé, pas seulement à cause de la fidélité, la frustration et les liens de valence qui étaient impliqués. Grâce à eux, j'ai appris beaucoup de nouvelles facettes de la matière condensée et des simulations numériques. Ils ont toujours été disponibles pour discuter, tout en me laissent les libertés en toute confiance. Ils ont pris le temps de relire mon manuscrit et m'ont donné des critiques et suggestions précieuses. Ce fut la première fois pour nous tous — une première fois que je peux vivement recommander.

Je voudrais aussi remercier Sylvain Capponi, qui a été impliqué dans plusieurs projets de cette thèse. Sa grande connaissance dans différents domaines a souvent donnée naissance à une discussion afin de débloquer et clarifier les idées. Ich möchte mich zudem auch bei Andreas Läuchli für die wissenschaftliche Betreuung während meines kurzen Aufenthaltes am Max–Planck–Institut in Dresden bedanken. Die dort gewonnenen Erkenntnisse haben nicht nur diese Dissertation sehr bereichert.

Je remercie également Bernard Bernu et Benjamin Canals d'avoir pris le temps de lire cette thèse et d'avoir accepté de faire partie de mon jury de thèse en tant que rapporteur. Un grand merci aussi à Michel Caffarel pour les discussions scientifiques que nous avons pu avoir ainsi que pour avoir été le président de mon jury de thèse. Ganz herzlich möchte ich mich auch bei Daniel Braun bedanken, der mich bei meiner Masterarbeit betreute und zu meiner Promotionsverteidigung Mitglied der Jury war, ebenso wie Roderich Moessner, der für die Teilnahme an meiner Promotionsverteidigung sogar Einfluss auf Hochzeitsplanungen eines befreundeten Paares nahm. I would also like to thank Anders Sandvik for having passed by Toulouse on the way from Boston to Trieste and for having taken part in the jury for my dissertation defense.

Je voudrais souligner les aides informatiques et administratives, données par Sandrine, Sylvia et Malika, qui ont sauvées des heures de travail. Je remercie également tous les amis, les collègues doctorants et post-doctorants au LPT, LCAR et LCC : Andreas, Fabien, Daniel, Clément, Ludovic, Thomas, Benoît, Sylvain, Wesley, Phillipp, Vincent, Michael, Carlos, Fabricio, Yasir, Anil, Vivek, Lorand, Xavier, Juan Pablo, ainsi qu'Aurélien, Michel, Georges, Carine, Micha, et tous les autres qui ont rendu les pauses et le temps en dehors du laboratoire plus agréables.

Ein ganz besonderer Dank gilt auch meiner ganzen Familie, insbesondere meinen Eltern und meinem Bruder Roland, die mich in all den Jahren immer unterstützt haben, auch und gerade, als es mich mit der Zeit nach Dresden, Sheffield und Toulouse ver-

schlug. Ohne euren Beistand und eure Fürsorge wäre diese Doktorarbeit sicher nicht zustande gekommen.

Enfin, je remercie surtout Laurie, pour m'avoir accompagné durant ces dernières années, pour tous ces beaux souvenirs, pour sa patience, pour m'avoir soutenu dans mon travail et mes absences lors des conférences, pour m'avoir changé les idées durant la période de rédaction — et pour avoir accepté de m'épouser.

Summary of the Contents

1. Introduction 9

I. Preliminaries 13

2. Elements of Valence Bond Theory 15

3. Numerical Methods 39

II. Quantum Information 55

4. Fidelity Approach to Quantum Phase Transitions 57

III. Quantum Dimer Models 71

5. Generalized Quantum Dimer Models 73

6. Application to the Kagomé and Honeycomb Antiferromagnet 93

7. Conclusion 117

IV. Supplementary Material 119

A. Overlap Expansion for the Kagomé Lattice 121

B. Overlap Expansion for the Honeycomb Lattice 129

List of Publications 135

Bibliography 137

List of Figures 149

List of Tables 151

1. Introduction

Shortly after the discovery of quantum mechanics and the Pauli exclusion principle, Sommerfeld developed the free electron model, which treats the valence electrons in metals as a gas of non–interacting fermions. Despite its simplicity this model succeeds in explaining the linear temperature dependency of specific heat for alkali metals up to a few Kelvin [1]. However, the absence of interactions is generally prohibitive if one wants to describe collective phenomena, such as magnetism in solids. This is particularly true for the so–called strongly correlated systems, where the non–interacting limit is not a good starting point.

One typical example of a strongly correlated system is given by the Hubbard model, which implements the competition between electron hopping on a lattice and their Coulomb repulsion. Although the model is quite simple, it allows to study the interplay of spin and charge degrees of freedom. For small Coulomb repulsion we are left with a tight binding model, which can describe metals and band–insulators, whereas for large repulsion the system becomes a Mott–insulator. In such a state charge fluctuations are suppressed, as the electron moves are limited due to strong interactions. At half–filling we obtain an effective spin model, characterized by Heisenberg interactions. This spin interaction is one ingredient to describe magnetism in insulating materials.

The Heisenberg model is probably one of the simplest models, being able to describe collective phenomena like ferromagnetism or antiferromagnetism. Despite this, an exact solution does not exist for realistic systems in dimension larger than one. This is basically due to the strong interactions between the spins, resulting in an exponential complexity of the problem, as usually observed for many–body systems. The difficulties are even amplified in the presence of competing interactions, caused by frustration.

From a theoretical point of view, frustrated antiferromagnets are very interesting, as new states of matter are expected to emerge, such as valence bond crystals or spin liquids. These states are characterized through the formation of singlets between pairs of electrons, a bonding which is often met in chemistry. In the case of valence bond crystals (VBC), these singlets are distributed very regularly over the material, breaking translational and rotational symmetry. However, in contrast to the antiferromagnetic (Néel) state, $SU(2)$ spin symmetry is not broken. In spin liquids no symmetries are broken, yielding a superposition of disordered patterns of valence bonds on the lattice. However, especially in two dimensions and for spin 1/2 the Heisenberg model is still poorly understood owing to the quantum fluctuations, being most pronounced in this case. Whereas valence bond crystal phases are already established, spin liquids are still extensively debated.

On the experimental side, finding magnetically disordered systems is relatively hard, as this does mostly not seem to be the preferred situation in nature [2]. Measuring the absence of magnetic order is also more difficult than measuring its presence. This

is even amplified for spin liquids, which are defined through the absence of any local order parameter, rendering their discovery rather challenging. Indeed, one may not just find a spin liquid through a single experiment, but rather by combining several different results.

One of the most promising candidates is probably the kagomé antiferromagnet, which is realized in herbertsmithite. However, not only experimentally, but also numerically this lattice is rather challenging. The exponential number of singlets below the singlet–triplet gap seems to be in favor of a spin liquid scenario. Nevertheless, large scale Monte Carlo simulations are precluded by the famous sign problem, whereas exact diagonalizations are hard to interpret, due to strong finite size effects. One possible way out is to define effective models, which only keep certain important physical aspects of a theory, in a very similar way than in the passage from the Hubbard model to the Heisenberg model. Such a step may be considered if it simplifies the problem sufficiently.

Valence bond crystals, spin liquids and other exotic ground states of the Heisenberg model are singlet states and can be described in terms of valence bonds. One simply has to pair all spins into singlets and consider a linear superposition of the resulting *valence bond states*. This way any singlet state can be formed, a result that has been found in the early days of quantum mechanics [3, 4, 5].

In my thesis I will present a novel analytical scheme, the so–called *generalized quantum dimer models*, which map the Heisenberg model to an effective Hamiltonian. The basic idea goes back to Rokhsar and Kivelson [6] and the resulting quantum dimer models are much easier to study, numerically and analytically. Indeed, liquids have been found in such models in the past [7, 8], as well as different valence bond crystal phases [7, 9].

I also present the fidelity concept, a method rooted in quantum information, which allows for the detection of quantum phase transitions without having prior knowledge about order parameters [10]. This method will as well be applied in the valence bond basis and may render the detection of valence bond crystals and spin liquids easier. Both techniques require the implementation of state–of–the–art numerical methods, such as Lanczos exact diagonalization for frustrated systems, and quantum Monte Carlo for non–frustrated ones, in order to make large system sizes numerically accessible.

This thesis is structured as follows: In chapter (2) I will introduce valence bonds, which naturally arise when coupling several spins antiferromagnetically. In fact, this chapter provides the basis for the rest of the manuscript, as all following chapters work with valence bond states. In particular, I will illustrate how to calculate their overlap in a graphical way, the *overlap rule* introduced by Sutherland [11]. The idea is simply to superimpose both valence bond states and to count the number of closed loops in the resulting graph. Interestingly, this scheme can also be used to evaluate expressions that not only contain valence bonds but also an arbitrary amount of singlet projectors. The underlying structure will be referred to as *generic overlap graphs* and I will show how the well–known overlap rule can be extended when singlet projectors are included.

In chapter (3) I discuss different required state–of–the–art numerical techniques, widely used in condensed matter and in particular in my thesis. These are the Lanczos exact diagonalization technique (ED), which is used to obtain the exact low–energy spectrum, as well as quantum Monte Carlo (QMC), which is used to calculate observables stochastically. Especially the recently proposed valence bond projector quantum Monte Carlo

is revisited [12] and in view of chapter (2) a possible interpretation without spins is pointed out for the loop version of the projector scheme [13].

Chapter (4) is devoted to the fidelity approach, allowing for the detection of quantum phase transitions. Within this method, rooted in quantum information theory, one compares different quantum states by calculating their overlap. Such a method has been suggested to detect quantum phase transitions, occurring at $T = 0$ [10]. I show how this method can be implemented within the valence bond projector quantum Monte Carlo and apply the scheme to a specific example, the 1/5th–depleted square lattice. Complementary SSE simulations have been carried out by F. Alet, whereas gauging exact diagonalizations were performed by S. Capponi [14].

Generalized quantum dimer models (GQDM) will be developed in detail in chapter (5), a work supervised by M. Mambrini [15]. It will be explained how to derive them on a rather general ground, only requiring Heisenberg interactions on some underlying lattice. The presented scheme goes well beyond the initial ideas by Rokhsar and Kivelson in two points. Firstly, exact amplitudes for the known plaquette resonances can be calculated and secondly more complicated processes are considered. This allows to establish a rigorous connection between a Heisenberg model and a quantum dimer model.

Whereas chapter (5) explains the general method to derive GQDM, I apply this scheme to the kagomé and the honeycomb lattice in chapter (6). The resulting effective Hamiltonian on the kagomé lattice has been studied with large scale Lanczos ED simulations by D. Poilblanc, conceptually confirming the derivation scheme. In this collaboration we have found evidence for a 36–site VBC, proposed earlier in literature [16, 17]. Furthermore, the Heisenberg model is found to be in the vicinity of a multi–critical point, separating a $\mathbb{Z}_2$ spin liquid phase from an even and odd parity version of the proposed VBC [18].

For studying the honeycomb lattice I went for a research stay to the Max–Planck institute in Dresden, where A. M. Läuchli instructed me in simulating generalized quantum dimer models. Complementary simulations in the spin basis have been carried out by A. M. Läuchli and S. Capponi, while A. F. Albuquerque has performed self–consistent mean–field simulations, as well as solving the general eigenvalue problem within the nearest neighbor valence bond basis. As a result, this collaboration, also involving M. Mambrini and B. Hetényi, helped to identify a magnetically disordered region as plaquette phase [19].

Part I.

Preliminaries

2. Elements of Valence Bond Theory

This first chapter aims to provide the reader with some basics in valence bond theory, such as it is needed in the later parts of this thesis. Much of this theory has been developed in the first half of the last century by Rumer [3, 4] and Pauling [5] in the context of the chemical bond. Indeed, in many compounds the covalent bond plays a vital role for the stabilization of the molecular structure.

Half a century later Anderson reintroduced "resonating valence bonds" as a variational approach in the context of frustrated antiferromagnetism on the triangular lattice [20] and superconductivity [21], and induced their revival, as illustrated by several other works in this realm [11, 22, 23].

Here we will start out with a very brief summary about quantum mechanics of the spin, as can be found in any introductory quantum physics textbook. Building up on this, valence bonds (VB) will be introduced by means of Young tableaux and in relation with the ground state of the antiferromagnetic (AF) Heisenberg model. We will look at different convenient sets of VB and their usage in describing the low energy physics on finite size bipartite and non–bipartite lattices.

At the end of the chapter, the reader will have heard about the overlap rule within the bosonic and fermionic convention, and loop estimators such as for spin–spin correlations.

2.1. Spin

Symmetries play a rather important role in physics, e.g. for conservation laws or in the context of phase transitions. Among them we can distinguish discrete symmetries, which are usually described through symmetry groups (i.e. space groups and point groups) and continuous ones, which have to be treated by Lie groups. Some reading on groups and symmetries in physics can be found in [24, 25]. Here we shall summarize some relevant points.

In quantum mechanics, one important Lie group is the special unitary group $SU(2)$, which comprises all unitary 2×2 matrices with unit determinant. The generators of the latter are the Pauli matrices

$$\hat{\sigma}^x = \begin{pmatrix} 0 & 1 \\ 1 & 0 \end{pmatrix} \quad \hat{\sigma}^y = \begin{pmatrix} 0 & -i \\ i & 0 \end{pmatrix} \quad \hat{\sigma}^z = \begin{pmatrix} 1 & 0 \\ 0 & -1 \end{pmatrix}, \tag{2.1}$$

and an arbitrary element of $SU(2)$ can be represented by

$$\hat{D}(\boldsymbol{\omega}) = e^{-\frac{1}{2} i \boldsymbol{\omega} \cdot \hat{\boldsymbol{\sigma}}}. \tag{2.2}$$

Here $\boldsymbol{\omega} = \theta \boldsymbol{n}$ corresponds to an angle θ about the direction $\boldsymbol{n}$ of a rotation axis, whereas $\hat{\boldsymbol{\sigma}} = (\hat{\sigma}^x, \hat{\sigma}^y, \hat{\sigma}^z)$ is a vector of the three Pauli matrices. The group elements generate rotations about $\boldsymbol{\omega}$ in $SU(2)$, and as such successive rotations about different axes do not commute. This is manifested in the commutation rules for the Pauli matrices, or more generally for the spin $\hat{\boldsymbol{S}} = \frac{\hbar}{2}\hat{\boldsymbol{\sigma}}$ with components $\hat{S}^x$, $\hat{S}^y$ and $\hat{S}^z$. We have

$$\left[\hat{S}^a, \hat{S}^b\right] = i\hbar\varepsilon^{abc}\hat{S}^c, \tag{2.3}$$

where ε^{abc} is the Levi–Civita symbol and $a, b, c \in \{x, y, z\}$. Obviously, the spin components do not commute with each other, which implies that they cannot be measured independently. One therefore has to privilege one component above the others, meaning that the possible spin states are expressed in terms of eigenstates of this component. When choosing the z–axis as quantization direction, one can introduce so–called ladder operators

$$\hat{S}^{\pm} = \hat{S}^x \pm i\hat{S}^y, \tag{2.4}$$

for which the commutation relations become

$$\left[\hat{S}^+, \hat{S}^-\right] = 2\hbar\hat{S}^z, \tag{2.5}$$

$$\left[\hat{S}^z, \hat{S}^{\pm}\right] = \pm\hbar\hat{S}^{\pm}. \tag{2.6}$$

The eigenvalue problem for the spin is then solved by observing, that each of its components commutes with $\hat{\boldsymbol{S}}^2 = (\hat{S}^x)^2 + (\hat{S}^y)^2 + (\hat{S}^z)^2$, i.e.

$$\left[\hat{\boldsymbol{S}}^2, \hat{S}^a\right] = 0, \quad \text{for} \quad a \in x, y, z, \pm. \tag{2.7}$$

Hence, $\hat{\boldsymbol{S}}^2$ and $\hat{S}^z$ can be diagonalized simultaneously and we have the following relations,

$$\hat{\boldsymbol{S}}^2 |s, m\rangle = \hbar^2 s(s+1) |s, m\rangle , \tag{2.8}$$

$$\hat{S}^z |s, m\rangle = \hbar m |s, m\rangle , \tag{2.9}$$

$$\hat{S}^{\pm} |s, m\rangle = \hbar\sqrt{s(s+1) - m(m \pm 1)} |s, m \pm 1\rangle . \tag{2.10}$$

Eqs. (2.8) and (2.9) are the eigenvalue equations for the spin with quantization into z–direction. The spin quantum number s can take on any non–negative integer or half–integer value, while the secondary spin quantum number represents the projection onto the quantization axis and is thus bounded, i.e we have $m \in \{-s, -s+1, \ldots, s-1, s\}$. Equation (2.10) illustrates the action of the ladder operators onto a given spin state, changing the secondary spin quantum number m by one.

The Pauli matrices can be recovered as fundamental representation of $SU(2)$, and describe for example electrons, which carry spin–$\frac{1}{2}$. The two possible spin orientations of such a doublet are usually written in short as

$$|\uparrow\rangle = \left|\frac{1}{2}, \frac{1}{2}\right\rangle \quad \text{and} \quad |\downarrow\rangle = \left|\frac{1}{2}, -\frac{1}{2}\right\rangle , \tag{2.11}$$

and can be transformed into each other by the ladder operators.

2.1.1. Angular Momentum Coupling

However, $SU(2)$ has an infinite number of irreducible representations, which are formed by hermitian, traceless matrices in general. These correspond to higher spins and are suitable for describing materials that typically contain much more than a single electron. The construction of higher dimensional representations is known as angular momentum coupling and is described in any quantum mechanics textbook. Nevertheless, we will try to illustrate this here as it will turn out to simplify the introduction of valence bonds.

We define the sum of several spins $\hat{\boldsymbol{S}}_k$ through

$$\hat{\boldsymbol{S}} = \sum_{k=1}^{N} \hat{\boldsymbol{S}}_k, \tag{2.12}$$

whose components apparently obey the commutation relations (2.3). Hence, this quantity can be called the total spin of a system and the remaining task is to find its allowed quantum numbers.

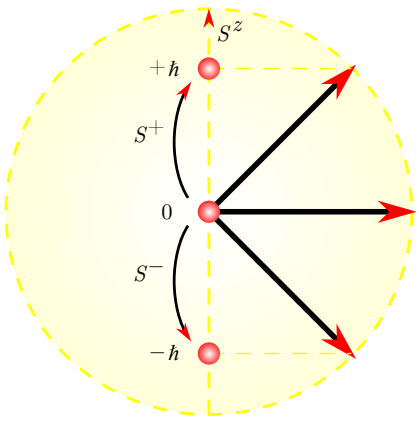

Fig. 2.1.: The spin triplet state $\{|1,1\rangle,\ |1,0\rangle,\ |1,-1\rangle\}$ with corresponding S^z–eigenvalues $\{+\hbar, 0, -\hbar\}$. The ladder operator $\hat{S}^+$ ($\hat{S}^-$) is used to increase (decrease) the quantum number m in quantization direction. In practice this is often taken to be the S^z–direction.

As an instructive example, the sum of two spins $\hat{\boldsymbol{S}}_1 + \hat{\boldsymbol{S}}_2$ forms an antisymmetric singlet ($s = 0$)

$$|0,0\rangle = \frac{|\uparrow_1\downarrow_2\rangle - |\downarrow_1\uparrow_2\rangle}{\sqrt{2}} \tag{2.13}$$

and a symmetric triplet state ($s = 1$)

$$\begin{aligned} |1,1\rangle &= |\uparrow_1\uparrow_2\rangle \\ |1,0\rangle &= \frac{|\uparrow_1\downarrow_2\rangle + |\downarrow_1\uparrow_2\rangle}{\sqrt{2}} \\ |1,-1\rangle &= |\downarrow_1\downarrow_2\rangle\,. \end{aligned} \tag{2.14}$$

Figure (2.1) depicts the latter, although the presentation of the S^x and S^y–axes is omitted as these components cannot be measured simultaneously with $\hat{S}^z$.

Young Diagrams

The coupling of more than two spins is straightforward, provided we know how to couple two of them, as this can be done iteratively. It is however easier to perform angular momentum coupling with the help of Young diagrams, which offer a systematic way for deriving irreducible representations of the Lie group $SU(N)$. A nice introduction to Young diagrams can be found in [26, 27, 28].

Here, we enumerate the basic properties of Young diagrams and Young tableaux, taken from [26].

- A Young diagram is a left justified set of rows of boxes, such that the number of boxes in each row weakly decreases along the rows from top to bottom.
- A semistandard Young tableau is a Young diagram filled with positive integers, such that the entries are weakly increasing from left to right and strictly increasing from top to bottom.
- A semistandard Young tableau that is filled with a permutation of $\{1, 2, \ldots, N\}$ is called standard.

In the case of $SU(2)$ the number of rows is restricted to two. The doublet spin–$\frac{1}{2}$ can be represented by $\boxed{1}$, where the integer 1 simply corresponds to the spin index. Indices in the same row are symmetric, whereas indices in the same column are antisymmetric. As the antisymmetrization is here applied after the symmetrization, the symmetric properties of indices usually get lost except in the case, where there is only one row or only one column in the Young tableau.

It is now easy to understand, that $\boxed{1}\boxed{2}$ corresponds to the triplet state (2.14), while $\begin{array}{|c|}\hline 1 \\ \hline 2 \\ \hline \end{array}$ represents the singlet (2.13). In Tab. (2.1), we give a summary of all resulting Young tableaux when coupling up to $N = 4$ spins. The important point here is that coupling N spins can be achieved by constructing all standard Young tableaux with N boxes. This is not a difficult task and there are a number of useful relations in the general case of Young diagrams with an arbitrary number of rows. Here, we shall list some of those in the special case of $SU(2)$. Denote by x_1 (x_2) the length of the first (second) row of the Young diagram, such that we have $N = x_1 + x_2$. The spin quantum number is then given by $s = \frac{x_1 - x_2}{2}$ and the multiplet contains

$$2s + 1 = x_1 - x_2 + 1 \tag{2.15}$$

different spin projections. Hence, in order to distinguish a singlet from a doublet or a triplet and so on, we have to look at the difference of length between both rows, i.e. singlet states are represented by rectangular Young tableaux, whereas in doublets (triplets) the first row contains one (two) more boxes than the second row.

Another interesting quantity is the number of different Young tableaux with the same shape, or in other words, how many linearly independent spin–s states can be formed when coupling N spin–$\frac{1}{2}$? The answer in the general case is given by Frame–Robinson–Thrall's hook–length formula [26, 23], which reduces for $SU(2)$ to

$$\mathcal{N}_N^s = \frac{(2s+1)N!}{\left(\frac{N}{2} + s + 1\right)!\left(\frac{N}{2} - s\right)!}. \tag{2.16}$$

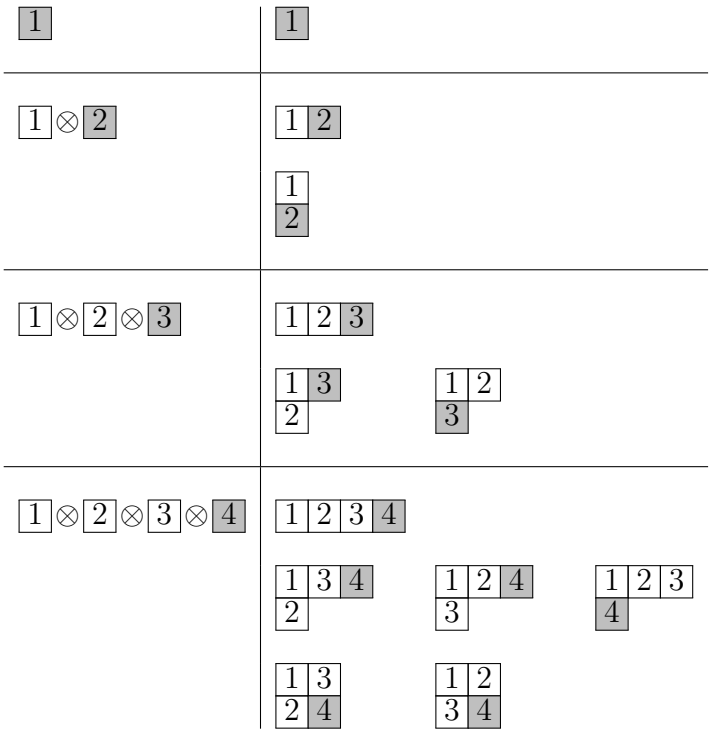

Tab. 2.1.: Illustration of the coupling of up to $N = 4$ spins. Notice, how the scheme on N sites arises successively by adding a new index to the existing Young tableaux for $N - 1$ spins. However, it is not necessary to proceed iteratively — in order to find all allowed spin multiplets by coupling N spins, we simply need to find all standard Young tableaux with the same number of boxes.

It is furthermore even possible to visualize all the spin orientations within a spin–multiplet, such that one can read off the secondary spin quantum number m. In order to achieve this, one simply has to consider semistandard Young tableaux, filled with the projected spin quantum number for a single spin $\left\{\frac{1}{2}, -\frac{1}{2}\right\}$ or simply $\{\uparrow, \downarrow\}$. As an example, the singlet state $\begin{array}{|c|}\hline 1 \\ \hline 2 \\ \hline \end{array}$ becomes $\begin{array}{|c|}\hline \uparrow_1 \\ \hline \downarrow_2 \\ \hline \end{array}$, while the triplet state $\begin{array}{|c|c|}\hline 1 & 2 \\ \hline \end{array}$ breaks down into $\left\{\begin{array}{|c|c|}\hline \uparrow_1 & \uparrow_2 \\ \hline \end{array}, \begin{array}{|c|c|}\hline \uparrow_1 & \downarrow_2 \\ \hline \end{array}, \begin{array}{|c|c|}\hline \downarrow_1 & \downarrow_2 \\ \hline \end{array}\right\}$.

At this point it becomes also clear, why for $SU(2)$ there are only 2 rows in a Young tableau. If there were more than two, then we would have either twice $\uparrow$ or twice $\downarrow$ in a column, and the antisymmetrization would thus vanish the entire state.

In summary, we have not only solved the eigenvalue problem for a single spin, but

also for the total spin of a system,

$$\hat{\boldsymbol{S}}^2 = \sum_{k,l=1}^{N} \hat{\boldsymbol{S}}_k \cdot \hat{\boldsymbol{S}}_l \tag{2.17}$$

$$\hat{S}^z = \sum_{k=1}^{N} \hat{S}_k^z. \tag{2.18}$$

The elegant way of using Young tableaux therefore turns out to be very helpful to classify all the eigenstates. However, there is a little price to pay for that simplicity.

First of all, there are still degeneracies, indicating that we have to take into account other quantum numbers in order to distinguish all the Young tableaux with the same shape. At this stage this is not that important, but we should keep in mind that the eigenvalue problem is not fully solved if there are still different states that are equal in all quantum numbers.

Secondly, one usually likes to find an orthonormal set of eigenfunctions, which is not the case here. Although Young tableaux of different shape induce states which are orthogonal to each other, this is not the case anymore for those with the same shape. In other words, all the singlets, doublets and higher multiplets still have to be orthogonalized if needed.

2.2. Heisenberg Model

We can now slightly generalize (2.17) by inserting some additional parameter J_{kl}, in order to arrive at the isotropic Heisenberg model,

$$\hat{\mathcal{H}} = \sum_{k,l=1}^{N} J_{kl} \hat{\boldsymbol{S}}_k \cdot \hat{\boldsymbol{S}}_l. \tag{2.19}$$

The goal of this is to modulate the interaction strength between the spins, in order to describe the situation in real materials. Whereas in (2.17) all spins interacted with each other in the same way, the Heisenberg model rather captures the highly localized character of the couplings, induced by the exchange integral. Depending on the spatial orientation of the electron orbitals and mediated by an interplay of the Pauli exclusion principle and the Coulomb repulsion [29], we can distinguish two different situations.

- The exchange coupling is negative ($J < 0$) and we observe **ferromagnetic** behavior, where symmetric alignment of the spins is energetically favored. This occurs in materials, such as $CrBr_3$, K_2CuF_4, EuO and others [30].
- A positive interaction ($J > 0$) with antisymmetric spin alignment is called **antiferromagnetic**, and can be observed in MnO, EuTe, NiO. For more materials see for example [30].

When all couplings are ferromagnetic, the ground state manifold consists simply of all fully symmetric states. The situation becomes however much more challenging when

there are only antiferromagnetic (AF) or both types of interactions. In this case it is very important to analyze the symmetries of the problem, which shall be done in the following.

The Heisenberg Hamiltonian is $SU(2)$ symmetric and therefore (2.19) commutes with the total spin squared (Eq. 2.17) and its projection onto the z–axis (Eq. 2.18), hence its eigenstates can also be classified by the quantum numbers of the total spin. It also commutes with any other component of the total spin, i.e. the ladder operators. Thus, every spin–s state will be $(2s+1)$–fold degenerate, similarly as in the special case of $J_{kl} = 1$, where all spins are equally coupled with each other and every spin–s multiplet has an energy of $s(s+1)\hbar^2$.

Further important symmetries are encoded in the coupling matrix J_{kl} and are usually referred to as *point symmetries*, in case of invariance by rotations and reflections, or *space symmetries*, when also translational invariance is taken into account. All these symmetries correspond to the automorphisms of the lattice graph, described by J_{kl}. For most lattices the corresponding symmetry groups can be found in literature [24].

Although the specific ground state of the Heisenberg model depends very much on the underlying lattice and its symmetries, a few general statements can be made. Before stating them, let us distinguish different types of lattices. In case the underlying lattice can be divided into two sublattices $\mathcal{A}$ and $\mathcal{B}$, such that interactions are only present between sites of different species, the lattice is called *bipartite*. Examples of bipartite lattices are the square and the hexagonal (honeycomb) lattice with first (nearest) neighbor interactions. On the other hand, if the product of the (negative) couplings

$$p_{\mathcal{L}} = \prod_{(k,l)\in\mathcal{L}} (-J_{kl}) \tag{2.20}$$

around a closed loop $\mathcal{L}$ on the lattice is negative we encounter *frustration* [31]. Lattices with frustration are for example the triangular and the kagomé lattice with nearest neighbor AF interactions, but also the J_1–J_2 square lattice with AF nearest neighbor (J_1) and second nearest neighbor (J_2) interactions. In all these examples the basic frustrated unit is a triangle of spins with AF interactions on every edge.

For finite bipartite lattices Marshall has shown that the ground state is actually a singlet ($s = 0$) state [32]. This was later extended by Lieb and Mattis to the case of intermediate frustration and we arrive at the following statement.

Lieb and Mattis theorem [33]. Let $E_0(s)$ be the lowest energy eigenvalue of all spin–s multiplets and $\{\mathcal{A}, \mathcal{B}\}$ a bipartition of the lattice. If there is a constant $g^2 \geq 0$, such that $J_{a,a} \leq g^2$, $J_{b,b} \leq g^2$ and $J_{a,b} \geq g^2 \;\forall\; a \in \mathcal{A}$ and $b \in \mathcal{B}$, then $E_0(s+1) > E_0(s)$.

Let us illustrate this by considering the following toy model [33, 29, 34], where N spins are situated on a bipartite lattice. There is no interaction within a sublattice ($J_{a,a} = 0 = J_{b,b}$), but every spin of sublattice $\mathcal{A}$ is coupled to every spin in $\mathcal{B}$, i.e. $J_{a,b} = 1$. Denoting the total spin on sublattice $\mathcal{A}$ ($\mathcal{B}$) by $\hat{\boldsymbol{S}}_A$ ($\hat{\boldsymbol{S}}_B$), we simply have

$$\hat{\mathcal{H}} = \frac{2}{N} \hat{\boldsymbol{S}}_A \cdot \hat{\boldsymbol{S}}_B, \tag{2.21}$$

where the factor $2/N$ compensates the extensive coordination number. Such a model is solved trivially by considering angular momentum coupling and we obtain the energy spectrum (provided $N/2$ even)

$$E(s, s_A, s_B) = \frac{1}{N}\big(s(s+1) - s_A(s_A+1) - s_B(s_B+1)\big), \tag{2.22}$$

with $s_A, s_B \in \{0, 1, \ldots, N/4\}$ and $s \in \{|s_A - s_B|, \ldots, s_A + s_B\}$. The eigenvalues in every spin–s sector are illustrated in Fig. (2.2) for a $N = 32$ sample.

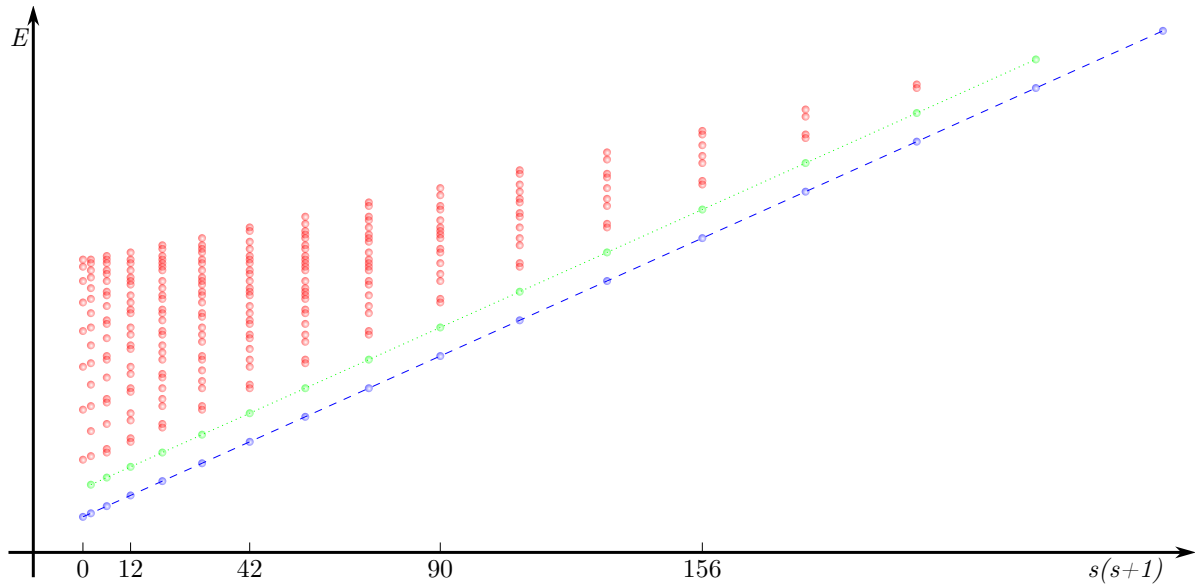

Fig. 2.2.: Spectrum of (2.21) for $N = 32$ plotted against $s(s+1)$. The Anderson tower of states structure (dashed blue line with a slope $\sim N^{-1}$) collapses to the absolute ground state in the thermodynamic limit, spontaneously forming the symmetry breaking Néel state. The first magnons (dotted green line) remain separated by a gap for this model. For a more realistic model, such as the Heisenberg antiferromagnet on the square lattice, this finite size gap will close in the thermodynamic limit, forming the Goldstone modes, associated to the symmetry breaking Néel state.

There are several important things to notice on this spectrum. First of all, the Lieb and Mattis theorem is satisfied as expected, and the lowest energy in every spin sector is given by

$$E_0(s) = \frac{s(s+1)}{N} - \frac{1}{2}\left(\frac{N}{4} + 1\right), \tag{2.23}$$

which is reminiscent of the eigenvalues of Eq. (2.17). These states form the so–called Anderson tower of states (TOS) [35] or the quasi–degenerate joint states (QDJS) [36, 37]. The first excitation in every sector is obtained by flipping a single spin and we have

$$E_1(s) = \frac{s(s+1)}{N} - \frac{N}{8}, \tag{2.24}$$

with the excitation energy

$$\Delta(s) = E_1(s+1) - E_0(s) \tag{2.25}$$

$$= \frac{2(s+1)}{N} + \frac{1}{2}. \tag{2.26}$$

Regarding the energies (Eq. 2.23) and (Eq. 2.24), we observe a linear dependancy in $s(s+1)$ with a slope $\sim N^{-1}$. Therefore, the states in the dashed (blue) curve in Fig. (2.2) will collapse to the absolute ground state, up to $s \sim \sqrt{N}$ [34, 38], forming a quasi–degenerate manifold. A careful symmetry analysis reveals, that the Néel state

$$\left|\psi^{\mathbf{Neel}}\right\rangle = |\uparrow_{\mathcal{A}}\downarrow_{\mathcal{B}}\uparrow_{\mathcal{A}} \cdots \downarrow_{\mathcal{B}}\uparrow_{\mathcal{A}}\downarrow_{\mathcal{B}}\rangle \tag{2.27}$$

(and any other Néel state) is precisely formed by the TOS structure [34]. Hence, the ground state is selected by spontaneous symmetry breaking (SSB) of $SU(2)$. Notice, that the Néel state also breaks the discrete translational symmetry.

The described behavior of the toy model considered above has several things in common with more realistic models. Indeed, it has been observed on the square lattice [39, 40] and on the honeycomb lattice [41] that the nearest neighbor AF Heisenberg model displays collinear Néel long range order (LRO). On the triangular lattice we observe non–collinear Néel LRO [36, 37] for the same type of interactions. In all three cases the typical tower of states structure, collapsing as $\sim N^{-1}$, indicates the breaking of $SU(2)$.

However, equation (2.21) describes a model in infinite dimension, hiding several features that are present in more realistic cases. A spin–wave approach reveals a subleading correction of order $\mathcal{O}(L^{-D-1})$ for the ground state energy per site [34]. Here, L is some characteristic length scale of the system, whereas D is the dimension. Furthermore, the first magnon excitations, corresponding to the dotted green curve in Fig. (2.2), will collapse as $\sim L^{-1}$. These states will form the Goldstone modes, associated to the continuous symmetry breaking [34].

The natural question is, to what extend the Néel state persists in presence of frustration. Obviously, this is the case on the triangular lattice, but on the honeycomb lattice next nearest neighbor interactions rather result a valence bond crystal (VBC) [41, 19], which breaks translational symmetry, but not $SU(2)$. Such a discrete symmetry breaking is also visible in finite–size spectra, where only a few singlet ($s = 0$) energy levels collapse onto the ground state [42].

A much more intriguing situation is met on the kagomé lattice, where an exponential number of singlet states is found below the first triplet excitation. This continuum of singlet states seems to be consistent with a spin liquid state, where no symmetries are broken. Therefore all order parameters vanish or become very small and correlations become short ranged [42].

Summarizing the preceding statements, there is very strong evidence for the ground state on finite samples to be a singlet in many realistic cases. This is of course proven for bipartite lattices, but seems to be the case for the triangular or the kagomé lattice as well. Therefore it seems justified to put some effort in understanding and using the singlet subspace, in order to push simulations to bigger system sizes.

2.3. Valence Bond Basis

As has been mentioned in the previous section, in many cases the AF Heisenberg model admits a singlet ground state on finite size samples. If in the thermodynamic limit triplet excitations remain gapped, it is very natural to study the subspace of total spin zero. But also when many different multiplets are quasi degenerate, the singlet states may play an important role. We have seen that these states are classified by standard Young tableaux that have two rows with the same number of boxes. In every column of such a diagram the two corresponding spins are antisymmetrized into a singlet state, thus giving rise to a tensor product of two–site singlet states. These two–spin singlets will be written as

$$|(k,l)\rangle := \frac{|\uparrow_k\downarrow_l\rangle - |\downarrow_k\uparrow_l\rangle}{\sqrt{2}}, \tag{2.28}$$

which can also be illustrated graphically as

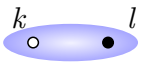

$$:= \frac{|\uparrow_k\downarrow_l\rangle - |\downarrow_k\uparrow_l\rangle}{\sqrt{2}}. \tag{2.29}$$

Notice that the orientation of the singlet (also called *dimer*) is important, as it is an antisymmetric object that changes sign upon permutation of the two indices,

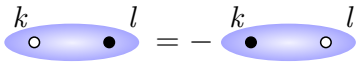

$$|(k,l)\rangle = -|(l,k)\rangle\,. \tag{2.30}$$

Often these dimers are also represented by arrows, pointing form one site to another. It is furthermore possible to define some convention that keeps track of the orientation implicitly (see section 2.3.2). In the latter case one usually avoids drawing oriented objects such as arrows.

Using this notation, we can replace all Young tableaux by products of singlets, as for example the following singlet state on 8 sites,

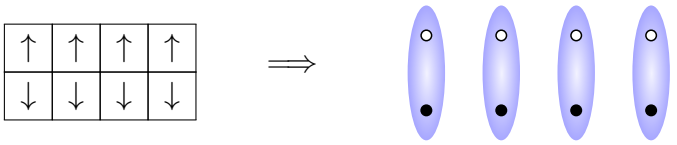

. (2.31)

This notation has already been introduced by Rumer [3, 4] and Pauling [5] as early as 1932 in a context that aimed to describe the valence electrons of chemical molecules (e.g. hydrazine). The advantage is obvious: it is much more illustrative to draw dimers on a lattice than crushing a lattice into a two–rowed Young tableau. Nowadays, only the name *valence bond* reminds us that these objects actually have their roots in chemistry. In physics, we can define this class of valence bond (VB) states as

$$|\mathbf{VB}\rangle = \bigotimes_{(k,l)\in \mathrm{YT}_0} |(k,l)\rangle\,, \tag{2.32}$$

where the product is taken over all columns within a standard Young tableau with total spin zero (YT_0). This construction guarantees that these VB states form a basis, as the standard Young tableaux are linearly independent [23]. Any singlet state $|\varphi\rangle$ can therefore be expressed within this basis

$$|\varphi\rangle = \sum_{\mathbf{VB}} c_{\mathbf{VB}} \, |\mathbf{VB}\rangle \,, \tag{2.33}$$

with $c_{\mathbf{VB}}$ being some generally complex coefficients.

At this point it is worth mentioning, that the concrete valence bond coverings of a lattice strongly depend on the chosen numbering of the spins. Of course, this can be changed and therefore we can find much more coverings than those that precisely span the singlet subspace. Considering every possible pairing of spins on a lattice of N sites, we have N possibilities to choose the first site, $N-1$ for the second, and so on. Every two sites form a pair, where the order in which we picked the two sites within this pair does not matter. This yields a factor $1/2$ and at the end the order of all the pairs does not matter either, yielding a factor of $1/(N/2)!$. Thus, the total number of valence bond coverings is given by

$$\mathcal{N}_N^{\mathbf{VB}} = \frac{N(N-1)}{2} \cdot \frac{(N-2)(N-3)}{2} \cdots \frac{2 \cdot 1}{2} \frac{1}{\left(\frac{N}{2}\right)!} = \frac{N!}{2^{N/2} \left(\frac{N}{2}\right)!} \sim \left(\frac{N}{e}\right)^{N/2} . \tag{2.34}$$

The total number of VB states is by construction bigger than the number of singlet states (Eq. 2.35), as can also be seen in Fig. (2.5). It is very clear that all the additional states lie in the same space and can therefore be expressed as linear combination of those obtained from the Young tableaux. But when working with spins situated on a lattice, it does not seem to be possible in general, to find a numbering on a given lattice that somehow respects all the lattice symmetries. However, one may not want to bias the calculation by an unsymmetrical choice of basis vectors. Therefore it is often advisable to enlarge or reduce the number of considered valence bond states and therefore building over– or non–complete sets of states. In this case the linear independence of the chosen VB states might not always be guaranteed, thus eventually rendering a decomposition of a singlet state (as Eq. 2.33) non–unique.

In the following, we will give an overview of possible choices of such sets together with their properties.

2.3.1. Non–crossing Valence Bond Basis

Assemble N spins on the circumference of a circle and construct all valence bond coverings such that none of the singlets intersect with each other. Rumer already noticed in 1932, that the number of all such configurations coincides with the number of available singlets

$$\mathcal{N}_N^{s=0} = \frac{N!}{\left(\frac{N}{2}+1\right)! \left(\frac{N}{2}\right)!} = \mathcal{C}_{N/2} \sim \frac{2^N}{N^{3/2}}, \tag{2.35}$$

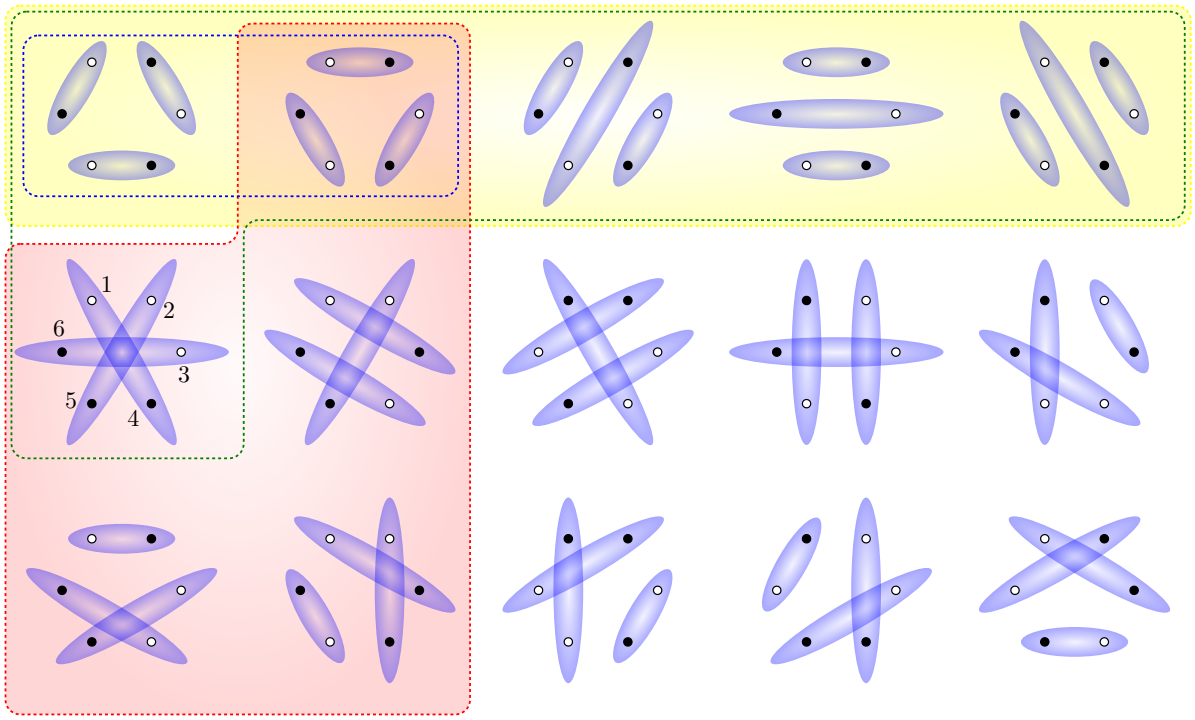

Fig. 2.3.: There are 15 different valence bond states on six sites. Five of them are linearly independent, as for example the non–crossing basis (yellow frame) or any basis induced by the standard Young tableaux (red frame), depending on the chosen ordering. If the sites are interpreted to be part of a hexagonal lattice, then there are two nearest neighbor VB states (blue frame) and six VB states do not contain any second nearest neighbor singlet, thus forming the set of bipartite valence bonds (green frame).

where $\mathcal{C}_n$ are the Catalan numbers that satisfy the recurrence relation

$$\mathcal{C}_{n+1} = \sum_{k=0}^{n} \mathcal{C}_k \mathcal{C}_{n-k}. \tag{2.36}$$

It is easy to see, that the last expression precisely imitates the way to construct non–crossing coverings recursively, i.e. divide the sites on the circle into two parts by putting a singlet across the circle and construct all non–crossing VB states on either part. Considering every possible position of the separating first singlet yields all the non–crossing coverings on the whole circle, an example of which can be seen in Fig. (2.3).

Furthermore Rumer demonstrated the linear independence of all those coverings [4], which was later shown again [23, 22]. Therefore, the non–crossing valence bond coverings form a basis of the singlet subspace, as much as the valence bond states that are obtained with the standard Young tableaux. The proof is based on some *uncrossing relation*, that relates all three different VB states that can be found on four sites.

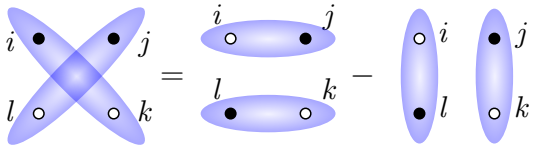

$$|(k,i)(l,j)\rangle = |(i,j)(k,l)\rangle - |(i,l)(k,j)\rangle \tag{2.37}$$

Indeed, this relation can be used to systematically build non–crossing VB states from arbitrary ones. The price to pay is that a single VB state can rapidly turn into an enormous sum of states, which is rather harmful for exact diagonalizations in this basis.

2.3.2. Bipartite Valence Bonds

Another set is formed by the bipartite valence bonds (BVB) that can be constructed as follows. Divide all spins into two different species, such that there are spins of type $\mathcal{A}$ and $\mathcal{B}$ and find all valence bond coverings that form singlets only between spins of different species. The number of possibilities for the first site (on $\mathcal{A}$) is $N/2$, as much as for the second site (on $\mathcal{B}$), thus forming the first singlet. For the second singlet the number of choices is reduced by one, and so on. At the end we have to divide by $(N/2)!$, as the ordering of the dimers within a VB state is not of importance. Therefore the number of bipartite valence bond configurations (see also Fig. 2.3) is given by

$$\mathcal{N}_N^{\mathrm{BVB}} = \frac{\left(\frac{N}{2}\right)^2 \left(\frac{N}{2}-1\right)^2 \cdots 1^2}{\left(\frac{N}{2}\right)!} = \left(\frac{N}{2}\right)! \tag{2.38}$$

It turns out, that for $N > 4$ the number of bipartite VB states grows much faster than the actual number of singlet states, although they span the same space (see Fig. 2.5). This means that there must be some dependencies within these states. Indeed, every crossing bipartite configuration can be expressed in terms of non–crossing coverings by means of Eq. (2.37). Moreover, this expression is also useful to turn any state into sums of bipartite ones. This is not that surprising, as the non–crossing basis is a subset of the bipartite VB states, i.e. all non–crossing singlets also connect spins of different species. This is easy to verify, by alternating the sublattices $\mathcal{A}$ and $\mathcal{B}$ around the circle. Notice, that the valence bonds that are induced by standard Young tableaux do not fulfill this condition, as illustrated in Fig. (2.3).

Whereas the full set of VB states is so far only of theoretical interest, the bipartite valence bonds are also of practical use. Especially on bipartite lattices this offers a natural way of orienting every singlet according to the lattice. Hence, one could in principle forget about the intrinsic orientation of the dimers. Physically, the interactions on a bipartite lattice even force the singlets to form bipartite valence bonds.

An interesting relation can be found when comparing the Néel state

$$|\mathbf{Neel}_z\rangle = \bigotimes_{a\in\mathcal{A},b\in\mathcal{B}} |\uparrow_a\downarrow_b\rangle \tag{2.39}$$

with a BVB state by calculating their overlap

$$\langle \mathbf{Neel}_z \mid \mathbf{BVB} \rangle = 2^{-N/4}. \tag{2.40}$$

Here the bipartite valence bond state is oriented such that every singlet contributes a factor of $1/\sqrt{2}$, when being contracted with the Néel state. The projection of the Néel state into the singlet subspace is then an equal superposition of all these correctly oriented BVB states.

Note, that orienting singlets such as the bipartite valence bonds is also called the *bosonic convention*. As we will see in section (2.3.4), most expressions become particularly simple in this case, rendering the use of bipartite valence bonds slightly more easy than arbitrary VB states. In particular, most expressions involving BVBs will turn out to be positive in sign, which opens the door for methods like Quantum Monte Carlo (QMC). Moreover, the much larger configuration space is not as much of a problem for QMC, while the gain from good variational wave functions, such as the VB ones, is enormous.

2.3.3. Nearest Neighbor Valence Bonds

In contrast to the previous example one can also decrease the number of valence bond configurations, in order to shrink the Hilbert space. In this case the valence bond approach becomes clearly variational and the quality of the results strongly depends on the way of truncating the singlet space. One possibility to achieve this is to restrict the VB coverings such that they only contain singlets connecting neighboring sites of an underlying lattice. The deeper reason for such a step is simple — one could ask which single VB state gives the best variational energy for the AF Heisenberg model. Provided that there are only interactions J_1 between nearest neighbors, we immediately find that all possible coverings that only include such nearest neighbor singlets have the lowest possible energy of $-3NJ_1/8$.

Another motivation comes from variational studies, where Liang, Douçot and Anderson (LDA) [43] assumed the amplitudes of VB states in (2.33) to be of a special form, such that short singlets are privileged, while longer ones are suppressed. The so–called *amplitude product state*, with the coefficients

$$c_{\mathbf{VB}} = \prod_{(k,l)\in\mathbf{VB}} h(k,l) \tag{2.41}$$

and $h(k,l)$ being some function to be optimized, proved to be a very good variational state for the square lattice in the case of AF nearest neighbor interactions. In fact, the best energy is obtained for this ansatz when $h(k,l) \sim |k-l|^{-\gamma}$ decays algebraically in the distance of the two sites k and l, with $\gamma \approx 4$ [43].

In practice nearest neighbor valence bond (NNVB) states are particularly useful when frustration plays a major role and destabilizes magnetic phases. Especially if a singlet–triplet gap opens up, and valence bond crystal or spin liquid phases arise, the restriction of arbitrary long singlets to nearest neighbor ones may be justified. Indeed, this has been

proven a powerful approach on the kagomé [44], square [45] and hexagonal lattice [19] in order to describe non–magnetic phases. Interestingly, NNVB states are linearly independent on many lattices, i.e. those previously mentioned [46, 47], and do therefore also form a basis in these cases. The subspace formed by NNVB states is also referred to as *nearest neighbor valence bond space*. This is of major importance for part III.

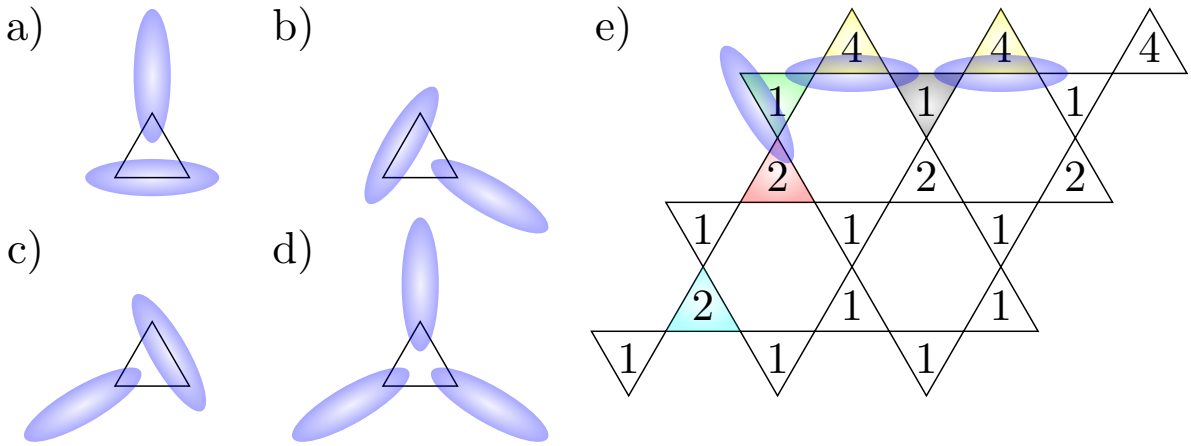

Fig. 2.4.: a–d) Every triangle on the kagomé lattice with PBC can be in one of four different states, when considering NNVBs. e) In order to find all NNVB coverings, we count the number of possibilities of every triangle state from left to right and top to bottom. In the first row, every triangle can be in one of four states. Given the yellow shaded triangles are in state (a), the black triangle can only be in state (d). Similarly, provided the green triangle being in state (c), the red one can be in either (a) or (d). In the last row the choice of the state for the cyan triangle fixes the remaining lattice. In average, every up triangle has two degrees of freedom, whereas down triangles always have one, except the cyan triangle in the last row, which yields another factor two.

In Figure (2.5) we compare the number of valence bond coverings with the full size of the Hilbert space for different choices of VB states. For the kagomé lattice with periodic boundary conditions (PBC) in both directions it is relatively easy to count the number of nearest neighbor configurations. This is described in [48] and relies on the fact that the whole lattice can be divided into two classes of triangles which point up and down respectively. Basically, every triangle can be in four different states, three for each edge that can carry a singlet and one when no edge is dimerized (Fig. 2.4). When glueing the triangles together to form a kagomé lattice, we are left with two degrees of freedom for every triangle of one species, whereas for the other sort of triangles the state is always imposed. Only at the very end, when closing along the boundary conditions we get another degree of freedom. As the total number of triangles is $2N/3$, we therefore have

$$\mathcal{N}_N^{\text{kagomé}} = 2^{\frac{N}{3}+1} \tag{2.42}$$

nearest neighbor valence bond coverings on the kagomé lattice. Notice, that there is also a nice representation by arrows [49, 8], which is completely equivalent to the dimer picture, but renders the counting of different coverings somehow easier.

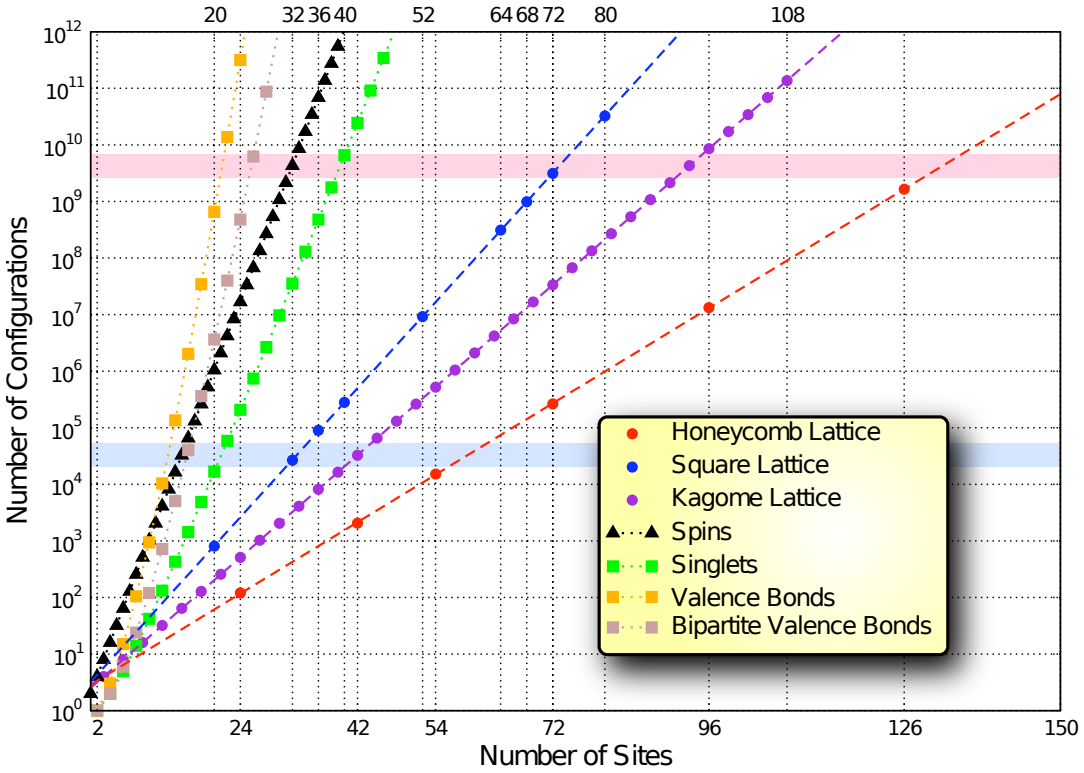

Fig. 2.5.: The size of the Hilbert space as it grows with number of sites for different choices of basis sets. In the S^z–basis there is a total number of 2^N possible spin configurations. Whereas the singlet subspace is much smaller, when sorting out to all VB coverings or only to the bipartite ones the number of configurations even exceeds the size of the Hilbert space very rapidly, signaling the massive over–completeness of such sets. On the other side, for different types of lattices, the nearest neighbor valence bond coverings form a basis of a much smaller subspace [46, 47]. The rough present–day limits for full diagonalization (light blue) and Lanczos ED (light red) are shown for the case where no lattice symmetries are applied.

Square lattice		Honeycomb lattice	
Sites	Coverings	Sites	Coverings
20	808	24	120
32	26 752	42	2 064
36	90 176	54	15 162
40	280 344	72	263 640
52	9 179 048	96	13 219 200
64	311 853 312	126	1 648 213 392
80	32 433 346 832		

Tab. 2.2.: Number of NNVB Coverings on the square lattice and the honeycomb lattice for different clusters with periodic boundary conditions.

On other lattices the number of configurations cannot be obtained as easily, although it is in principle possible to find analytical expressions in some cases. In fact, Fisher [50, 51], Kasteleyn [52, 53] and Temperley [51] have found a method to count the number of NNVB coverings on arbitrary planar graphs, as for instance two–dimensional lattices with open or spherical boundary conditions. The basic idea is to represent the connectivity of the underlying lattice by a skew–symmetric $N \times N$ matrix with entries ± 1 (0) if the corresponding sites are (not) connected. In case the signs in such a matrix are chosen properly, we obtain the number of NNVB tilings by its Pfaffian, which can be calculated efficiently. The difficulty comes from the construction of the right skew–symmetric matrix, which does not seem to be possible for non–planar graphs in general. For planar lattices one can use the Kasteleyn rule [52, 53], which is named after its inventor.

In practice one is often concerned with two–dimensional lattices with toroidal boundary conditions, in which case four Pfaffians have to be evaluated [52, 53]. Here we content ourselves with presenting the results from numerical enumerations, which are summarized in Table (2.2) for the square lattice and the hexagonal one. These values are also plotted in Fig. (2.5) and show that in any case one keeps the exponential growth of the Hilbert space. Restricting the length of the singlets can merely reduce the growth rate, which is however quite an important issue if one wants to use techniques such as exact diagonalization, which attains its limits according to the number of basis states to consider. Therefore, even though the NNVB approach is a variational approximation, it is rather valuable in order to reduce numerical complexity.

2.3.4. Bipartite Overlap Graphs

After having introduced the different types of valence bond states and their graphical representation by oriented dimers, it is now advisory to look at the action and representation of a singlet projection operator onto such a state. It can be shown easily, that a singlet projector is related to the spin operators by

$$\hat{P}^{s=0}_{kl} := |(k,l)\rangle \langle (k,l)| = \frac{1}{4} - \hat{\boldsymbol{S}}_k \cdot \hat{\boldsymbol{S}}_l. \tag{2.43}$$

As this operator consists of a tensor product of two singlets defined on the same sites, it is certainly symmetric under the exchange of the site indices and we can express this graphically as

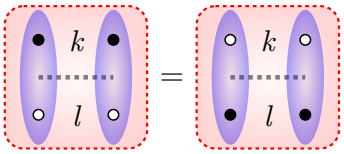

$$\hat{P}^{s=0}_{lk} \quad = \quad \hat{P}^{s=0}_{kl}. \tag{2.44}$$

The fact that the two singlets form one object is illustrated by a dashed gray line. Now, in order to establish the rules to evaluate more complex expressions containing valence bonds we need to express several of their properties and relations to the singlet projector.

First of all, the singlets are normalized, which can be illustrated by the following equation

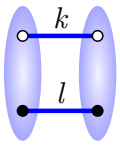

$$= 1$$

$$\langle (k,l) \mid (k,l) \rangle = 1. \tag{2.45}$$

Notice, that the scalar product is represented by straight (blue) lines, which indicate over which indices we have to contract the singlets in order to get a number. The action of a singlet projector onto a singlet can be represented in a similar way

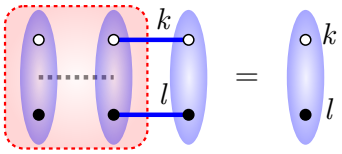

$$\hat{P}^{s=0}_{kl} \quad |(k,l)\rangle = |(k,l)\rangle\,, \tag{2.46}$$

where we simply get a singlet as result. Notice, that this rule appears as if there was not the dashed line within the operator and we just applied rule (2.45). This is of course no surprise, as exactly the same behavior is already encoded in the Dirac notation. It should be noticed furthermore, that the orientation of the singlet projector with respect to the dimer does not matter, as the singlet projector is a symmetric object (2.44).

When applying a singlet projector on two sites that are part of two distinct singlets, there are in principle two different possibilities. At the moment it is sufficient to consider the first one, where all dimers are oriented according to the bipartite convention (see section 2.3.2). Within such a convention we do not generate a sign and it is easy to verify that

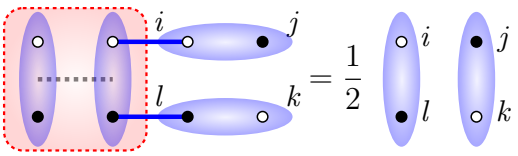

$$\hat{P}^{s=0}_{il} \quad |(i,j)(k,l)\rangle = \frac{1}{2}\,|(i,l)(k,j)\rangle\,. \tag{2.47}$$

This relation can for example be shown by using the definition of a singlet (2.28). The important thing to notice here is that three connected singlets are replaced by one and the loss is compensated by a factor 1/2.

We can now construct *bipartite overlap graphs*, that consist of a projection chain of bipartite singlet projectors, sandwiched between bipartite valence bonds. Such a graph will always form a certain number of *closed loops*. The important point here is that every singlet has to connect a site of type $\mathcal{A}$ with a site of type $\mathcal{B}$, as depicted in Fig. (2.6). This ensures that every contraction is performed between sites of the same type and described by equations (2.45), (2.46) or (2.47).

The contraction rules are summarized as follows: Whenever two singlets disappear as result of a contraction over two sites, we generate a factor 1/2, except in the case where a closed loop disappears as well. Therefore, a bipartite overlap graph can be evaluated graphically by

$$\langle \mathbf{BVB}_1 | \prod_{(k,l)\in \mathbf{BVB}} \hat{P}^{s=0}_{kl} \, | \mathbf{BVB}_2 \rangle = 2^{N_\bigcirc - N_D/2}, \tag{2.48}$$

where $N_\bigcirc$ denotes the number of loops that disappeared, N_D is the corresponding number of singlets and the product is made over a set of bipartite indices $(k,l) \in \mathbf{BVB}$.

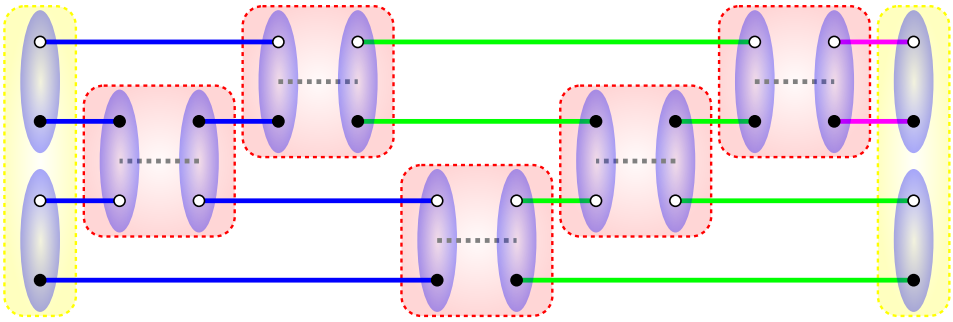

Fig. 2.6.: Bipartite overlap graph of two BVB states (yellow frames) with five singlet projectors in between (red frames). There are $N_\bigcirc = 3$ closed loops (blue, green and magenta) and $N_D = 14$ singlets in total, hence this graph evaluates to $2^{3-14/2} = 1/16$. The total graph resides on 4 sites that can be found in the vertical direction, whereas the horizontal one corresponds to the projection.

It should be noticed additionally, that the number of sites N in a closed overlap graph is related to the number of singlet projectors N_P by

$$N_D = N + 2N_P. \tag{2.49}$$

Hence, when there are no projectors in such a graph we recover the well–known overlap rule for bipartite VB states [11]

$$\langle \mathbf{BVB}_1 \mid \mathbf{BVB}_2 \rangle = 2^{N_\bigcirc - N/2}. \tag{2.50}$$

Therefore, VB states are always non–orthogonal to each other, which explains how the set of arbitrary ranged valence bond states can contain much more elements than the actual size of the singlet space. This is indeed a major problem when working with VBs, as it involves solving the general eigenvalue problem in order to diagonalize a Hamiltonian in a non–orthogonal basis.

Note, that the substitution of the bipartite valence bond state $|\mathbf{BVB}_1\rangle$ in Eq. (2.48) by the Néel state $|\mathbf{Neel}_z\rangle$ would result in an open overlap graph. In absence of any singlet projector, the number of closed loops $N_\bigcirc$ would be zero and the number of dimers N_D would be half the number of sites. This is hence another way to derive Eq. (2.40).

A further rule can be established if we try to insert a singlet projector $\hat{P}^{s=0}_{kl}$ into an existing bipartite overlap graph. There are in principle two possible scenarios.

- First of all, the site indices k and l can be situated on the same loop, such that $\hat{P}_{kl}^{s=0}$ divides it into two. Therefore we would generate a new graph with one additional loop, but also two supplementary singlets, yielding a graph that evaluates to the same value as the initial one. This corresponds to case a) in Fig. (2.7), where the blue loop is divided into a blue and a red one.
- Secondly, k and l can lie on two distinct loops, such that $\hat{P}_{kl}^{s=0}$ would finally join them. Thus, we destroy a closed loop while still adding two singlets. This time the new graph can be contracted to a value of one quarter of the initial graph. The situation is depicted in case b) of Fig. (2.7), with the projector joining the blue and the green loop.

Summarizing the two cases, we find the following result for bipartite overlap graphs

$$\frac{\langle \mathbf{BVB}_1 | \, \hat{P}_{kl}^{s=0} \, | \mathbf{BVB}_2 \rangle}{\langle \mathbf{BVB}_1 \mid \mathbf{BVB}_2 \rangle} = 4^{\delta_{\lambda_k,\lambda_l}-1}, \tag{2.51}$$

where $\delta_{\lambda_k,\lambda_l}$ is one (zero) if k and l lie one the same (different) loop. This result is also well–known [11, 54] and is an example of observables which can be obtained simply from the loop structure of the overlap graph of two superimposed VB states.

2.3.5. Generic Overlap Graphs

Up to this point contractions were always performed between sites of the same species, i.e. sites that are both illustrated by the same color. In general however, it is also possible to contract over different kinds of sites, which usually happens when the lattice is not bipartite anymore. In such a situation we simply need to flip the singlets on every loop in order to restore the matching of the sites, e.g.

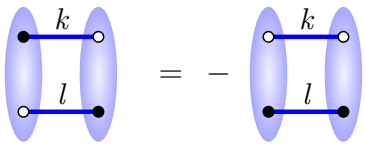

$$\begin{aligned} \langle (l,k) \mid (k,l) \rangle &= - \langle (k,l) \mid (k,l) \rangle \\ &= -1. \end{aligned} \tag{2.52}$$

Performing this wherever necessary, we will end up with a *regular overlap graph*, that only contains contractions over sites of the same color (see Figs. 2.6 and 2.7). This is always possible, as every loop contains by construction an even number of dimers. However, we will introduce a factor -1 for every flipped singlet (compare Eq. 2.30) and thus a general overlap graph evaluates to

$$\langle \mathbf{VB}_1 | \prod_{(k,l)\in\mathbf{VB}} \hat{P}_{kl}^{s=0} \, | \mathbf{VB}_2 \rangle = (-1)^{n_{fs}} 2^{N_\bigcirc - N_D/2}, \tag{2.53}$$

where n_{fs} denotes the number of singlets to flip in order to heal the contraction mismatches. In contrast to Eq. (2.48), here we not only need to count the number of loops

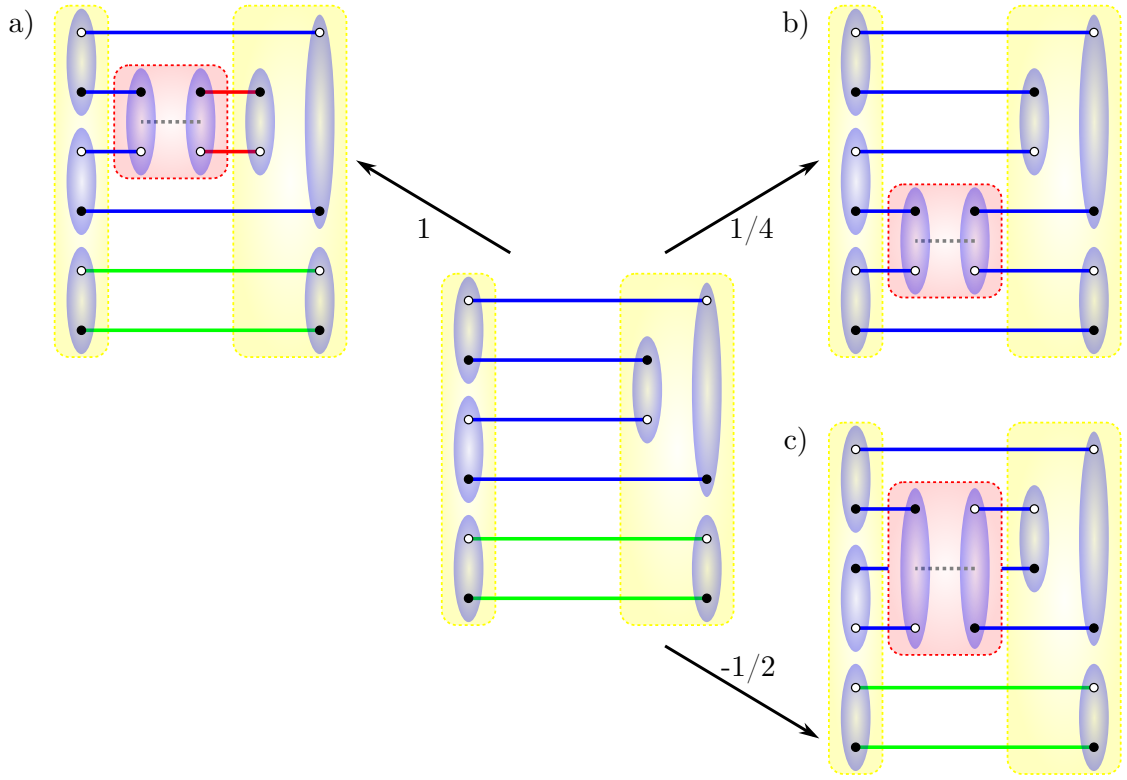

Fig. 2.7.: Possible values of the loop estimator $\langle \mathbf{VB}_1 | \hat{P}_{kl}^{s=0} | \mathbf{VB}_2 \rangle / \langle \mathbf{VB}_1 \mid \mathbf{VB}_2 \rangle$. The insertion of a projector also adds two singlets to the graph. a) One additional loop (red) is formed when there is an odd number of singlets between the two sites k and l. b) The two initial loops (blue and green) are joined to a single one (blue) in case k and l lie on different loops. c) No additional loop is formed, but three singlets have to be flipped in order to match the contraction sites. Here the number of singlets between k and l is even.

but also flip singlets in order to evaluate the overall sign. This is rather undesirable for practical calculations and we therefore present a way out in the following.

Firstly, generalizations of the loop estimator $\langle \mathbf{VB}_1 | \hat{P}_{kl}^{s=0} | \mathbf{VB}_2 \rangle / \langle \mathbf{VB}_1 \mid \mathbf{VB}_2 \rangle$ that were not allowed in the bipartite case (Eq. 2.51) have to be considered. Here, we need to distinguish three different cases, which are summarized in Fig. (2.7).

- The singlet projector $\hat{P}_{kl}^{s=0}$ can be inserted into one loop, such that the two site indices k and l are separated by an odd number of singlets. In this case the loop estimator evaluates to one.

- $\hat{P}_{kl}^{s=0}$ can join two loops and the loop estimator will be $1/4$.

- A new case appears, when the projector is inserted into a single loop, but the separation of the two sites k and l is given by an even distance. This yields a factor $-1/2$ and is not allowed in the bipartite case.

The interesting point is that apparently the allowed values are multiples of $-1/2$ and we can apply this to a normalized reference state $\langle \mathbf{VB}_0 \mid \mathbf{VB}_0 \rangle = 1$. Overlap graphs containing this state will always evaluate to

$$\langle \mathbf{VB}_0 | \prod_{(k,l)\in \mathbf{VB}} \hat{P}_{kl}^{s=0} | \mathbf{VB}_0 \rangle = (-2)^{N_\bigcirc - N_D/2}. \tag{2.54}$$

Of course, this is true for any valence bond state, and is not in contradiction to Eq. (2.48). Indeed, if we restrict ourselves to bipartite interactions, the minus sign will be absorbed by an even exponent. Furthermore, here the projection chain is sandwiched between the same state $|\mathbf{VB}_0\rangle$. However, it would be desirable to have a formula for every overlap graph such that the sign can be absorbed into the basis. In that case it would not be necessary anymore to count the number of singlets to flip. This is indeed possible [55, 15] and is called the *fermionic convention*.

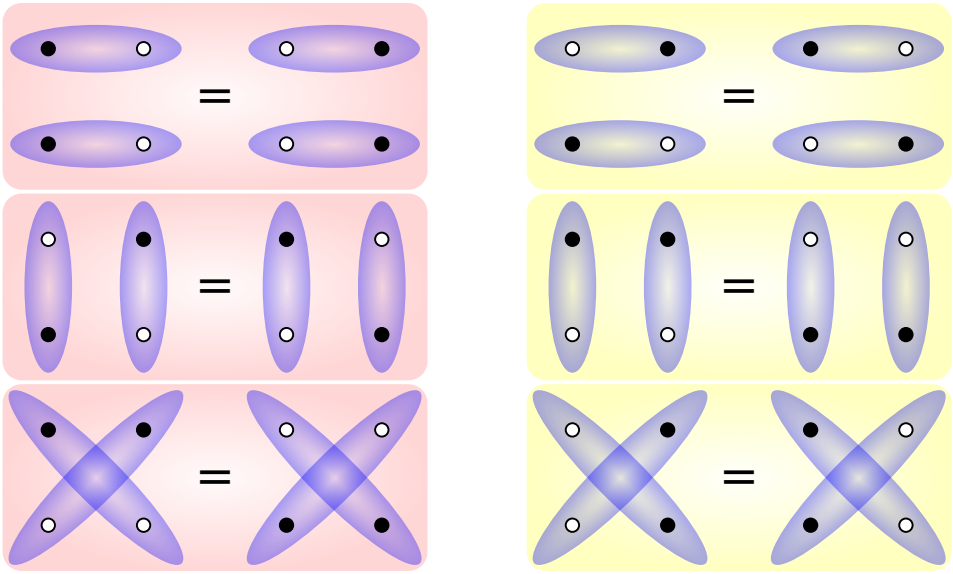

Fig. 2.8.: Fermionic convention. There is a total number of twelve valence bond states on four sites, only 3 of which are not related by a phase factor. The red frame shows one set of VB states within a fermionic convention. The other possible fermionic convention is obtained by flipping one singlet (yellow frame).

The idea is that when choosing the set of valence bond states we have actually neglected some degrees of freedom which we will now account for. Every singlet can be flipped by permuting the two site indices on which it is defined, hence introducing a sign into the overall VB state. As an example, on four sites there is a total number of 12 VB states (see Fig. 2.8). However, only three of them are not related by a relative phase factor. The goal is now to pick the right states among the full set of VB states, such that every overlap graph contracts to

$$\langle \mathbf{VB}_1 | \prod_{(k,l)\in \mathbf{VB}} \hat{P}_{kl}^{s=0} | \mathbf{VB}_2 \rangle = (-2)^{N_\bigcirc - N_D/2}. \tag{2.55}$$

The way to do this is already given in Eq. (2.54). We simply need to use all valence bond states which are included in the reference overlap graph, that is

$$(-2)^x \left|\mathbf{VB}_1\right\rangle := \prod_{(k,l)\in\mathbf{VB}} \hat{P}_{kl}^{s=0} \left|\mathbf{VB}_0\right\rangle, \tag{2.56}$$

and x has to be chosen such that $\langle \mathbf{VB}_1 \mid \mathbf{VB}_1\rangle = 1$ is normalized. Fig. (2.8) illustrates the fermionic convention on four sites.

Therefore it is possible to systematically absorb the sign in the overlap rule. It should be emphasized, that the fermionic convention is always possible, on any lattice. However, the sign is generally not desirable, especially if we want to do Monte Carlo simulations. Therefore, on bipartite lattices one will always sort out to the bosonic convention, which does not introduce a negative sign into the overlap rule.

We can now extend Eq. (2.51) by considering all cases in Fig. (2.7). Using Eq. (2.43) we arrive at the well–known result for spin–spin correlations in the general case

$$\frac{\langle \mathbf{VB}_1 | \, \hat{\boldsymbol{S}}_k \cdot \hat{\boldsymbol{S}}_l \, |\mathbf{VB}_2\rangle}{\langle \mathbf{VB}_1 \mid \mathbf{VB}_2\rangle} = \varepsilon_{kl} \delta^{\lambda_k,\lambda_l} \frac{3}{4}, \tag{2.57}$$

where $\varepsilon_{kl} = 1$ ($\varepsilon_{kl} = -1$) when k and l lie at an even (odd) distance on the same loop and λ_k and λ_l are the loop indices. Thus, we only have non–zero spin–spin correlations when the two sites lie on the same loop. This relation, as well as a derivation of four spin correlations can be found in [54] for example. This review also provides many other results about valence bond states.

2.4. Partial Conclusion

In this chapter we have introduced the basic concepts of valence bond theory, such that they can be applied in the following chapters. We have shown how valence bond states describe the $\hat{\boldsymbol{S}}^2 = 0$ subspace for spins and illustrated the connection to Young tableaux.

The key result of this chapter is the slight generalization of the well–known overlap formula for two valence bond states $|\mathbf{VB}_1\rangle$ and $|\mathbf{VB}_2\rangle$ sandwiching a chain of singlet projectors

$$\langle \mathbf{VB}_1 | \prod_{(k,l)\in\mathbf{VB}} \hat{P}_{kl}^{s=0} \left|\mathbf{VB}_2\right\rangle = (\pm 2)^{N_\bigcirc - N_D/2}. \tag{2.58}$$

This important formula only needs the number of loops $N_\bigcirc$ of the overlap graph, as well as the number N_D of singlets that it contains. While the "+" applies only to bipartite lattices by choosing the bosonic convention, the "−" is true in any case. One simply has to take the fermionic convention, which in principle needs a reference state $|\mathbf{VB}_0\rangle$. However, this state is only of theoretical interest, as the evaluation in practice does not rely on the specific choice of such a state.

The existence of both, the bosonic and the fermionic convention allows furthermore for a simplification of the representation of singlets. It is not necessary anymore to keep

track of their orientation, only the chosen convention has to be remembered of. Hence, we can in principle draw a singlet as

without any orientation.

This rises another interesting question: How many regular overlap graphs are actually contained in such an orientationless one? The answer is simple, every closed loop can be in one of two possible states, which can be obtained from each other by flipping all of their singlets. Thus, there is a total number of $2^{N_\bigcirc}$ regular loops that are fully equivalent, illustrating another way in which the overlap rule can be interpreted: an overlap graph can also be represented by the sum over all equivalent regular ones, where the evaluation of each of these does not account for the number of loops $N_\bigcirc$ but only for the number of singlets N_D.

Another important fact that follows from Eq. (2.58) is that valence bond states are strictly non–orthogonal. This renders any computation non–standard and more complicated if one was to diagonalize matrices exactly within for example the Lanczos ED method. Furthermore, the vast over–completeness of VB states yields an extra limitation factor for such methods.

On the other side both, over–completeness and non–orthogonality are not that difficult to handle within stochastic schemes like Quantum Monte Carlo. Indeed, the recently developed valence bond QMC [12, 13, 56] turns out to be a quite powerful method to describe the ground state of the antiferromagnetic Heisenberg model. However, this method suffers from the famous sign problem and is therefore not adapted to frustrated systems.

Finally, it shall be mentioned that observables, which contain $\hat{\boldsymbol{S}}_k \cdot \hat{\boldsymbol{S}}_l$, $\hat{P}_{kl}^{s=0}$ or the permutation operator $\hat{\mathcal{P}}_{kl} = 1 - 2\hat{P}_{kl}^{s=0}$, can all be expressed in terms of loop estimators, similar to Eq. (2.57) [54]. Furthermore, these estimators do not depend on whether the fermionic or the bosonic convention is chosen. Therefore, energy, sublattice magnetization and other important quantities can be calculated very easily within the valence bond basis picture [13].

3. Numerical Methods

Although the Schrödinger equation looks very simple, its solutions are generally very non–trivial and hard to find. This can be seen from the fact, that the number of exactly solvable models that an undergraduate student sees when learning quantum mechanics is usually very small, compared to classical physics. Another indicator are models, which have been proposed in the early days after the formulation of quantum mechanics, such as the Heisenberg model, that are still not fully solved and therefore play an important role in current research.

One of the major problems in solving the Schrödinger equation comes from the fact that the size of the Hilbert space grows exponentially with the number of particles. This is where computational resources and numerical methods become very interesting, as these help to solve problems in a reasonable amount of time, when analytical solutions are non–accessible.

In order to solve physical problems on computers, we need appropriate algorithms that can be efficiently executed. Cipra [57] names the top 10 algorithms of the 20th century and it is very interesting to see that most of them play a very active role in solving quantum mechanical problems.

Undoubtedly, the development of the Fortran compiler by Backus has opened the door for simulations among the physicists community. But also the Householder decomposition and the QR algorithm are that important, that they are implemented in standard linear algebra packages such as LAPACK [58], which is written in Fortran and widely used in physics. Other examples, like Quicksort and the fast Fourier transform, belong to the standard algorithms taught in computer science or physics.

Moreover, there are two other algorithms among the top 10, which are particularly important in condensed matter, namely the Monte Carlo (Metropolis) [59] and the Lanczos algorithm [60, 61], which shall be illustrated in this chapter.

3.1. Monte Carlo Algorithm

The solution to many problems in physics lies in the evaluation of higher dimensional integrals and sums, which in the vast majority of the cases, has to be done numerically or approximatively, because the underlying model is not integrable. Consider for example a sum[1] of the form

$$\mathcal{S} = \sum_{u \in \mathcal{C}} f(u), \tag{3.1}$$

[1] Integrals can be treated in precisely the same way.

where $f(u)$ is some function defined in the configuration space $\mathcal{C}$ and u labels all points in the latter. The idea is to rewrite the sum by means of another function $w(u)$

$$\mathcal{S} = \sum_{u\in\mathcal{C}} \frac{|w(u)|}{\sum_v |w(v)|} \cdot \frac{f(u)\sum_v |w(v)|}{|w(u)|} \tag{3.2}$$

$$= \sum_{u\in\mathcal{C}} \Pi(u)\cdot O(u), \tag{3.3}$$

with

$$\Pi(u) = \frac{|w(u)|}{\sum_v |w(v)|} \tag{3.4}$$

being a weight function, i.e. $\Pi(u) \geq 0$ and $\sum_u \Pi(u) = 1$. The result can now be interpreted as the expectation value of the function $O(u)$, thus indicating a possible stochastic evaluation very similar to a measurement. This can be achieved by randomly picking $u \in \mathcal{C}$ according to the distribution $\Pi(u)$, and calculating the mean of $O(u)$ of the different *measured* $O(u)$, hence

$$\mathcal{S} = \langle O(u)\rangle_{\Pi(u)}\,. \tag{3.5}$$

However, when sorting out to stochastic integration, we are concerned with statistical errors, which are given by the sample standard deviation

$$\Delta\mathcal{S} = \sqrt{\frac{\langle O(u)^2\rangle_{\Pi(u)} - \langle O(u)\rangle^2_{\Pi(u)}}{N-1}}. \tag{3.6}$$

This actually defines the duration of a Monte Carlo simulation, as the error decreases as $\propto 1/\sqrt{N}$. Thus we need to gather a sufficient amount of measurements to increase the precision, resulting in potentially rather long simulations. To work around this one can also introduce *improved estimators*, which are simply other quantities that have the same mean with a smaller variance. Every improvement on the variance is also an improvement on CPU time, as we reduce fluctuations with this technique! Therefore it is worth, putting some effort on that before actually implementing the algorithm. A very general way of finding improved estimators is shown in [62] and tries to find a response function that compensates the fluctuations.

It should be noticed, that Eqs. (3.5 and 3.6) are true for any type of Monte Carlo simulation, if the measurements are statistically independent. Therefore ideally we want to have (quasi–)uncorrelated data. Quantitatively, we can measure the autocorrelation[2]

$$K_{\mathcal{S}}(t) = \langle O(u_0)O(u_t)\rangle_{\Pi(u)} - \langle O(u_0)\rangle_{\Pi(u)}\langle O(u_t)\rangle_{\Pi(u)} \tag{3.7}$$

between different measurements, which should vanish for uncorrelated data. In practice $K_{\mathcal{S}}(t)$ will rather decay exponentially for long times with some characteristic time τ, which is called *autocorrelation time*. This time should be smaller than the time between subsequent measurements, otherwise we risk to sample the configuration space inefficiently, resulting in much longer simulation times.

[2]This quantity is also called *autocovariance* sometimes.

The autocorrelation has to be accounted for when calculating the mean or the variance. Furthermore, analyzing (relatively) small samples of measurements can be a bit tricky if one wants to have reliable information about the full configuration space. For this purpose there are methods like bootstrap [63] or Jackknife [64, 65], which are basically resampling the sample in a different way, in order to account for possible fluctuations in the result. These methods allow also for computing the autocorrelation time.

Another possible source of error can be the use of unreliable random number generators. In fact, computers can generally only create pseudo–random numbers, which are rooted in deterministic algorithms. However, there are different generators like the Mersenne twister [66] as well as the Lagged Fibonacci generator, which are sufficient for most practical purposes. Nevertheless, we should keep in mind that data can depend on the random number generator and it is therefore always a good idea to double check this if the solution we get seems to be unphysical.

Fortunately, fast and reliable random number generators as well as analysis tools such as Jackknife are implemented in the *Algorithms and Libraries for Physics Simulations* (ALPS [67, 68]). These are written in `C++` and allow for an easy and platform independent implementation of sophisticated simulations like Monte Carlo. Furthermore, also parallelization and scheduling are already implemented, allowing for high performance simulations without much prior knowledge on clusters and supercomputers.

3.1.1. Metropolis–Hastings Algorithm

The Monte Carlo method introduced in the previous section only works this easily, when the probability distribution $\Pi(u)$ is uniform or at least very simple and the configuration space $\mathcal{C}$ bounded. Furthermore, we would need a direct mapping from the configuration space label $u \in \mathcal{C}$ to the actual configurations. In most practical cases however, at least one of the previous conditions is not satisfied. Therefore, there is no obvious way to generate configurations with the distribution $\Pi(u)$ simply by picking random numbers.

The way out of this is considering Markov chains, where subsequent configurations are created from previous ones. This has first been realized by Metropolis *et al.* [59] and was later generalized and formalized by Hastings [69]. Using this approach, it is in principle possible to sample any complicated weight function $\Pi(u)$, even if its precise normalization constant is not known. Some theory on this will be presented in following, based on [70]. We will however try to put matrices and vectors in Dirac notation, which makes the formulae look much simpler.

Firstly, we notice that the coordinates u in the configuration space $\mathcal{C}$ can generally be represented by an orthonormalized set of basis vectors $|u\rangle$. The (real–valued) weight $\Pi(u)$ and the estimator $O(u)$ can be seen as vectors defined on every point in configuration space. Thus we interpret the weighted sum

$$\mathcal{S} = \sum_{u \in \mathcal{C}} \Pi(u) \cdot O(u) \tag{3.8}$$

$$= \langle \Pi \mid O \rangle \tag{3.9}$$

as scalar product between the weight vector and the estimator vector. We then formally define some vector, which is the equal superposition of all basis states $\{|u\rangle\}$

$$|\oplus\rangle = \sum_u |u\rangle \,. \tag{3.10}$$

For this vector we clearly have $\langle u|\oplus\rangle = 1 \quad \forall u$, and the fact that we want $\Pi(u)$ to be normalized can be expressed as

$$\langle\oplus|\Pi\rangle = \sum_u \langle u|\Pi\rangle \tag{3.11}$$

$$= 1. \tag{3.12}$$

Notice that here the word *normalized* has to be seen in a probabilistic and not in a quantum mechanical sense, where we would like the sum of the squares to be equal to one. But this is only a technical issue and is much of importance than the fact that $\Pi(u)$ needs to be strictly positive. By construction, the weight function is non–negative and we will now exclude all points from configuration space that accidentally happen to have zero weight. These do not change the sum $\mathcal{S}$ and can always be explicitly avoided in an algorithm.

What we then want is a prescription that takes us randomly through the points in configuration space

$$|u_0\rangle \to |u_1\rangle \to |u_2\rangle \to |u_3\rangle \to \cdots \to |u_N\rangle \,.$$

This Markov chain can be built with a left stochastic matrix P, i.e. a matrix with left eigenvector $\langle\oplus|\, P = \langle\oplus|$ and with eigenvalue 1. If the corresponding right eigenvector is $P\,|\Pi\rangle = |\Pi\rangle$ and P is ergodic then the Markov chain converges to the stationary distribution $|\Pi\rangle$. The demonstration is very short and shall be presented in the following.

The requirement of P being ergodic is simply the property that each configuration can be reached from every other one in a finite number of steps. This means that the whole configuration space will be sampled, if the simulation is long enough. In other words, there is some power n, for which P^n has only strictly positive matrix elements $\langle v|P^n|u\rangle > 0$. In that case the Perron–Frobenius theorem states that the spectral radius of P is a unique eigenvalue with strictly positive (left and right) eigenvector. These eigenvectors are readily given by $\langle\oplus|$ and $|\Pi\rangle$ and therefore we have $\lim_{n\to\infty} P^n = |\Pi\rangle\langle\oplus|$. Starting with some arbitrary configuration $|u_0\rangle$, we immediately see, that

$$\lim_{n\to\infty} P^n\,|u_0\rangle = |\Pi\rangle\langle\oplus|u_0\rangle \tag{3.13}$$

$$= |\Pi\rangle \,. \tag{3.14}$$

The interpretation of the last equation is the following: we start with some (deterministic) configuration $|u_0\rangle$ and with the help of the stochastic transition matrix P we randomly create a new configuration $|u_1\rangle$. The randomness comes from the fact, that we only know that the possible new configurations are distributed as $|u_1\rangle \sim P\,|u_0\rangle$. But this is not precisely what we want — we rather need $|u_n\rangle \sim |\Pi\rangle$. Therefore we need

to wait several steps, until n is large enough and the Markov chain has finally reached the stationary distribution $|\Pi\rangle$. In the language of Monte Carlo simulations we call this effect *thermalization*.

The thermalization effect is usually visible in Markov chain Monte Carlo, where the first measurements are often far off the rest. Therefore one normally discards these data and only calculates observables after the Markov chain has reached equilibrium. A thumb rule is that for about 10% of the simulation we do not measure anything and after that we suppose the system to have thermalized. However, this can be checked by visualizing the time evolution of the measurements, or simply by considering autocorrelation times.

The remaining question is how the transition matrix P is actually constructed explicitly. The answer to this is given in [59, 69]. There, the transition probability is split up into *proposal* $\langle u_{n+1}|S|u_n\rangle$ and *acceptance* $\langle u_{n+1}|A|u_n\rangle$

$$\langle u_{n+1}|P|u_n\rangle = \langle u_{n+1}|S|u_n\rangle \langle u_{n+1}|A|u_n\rangle . \tag{3.15}$$

This means that a new configuration is suggested with $\langle u_{n+1}|S|u_n\rangle$ and is then accepted with $\langle u_{n+1}|A|u_n\rangle$. In most cases one chooses S to be symmetric and uniform, which is however not necessary. The standard choice for the acceptance probability in the Metropolis–Hastings algorithm is given by

$$\langle u_{n+1}|A|u_n\rangle = \min\left(1, \frac{\langle u_n|S|u_{n+1}\rangle \langle u_{n+1}|\Pi\rangle}{\langle u_{n+1}|S|u_n\rangle \langle u_n|\Pi\rangle}\right). \tag{3.16}$$

A suggested move $|u\rangle \to |v\rangle$ can therefore be accepted or rejected. In the latter case we end up with $|u_{n+1}\rangle = |u_n\rangle$, so we keep the last configuration and have to *measure again* in the same state. This is an effect which is usually unwanted, as Monte Carlo simulations aim to sample a large amount of the configuration space. Therefore the goal is to construct an algorithm with a rather important acceptance probability in order to increase the chance of independent measurements.

This essentially means to decrease the autocorrelation time and for this purpose there is another important issue. It is actually quite important to choose a clever updating scheme, i.e. the suggested move should not only be accepted with high probability, but also generate a configuration which is sufficiently far away in configuration space. A very successful strategy to tackle both problems is to consider cluster updates instead of local ones. This way the configuration space can be sampled rather efficiently and not only in a single region. An example of such cluster methods are loop updates, which are applied in several QMC schemes [71, 72, 73, 74, 13].

For the remaining part of this section we will demonstrate, that the Metropolis–Hastings acceptance rate (Eq. 3.16) does indeed build the required Markov chain. Clearly, P is ergodic, if S is, that means, if the suggested moves allow to reach every possible configuration after some time, then there is also some finite probability that all of these are indeed sampled.

Secondly, we have to consider rejected moves properly, which leads to

$$\langle u|P|u\rangle = \langle u|S|u\rangle + \sum_{v\neq u} \langle v|S-P|u\rangle \tag{3.17}$$

$$= \langle \oplus|S|u\rangle - \sum_{v\neq u} \langle v|P|u\rangle\,, \tag{3.18}$$

where the first term corresponds to the case that does not suggest any move (Eq. 3.15), while the second term accounts for all rejected moves. Thus, it is easy to see that if S is a left stochastic matrix, then P does meet the same condition, i.e $\langle\oplus| = \langle\oplus|\,S = \langle\oplus|\,P$. Finally, we show that P satisfies the *detailed balance* condition, which is expressed as

$$\langle v|P|u\rangle\,\langle u|\Pi\rangle = \min\left(\langle v|S|u\rangle\,\langle u|\Pi\rangle\,, \langle u|S|v\rangle\,\langle v|\Pi\rangle\right) \tag{3.19}$$

$$= \langle u|P|v\rangle\,\langle v|\Pi\rangle\,, \tag{3.20}$$

and can be seen easily by replacing Eq. (3.16) into Eq. (3.15). This is a sufficient but not a necessary condition for $|\Pi\rangle$ being a right eigenvector of P, as

$$\langle v|P|\Pi\rangle = \sum_u \langle v|P|u\rangle\,\langle u|\Pi\rangle \tag{3.21}$$

$$= \sum_u \langle u|P|v\rangle\,\langle v|\Pi\rangle \tag{3.22}$$

$$= \langle v|\Pi\rangle\,. \tag{3.23}$$

Here the second line was obtained by applying detailed balance, and the last line through $\langle\oplus|\,P = \langle\oplus|$ and $\langle\oplus|v\rangle = 1$. Hence, the Metropolis–Hastings acceptance rate will make the Markov chain converge into the stationary distribution $|\Pi\rangle$.

A very useful property of this algorithm is that the calculation of the acceptance rate does not require the overall normalization factor of the weight function $w(u)$, as $\Pi(u_{n+1})/\Pi(u_n) = w(u_{n+1})/w(u_n)$. Indeed, in practice this overall factor is not known or cannot be obtained easily. However, the particular structure of Eq. (3.16) will induce that regions with more weight $w(u)$ will be scanned with higher probability. This effect is called *importance sampling*.

Another point that should be mentioned is that the Metropolis–Hastings algorithm satisfies the detailed balance condition as much as Glauber dynamics or the heat bath algorithm, which calculate the acceptance rate in a different way. However, there are Markov chain Monte Carlo schemes, that do not explicitly obey this. Suwa and Todo have demonstrated recently, how to improve on the acceptance rate by relinquishing the detailed balance [75].

In practice one often distinguishes the *classical Monte Carlo* from *Quantum Monte Carlo* (QMC). This distinction comes simply from the fact, that we can simulate classical systems as well as quantum mechanical ones. It should be emphasized, that this has no deeper mathematical meaning, as both types are based on the stochastic evaluation of sums like Eq. (3.1). Historically, this distinction is based on the fact that weight factors from statistical physics, such as the Boltzmann factor, are always positive, while in quantum mechanics we often meet negative (or complex) factors.

3.1.2. Valence Bond Monte Carlo

Recently, Sandvik [12, 56, 13] has proposed a Quantum Monte Carlo scheme within the valence bond basis, which extracts ground state properties of bipartite $SU(2)$ models. This algorithm is a stochastically evaluated projection formalism, which is expressed by bipartite valence bonds as introduced in chapter 2.

The ground state projection is based on the fact that the eigenvector $|v_0\rangle$, corresponding to the dominant eigenvalue of a hermitian operator $\hat{\mathcal{H}}_0$, can be extracted by repeatedly applying $\hat{\mathcal{H}}_0$ to some initial vector $|u\rangle$, i.e.

$$|v_0\rangle \sim \frac{\hat{\mathcal{H}}_0^n |u\rangle}{\sqrt{\langle u| \hat{\mathcal{H}}_0^{2n} |u\rangle}}. \tag{3.24}$$

We only require that the initial vector is not orthogonal to the dominant eigenvector $\langle u \mid v_0\rangle \neq 0$ and all other eigenvalues are smaller in absolute value than the dominant one. Numerically, the first requirement is in practice always satisfied, as it is almost impossible to arbitrarily generate a vector orthogonal to $|v_0\rangle$, provided the initial vector is from the right symmetry sector. Indeed, one can choose $|u\rangle$ to be a triplet state, such that $|v_0\rangle$ becomes the ground state of the triplet sector [56]. Such a behavior should in principle be possible in every sector of symmetry. Within a given sector, even if one accidentally succeeds to choose a $|u\rangle$ orthogonal to $|v_0\rangle$, rounding errors will most probably lift the orthogonality and a small finite overlap with $|v_0\rangle$ will guide the projection to the right ground state.

For the second condition we need to make sure, that there is only one dominant eigenvalue, which can in principle be degenerated. This can always be achieved by shifting the operator $\hat{\mathcal{H}}_0$ appropriately. For the AF Heisenberg model

$$\hat{\mathcal{H}} = \sum_{k,l=1}^{N} J_{kl} \hat{\boldsymbol{S}}_k \cdot \hat{\boldsymbol{S}}_l \tag{3.25}$$

we know the highest energy eigenvalue

$$E_{max} = \frac{1}{4} \sum_{k,l=1}^{N} J_{kl}, \tag{3.26}$$

hence the spectrum of

$$\hat{\mathcal{H}}_0 = E_{max} - \hat{\mathcal{H}} = \sum_{k,l=1}^{N} J_{kl} \hat{P}_{kl}^{s=0} \tag{3.27}$$

is positive with its dominant eigenspace corresponding to the ground space of $\hat{\mathcal{H}}$. Here we have used Eq. (2.43) to relate the singlet projector $\hat{P}_{kl}^{s=0}$ to the spin variables.

Using Eq. (3.24), this allows for calculating any observable O in the ground state of the AF Heisenberg model by

$$\langle \hat{O} \rangle = \frac{\langle \varphi| \hat{\mathcal{H}}_0^n \hat{O} \hat{\mathcal{H}}_0^n |\varphi\rangle}{\langle \varphi| \hat{\mathcal{H}}_0^{2n} |\varphi\rangle}, \tag{3.28}$$

for n sufficiently large. In principle, the trial state $|\varphi\rangle$ can be any quantum state, but should have some non–vanishing contribution in the singlet sector. The idea in [12] is to explicitly work in the singlet subspace, by using a bipartite valence bond state (Eq. 2.33) for the trial state. Furthermore, the powers of $\hat{\mathcal{H}}_0$ are expanded for a fixed projection length n. Therefore we immediately relate the denominator in Eq. (3.28) to a bipartite overlap graph

$$\langle\varphi|\,\hat{\mathcal{H}}_0^{2n}\,|\varphi\rangle = \sum_{L,l,r,R} c_L^\star c_R \,\langle L|\,P_l P_r\,|R\rangle\,, \tag{3.29}$$

where $|L\rangle$ and $|R\rangle$ are bipartite VB states and P_l and P_r are all possible products of n singlet projectors and couplings $J_{kl}\hat{P}_{kl}^{s=0}$ that contribute to $\hat{\mathcal{H}}_0^n$. Here, it is very natural to choose the bipartite convention for evaluating overlap graphs. Initially, the first algorithm [12] suggested to perform the evaluation by counting the number of contained loops. This was done indirectly by contracting out all singlet projectors with the help of Eq. (2.47) and turned out to be rather inefficient. An improved algorithm [13] then replaced the factor $2^{N_\bigcirc}$ by an enlarged configuration space, where all contributing regular overlap graphs (see Sec. 2.3.5) are sampled. These account precisely for the neglected factor, but enforce the overlap graph to be regular at all times. Notice, that in [13] this was explained by sampling compatible spin configurations, which is fully equivalent to sampling regular overlap graphs. It should however be pointed out here, that it is not necessary to sort out to the spin picture. Everything can be explained consistently by considering valence bonds exclusively.

We can now rewrite Eq. (3.28) as

$$\langle\hat{O}\rangle = \sum_{L,l,r,R} \Pi_{L,R}^{r,l} O_{L,R}^{r,l}, \tag{3.30}$$

where the sampling weight is given by

$$\Pi_{L,R}^{r,l} = \frac{c_L^\star c_R \,\langle L|\,P_l P_r\,|R\rangle}{\sum_{L',l',r',R'} c_{L'}^\star c_{R'}\,\langle L'|\,P_{l'}P_{r'}\,|R'\rangle} \tag{3.31}$$

and the loop estimator reads

$$O_{L,R}^{r,l} = \frac{\langle L|\,P_l\hat{O}P_r\,|R\rangle}{\langle L|\,P_l P_r\,|R\rangle}. \tag{3.32}$$

Notice, that if the coefficients c_L and c_R for the valence bond states are chosen positive, as for example the LDA [43] amplitude product state (see Eq. 2.41), then the weight $\Pi_{L,R}^{r,l}$ will be guaranteed to be positive as well. The estimator $O_{L,R}^{r,l}$ can be obtained with Eq. (2.57), if the observable can be expressed in terms of spin operators. This is done by inserting the observable in the middle of an overlap graph.

Having defined the configuration space as the ensemble of regular overlap graphs, consisting of bipartite VB states and projection chains of length $2n$, we can now proceed to the heart of the method. How the valence bond QMC algorithm works is described in detail in [13]. Basically, we have to define the proposal matrix S, which has been introduced in Eq. (3.15). This is done by defining the possible *updates* on the regular overlap graphs. The ergodicity condition is satisfied, if the updates allow to produce every allowed loop structure.

State updates

The first kind of updates is performed on the valence bond states $|L\rangle$ and $|R\rangle$. It turns out, that the LDA amplitude product state (Eq. 2.41) is actually a very good variational state for the AF Heisenberg model on the square lattice [43, 76], and an admissible acceptance rate is reached, when the lengths of the updated singlets does not change much. Therefore, one can pick randomly two next nearest neighbor sites and exchange the singlets on them

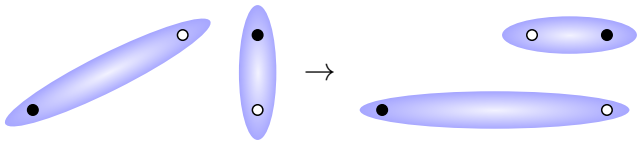

$$|(i,l)(k,j)\rangle \quad \rightarrow \quad |(i,j)(k,l)\rangle\,. \tag{3.33}$$

This move is then accepted with a probability

$$\langle (i,j)(k,l)|\, A\, |(i,l)(k,j)\rangle = \min\left(1, \frac{h(i,j)h(k,l)}{h(i,l)h(k,j)}\right). \tag{3.34}$$

It is clear, that such a move will transform any regular overlap graph into a regular one and it is turns out to be useful to do several state updates within a Monte Carlo step. Notice, that the amplitudes $h(k,l)$ can be optimized by some variational Monte Carlo, as described in [76, 56].

Loop updates

Another kind of updates concerns the entire loop structure of a graph, which contains $2^{N_\bigcirc}$ regular overlap graphs. All of these have precisely the same weight and one can thus pick any of them randomly and accept it with 100%. In practice, we will rather treat every loop separately and switch it with a probability of 50%. The two possible states of the loops can actually be illustrated by coloring every loop in either blue or red, as illustrated in Fig. (3.1).

Operator updates

The last kind of update is a move of a singlet projector to another position. This can be split into removing an operator and inserting it somewhere else. As we only want to allow regular overlap graphs, we have to prohibit moves, which leave a non–regular graph. Therefore, one can only remove an operator, if the colors on both contained singlets match. These singlet projectors are equivalent to diagonal operators in the spin language [13]. The same remains true for inserting an operator, which is only allowed if the overlap graph remains regular. This means, that the colors on both sites of the operator have to match, i.e. one cannot join a red with a blue loop by inserting a singlet projector. This is illustrated in Fig. (3.1).

An operator update thus consists of randomly picking an operator $\hat{P}^{s=0}_{kl}$ and — in case it can be removed — randomly suggesting a new position ij. If the operator can

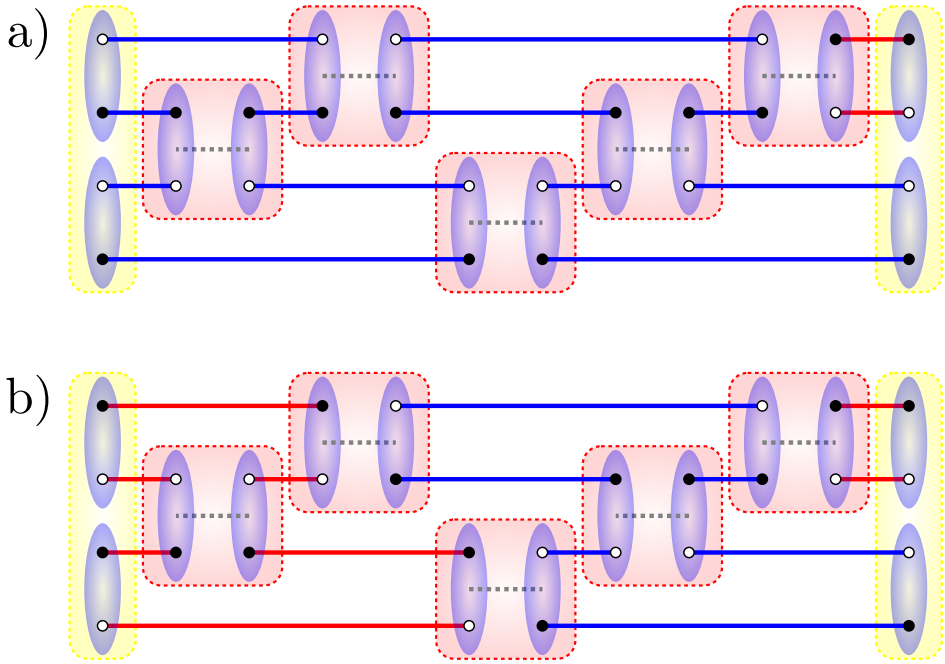

Fig. 3.1.: a) Regular overlap graph before a loop update. The first four operators (from the left) can be safely removed, while eliminating the last operator would create a graph that is not regular anymore. b) The first loop has been updated, freezing the second and the third operator at their position. The first singlet projector is still movable.

be inserted at the new position, then the move is accepted with

$$\langle ij|\, A\, |kl\rangle = \min\left(1, \frac{J_{ij}}{J_{kl}}\right). \tag{3.35}$$

In practice, we will randomly suggest a new position for every movable singlet projector and thus try to update the entire overlap graph at once during a Monte Carlo step.

Miscellaneous

Using the LDA amplitude product state as trial wave function on the square lattice [43], we need roughly a projection length n which is of the same order as the number of sites N [56]. The biggest accessible system sizes are about $\sim 256^2$ spins [13]. This is fairly good compared to finite temperature methods such as *stochastic series expansion* (SSE), which is limited by an operator chain length that scales roughly as $\sim \beta N$ [74]. Therefore, ground state properties (requiring $\beta \gg 1$), are not easily accessible.

The deeper reason for this behavior lies in the finite size gap, which governs the convergence of the projection scheme. As can be seen in figure (2.2), for bipartite lattices the lowest singlet excitation is usually separated by a larger gap, than the lowest triplet excitation. Therefore, it is more advantageous to carry out the ground state projection in the singlet sector.

It also should be noticed, that the present algorithm can be extended the other models. As an example, one can implement higher symmetry than $SU(2)$, such as $SU(N)$ [77]. In this case basically the overlap rule (2.48) becomes modified, by replacing the basis 2 by N. The entire QMC scheme can than be adapted accordingly. Another possible generalization is the consideration of four spin interactions [78] or six spin interactions [79]. This leads to the study of J–Q like models, which are also very present in literature.

3.2. Lanczos Exact Diagonalization

Another important algorithm is the Lanczos method, which was developed by Cornelius Lanczos in 1950 [60, 61]. This technique is a Krylov subspace method, diagonalizing a hermitian matrix H in the Krylov space

$$\mathcal{K}_H = \{|\varphi\rangle, H|\varphi\rangle, H^2|\varphi\rangle, \ldots, H^{n-1}|\varphi\rangle\}. \tag{3.36}$$

Preliminaries

In order to understand this method, it is very instructive to start out with similar algorithms, which are all to be found in [80]. One of these algorithms is the well–known *Gram–Schmidt process*. This algorithm is suitable for orthonormalizing a set of vectors $\{|u_1\rangle, |u_2\rangle, \ldots, |u_n\rangle\}$. The basic idea is very simple:

- Normalize the first vector $|q_1\rangle := |u_1\rangle / \sqrt{\langle u_1 \mid u_1\rangle}$
- Assume we have already obtained the orthonormalized set $\mathcal{Q}_k = \{|q_1\rangle, \ldots, |q_k\rangle\}$, then subtract the projections of $|u_{k+1}\rangle$ onto all vectors in $\mathcal{Q}_k$ from $|u_{k+1}\rangle$ and finally normalize the obtained vector, yielding $|q_{k+1}\rangle$. We then get $\mathcal{Q}_{k+1}$ by adding the new vector $|q_{k+1}\rangle$ to the set $\mathcal{Q}_k$.

However, the direct implementation of such an algorithm is not very stable. It is therefore preferable to use a mathematical equivalent form, which minimizes rounding errors. The *modified Gram–Schmidt* procedure reads in pseudo–code

- *for* $k = 1, \ldots, n$
  1. *for* $l = 1, \ldots, k-1$
     a) $R_{lk} := \langle q_l \mid u_k\rangle$
     b) $|u_k\rangle := |u_k\rangle - R_{lk}|q_l\rangle$
  2. $R_{kk} := \sqrt{\langle u_k \mid u_k\rangle}$
  3. $|q_k\rangle := \frac{|u_k\rangle}{R_{kk}}$

This algorithm is not only very useful to handle a set of linear independent non–orthogonal vectors (such as NNVB states on several lattices), it produces furthermore a triangular matrix R, which appears in the QR–decomposition: Define the two matrices $A = (|u_1\rangle, |u_2\rangle, \ldots, |u_n\rangle)$ and $Q = (|q_1\rangle, |q_2\rangle, \ldots, |q_n\rangle)$, then we have

$$A = QR. \tag{3.37}$$

Therefore we should keep in mind, that the Gram–Schmidt process orthonormalizes a set of linear independent vectors, but it also decomposes a non–singular matrix into an upper triangular and an orthogonal one. As such, it can be used for the QR–algorithm [81], which is based on the fact that

$$RQ = Q^\dagger AQ \tag{3.38}$$

is similar to A, but has smaller off–diagonal elements. Therefore, iterating the last equation, we can diagonalize A. Such a method is implemented in a more sophisticated form in any mathematical Software package, such as Lapack [58]. One important constraint is, that it can only be used for relatively small matrices.

Therefore, in quantum mechanics we still use Krylov methods, which were historically invented before the QR algorithm. One such Krylov subspace method is the *Arnoldi algorithm* [80], which is essentially a Gram–Schmidt process applied to a set of Krylov basis vectors $\mathcal{K}_A$ of a matrix A. We do not want to go into more detail, but noticing that the result will be a Hessenberg matrix, which is similar to the original one.

Lanczos Algorithm

The Arnoldi method is designed for any type of matrix, but if applied to a hermitian one, the resulting Hessenberg matrix has to be hermitian as well. Therefore it must be tridiagonal, allowing for a simplification of the algorithm. What we get is the Lanczos method, which shall now be described in more details [80].

One way to present this, is to start with an arbitrary normalized trial vector $|\varphi_1\rangle$ and to ask for an orthonormalized set $\{|\varphi_k\rangle\}$ with $\langle\varphi_k \mid \varphi_l\rangle = \delta_{k,l}$. The first step is to calculate

$$\alpha_1 = \langle\varphi_1| H |\varphi_1\rangle . \tag{3.39}$$

Next, we determine $|\varphi_2\rangle$ with some normalization factor β_2 and therefore put

$$H |\varphi_1\rangle = \alpha_1 |\varphi_1\rangle + \beta_2 |\varphi_2\rangle \tag{3.40}$$
$$\langle\varphi_1| H^2 |\varphi_1\rangle = \alpha_1^2 + |\beta_2|^2 \tag{3.41}$$
$$\alpha_2 = \langle\varphi_2| H |\varphi_2\rangle . \tag{3.42}$$

Notice, that Eq. (3.41) follows directly from Eq. (3.40). Moreover, α_k is real, as can be deduced from Eqs. (3.39 and 3.42). Realizing, that $\beta_k = \langle\varphi_k| H |\varphi_{k-1}\rangle = \langle\varphi_{k-1}| H |\varphi_k\rangle^\star$, the scheme continues for $k \geq 2$ as

$$H |\varphi_k\rangle = \alpha_k |\varphi_k\rangle + \beta_k^\star |\varphi_{k-1}\rangle + \beta_{k+1} |\varphi_{k+1}\rangle \tag{3.43}$$
$$\langle\varphi_k| H^2 |\varphi_k\rangle = \alpha_k^2 + |\beta_k|^2 + |\beta_{k+1}|^2 \tag{3.44}$$
$$\alpha_{k+1} = \langle\varphi_{k+1}| H |\varphi_{k+1}\rangle . \tag{3.45}$$

The phase factor of β_k is not determined by any of the above equations, thus for simplicity the standard choice is to assume it to be real. If β_k happens to be zero at some moment,

the algorithm stops and we can diagonalize the Hamiltonian

$$U^\dagger H U = \begin{pmatrix} \alpha_1 & \beta_2 & & & & & \\ \beta_2 & \alpha_2 & \beta_3 & & & & \\ & \beta_3 & \alpha_3 & \beta_4 & & & \\ & & \beta_4 & \alpha_4 & \beta_5 & & \\ & & & \beta_5 & \alpha_5 & \ddots & \\ & & & & \ddots & \ddots & \beta_n \\ & & & & & \beta_n & \alpha_n \end{pmatrix}, \tag{3.46}$$

where $U = (|\varphi_1\rangle, |\varphi_2\rangle, \ldots, |\varphi_n\rangle)$ is a unitary matrix.

The resulting tridiagonal matrix can be efficiently diagonalized with standard methods, such as the QR–algorithm or any other suitable Lapack [58] routine. Fig. (3.2) shows how the spectrum of a Hamiltonian evolves, when the size of the Krylov subspace n is increased. One characteristic property is that extremal eigenvalues converge first, while it is generally difficult to obtain informations about the middle of the spectrum. This is particularly useful when only low–energy excitations or simply the ground state of a Hamiltonian is of interest. It is very important to note, that a few number of iterations usually suffices to converge the ground state energy, even when the actual Hilbert space is much larger than n. Therefore, in practice the algorithm is often stopped after a few hundred iterations at most.

However, one drawback of the method are numerical rounding errors, which cause the basis $\{|\varphi_k\rangle\}$ to become non–orthogonal at large k. An artifact of this effect is the emergence of so–called *ghost states*, which let certain eigenvalues appear with a higher multiplicity than they should have (see Fig. 3.2). Such an effect makes it also difficult to detect real degeneracies. One way out of this is to use block– or band–Lanczos methods [80]. Another possibility consists in reorthogonalizing the basis vectors $|\varphi_k\rangle$ after every iteration and is implemented in the Davidson algorithm [80]. The implementation of these algorithms is slightly more complicated and the performance is not as good as for the Lanczos process.

A practical implementation of the Lanczos method is the *modified Lanczos algorithm*, which is mathematically equivalent. However, the numerical stability is increased in a similar way as observed for the modified Gram–Schmidt process and the pseudo–code becomes the following

- pick $|\varphi_1\rangle$ normalized, put $\beta_1 = 0$ and $|\varphi_0\rangle = 0$
- *for* $k = 1, \ldots, n-1$
  1. $|\psi\rangle := H|\varphi_k\rangle - \beta_k|\varphi_{k-1}\rangle$
  2. $\alpha_k := \langle\varphi_k \mid \psi\rangle$
  3. $|\psi\rangle := |\psi\rangle - \alpha_k|\varphi_k\rangle$
  4. $\beta_{k+1} := \sqrt{\langle\psi \mid \psi\rangle}$
  5. $|\varphi_{k+1}\rangle := \frac{|\psi\rangle}{\beta_{k+1}}$

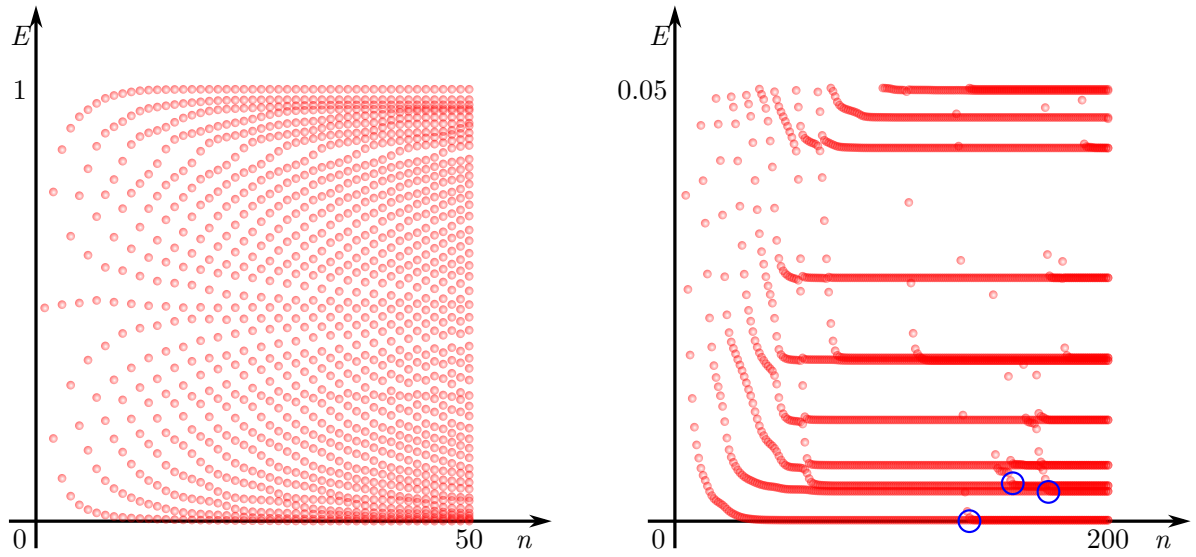

Fig. 3.2.: Left panel: Illustration of the convergence of the eigenvalues of a tridiagonal matrix (Eq. 3.46) as a function of the dimension n of the Krylov subspace. The fastest convergence is generally observed at the border of the spectrum, where informations are obtained for n much smaller than the Hilbert space. Right panel: A zoom on the spectrum reveals the appearance of ghost states, indicated by blue circles.

This method becomes particularly powerful when the Hamiltonian is represented by a sparse matrix, such as in the case of short–range interactions. The matrix multiplication $H\,|\varphi_k\rangle$ is then of order of the Hilbert space size and costs only as much as simple vector multiplications. Furthermore, the knowledge of H as a functional mapping when acting on a vector is sufficient. At the end, we only need to store three vectors in memory, reducing the demand on computational infrastructure, or enabling the access to bigger system sizes.

The main limitation of the Lanczos algorithm is indeed the size of the vectors, which is proportional to the one of the Hilbert space. In order to increase the performance, one needs to implement the symmetries of the Hamiltonian. For spin models the corresponding sectors are those with constant magnetization quantum number m, i.e. one uses the conservation of $\hat{S}^z$. Sometimes spin flip invariance is used in the $m = 0$ sector, distinguishing subspaces with even and odd total spin [38]. Additionally, spatial symmetries can be implemented, which are translational invariance in case of periodic boundary conditions and the point group for the underlying lattice. For the square lattice this is C_{4v}, whereas for the hexagonal, the triangular and kagomé lattices C_{6v} is the appropriate point group.

Making use of the symmetries has two major advantages: firstly, this allows to break the full matrix down into several independent blocks, which can be diagonalized separately. Basically, this amounts to choosing another set of basis vectors, in which the

Hamiltonian has a block–diagonal form

$$H = \begin{pmatrix} * & * & & & & & & & \\ * & * & & & & & & & \\ & & * & * & * & & & & \\ & & * & * & * & & & & \\ & & * & * & * & & & & \\ & & & & & * & * & * \\ & & & & & * & * & * \\ & & & & & * & * & * \end{pmatrix}. \tag{3.47}$$

Mathematically this is covered within the representation theory of finite groups, which is a very beautiful and well developed subject. Some introductory notes on this can be found in [82]. Some further reading and also a list of character tables are to be found in [24].

Another advantage of using symmetries is that this allows to assign quantum numbers to the eigenstates. Ideally, one would expect to lift all degeneracies through a full set of commuting observables, which simplifies the physical interpretation of the obtained spectrum. A rather nice side effect is also the avoidance of complicated algorithms to detect degeneracies and access to some excitations in the spectrum, which are simply the ground state of another symmetry sector.

It should be mentioned, that the afore described Lanczos procedure is not appropriate for solving generalized eigenvalue problems, which arise when using non–orthogonal valence bond states, even though an extension to the Lanczos method for such a case can be found in [80]. However, this requires inverting the overlap matrix, which is computationally rather demanding.

3.3. Partial Conclusion

In this chapter we have seen two different numerical methods which are used to solve strongly correlated problems in condensed matter physics. The Lanczos exact diagonalization (ED) is suited for any model, and when combined with some group theory allows to gain deep insight into the low–energy spectrum of a system and to detect for instance symmetry breaking on finite samples [38]. Another aspect is the possibility to access not only the spectrum, but also the corresponding eigenstates. This can be rather useful for calculating any observable in such states. ED is nevertheless limited to relatively small samples (~ 40 spins 1/2 using all symmetries), which are not always sufficient to understand the thermodynamic limit $N \to \infty$.

For this purpose there are algorithms which are based on stochastic sampling, such as Quantum Monte Carlo. Especially, the valence bond projector QMC allows to access rather large clusters ($\sim 256^2$ spins), but only provides information about ground state observables and not the ground state itself. Though, this is not really a disadvantage, as the ground state cannot be examined directly because of its rather large size. Even in

ED one has to use observables in order to understand physical properties of the obtained eigenstates. However, the full spectrum of the Hamiltonian is not accessible and other properties of most excited states neither.

This can be partly cured by using path integral Monte Carlo [71] or equivalently stochastic series expansion [83, 84, 74], which are both based on the stochastic sampling of the partition function at finite temperature. The path integral scheme rather splits the partition function into parts by means of the Suzuki–Trotter formula [85, 86], whereas the SSE inserts identity operators in order to create an operator chain with fixed length. Therefore the SSE scheme shares several similarities with the valence bond QMC. However, while the later is designed for the extraction of ground state, i.e zero temperature properties, the SSE and path integral formalism are suitable to describe finite temperature properties of a system.

One major problem for most Monte Carlo schemes are however frustrated systems, which generally come with the so–called *sign problem*. The roots of this are to be found in the fact that the considered integrals contain negative parts, which have to be incorporated in the estimator, resulting in very large fluctuations. Notice, that often fluctuating terms can be compensated with a proper weight function. This is however intrinsically impossible for terms with negative sign.

For the valence bond Monte Carlo the origin of the sign problem lies precisely in the difference of bipartite (Sec. 2.3.4) and generic overlap graphs (Sec. 2.3.5). On bipartite lattices, overlap graphs can always be evaluated to some positive number, while on frustrated systems, contracting projection chains can also yield a negative sign.

Besides the two afore–mentioned methods there are also some other algorithms which are quite important in condensed matter systems. Firstly, there is the *density matrix renormalization group* (DMRG) method [87, 88] which does not suffer from something like a sign problem. Indeed, this is the algorithm of choice for many one dimensional systems, where it deploys its full power and scales much better then exact diagonalization. It can actually be shown, that the extension of DMRG to higher dimension can be understood in terms of matrix product states [89]. However, this becomes computationally very hard and explains, why DMRG is not so much employed for 2D systems, even though recent progresses have been made [90].

Secondly, Variational Monte Carlo (VMC) is a quite powerful technique to optimize parameters of an ansatz for the ground state of a given system [91, 92]. This method does not suffer from the sign problem, but for fermionic systems we have to evaluate slater determinants, which can become rather costly for large clusters. However, this method remains variational and thus depends on the quality of the ansatz for the ground state.

Part II.

Quantum Information

4. Fidelity Approach to Quantum Phase Transitions

Phase transitions play an important role in statistical physics and condensed matter. They occur in the thermodynamic limit $N \to \infty$ in many–body systems and can be distinguished by the correlation length ξ. When the correlations remain finite we talk about *first order phase transitions*, whereas *continuous phase transitions* are observed when $\xi \to \infty$ diverges. This involves the absence of coexisting phases or a latent heat through a transition of continuous type. From the theoretical point of view continuous phase transitions are rather interesting, as they can be described by universal quantities such as critical exponents [93]. The latter quantify the leading divergence of the correlation length, the specific heat, susceptibility etc. and are tabulated according to the symmetry, the dimension and the interaction range of the underlying Hamiltonian.

One can further distinguish *classical phase transitions*, which are induced by thermal fluctuations and *quantum phase transitions* (QPT), that are governed by quantum fluctuations. At finite temperature thermal fluctuations will always dominate, hence we observe QPT only at $T = 0$ [93]. Whereas classical phase transitions have temperature as the driving parameter, the corresponding parameter for quantum phase transitions can for example be some coupling or other coefficients in the Hamiltonian. Continuous QPT show also universal behavior, with the dynamical scaling exponent z as additional critical exponent [93].

The occurrence of phase transitions is limited by the *Mermin–Wagner theorem* [94, 95, 96], which states that continuous symmetries cannot be broken at finite temperature in one or two dimensions for systems with short–range interactions. This basically means, that for example antiferromagnetic order, which is observed in the 2D Heisenberg model at zero temperature on the square lattice or triangular one will be destroyed by thermal fluctuations at finite temperature. As can be seen in this example, the Mermin–Wagner theorem does not apply at $T = 0$ [29]. However, quantum field theories in D dimensions can usually be transformed into classical field theories in $D + 1$ [93], hence predicting the absence of broken continuous symmetries only in one dimensional systems. Notice, that discrete broken symmetries are *not* affected by the Mermin–Wagner theorem.

Usually, classical or quantum phase transitions can be understood within the Landau–Ginzburg–Wilson (LGW) paradigm [97, 93, 98], where it is possible to define an order parameter according to the expected broken symmetry. This is the traditional way of studying a many–body system and requires some *a priori* knowledge about the system in order to identify the correct order parameter. Sometimes however, it is not clear which symmetry will be broken. Furthermore, it has been argued that some quantum phase transition may not be understood within the LGW paradigm [99, 100].

Thus, it seems to be appealing to consider approaches, that detect phase transitions

independently of an order parameter. In the finite temperature case, thermodynamical measurements, such as the specific heat, can signal a phase transition. At $T = 0$ however, these measurements are not available. In the last decade people have therefore started to search for alternative approaches and especially influences from *quantum information theory* turned out to be rather fructuous.

In fact, it is almost natural to expect correlations in a quantum phase transition to also have quantum nature. One of the early discovered purely quantum–like correlations is *entanglement* and it has indeed been shown, that entanglement is related to QPT [101, 102, 103]. Another recent suggestion is even much more basic and directly compares the ground states of systems with different driving parameter. The simplest measure to achieve this is the *fidelity*, which is nothing but the ground state overlap [10, 104].

4.1. Fidelity

The idea is very basic: as quantum phases are only described by the properties of the ground state manifold of a corresponding system, one might expect that their overlap between different systems depends on whether there is a phase transition in between or not. Consider for example the Hamiltonian

$$\hat{\mathcal{H}} = \hat{\mathcal{H}}_0 + \lambda \hat{\mathcal{H}}_\lambda, \tag{4.1}$$

where λ is the parameter that shall drive the system through a quantum phase transition. For pure states[1], fidelity is defined as the modulus of the overlap between the ground state of $\hat{\mathcal{H}}$ at two different values of λ,

$$F(\lambda_1, \lambda_2) = |\langle \varphi_0(\lambda_1) \mid \varphi_0(\lambda_2) \rangle| \tag{4.2}$$

and it has indeed been shown, that the fidelity drastically decreases when λ_1 or λ_2 approaches a critical point λ_c [10]. This behavior becomes immediately clear by noticing that the fidelity can be used to define a metric on the Hilbert space [105]. Generally, an inner product induces a norm, which itself induces a metric. This way the most natural definition of a metric in terms of fidelity turns out to be *Bures distance* [106], defined through

$$d(\lambda_1, \lambda_2) = \sqrt{2 - 2F(\lambda_1, \lambda_2)}. \tag{4.3}$$

In other words, the fidelity approach simply tries to measure the distance between ground states. Loosely speaking, one somehow expects that states within the same phase are closer to each other than two states, which are separated by a critical point and thus fidelity might be a good measure to detect such a point. Quantum phase transitions take place in the thermodynamic limit $N \to \infty$, and it is known, that in such a limit basically all states become orthogonal to each other (see Fig. 4.1). This effect is related to the *Anderson orthogonality catastrophe* [107], and can be circumvented by studying the *fidelity per site* [108]

$$\ln f(\lambda_1, \lambda_2) = \frac{\ln F(\lambda_1, \lambda_2)}{N}, \tag{4.4}$$

[1] For mixed states one can define fidelity through $F(\lambda_1, \lambda_2) = \mathrm{Tr}\sqrt{\rho^{1/2}(\lambda_1)\rho(\lambda_2)\rho^{1/2}(\lambda_1)}$ [105, 106]. This shall however not be discussed here.

which is well behaved in the thermodynamic limit. Hence, $f(\lambda_1, \lambda_2)$ can be used to detect quantum phase transitions.

Instead of studying fidelity as a function of two variables, one can define some $\delta\lambda = \lambda_2 - \lambda_1$, which is kept constant but very small. In the limit $\delta\lambda \to 0$ one can re–express f by its leading correction[2], the *fidelity susceptibility* χ_F [109],

$$f(\lambda, \lambda + \delta\lambda) \simeq 1 - \chi_F(\lambda)\frac{\delta\lambda^2}{2N}. \tag{4.5}$$

Consequently, a drop in fidelity, visible close to a quantum phase transition [106], is translated into a peak in fidelity susceptibility (cf. Fig. 4.1).

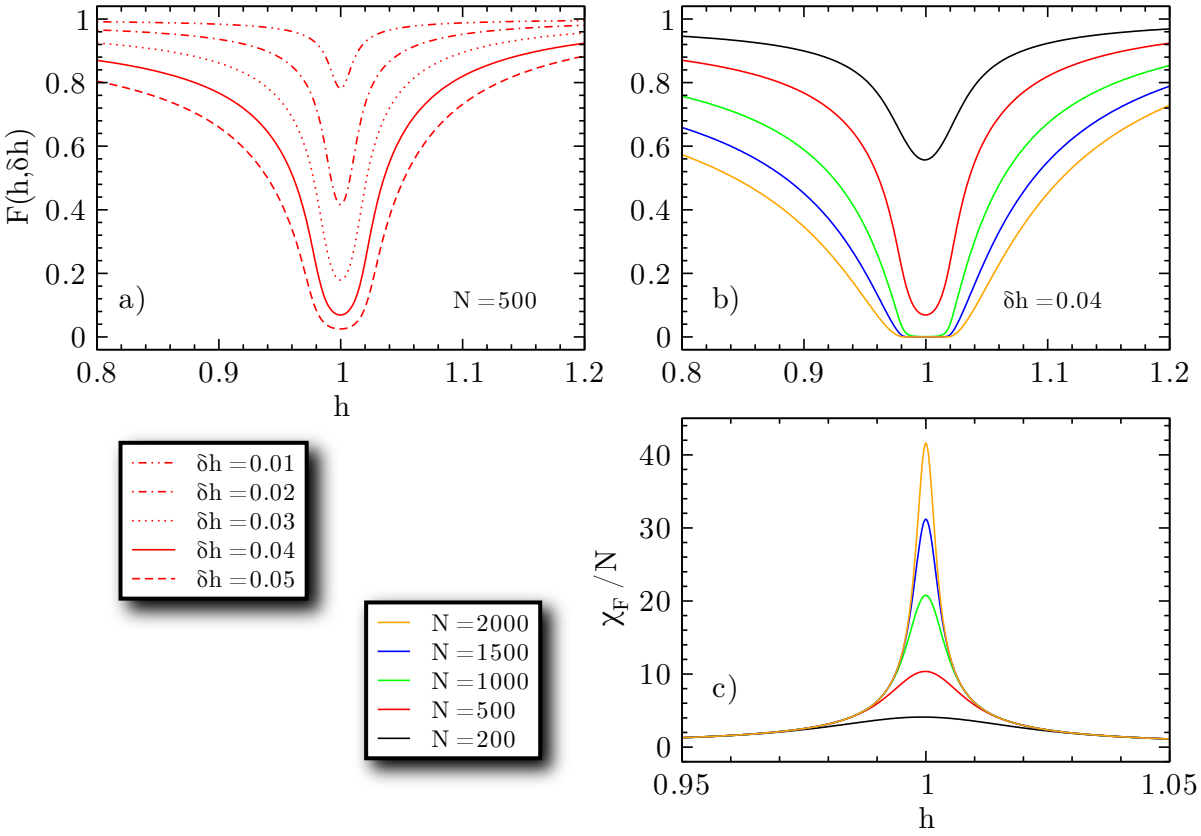

Fig. 4.1.: Illustration of fidelity and its susceptibility for the transverse–field Ising model on a chain with periodic boundary conditions, as studied in [10, 108, 106]. This system displays a QPT at $h_c = 1$, and the magnetic field h takes the role of the driving parameter λ. a) The fidelity $F(h, \delta h) := F(h - \delta h/2, h + \delta h/2)$ drops close to the QPT. Also, for bigger δh the ground states have a larger (Bures) distance, resulting in a more pronounced feature. b) When increasing the system size the ground states become more and more orthogonal, reminiscent of the orthogonality catastrophe. c) The susceptibility per site develops a peak at the QPT. Deep in a given phase χ_F is extensive.

[2]There is no linear contribution in $\delta\lambda$, as can be seen from the fact that $\partial_\lambda f(\lambda, \lambda) = 0$.

For practical purposes one can calculate χ_F with the fidelity per site through

$$\frac{\chi_F(\lambda)}{N} = \lim_{\delta\lambda\to 0}\left(-2\frac{\ln f(\lambda,\lambda+\delta\lambda)}{\delta\lambda^2}\right). \tag{4.6}$$

Using first order perturbation theory for f, the last expression can be recast into [106]

$$\chi_F(\lambda) = \sum_{n\neq 0}\frac{|\langle\varphi_n(\lambda)|\,\hat{\mathcal{H}}_\lambda\,|\varphi_0(\lambda)\rangle|^2}{(E_n(\lambda)-E_0(\lambda))^2}, \tag{4.7}$$

which reminds of the second order perturbation result for the ground state energy [110, 106]

$$\chi_E(\lambda) = -\frac{\partial^2}{\partial\lambda^2}E_0(\lambda) = 2\sum_{n\neq 0}\frac{|\langle\varphi_n(\lambda)|\,\hat{\mathcal{H}}_\lambda\,|\varphi_0(\lambda)\rangle|^2}{E_n(\lambda)-E_0(\lambda)}. \tag{4.8}$$

Indeed, the only difference here is the denominator, which is squared for χ_F, but is not for the energy susceptibility χ_E.

This leads to the following interpretation [110]. For a second order phase transition the second derivative of the ground state energy will have singular behavior. However, this will be even more pronounced in χ_F, since the vanishing denominator, causing the divergence, becomes even squared. Therefore, a second order QPT should be detectable within the fidelity approach, as well as a first order transition. Indeed, for the latter we observe a level–crossing, resulting in a clear drop of fidelity. The situation is however less obvious in case of higher order quantum phase transitions, as for example for Kosterlitz–Thouless transitions [110].

It should be mentioned, that the clear peak in fidelity susceptibility is not the only reason in favor to use the fidelity probe. The real advantage comes from the fact, that fidelity is such an elementary quantity, which can be computed rather easily without any prior knowledge about the system. Certainly, we do not have to find an order parameter for the expected broken symmetry. Moreover the approach is rather general, as all we need is to compute the ground state overlap.

4.1.1. Universal Behavior

As happening for continuous quantum phase transitions, we would expect to find some universal scaling within the fidelity approach as well. In fact, the fidelity susceptibility has a scaling behavior, which can be expressed with usual critical exponents [111, 14, 112, 106]. To see this, first recall the critical scaling for the correlation length close to the quantum critical point λ_c

$$\xi \sim |\lambda-\lambda_c|^{-\nu}. \tag{4.9}$$

On finite size samples the correlation length can however not be larger than the cluster size, such that essentially $\xi \sim L$, where L is some characteristic length scale of the studied sample. Therefore, at criticality we find

$$\lambda \sim L^{-1/\nu}, \tag{4.10}$$

which shall be written in short as

$$[\lambda] = \frac{1}{\nu}. \tag{4.11}$$

Here, the *scaling dimension* $[A]$ of a quantity A close to a critical point is defined by $A \sim L^{-[A]}$, and ν is the critical exponent of the correlation length. The scaling dimension of (imaginary) time τ is related to the one in space by the dynamical critical exponent z [93]. Therefore, the same must be true for energy scales, and we obtain

$$[\hat{\mathcal{H}}] = -[\tau] = z. \tag{4.12}$$

From equation (4.1) we deduce the critical scaling of $\hat{\mathcal{H}}_\lambda$,

$$[\hat{\mathcal{H}}_\lambda] = [\hat{\mathcal{H}}] - [\lambda] = z - \frac{1}{\nu}. \tag{4.13}$$

Finally, Eq.(4.7) gives the necessary relation for the scaling of the fidelity susceptibility, and we obtain,

$$\left[\frac{\chi_F}{N}\right] = 2[\hat{\mathcal{H}}_\lambda] - 2[\hat{\mathcal{H}}] + D = D - \frac{2}{\nu}, \tag{4.14}$$

where we used $N \sim L^D$ and D is the spatial dimension. This explains the observed behavior in Fig. (4.1), where χ_F/N builds up a pronounced peak in the vicinity of the quantum critical point. Hence, quantum phase transitions can be detected through χ_F as long as

$$D < \frac{2}{\nu}, \tag{4.15}$$

as remarked in [106]. The validity of this scaling relation has been thoroughly checked within QMC simulations of the two–dimensional transverse field Ising model [113].

We finally end up by remarking that the reasoning here only applies for χ_F in the vicinity of a quantum phase transition. The scaling in a more general context has recently been discussed in [114, 115].

4.1.2. Valence Bond QMC Approach

Despite the fact that the ground state overlap is a conceptually simple quantity, it is difficult to compute in case of many–body systems. This can be illustrated by the limited number of analytical results that exist [106]. Away from that, it seems obvious to use exact diagonalization techniques as well as DMRG [87] and tensor network methods [116], which directly compute the ground state of a system. These approaches are however only restricted to either rather small system size or essentially limited to one–dimensional systems. Tensor network methods can also be used in higher dimension for relatively large N, but have however the limitation of being variational.

Recently, it has been shown how to devise several large scale Quantum Monte Carlo schemes, combined with the fidelity approach [14, 113]. One of them is explicitly using the valence bond projector [12], presented in section (3.1.2) and shall be presented in the following.

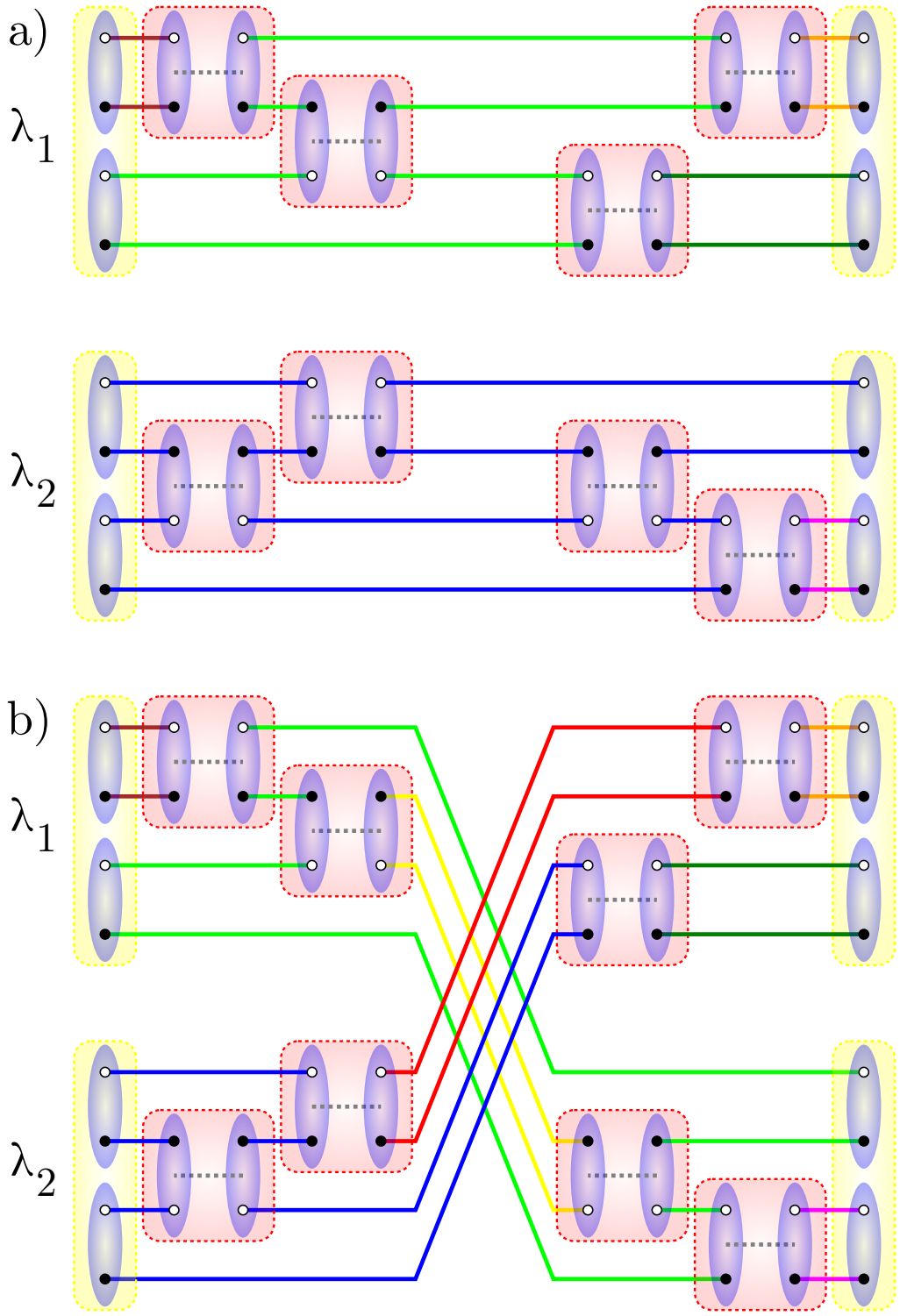

Fig. 4.2.: (a) Illustration of the two propagation chains for λ_1 and λ_2. Both chains are simulated independently and the total number of *uncrossed* loops is $N_{\bigcirc}^{0} = 6$ (indicated by different colors). (b) When measuring the swap operator, the two previously independent chains become connected, changing the total number of loops by $N_{\bigcirc}^{X} - N_{\bigcirc}^{0}$. Here, we have a total number of $N_{\bigcirc}^{X} = 8$ (*crossed*) loops (highlighted with different colors). The swap estimator is simply given by $\mathrm{Swap}_{L,R}^{r,l} = 2^{N_{\bigcirc}^{X} - N_{\bigcirc}^{0}} = 4$.

Consider two copies of the Hilbert space with the ground states $|\varphi(\lambda_1)\rangle$ and $|\varphi(\lambda_2)\rangle$ in each of them. Define the combined state

$$|\psi(\lambda_1, \lambda_2)\rangle = |\varphi(\lambda_1)\rangle \otimes |\varphi(\lambda_2)\rangle \,, \tag{4.16}$$

living in the combined Hilbert space. Now, denoting a single system by Ω, we can define a swap operator [117], by

$$\mathrm{Swap}_\Omega \, |\psi(\lambda_1, \lambda_2)\rangle := |\psi(\lambda_2, \lambda_1)\rangle \,. \tag{4.17}$$

Obviously, this operator simply exchanges the two ground states within the full state $|\psi\rangle$, and we obtain an expression for the squared fidelity

$$F^2(\lambda_1, \lambda_2) = \langle\psi(\lambda_1, \lambda_2)| \, \mathrm{Swap}_\Omega \, |\psi(\lambda_1, \lambda_2)\rangle \tag{4.18}$$

$$= |\, \langle\varphi(\lambda_1) \mid \varphi(\lambda_2)\rangle \,|^2 \tag{4.19}$$

in terms of the swap operator. The last expression is still general and can therefore also be used for a spin model with a singlet ground state, as for example the AF Heisenberg model. In such a case the valence bond QMC can be used to measure the expectation of the swap operator in the ground state [14]. In the spirit of equation (3.30), we have

$$\langle \mathrm{Swap}_\Omega \rangle = \sum_{L,l,r,R} \Pi^{r,l}_{L,R} \mathrm{Swap}^{r,l}_{L,R}, \tag{4.20}$$

with the sampling weight

$$\Pi^{r,l}_{L,R} = c^\star_L c_R \, \langle L| \, P_l P_r \, |R\rangle \tag{4.21}$$

and the loop estimator

$$\mathrm{Swap}^{r,l}_{L,R} = \frac{\langle L| \, P_l \mathrm{Swap}_\Omega P_r \, |R\rangle}{\langle L| \, P_l P_r \, |R\rangle}. \tag{4.22}$$

Notice, that here, as well as in the general case [12], we have chosen a projected valence bond trial state as ansatz for $|\psi\rangle$. The trial state can still set to be an LDA amplitude product state [43]. However, in the present case the formal state $|\psi\rangle$ is actually a tensor product of the two considered ground states (4.16), resulting in a simulation of two independent projection chains. This means, we have to implement two double propagations [13], one for each value of λ. For every measurement of the swap estimator we have to connect the two propagation chains, as shown in Fig. (4.2).

The change of the number of loops directly allows for the calculation of the swap estimator. It should be pointed out, that Swap_Ω is in fact related to the permutation operator $\hat{\mathcal{P}}_{kl}$, mentioned in chapter (2). It can be shown [15], that the latter only changes the number of loops by ± 1 or 0. The swap operator indeed permutes the full number N of sites and can therefore take values in the range $[2^{-N}, 2^N]$. We will see in the next section, that such a fluctuation range sets a certain limit on the accessible system size, as the simulation may have convergence issues for large N.

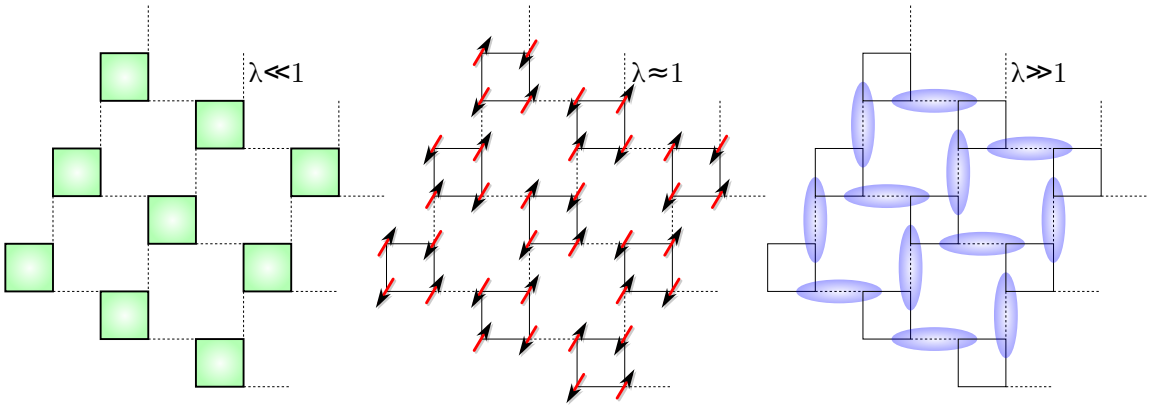

Fig. 4.3.: Illustration of the CaVO lattice with nearest neighbor interactions of type λ (dashed lines) and unit interactions on the solid bonds. Such a Heisenberg model is in a plaquette VBC phase for $\lambda \ll 1$ (left panel), shows Néel order for $\lambda \simeq 1$ (middle panel) and becomes a dimerized valence bond crystal for $\lambda \gg 1$ (right panel).

4.1.3. 1/5–depleted Square Lattice

We will now present the results of implementing the fidelity QMC scheme on an example, the CaVO lattice. This lattice is essentially a square lattice with 20% of the sites dropped and can be found in the compound CaV_4O_9 (see Fig. 4.3).

The Heisenberg model on the CaVO lattice comprises a reference coupling of strength one on the plaquettes, as well as a tunable interaction λ in between. It is in a plaquette VBC for $\lambda \ll 1$ and passes through a Néel phase into a dimerized VBC, when λ is increased [118, 119]. These findings were obtained by QMC simulations, measuring the order parameter and the spin gap.

Here, we study the same model within the fidelity approach, and clusters up to $N = 32^2$ could be simulated. The obtained results for the fidelity per site are plotted in Fig. (4.4). The overlap rapidly decreases, when moving away from the diagonal with $f(\lambda, \lambda) = 1$. It can be observed, that two features build up, where the fidelity drops much faster when leaving the diagonal. These *pinch points* can roughly be located at $\lambda_c^1 \in [0.8, 1.1]$ and $\lambda_c^2 \in [1.5, 1.8]$, in agreement with the reported quantum critical points at the plaquette–Néel and the Néel–dimerized transitions, respectively [118].

The precise location of the quantum critical points is however quite difficult, due to the statistical errors for large clusters (up to $\sim 2\%$). It is crucial to understand, that such a behavior comes from the measurement of the swap operator in the valence bond basis. This can actual be overcome, by limiting the number of permutations to a small amount, as shown in [117]. Such an approach is however not that suitable for measuring fidelity. Another way out might be to measure directly in the spin basis, resulting in an estimator that fluctuates only between zero and one. This has not been tested so far, but might be implemented straightforwardly in the present scheme.

On the other side, for locating the QPT accurately, one is actually interested in the limit $\delta\lambda \to 0$, where a drop in fidelity is most pronounced. A naturally defined quantity

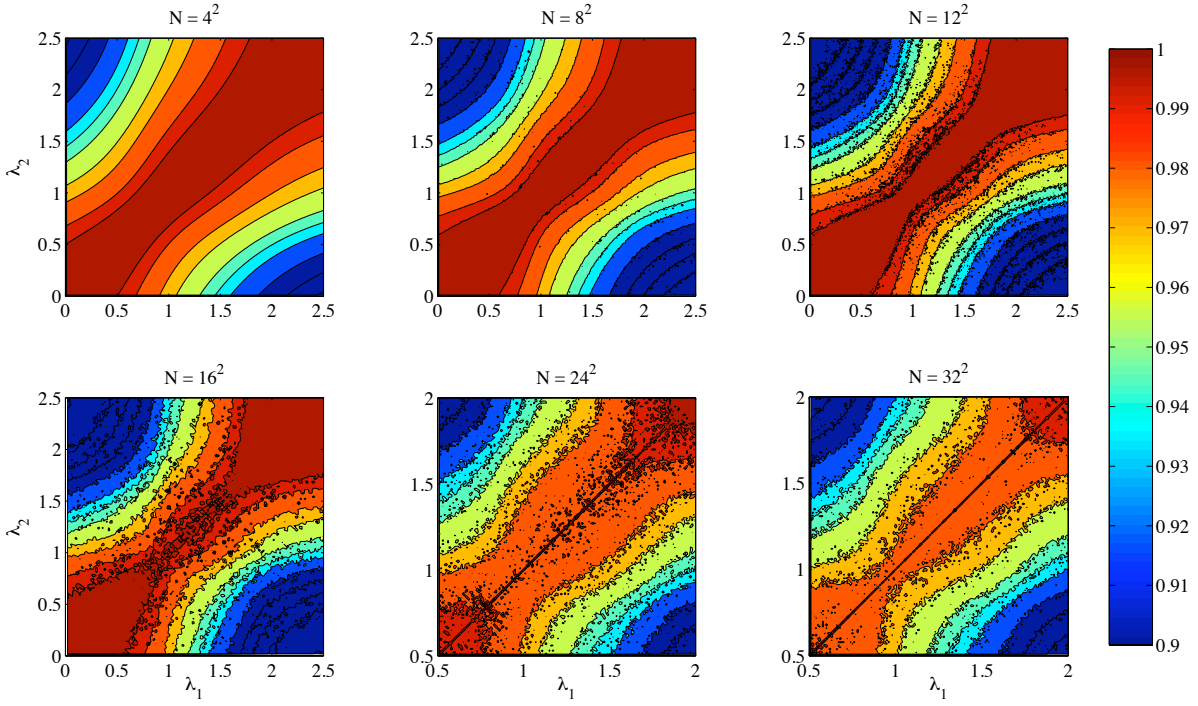

Fig. 4.4.: Contour plot for the fidelity per site on the CaVO lattice for different clusters. The relevant parameter region was scanned two dimensionally for $\lambda_k \in [0, 2.5]$ on the smallest samples $N \leq 16^2$ and $\lambda_k \in [0.5, 2]$ for $N \geq 24^2$. The resolution $\Delta\lambda$ is 0.02 for $N = 16^2$ and 0.01 for all other samples. The chosen propagation length n for the ground state projection with $\hat{\mathcal{H}}^n$ is $n/N = 20$ for $N \leq 12^2$, 10 for $N = 16^2$ and 4 for $N \geq 24^2$ [14].

in this limit is however the susceptibility χ_F, which can be measured within stochastic series expansion [14]. Indeed, this approach will solve the convergence issues within the valence bond QMC, discussed previously, in a satisfactory way.

A crucial step is to define some finite temperature generalization of the susceptibility [14, 113],

$$\chi_F(\beta) = \int_0^{\beta/2} d\tau\tau \left(\left\langle \hat{\mathcal{H}}_\lambda(0)\hat{\mathcal{H}}_\lambda(\tau) \right\rangle - \left\langle \hat{\mathcal{H}}_\lambda(0) \right\rangle^2 \right), \tag{4.23}$$

which has the correct asymptotic behavior $\chi_F = \lim_{\beta\to\infty} \chi_F(\beta)$. This definition is equivalent to the one for Bures distance, in the sense, that it has the same scaling behavior [113]. Whereas Bures distance is largely used in the quantum information community [120], the above $\chi_F(\beta)$ can be efficiently simulated within SSE. The results, which were obtained by F. Alet [14], are presented in Fig. (4.5) and reveal two clear peaks at $\lambda_c^1 = 0.94(1)$ and $\lambda_c^2 = 1.65(1)$, in agreement with previous studies [118]. Furthermore, one can check the scaling of χ_F at the critical points and obtains $\chi_F(\lambda_c)/N \sim L^\omega$, with $\omega^1 = 0.73(3)$ and $\omega^2 = 0.79(6)$. This is in agreement with the expected scaling of $\omega = 2/\nu - D \simeq 0.812$, when using the critical exponent ν for the universality class of the 3D classical Heisenberg model [121]. Moreover, far enough away from criticality the susceptibility is an

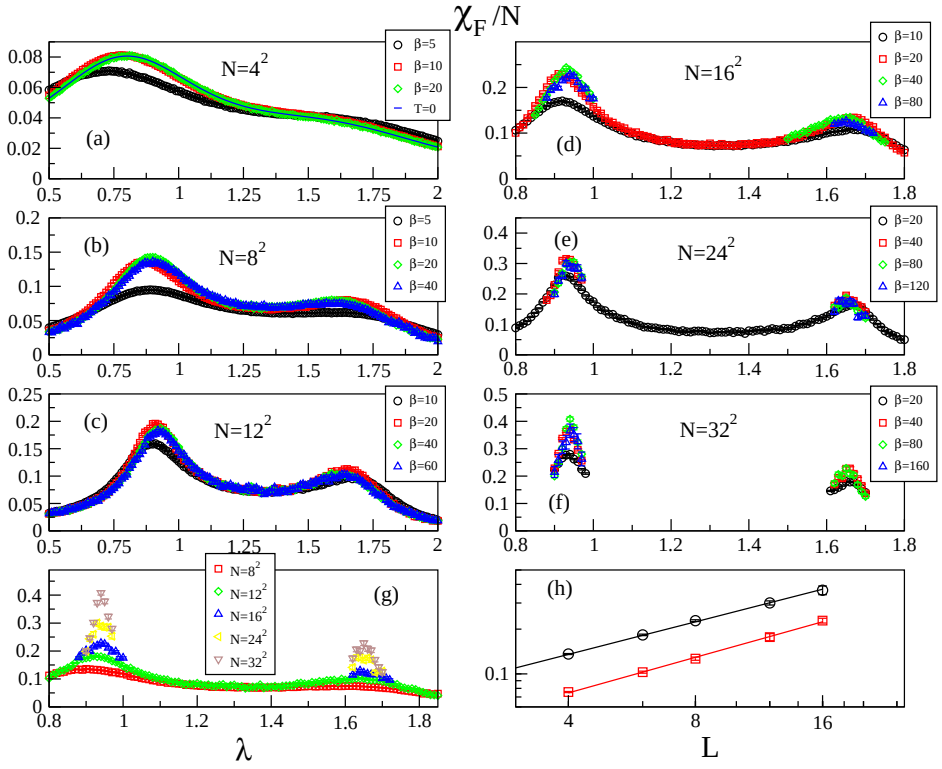

Fig. 4.5.: (a)-(f) Fidelity susceptibility per site for the same clusters as in Fig. (4.4). (g) Superposition of all finite size $\chi_F(\beta)$ at lowest simulated temperatures. (h) Finite size scaling of the two peaks, with a log–log scale and power–law fits. The data were produced by F. Alet and the figure is taken from [14].

extensive quantity, as expected.

The behavior of the fidelity susceptibility also explains the pinch points in Fig. (4.4). Whereas the first peak at λ_c^1 is well developed, the second one is much smaller. Therefore, the pinch point for fidelity at λ_c^1 is also expected to be visible easier than the second one, as being observed.

4.2. Bipartite Entanglement

Measuring the amount of entanglement is another prominent approach to characterize quantum phase transitions. Similarly to the fidelity method, it is also located at the interface between quantum information and condensed matter. The basic idea is quite simple: the eigenstates of a Hamiltonian are pure states on the whole system Ω, but if one considers a bipartition of a system into two subsystems $\mathcal{A}$ and $\mathcal{B}$, the states on the subsystems are generally not pure. Indeed, it can be shown, that the states on the subsystems are pure if and only if the overall state $|\psi\rangle$ is a product state [25]. In other words, if we observe bipartite entanglement between the two subsystems, then we will

generate a mixed state

$$\rho_{\mathcal{A}} = \mathrm{Tr}_{\mathcal{B}} |\psi\rangle \langle\psi| \tag{4.24}$$

by tracing out the other system. Therefore, one can use the entropy of $\rho_{\mathcal{A}}$ (or equivalently $\rho_{\mathcal{B}}$), as one possible entanglement measure, to quantify the amount of bipartite entanglement in the system Ω [122]. Initially, the von Neumann entropy

$$S_1(\rho_{\mathcal{A}}) = -\mathrm{Tr}(\rho_{\mathcal{A}} \ln \rho_{\mathcal{A}}) \tag{4.25}$$

was used for this purpose, resulting however in a measure that cannot be obtained very easily for many–body systems.

Here, we shall mention other entanglement measures, which are very much related to the previously discussed topics. Firstly, Rényi entropies

$$S_n(\rho_{\mathcal{A}}) = \frac{1}{1-n} \ln \left(\mathrm{Tr}\rho_{\mathcal{A}}^n\right) \tag{4.26}$$

are a generalization of the von Neumann entropy, the latter being recovered in the limit $n \to 1$. For all Rényi entropies we have $S_n \geq S_m$ when $n < m$, i.e. S_2 is a lower bound of the von Neumann entropy. Furthermore, one can show [117] that S_2 can be expressed with a generalized swap operator (Sec. 4.1.2), where we only exchange the subsystem $\mathcal{A}$ instead of the entire one. We have

$$S_2(\rho_{\mathcal{A}}) = -\ln \langle\psi| \,\mathrm{Swap}_{\mathcal{A}} \,|\psi\rangle\,, \tag{4.27}$$

with $|\psi\rangle = |\varphi\rangle \otimes |\varphi\rangle$ being a tensor product of for example two copies of the ground state $|\varphi\rangle$ of a system. When the latter is a singlet state, we can use the valence bond projector fidelity scheme (Sec. 4.1.2) with only slight modifications in order to measure $\langle\psi| \,\mathrm{Swap}_{\mathcal{A}} \,|\psi\rangle$ [117]. Indeed, instead of considering two states $|\varphi(\lambda_1)\rangle$ and $|\varphi(\lambda_2)\rangle$, we simply put $\lambda = \lambda_1 = \lambda_2$. On the other side, Ω becomes replaced by a subsystem $\mathcal{A}$.

It is observed, that the convergence becomes quite poor, when the number of sites in the subsystem $\mathcal{A}$ increases [117], as illustrated in Fig. (4.6). This has precisely the same reasons, as for the fidelity QMC scheme, discussed in section (4.1.2). The possible values of a single measurement of the swap operator fluctuate within a range that exponentially increases with the size of $\mathcal{A}$. It has been suggested to improve this, by initially only swapping a very small region $\mathcal{A}_k$. In a subsequent simulation one can swap further sites of a region $\mathcal{A}_{k+r}$ with respect to an already crossed overlap graph [117]. Essentially, one measures only the *relative* swap of the zone $\mathcal{A}_{k+r} \backslash \mathcal{A}_k$ and thus builds up the full curve iteratively. This is quite useful, as one would like to vary the size of the region $\mathcal{A}$ in any case, contrary to the situation in section (4.1.2), where one only wants to swap the entire system Ω.

The scaling of the Rényi entropies for critical one dimensional systems can be found with conformal field theories (CFT) and shows basically logarithmic behavior in the block size of $\mathcal{A}$ [123, 124]. This is illustrated in Fig. (4.6), where a Heisenberg spin chain with periodic boundary conditions was simulated. The deviations of the numerical results from the leading logarithmic scaling are known as parity effects and can also be predicted analytically [123].

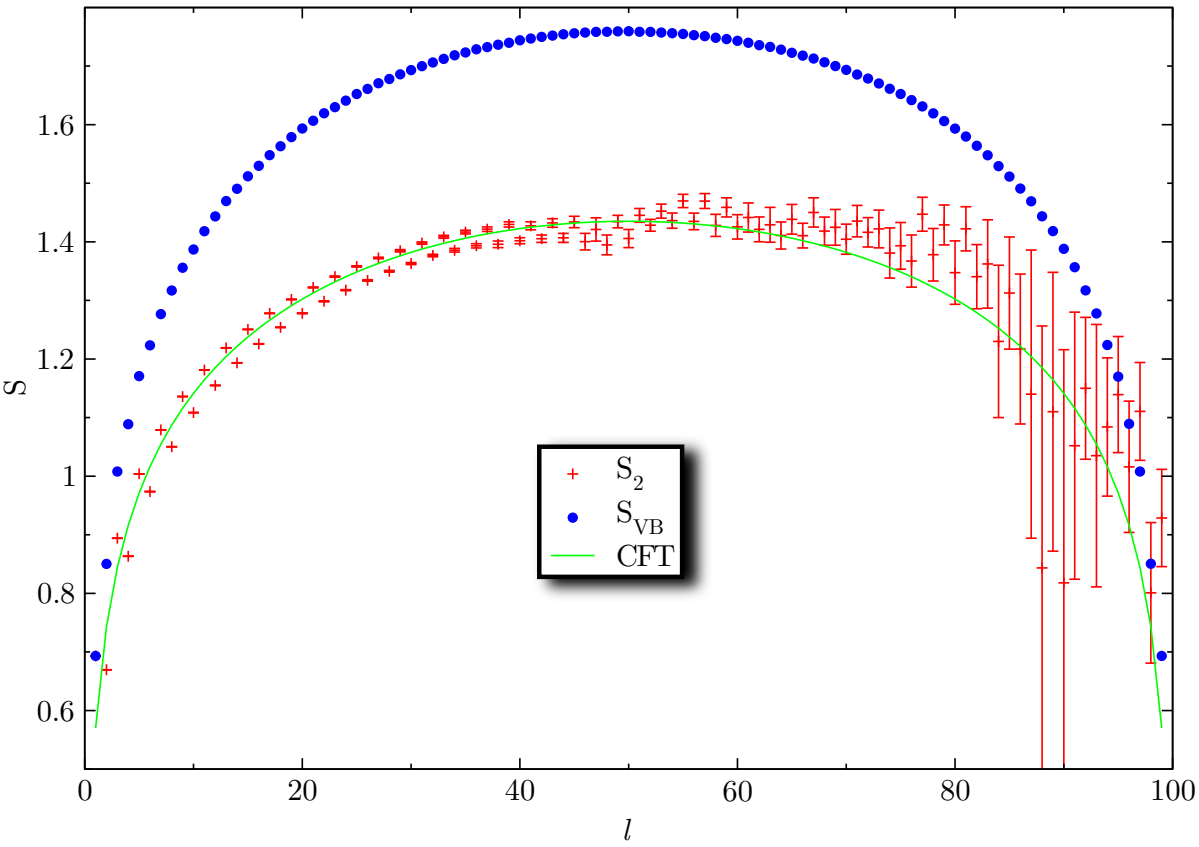

Fig. 4.6.: Scaling of the Rényi entropy S_2 and the valence bond entropy S_{VB} with block size l for a spin chain with $L = 100$ and periodic boundary conditions. Both show logarithmic behavior, with S_2 oscillating around the CFT prediction $S_n^{\mathrm{CFT}}(l) = c/6(1 + n^{-1}) \ln(L/\pi \sin(\pi l/L)) + K$, indicating the presence of subleading corrections [123]. The central charge for the Heisenberg model is $c = 1$, whereas K is a non–universal constant.

Another interesting entanglement measure can be obtained by noticing that the von Neumann entanglement entropy for a valence bond state is simply given by the number of singlets, crossing the boundary between the two subsystems $\mathcal{A}$ and $\mathcal{B}$ [125, 126]. Therefore, in some sense one can interpret a singlet as the basic unit of entanglement. Indeed, for the reduced density operator $\rho_{\mathcal{A}} = \mathrm{Tr}_{\mathcal{B}} |\mathbf{VB}\rangle \langle \mathbf{VB}|$ of a valence bond state $|\mathbf{VB}\rangle$ we have

$$S_{\mathrm{VB}}(\rho_{\mathcal{A}}) = \ln 2 \cdot n_{\mathcal{AB}}, \tag{4.28}$$

where $n_{\mathcal{AB}}$ counts the number of boundary crossing singlets. For arbitrary singlet states one can define different types of averages [125, 126, 127]. The obtained valence bond entanglement entropy does not coincide with the Rényi entropies for arbitrary singlet states, as can be seen in Fig. (4.6) for $n = 2$. However, it also shows logarithmic scaling [128]. It shall be mentioned, that it is also possible to define some loop entanglement entropy [127], where the number of boundary crossing loops is counted, rather than the number of singlets. Such a quantity can also be measured within the valence bond QMC algorithm [12]. The reason of relating these entropy measures to the boundary proper-

ties of a subsystem comes from the well–known area law behavior. Indeed, away from criticality the entropy usually scales as $S \sim L^{D-1}$, whereas at the critical point there are corrections that may emerge, which can be of logarithmic type [129, 89].

The interest in detecting quantum phase transitions by entanglement entropies comes precisely from the corrections to the area law, which can be interpreted as fingerprints of criticality. As an example, for the well–documented one–dimensional case, an increase of entropy may be used as indicator for a QPT. Thus, exactly as for the fidelity approach, this characterization of quantum phase transitions does not require any a priori information, such as an order parameter. Furthermore, in the case of a conformal invariant quantum phase transition, the logarithmic corrections can be used to obtain informations about the associated central charge.

4.3. Partial Conclusion

In summary, we have presented a way to measure fidelity with large scale QMC algorithms, which can in principle be applied in any dimension. This enlarges the class of accessible many body systems and cluster sizes. It has been shown, how these schemes can be used to detect quantum phase transitions within an approach, that does not require any specific information about the system, like the appropriate order parameter. Whereas the fidelity approach is in principle suitable for any many body system, the used Monte Carlo schemes are more restricted.

The valence bond QMC algorithm is designed for $SU(2)$ systems, like the Heisenberg model. It qualitatively captures the quantum phase transitions, but has however not proven to precisely detect them, so far. The stochastic series expansion can be applied to a much wider class of systems, but is rather defined for finite temperature. It is however able to detect QPT, by measuring the fidelity susceptibility at low enough temperature instead of fidelity itself.

We have also related the used fidelity QMC scheme to entanglement entropy measuring methods, providing another generic scheme to detect quantum phase transitions. Especially, Rényi entropies can be obtained with only minor changes of the algorithm. Both methods suffer from the same fluctuation problem, which is caused by measuring the swap operator in the valence bond basis. There are different more or less satisfactory ways out [14, 117], but it might be interesting to heal this with a more general projector quantum Monte Carlo scheme, allowing to measure zero–temperature properties of a much wider class of problems. Such a scheme would allow to measure observables in the spin basis, and therefore be much more suitable for measuring the swap operator.

Measuring the fidelity susceptibility within the stochastic series expansion furthermore helped to verify its critical scaling numerically. It was moreover possible to relate the latter to standard critical exponents [14], illustrating the potential of measuring F and χ_F within QMC methods.

Part III.

Quantum Dimer Models

5. Generalized Quantum Dimer Models

After Anderson had proposed a resonating valence bond (RVB) ground state for the triangular lattice [20], physicists reinforced their interest in valence bond states in general. The question was whether and under which circumstances the Heisenberg model could admit such a ground state.

Motivated by the results obtained by Majumdar and Ghosh in one dimension for a specific frustrated model [130], Klein was the first to explicitly construct Hamiltonians with VB ground states [131]. As in the one–dimensional Majumdar–Ghosh model, he restricted himself to nearest neighbor valence bond states, described in section (2.3.3). In order to have these as ground states, his Hamiltonian contained only terms that entirely symmetrize a spin with its nearest neighbors, i.e. projecting those into a state of maximal spin s. Hence, all nearest neighbor singlet states will be annihilated. Being a sum of projectors, the underlying Hamiltonian can only have positive eigenvalues, thus the nearest neighbor VB states are indeed ground states of the models suggested by Klein.

Such models can also be expressed in terms of spin operators [132], containing however more than only two–spin interactions. This is of course quite clear, as every permutation can be expressed in terms of transpositions and the latter are related to the two–spin Heisenberg interaction. This approach allowed to construct complex models with Heisenberg–like interactions for which (some of) the ground states are exactly known and simple.

This offered the possibility of connecting rather complex Heisenberg interaction containing models with Hamiltonian of which the ground state is known exactly.

Another approach was suggested by Rokhsar and Kivelson [6], where the Heisenberg model was mapped onto a so–called *quantum dimer model* (QDM) of orthogonal nearest neighbor dimer states. The basic idea was that the initial realistic spin model was expressed in the (variational) nearest neighbor valence bond basis, resulting in a generalized eigenvalue problem due to the non–orthogonality of VB states. This problem could be transformed into an ordinary eigenvalue problem by means of an overlap expansion. At the end one was left with a quantum dimer model, acting as (lowest order) effective model for the Heisenberg Hamiltonian. This strategy opened access to exact solutions and also larger accessible clusters in case of non–integrable models.

However, the overlap expansion was essentially stopped at lowest order, resulting in unsatisfactory results. The principle idea to connect Heisenberg models to QDM was nevertheless kept in mind for the future. In principle there were two ways to improve the matching between both types of models. The first one was to somehow derive more complicated Heisenberg–like Hamiltonians, which correspond to very simple QDM.

This has been done by starting out from a Klein model, and perturb it to obtain a quantum dimer model. In order to make the required overlap expansion exact, the lattice was decorated with supplementary spins [133]. A more recent proposal in the realm of quantum dimer models managed to get rid of the decoration procedure, by adding supplementary complex multi–spin interactions [134].

Here we shall explain the opposite scheme, where one starts with a simple Heisenberg model, and pushes the overlap expansion to higher order. The resulting QDM is necessarily more complicated and will have to be studied numerically in most cases.

5.1. Overlap Expansion Scheme

The approach is based on the observation, that frustrated spin models tend to preserve $SU(2)$ symmetry, resulting in a singlet ground state with a finite singlet–triplet gap. Especially in the most interesting two–dimensional case one furthermore often observes short range spin–spin correlations, which are intimately connected with a rapidly decaying singlet length distribution [43]. Such a behavior strongly suggests the nearest neighbor valence bond (NNVB) states as variational ansatz, which has proven its viability in practice on the square lattice [45], the hexagonal lattice [19] and the kagomé lattice [44, 135]. In all of these cases, the variational solution had to be compared to the exact ground state energy on numerically accessible cluster sizes, being so far the only reliable quality check for the NNVB ansatz. This is however a necessary validity test for the method.

The main obstacle of the NNVB approach comes from the non–orthogonality of the VB states, resulting in a generalized eigenvalue problem, which is numerically harder than ordinary eigenvalue problems. As demonstrated in section (2.3.5), the overlap between two arbitrary valence bonds states is given by

$$\langle \varphi \mid \psi \rangle = \alpha^{N-2N_{\bigcirc}}, \tag{5.1}$$

where N corresponds to the number of sites and $N_{\bigcirc}$ is the number of closed loops in the overlap graph formed by superimposing $|\varphi\rangle$ and $|\psi\rangle$. The parameter α accounts for the possible sign conventions with $\alpha_b = 1/\sqrt{2}$ ($\alpha_f = i/\sqrt{2}$) representing the bosonic (fermionic) convention respectively. Notice, that the overlap formula above corresponds precisely to Eq. (2.58).

5.1.1. Dual Basis and Effective Hamiltonian

Whereas valence bond states are generally not linearly independent, it can be shown that linear independence can be recovered for NNVB states on several lattice geometries. Especially on the square lattice, the hexagonal one, and the kagomé lattice this is indeed the case [46, 47]. Such a behavior is essential for the following, as it means that nearest neighbor valence bond states form a (non–orthogonal) basis on the here considered lattices.

Mathematically, one can formalize the notion of non–orthogonal bases $\{|\varphi\rangle\}$ by considering their *dual bases* $\{|\varphi^\star\rangle\}$, defined through

$$\langle\varphi^\star \mid \psi\rangle = \delta_{\varphi,\psi}. \tag{5.2}$$

It is obvious, that the dual basis to the NNVB states does not contain any valence bond state, but can rather be expressed as linear superposition of the latter. In order to see this, we can define an operator

$$\hat{\mathcal{O}} = \sum_{\chi} |\chi\rangle \langle\chi| , \tag{5.3}$$

that transforms the dual basis into NNVB states, $\hat{\mathcal{O}}\,|\psi^\star\rangle = |\psi\rangle$. Such an operator always exists, its inverse is however only defined if $\hat{\mathcal{O}}$ is non–singular. This is precisely the point where we need the NNVB states to be linearly independent. A simple check of the last property can be performed by showing that the determinant of $\hat{\mathcal{O}}$ is non–zero, in which case we may define

$$\hat{\mathcal{O}}^{-1} = \sum_{\chi} |\chi^\star\rangle \langle\chi^\star| . \tag{5.4}$$

This operator precisely transforms the NNVB states into its dual basis. Loosely speaking, it projects an arbitrary state into the dual NNVB subspace, whereas $\hat{\mathcal{O}}$ projects a state into the NNVB space. In that sense $\hat{\mathcal{O}}$ is only invertible within the space spanned by the nearest neighbor valence bond states. A projector in the strict mathematical sense can be formed by setting $\hat{\mathcal{I}} = \hat{\mathcal{O}}\hat{\mathcal{O}}^{-1}$, which is the identity operator within the NNVB subspace. Notice, that for an orthonormal basis we would have $\hat{\mathcal{I}} = \hat{\mathcal{O}}$.

Denoting the Heisenberg Hamiltonian conveniently by

$$\hat{\mathcal{H}}_H = \frac{4}{3} \sum_{i,j} J_{ij} \hat{\boldsymbol{S}}_i \cdot \hat{\boldsymbol{S}}_j + \frac{J_1 N}{2}, \tag{5.5}$$

with the nearest neighbor interaction J_1, the projection of $\hat{\mathcal{H}}_H$ into the NNVB subspace is given by

$$\hat{\mathcal{H}} := \hat{\mathcal{O}}\hat{\mathcal{H}}_H\hat{\mathcal{I}}. \tag{5.6}$$

Here, we project in a different manner from both sides, for a reason that will become clear shortly. For the moment we only remark, that equation (5.6) formalizes the variational NNVB approach, defining an operator $\hat{\mathcal{H}}$ with presumably the same low–energy spectrum as $\hat{\mathcal{H}}_H$. This assumption is however subject to verification in a particular problem.

In the following we will calculate matrix elements of operators, which can be defined through

$$\begin{aligned} \mathcal{A}_{\varphi,\psi} &= \langle\varphi^\star|\, \hat{\mathcal{A}}\, |\psi\rangle \\ &= \langle\varphi|\, \hat{\mathcal{O}}^{-1}\hat{\mathcal{A}}\, |\psi\rangle , \end{aligned} \tag{5.7}$$

in a non–orthogonal basis. Thus, we can express the matrix elements of the *overlap matrix* $\hat{\mathcal{O}}$ and the projected Heisenberg Hamiltonian $\hat{\mathcal{H}}$ by

$$\mathcal{O}_{\varphi,\psi} = \langle\varphi \mid \psi\rangle , \tag{5.8}$$

$$\mathcal{H}_{\varphi,\psi} = \langle\varphi|\, \hat{\mathcal{H}}_H\, |\psi\rangle . \tag{5.9}$$

At this stage we see why we precisely defined the operators $\hat{\mathcal{O}}$ and $\hat{\mathcal{H}}$, which have matrix elements that can be obtained directly from the basis $\{|\varphi\rangle\}$ by means of the overlap rule (Eq. 5.1) and equation (2.57).

In the above notation the generalized eigenvalue problem for diagonalizing $\hat{\mathcal{H}}_H$ in the variational basis $\{|\varphi\rangle\}$ becomes

$$\det(\hat{\mathcal{H}} - E\hat{\mathcal{O}}) = 0. \tag{5.10}$$

The idea suggested by Rokhsar and Kivelson [6], is to transform this problem into an ordinary eigenvalue problem. This leads to the definition of an effective Hamiltonian

$$\hat{\mathcal{H}}_{\text{eff}} = \hat{\mathcal{O}}^{-1/2}\hat{\mathcal{H}}\hat{\mathcal{O}}^{-1/2} \tag{5.11}$$

$$= \hat{\mathcal{O}}^{1/2}\hat{\mathcal{I}}\hat{\mathcal{H}}_H\hat{\mathcal{I}}\hat{\mathcal{O}}^{-1/2}, \tag{5.12}$$

as it is often the case in physics [136]. Two important points have to be highlighted here. Firstly, $\hat{\mathcal{H}}_{\text{eff}}$ is nothing but a similarity transformation of $\hat{\mathcal{I}}\hat{\mathcal{H}}_H\hat{\mathcal{I}}$, and should therefore have exactly the same spectrum. We will indeed see, that the effective Hamiltonian describes the same physics as the NNVB–projected one, i.e. the eigenvalue problem

$$\det(\hat{\mathcal{H}}_{\text{eff}} - E) = 0, \tag{5.13}$$

is fully equivalent to equation (5.10) and should therefore have the same low–energy spectrum as the Heisenberg Hamiltonian $\hat{\mathcal{H}}_H$.

Secondly, the resulting effective Hamiltonian (Eq. 5.11) is symmetric in the matrices $\hat{\mathcal{O}}_{\varphi,\psi}$ and $\hat{\mathcal{H}}_{\varphi,\psi}$ and can therefore be expressed in terms of anticommutators. It is for example trivial to see, that one can also write

$$\hat{\mathcal{H}}_{\text{eff}} = \frac{1}{2}\left\{\hat{\mathcal{O}}^{-1/2}, \left\{\hat{\mathcal{O}}^{-1/2}, \hat{\mathcal{H}}\right\}\right\} - \frac{1}{2}\left\{\hat{\mathcal{H}}, \hat{\mathcal{O}}^{-1}\right\}, \tag{5.14}$$

where we expressed the entire Hamiltonian by means of symmetric products. However, this cannot be evaluated exactly, as $\hat{\mathcal{O}}^{-1/2}$ is defined through a power series

$$\hat{\mathcal{O}}^{\tau} = \sum_{k=0}^{\infty} \frac{\Gamma(1+\tau)}{\Gamma(1+\tau-k)\Gamma(1+k)}(\hat{\mathcal{O}} - \hat{1})^k, \tag{5.15}$$

which has to be truncated in practice. Notice, that up to this point everything is quite general, independently of the specific choice for $\{|\varphi\rangle\}$. In principle we only required the linear independence, and we could therefore also use any other variational basis to derive an effective Hamiltonian.

5.1.2. Overlap Matrix Expansion and Fusion Rules

The basic insight by Rokhsar and Kivelson [6] was, that the overlap matrix contains different negative powers of two, enabling an approximation into a power series. In the original scheme this series has been truncated at the lowest order, while later higher

order corrections have been considered [15]. Such a scheme could successfully be applied to the square lattice [137], the kagomé lattice [18] and to the hexagonal one [19].

In order to carry out such a scheme, a rigorous notation has to be established and shall be presented here. The overlap matrix can be expanded as

$$\hat{\mathcal{O}} = \sum_{\varphi,\psi} |\varphi\rangle \langle \varphi \mid \psi\rangle \langle \psi^\star| \tag{5.16}$$

$$= \sum_{\varphi,\psi} \alpha^{\mathcal{L}_{\varphi,\psi} - 2\mathcal{N}_{\varphi,\psi}} |\varphi\rangle \langle \psi^\star| \,, \tag{5.17}$$

where $\mathcal{L}_{\varphi,\psi}$ is the net length of all non–trivial (i.e. length–2) loops and $\mathcal{N}_{\varphi,\psi}$ is their number. Here we used the overlap rule (Eq. 5.1) and the fact that it can be expressed exclusively in terms of loops, that contain more than two dimers. Indeed, the number of trivial loops is given by [15]

$$N_{\bigcirc} - \mathcal{N}_{\varphi,\psi} = \frac{N - \mathcal{L}_{\varphi,\psi}}{2}. \tag{5.18}$$

The main consequence is that we can classify all processes $|\varphi\rangle \langle \psi^\star|$ by their non–trivial contributions and introduce a graphical representation, which neglects the trivial loops. As an example, on lattices containing a hexagon we may define

$\hat{\omega}_{g_1} =$ 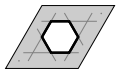 $:= \sum_{\hexagon}$ 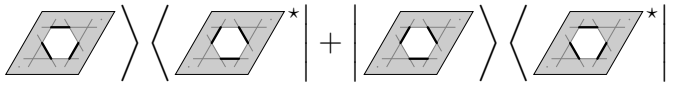 , (5.19)

which acts on every state that contains a *flippable* plaquette of dimers, by flipping them around the hexagon. The sum goes over all plaquettes on the lattice, consequently $\hat{\omega}_{g_1}$ acts on all flippable hexagons. Such a *kinetic* (*off–diagonal*) process has been suggested by Rokhsar and Kivelson in the case of a square lattice [6]. Inspecting this process, it appears that $\hat{\omega}_{g_1}$ is symmetric in the two participating dimer configurations. This fact can be formally expressed as

$$(\hat{\omega}_g \hat{\mathcal{O}})^\dagger = \hat{\omega}_g \hat{\mathcal{O}}, \tag{5.20}$$

and shall be the defining property for a process to be representable as a diagram. As equation (5.15) suggests, products of processes will play a vital role for the overlap expansion. Here it is obvious, that for two processes $\hat{\omega}_1$ and $\hat{\omega}_2$ the product $\hat{\omega}_1\hat{\omega}_2$ will not be representable as a diagram. We can convince ourselves however, that the symmetrized form

$$\hat{\omega}_g = \frac{1}{2} \{\hat{\omega}_1, \hat{\omega}_2\} \tag{5.21}$$

satisfies (5.20), provided this holds for $\hat{\omega}_1$ and $\hat{\omega}_2$. This is another way to see the symmetric nature of the diagrams and together with Eq. (5.14) manifests the possibility to express the effective Hamilton in diagrammatic form.

Making use of the diagrammatic notation, we can rewrite equation (5.17) as

$$\hat{\mathcal{O}} = \sum_g \alpha^{2\mathrm{n}(g)} \hat{\omega}_g, \tag{5.22}$$

where

$$\mathrm{n}(g) = \frac{\mathcal{L}_{\varphi,\psi}}{2} - \mathcal{N}_{\varphi,\psi} \tag{5.23}$$

is half the *order* of the diagram $\hat{\omega}_g$ according to the development parameter α. Notice, that such a development has been considered in literature by simply taking the loop length into account [6, 138, 133]. This is fully justified if only one non–trivial loop occurs. Here however, we have to take the number of loops into account as well, in order to establish an expansion scheme that is well defined for higher orders. The identification of this order is in some sense the crucial key to develop general quantum dimer models beyond the Rokhsar–Kivelson (RK) QDM [15]. As an example, the flip around a hexagon $\hat{\omega}_{g_1}$ from equation (5.19) has a loop length 6 and is therefore of order $2\mathrm{n}(g) = 2(6/2 - 1) = 4$.

Regarding the overlap expansion (Eq. 5.22), we firstly note, that the exponent $2\mathrm{n}(g)$ is always an even number and only zero for trivial processes. Such terms are accounted for in a process $\hat{1}$, which acts as unity operator on a dimer state. Further terms in the overlap expansion are all of kinetic character and consist simply of one or several closed loops, that flip dimers around their boundary. The symmetric multiplication (Eq. 5.21) of diagrams can however involve more complicated processes, which can still be represented in terms of diagrams. We therefore call the symmetric multiplication a *fusion* of diagrams. The different emerging classes of diagrams are quite general, their explicit notation depends however heavily on the underlying lattice. Following [15], we will here give several representative examples on the kagomé lattice.

Let us illustrate the fusion of diagrams by considering a simple example, where two hexagon flips encounter each other

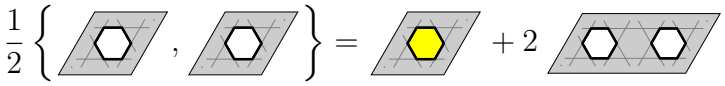

(5.24)

resulting in the emergence of two other diagrams. The yellow shaped one is quite general and illustrates the fact, that a kinetic process can be applied twice on the same hexagon,

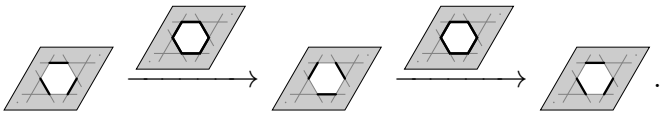

(5.25)

This does not change the state of the plaquette, but rather checks whether the plaquette is flippable. Therefore, the *potential* (*diagonal*) process

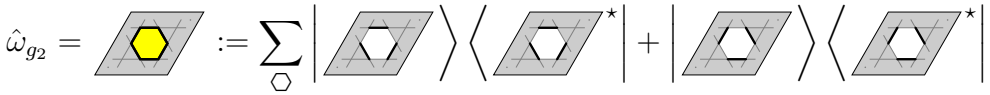

(5.26)

counts the number of flippable hexagons within a dimer state. Potential processes will always be represented by diagrams with yellow shape within this notation. Such a process is actually the second term considered in the original work by Rokhsar and Kivelson [6]. Indeed, the analogue of the RK–model on the kagomé lattice could be written with the above notation as

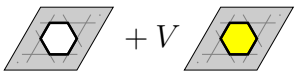

(5.27)

Another type of diagrams emerges in Eq. (5.24), when the hexagon flips act on distant plaquettes,

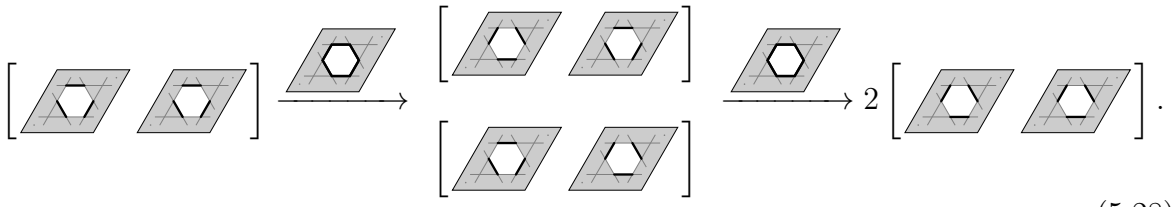

(5.28)

This results in a kinetic process where two plaquettes are flipped independently, regardless of their relative position. We therefore call such a process *non–connected* in contrast to *connected* terms as the flip around a single hexagon. Non–connected terms play a role in the overlap expansion scheme, but vanish in the effective Hamiltonian [15]. The factor two in Eq. (5.24) comes from the possibility to flip both plaquettes in two different orders. Notice, that the two flips have to take place on different plaquettes, otherwise we create the potential term (Eq. 5.26). Moreover, it shall be mentioned, that a two–hexagon flip like Eq. (5.28) also appears naturally in the overlap expansion of $\hat{\mathcal{O}}$, which is however not the case for any potential term. The latter can only be created through fusion processes.

Besides the two possibilities of processes happening either at precisely the same location or at distant positions, it is also observed that process act on dimers nearby each other. For example, on the kagomé lattice we find the following relations

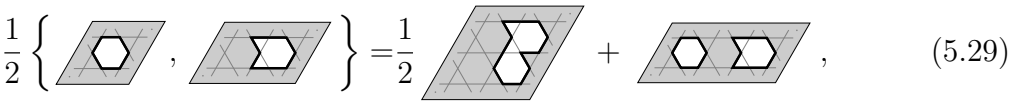

(5.29)

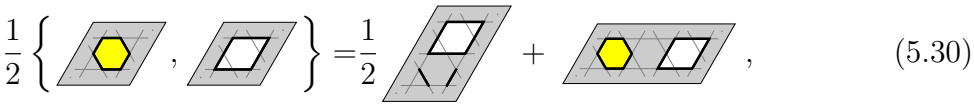

(5.30)

which illustrate the formation of other connected processes. The first fused diagram (Eq. 5.29) can be formed by

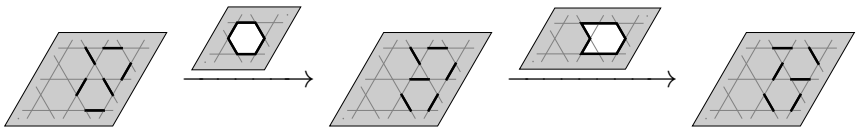

(5.31)

as one contributing part of the anticommutator. The other half can be built by reading equation (5.31) from the right to the left, i.e. when two diagrams of different shape are fused, the anticommutator is the precise way to form a valid diagram. This particularity explains also the factor 1/2 in the fusion rule in Eq. (5.29). Notice moreover, that the here considered diagrams do not only comprise all translations of the flipped pattern, but also all rotations and reflexions on the underlying lattice. Hence, no diagram breaks any lattice symmetry.

Finally, another class of occurring diagrams are the so–called *assisted* kinetic processes

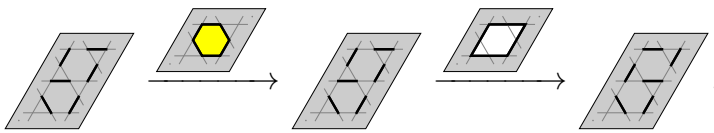

(5.32)

depicted in equation (5.30). These are conditioned by the presence of dimers close to the flipped pattern, but not participating in any rearrangement. Here we also only obtain half the anticommutator by reading Eq. (5.32) from the left to the right, hence yielding the factor 1/2 in the fusion rule (5.30).

As illustrated, $\hat{\mathcal{O}}$ only contains kinetic processes, which are essentially formed by the non–trivial loop structure of superimposed NNVB states. These can thus be represented by closed loops, which describe a flip along them between the two possible dimer configurations. Diagrams that are contained in $\hat{\mathcal{O}}$ can be attributed an order $2n(g)$, which depends on the loop lengths and their number. Interestingly, non–connected diagrams have an order which is simply the sum over their connected parts. This is a fact, that can be seen quite easily.

More complicated diagrams emerge through the notion of fusion and generally fill up the number of processes connecting a family of dimer states. On a single hexagon for example there are only two possible NNVB states. The resonating term between both is the hexagonal flip (Eq. 5.19), which appears in $\hat{\mathcal{O}}$. The missing term in this configuration space counts the number of flippable plaquettes and can only be generated by a fusion of two kinetic processes. Sometimes, the missing pieces describe rather peculiar processes and have to be accounted for by adapted diagrams [137]. However, the emerging diagrams are always of an order which is the sum of their fusing parts.

5.1.3. Hamiltonian Expansion

The fusion rules we have seen so far allow to expand any power of $\hat{\mathcal{O}}$ to arbitrary precision. However, to express the effective Hamiltonian (Eq. 5.11) in terms of diagrams we still need to expand $\hat{\mathcal{H}}$. Fortunately, the evaluation of its matrix elements (Eq. 5.9) can also be obtained from the overlap graph, as we have seen in Eq. (2.57). More precisely, for the Heisenberg Hamiltonian (Eq. 5.5) one can obtain the matrix elements through [11, 15]

$$\langle\varphi|\,\hat{\mathcal{H}}_H\,|\psi\rangle = \sum_{i,j} J_{ij}\;\varepsilon_{ij}^{\varphi,\psi}\,\langle\varphi\mid\psi\rangle\,, \tag{5.33}$$

where $\varepsilon_{ij}^{\varphi,\psi}$ is defined distinguishing three different cases:

a. i and j are two sites lying at an odd distance on the same loop in the overlap graph of $|\varphi\rangle$ and $|\psi\rangle$ and $\varepsilon_{ij}^{\varphi,\psi} = -1$,

b. i and j are on two distinct loops in the overlap graph of $|\varphi\rangle$ and $|\psi\rangle$ and $\varepsilon_{ij}^{\varphi,\psi} = 0$,

c. i and j are two sites lying at an even distance on the same loop in the overlap graph of $|\varphi\rangle$ and $|\psi\rangle$ and $\varepsilon_{ij}^{\varphi,\psi} = +1$.

Recasting equation (5.33) as

$$\mathcal{H}_{\varphi,\psi} = h_{\varphi,\psi}\mathcal{O}_{\varphi,\psi}, \tag{5.34}$$

and splitting the sum into contributions from trivial and non–trivial loops, we obtain

$$h_{\varphi,\psi} = J_1\frac{\mathcal{L}_{\varphi,\psi}}{2} + \sum_{\substack{(i,j)\in \text{ non-}\\ \text{trivial loops}}} J_{ij}\varepsilon_{ij}^{\varphi,\psi}. \tag{5.35}$$

Here it is crucial to see, that $h_{\varphi,\psi}$ can be expressed in terms of non–trivial loops exclusively. Indeed, for trivial loops we have $\varepsilon_{ij}^{\varphi,\psi} = -1$ and expressing their number by equation (5.18), the above expression (5.35) is readily obtained. An important consequence is that every diagram $\hat{\omega}_g$ can be attributed an *energy* h_g ($\equiv h_{\varphi,\psi}$), which is given by Eq. (5.35). In particular, the identity $\hat{1}$, which contains only trivial loops, has a weight $h_{\hat{1}} = 0$. In analogy to Eq. (5.22) [15], we can thus write

$$\hat{\mathcal{H}} = \sum_g \alpha^{2\mathrm{n}(g)} h_g \hat{\omega}_g, \tag{5.36}$$

where precisely the same diagrams $\hat{\omega}_g$ as in the expansion of $\hat{\mathcal{O}}$ appear.

Regarding non–connected diagrams we have to underline the fact, that their energy is simply the sum of their connected parts. Therefore, it is sufficient to derive orders and energies for all connected diagrams contributing to $\hat{\mathcal{O}}$, in order to expand $\hat{\mathcal{O}}$ and $\hat{\mathcal{H}}$ to arbitrary order. Finally, to give an example, the energy of the hexagon flip (Eq. 5.19) is given by $h_{g_1} = 3J_1 - 6J_1 = -3J_1$, when only nearest neighbor interactions are considered. When also next nearest neighbor interactions are taken into account, this energy will change. However, the overall expansion structure (Eq. 5.36) will remain the same for any Hamiltonian, that contains only two–spin Heisenberg interactions.

5.1.4. Effective Hamiltonian Expansion

Having established the expansion of $\hat{\mathcal{O}}$ and $\hat{\mathcal{H}}$ within a diagrammatic language (Eqs. 5.22 and 5.36), we can now expand the effective Hamiltonian. This can in principle be done in two different ways. The first possibility is to insert the expansions of $\hat{\mathcal{O}}$ and $\hat{\mathcal{H}}$ into Eqs. (5.14) and (5.15), establishing an expression, which explicitly contains all required fusions in order to derive the effective Hamiltonian. In practice, this will be carried out by limiting the expansion scheme *a priori* to a certain order $2\mathrm{n}(g)$. This introduces a truncation in the diagrammatic expansions of $\hat{\mathcal{O}}$ and $\hat{\mathcal{H}}$, as well as in the fusions. Such a scheme has been studied in [15] for the kagomé lattice and is also illustrated in appendix (A). Notice furthermore, that the original work by Rokhsar and Kivelson [6] can be interpreted as truncation at lowest order.

The previous method has however one disadvantage, which lies in the fact, that one computes the weight of every process up to a certain order in α. Regarding for example the following succession of processes

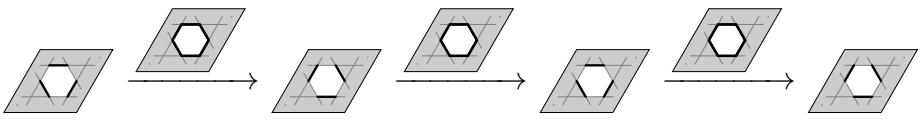

(5.37)

we see that acting three times on the same plaquette with a kinetic term of order α^4, we effectively obtain a flip of order α^{12}, also contributing to the effective Hamiltonian. In fact, every diagram will appear at an infinite number of different orders, which one would like to sum up, to obtain the correct amplitude for a given process. Using the above method, this will require to consider an infinite number of fusions, which can render the derivation rather difficult.

Another approach consists in calculating the exact weight of a given diagram. The difference here is to choose the processes one is interested in, rather than the order at which the effective Hamiltonian shall be at the end. The advantage of this technique is, that we directly obtain the weight of a process, with a rather small number of fusions, instead of summing up an infinite series (Eq. 5.15). This is possible because of the following observation. Whenever we fuse two different diagrams, the resulting processes will be at least as complex as the initial ones. To illustrate this we simply consider the two simplest terms on the kagomé lattice, which are those defined on a hexagon, a kinetic diagram (Eq. 5.19) and its potential counterpart (Eq. 5.26). These two diagrams can only be obtained within fusions among themselves (Eq. 5.24), but not when fusing with any other process, living on two or more hexagons.

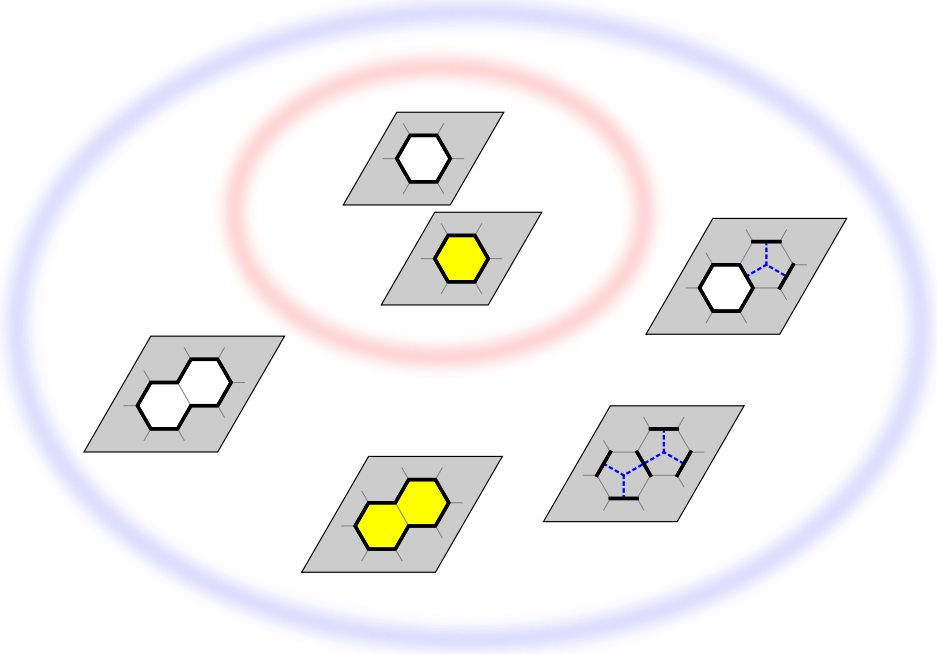

Fig. 5.1.: Dependency of processes on the honeycomb lattice. The two diagrams in the red frame can only be obtained by fusions among themselves, restricting the number of required fusion rules. The other four processes depend on fusions among *all six* diagrams in the blue frame. For an explanation of these processes see Fig. (6.11).

A second example is given in Fig. (5.1), where we consider some processes on the honeycomb lattice. In order to compute the exact weights of the diagrams in the red frame, it is sufficient to consider fusions among these two processes. Indeed, fusions with any other diagram will not contribute to the weight of the diagrams in the red frame. When enlarging the basis to all six diagrams in the blue frame, we need to consider every possible fusion among these six diagrams. Of course, this will not change the weight of the processes in the red frame and on the other side, there are no further diagrams to be considered when we are only interested in the exact weight of these six diagrams.

It is straightforward to recognize, that we will always be able to construct arbitrarily

large families of diagrams, which only depend on themselves and thus somehow form a closed set. We will call this set a *basis of diagrams*, in which we express the whole expansion scheme. One side effect is the possibility of considering *reduced fusion rules*, which contain only the processes from the chosen basis, i.e. we will systematically neglect all other diagrams. Another direct consequence is, that we will be able to express fusions as products of matrices with vectors, and thereby transform our problem to an ordinary linear algebra one. An example of this can be found in appendix (B), where we derive an effective Hamiltonian for the honeycomb lattice.

In order to formally define our linear algebra problem, we introduce different notations. Firstly, it is very useful to split expansions into contributions from trivial loops and non–trivial ones. Trivial loops contribute only to zeroth order and we therefore write

$$\hat{\mathcal{O}} = \hat{1} + \hat{\mathcal{X}}, \tag{5.38}$$

$$\hat{\mathcal{O}}^{-1} = \hat{1} - \hat{\mathcal{Y}}, \tag{5.39}$$

$$\hat{\mathcal{O}}^{-1/2} = \hat{1} - \hat{\mathcal{R}}, \tag{5.40}$$

where $\hat{1}$ is the identity operator and the diagrams contributing to $\hat{\mathcal{X}}$, $\hat{\mathcal{Y}}$ and $\hat{\mathcal{R}}$ are all of order $2\mathrm{n}(g) \geq 2$. The aim of this manipulation is that we can now formally write $\hat{\mathcal{X}}$, $\hat{\mathcal{Y}}$ and $\hat{\mathcal{R}}$ as vectors in the basis of diagrams. However, for technical reasons we do not want to include the identity process $\hat{1}$ into this basis, justifying the splitting above. Notice, that an analogue manipulation for $\hat{\mathcal{H}}$ is not necessary, as the identity $\hat{1}$ is already suppressed, due to $h_{\hat{1}} = 0$.

Additionally, we may define an anticommutator as a linear operator $\{A, \bullet\}$, by

$$\{A, \bullet\}\, B := \{A, B\}\,. \tag{5.41}$$

This offers the possibility to interpret an anticommutator as matrix, hence a fusion of two diagrams is nothing but a multiplication of a matrix with a vector. Using the above notation one can formally express the relations between $\hat{\mathcal{X}}$, $\hat{\mathcal{Y}}$ and $\hat{\mathcal{R}}$. Firstly, $\frac{1}{2}\left\{\hat{\mathcal{O}}, \hat{\mathcal{O}}^{-1}\right\} = \hat{1}$ becomes

$$\hat{\mathcal{Y}} = \left(\hat{1} + \frac{1}{2}\left\{\hat{\mathcal{X}}, \bullet\right\}\right)^{-1} \hat{\mathcal{X}}, \tag{5.42}$$

which can thus be readily used to obtain $\hat{\mathcal{O}}^{-1}$ from the overlap expansion of $\hat{\mathcal{O}}$. Indeed, in order to obtain $\hat{\mathcal{Y}}$ we simply need to invert the known matrix $\hat{1} + \frac{1}{2}\left\{\hat{\mathcal{X}}, \bullet\right\}$ and multiply the result with the known vector $\hat{\mathcal{X}}$. Therefore, $\hat{\mathcal{Y}}$ can always be computed analytically, provided $\hat{1} + \frac{1}{2}\left\{\hat{\mathcal{X}}, \bullet\right\}$ is not singular. Similarly, we have $\frac{1}{2}\left\{\hat{\mathcal{O}}^{-1/2}, \hat{\mathcal{O}}^{-1/2}\right\} = \hat{\mathcal{O}}^{-1}$, which can be rewritten as

$$\hat{\mathcal{R}} = \left(2 \cdot \hat{1} - \frac{1}{2}\left\{\hat{\mathcal{R}}, \bullet\right\}\right)^{-1} \hat{\mathcal{Y}}. \tag{5.43}$$

This implicit equation in $\hat{\mathcal{R}}$ cannot be solved analytically. It turns however out, that we can guess some initial vector $\hat{\mathcal{R}}$ and use equation (5.43) to iteratively obtain its

numerical approximation. We simply need to apply all the reduced fusion rules to $\hat{\mathcal{R}}$, in order to obtain the matrix $\left\{\hat{\mathcal{R}}, \bullet\right\}$. Inverting $2 \cdot \hat{1} - \frac{1}{2}\left\{\hat{\mathcal{R}}, \bullet\right\}$ and multiplying the result with $\hat{\mathcal{Y}}$, we get a better approximation of $\hat{\mathcal{R}}$. This procedure can be repeated until $\hat{\mathcal{R}}$ is numerically exact, and has proven to converge rather rapidly [19].

Finally, one can recast the effective Hamiltonian (Eq. 5.14) into a form, explicitly being expressed in terms of $\hat{\mathcal{Y}}$ and $\hat{\mathcal{R}}$,

$$\hat{\mathcal{H}}_{\text{eff}} = \hat{\mathcal{H}} - \frac{1}{2}\left\{\hat{\mathcal{H}}, \hat{\mathcal{Y}}\right\} - \frac{1}{2}\Big[\left\{\hat{\mathcal{H}}, \bullet\right\}, \left\{\hat{\mathcal{R}}, \bullet\right\}\Big]\hat{\mathcal{R}}. \tag{5.44}$$

Here we see, that the effective Hamiltonian is approximated by $\hat{\mathcal{H}}$ in lowest order. Furthermore, the first and the second term can be calculated exactly for any diagram. The only numerical approximation comes from the calculation of $\hat{\mathcal{R}}$, which enters in the last term. Notice, that this last term is simply a commutator of two matrices, which can be easily computed, provided we know $\hat{\mathcal{R}}$.

5.1.5. Elementary Processes

In this section we will explicitly perform the overlap expansion, by applying equation (5.44) to a special family of diagrams. These processes correspond to diagrams, which cannot be cut into others. Alternatively, it is in some sense the innermost or smallest family of diagrams we can find (see Fig. 5.1). We will call these diagrams *elementary processes*, as all other diagrams can be defined by fusions of these elementary bricks [15].

Basically this smallest family with the elementary diagrams has rather general and simple reduced fusion rules, because of two reasons. Firstly, such a family consists of precisely two diagrams, a kinetic process and its potential counterpart. Secondly, these diagrams cannot be built by any other diagrams through fusions, hence there are only three reduced fusion rules, which are independent of the chosen lattice. Consider for example the hexagonal diagrams on the kagomé lattice, which form the following basis of processes

$$\left\{ \begin{pmatrix} 1 \\ 0 \end{pmatrix} = \quad , \begin{pmatrix} 0 \\ 1 \end{pmatrix} = \quad \right\}.$$

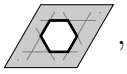
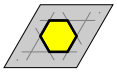

Notice, that here we simply used a vector notation for all basis diagrams. This will allow to systematically express diagrams as vectors and anticommutators as matrices. In general, the kinetic elementary process will have a loop length $\mathcal{L}$ and an energy h. Hence, the overlap expansion in Eq. (5.22), can be expressed in the chosen basis by

$$\hat{\mathcal{X}} = \alpha^{\mathcal{L}-2} \begin{pmatrix} 1 \\ 0 \end{pmatrix}, \tag{5.45}$$

which can be written in case of the kagomé lattice (setting $\mathcal{L} = 6$) as

$$\hat{\mathcal{X}} = \alpha^4 \quad . \tag{5.46}$$

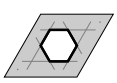

Similarly, the Hamiltonian $\hat{\mathcal{H}}$ is given by its expansion (5.36) and thus we obtain

$$\hat{\mathcal{H}} = h\alpha^{\mathcal{L}-2} \begin{pmatrix} 1 \\ 0 \end{pmatrix}. \tag{5.47}$$

In the chosen basis the reduced fusion rules will be of the following form

$\frac{1}{2}\left\{ \right.$ 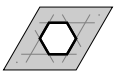 $\left. \right\} =$ 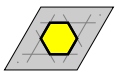 , (5.48)

$\frac{1}{2}\left\{ \right.$ 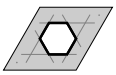 $\left. \right\} =$ 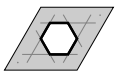 , (5.49)

$\frac{1}{2}\left\{ \right.$ 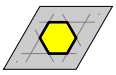 $\left. \right\} =$ 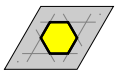 . (5.50)

Based on these fusion rules, we easily find

$$\frac{1}{2}\left\{ \begin{pmatrix} 1 \\ 0 \end{pmatrix}, \bullet \right\} = \begin{pmatrix} 0 & 1 \\ 1 & 0 \end{pmatrix}, \tag{5.51}$$

$$\frac{1}{2}\left\{ \begin{pmatrix} 0 \\ 1 \end{pmatrix}, \bullet \right\} = \begin{pmatrix} 1 & 0 \\ 0 & 1 \end{pmatrix}. \tag{5.52}$$

Notice, that even though we presented the fusion rules on the kagomé lattice, Eqs. (5.51) and (5.52) are valid for any elementary process on any lattice. Furthermore, it shall be mentioned again, that the above three reduced fusion rules represent precisely all possible fusions among this family of elementary diagrams.

Putting equations (5.45) and (5.51) together, we obtain the anticommutator

$$\frac{1}{2}\left\{ \hat{\mathcal{X}}, \bullet \right\} = \alpha^{\mathcal{L}-2}\hat{\sigma}_x, \tag{5.53}$$

where $\hat{\sigma}_x$ is a Pauli matrix. In the same spirit we find

$$\frac{1}{2}\left\{ \hat{\mathcal{H}}, \bullet \right\} = h\alpha^{\mathcal{L}-2}\hat{\sigma}_x. \tag{5.54}$$

These equations can be used to calculate the inverse overlap matrix $\hat{\mathcal{O}}^{-1} = \hat{1} - \hat{\mathcal{Y}}$. Inserting equations (5.45) and (5.53) into (5.42), we directly obtain

$$\hat{\mathcal{Y}} = \frac{\alpha^{\mathcal{L}-2}}{1-\alpha^{2\mathcal{L}-4}} \begin{pmatrix} 1 \\ -\alpha^{\mathcal{L}-2} \end{pmatrix}. \tag{5.55}$$

Finally, we have everything to write down the effective Hamiltonian for elementary processes. We only need to apply Eq. (5.44), by noticing the important point that in the special case of elementary processes we do not need to explicitly calculate $\hat{\mathcal{R}}$. It is very clear, that $\left\{ \hat{\mathcal{R}}, \bullet \right\}$ will be a linear combination of $\hat{\sigma}_x$ and $\hat{1}_{2\times 2}$, both commuting

with $\left\{\hat{\mathcal{H}}, \bullet\right\}$. Hence, the latter also commutes with $\left\{\hat{\mathcal{R}}, \bullet\right\}$ and thus (5.44) reduces for elementary processes to

$$\hat{\mathcal{H}}_{\text{eff}} = \hat{\mathcal{H}} - \frac{1}{2}\left\{\hat{\mathcal{H}}, \hat{\mathcal{Y}}\right\} \tag{5.56}$$

$$= h\frac{\alpha^{\mathcal{L}-2}}{1-\alpha^{2\mathcal{L}-4}}\begin{pmatrix} 1 \\ -\alpha^{\mathcal{L}-2} \end{pmatrix}. \tag{5.57}$$

Remember (see section 5.1.3), that for the hexagonal flip on the kagomé lattice we have a loop length of $\mathcal{L} = 6$ and $h = -3J_1$. Hence we obtain an effective Hamiltonian of [15]

$$\hat{\mathcal{H}}_{\text{eff}} = -3J_1\frac{\alpha^4}{1-\alpha^8}$$ 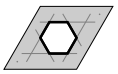 $$+\,3J_1\frac{\alpha^8}{1-\alpha^8}$$ 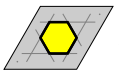 $$. \tag{5.58}$$

In the case of the kagomé lattice there are actually much more elementary diagrams, which can all be calculated exactly. On the square lattice and the hexagonal one we have only two elementary processes, which are precisely those that are contributing in the original Rokhsar–Kivelson model [6]. Notice however, that here we were able to calculate their exact amplitudes, whereas in earlier works [6] the expansion has been truncated at lowest order in α. This is actually one of the main results of the present work. Another important result is that one can calculate the contribution of any other diagram with arbitrary numerical precision. One would then have to consider a bigger basis of diagrams, hence yielding vectors and matrices of higher dimension. This becomes analytically more complicated, but is numerically feasible, an example of which is illustrated in appendix (B).

Performing such a calculation reveals a vanishing amplitude for non–connected diagrams for the effective Hamiltonian. With the present scheme this can be calculated explicitly for any of such processes. In the following section we will show that this holds for all non–local processes.

5.1.6. Locality of the Effective Hamiltonian

The appearance of non–connected diagrams in the expansion of $\hat{\mathcal{O}}$ and $\hat{\mathcal{H}}$ might at first glance be rather surprising, as these describe processes happening at arbitrary distance and independently of each other, although the Heisenberg Hamiltonian $\hat{\mathcal{H}}_H$ contains only local interactions. Fortunately, these diagrams cancel out when performing the overlap expansion for $\hat{\mathcal{H}}_{\text{eff}}$, a fact that has been demonstrated in [15]. This is quite important, as it shows some kind of self–consistence of the overlap expansion scheme.

The basis idea was to establish a connection to a linked cluster theorem, stating that the logarithm of some generating function $\hat{\mathcal{Z}}$ consists only of connected diagrams. These connected diagrams were obtained from cumulants, which could be interpreted as reduction of fusions to connected processes, only. At the end, the effective Hamiltonian could be expressed in terms of $\ln\hat{\mathcal{Z}}$, proving its locality [15]. This proof is rather nice as it makes the connection to the well–known cluster theorem. However, the presentation is admittedly quite lengthy and difficult to follow. Therefore, we shall give an alternative demonstration in the remaining part of this section.

The basic observation is the deep connection between $\hat{\mathcal{O}}$ and $\hat{\mathcal{H}}$, which can be expressed by some generating function

$$\hat{\mathcal{Z}}(\mu) = \sum_g \alpha^{2\mathrm{n}(g)} e^{\mu h_g} \hat{\omega}_g. \tag{5.59}$$

Comparing with Eqs. (5.22) and (5.36), we immediately find

$$\hat{\mathcal{O}} = \hat{\mathcal{Z}}(0), \tag{5.60}$$

$$\hat{\mathcal{H}} = \partial_\mu \hat{\mathcal{Z}}(0). \tag{5.61}$$

Therefore, the effective Hamiltonian (Eq. 5.11) can be conveniently rewritten as

$$\hat{\mathcal{H}}_{\text{eff}} = \lim_{\mu\to 0} \hat{\mathcal{Z}}^{-1/2} \left(\partial_\mu \hat{\mathcal{Z}}\right) \hat{\mathcal{Z}}^{-1/2} \tag{5.62}$$

$$= \lim_{\mu\to 0} \pm \left\{ \hat{\mathcal{Z}}^{\mp 1/2}, \partial_\mu \hat{\mathcal{Z}}^{\pm 1/2} \right\}, \tag{5.63}$$

where we used the product rule in the last line and both contained expressions are equivalent.

Set up for the Proof

In order to establish the locality, we may first state the most important properties of the generating function $\hat{\mathcal{Z}}$.

- The coefficient in front of every non–connected diagram is the product of the coefficients of its contributing pieces. This simply means, that the order and the energy of a non–connected diagram can be obtained as sum over the constituents. To illustrate this, remember, that is of order α^4, whereas is of order α^8, as it contains twice the first diagram.

- The fusion rules preserve this behavior, that is, the amplitudes of fused diagrams can be obtained as product over their fusing parts. Thus, it is in principle possible to define an order and an energy for diagrams which are not contained in the overlap expansion of $\hat{\mathcal{O}}$ and $\hat{\mathcal{H}}$.

These two properties will be referred to as *energy additivity* or equivalently *order additivity*, as suggested by equation (5.59) for the behavior of the order $2\mathrm{n}(g)$ or the energy h_g. What we are going to prove in the following, is that the above two properties of $\hat{\mathcal{Z}}$ are sufficient for

$$\left\{ \hat{\mathcal{Z}}^{-1}, \partial_\mu \hat{\mathcal{Z}} \right\} \tag{5.64}$$

to be local. Notice, that this expression is not the effective Hamiltonian, but simply some anticommutator that looks a bit similar to Eq. (5.63). However, here we claim that expression (5.64) does *not* contain any non–connected processes, as a consequence of energy and order additivity of $\hat{\mathcal{Z}}$. It follows directly, that *if* $\hat{\mathcal{Z}}^{1/2}$ obeyed these rules of additivity, the effective Hamiltonian (Eq. 5.63) would also be local.

Now it is very easy to see, that $\hat{\mathcal{Z}}^{1/2}$ indeed obeys additivity. It is sufficient to notice, that the preservation of order additivity through fusions requires that all (positive) integer powers of $\hat{\mathcal{Z}}$ also obey additivity. On the other side, fusions also preserve non–additivity, which is simply the fact that (positive) integer powers of non–additive expansions are also not additive, a fact that can also be seen easily. This however implies, that $\hat{\mathcal{Z}}^{1/2}$ must be additive, such as $\hat{\mathcal{Z}}$, obtained through the fusion $\frac{1}{2}\left\{\hat{\mathcal{Z}}^{-1/2}, \hat{\mathcal{Z}}^{-1/2}\right\}$.

Therefore, it is indeed sufficient to prove the locality for expression (5.64), which allows us to recycle notations used earlier. All arguments will carry over to the effective Hamiltonian (Eq. 5.63) as well. The proof will be split into two parts. Firstly, we will study the coefficients c_g of non–connected processes in $\hat{\mathcal{Z}}^{-1} = \hat{1} - \hat{\mathcal{Y}}$, given the weights d_g at which they arise in $\hat{\mathcal{Z}} = \hat{1} + \hat{\mathcal{X}}$. In other words, we will derive the amplitudes of disconnected processes in the inverse of $\hat{\mathcal{Z}}$. The latter is related to $\hat{\mathcal{Z}}$ by (cf. Eq. 5.42)

$$\hat{\mathcal{X}} - \hat{\mathcal{Y}} = \frac{1}{2}\left\{\hat{\mathcal{X}}, \hat{\mathcal{Y}}\right\}. \tag{5.65}$$

Secondly, we will show that the overall weights of non–connected diagrams in (5.64) vanish. In the same spirit as above we rewrite expression (5.64) as

$$\partial_\mu \hat{\mathcal{X}} - \frac{1}{2}\left\{\partial_\mu \hat{\mathcal{X}}, \hat{\mathcal{Y}}\right\} \tag{5.66}$$

and show, that the latter does not contain any non–connected process. Notice, that both parts of the proof are simply a matter of combinatorics and can be seen in analogy to each other.

Proof (part I)

Introducing some short hand coefficients d_g and c_g in (5.59), we can express $\hat{\mathcal{X}}$, $\partial_\mu \hat{\mathcal{X}}$ and $\hat{\mathcal{Y}}$ as

$$\hat{\mathcal{X}} = \sum_g d_g \hat{\omega}_g, \tag{5.67}$$

$$\partial_\mu \hat{\mathcal{X}} = \sum_g h_g d_g \hat{\omega}_g, \tag{5.68}$$

$$\hat{\mathcal{Y}} = \sum_g c_g \hat{\omega}_g. \tag{5.69}$$

This can be inserted into (5.65), which is nothing but asking that $\hat{\mathcal{Z}}^{-1}$ be the inverse of $\hat{\mathcal{Z}}$. We obtain,

$$\hat{\mathcal{X}} - \hat{\mathcal{Y}} = \sum_g (d_g - c_g)\hat{\omega}_g, \tag{5.70}$$

$$\frac{1}{2}\left\{\hat{\mathcal{X}}, \hat{\mathcal{Y}}\right\} = \sum_{g,g'} d_g c_{g'} \frac{1}{2}\left\{\hat{\omega}_g, \hat{\omega}_{g'}\right\}, \tag{5.71}$$

where the fusion of $\hat{\omega}_g$ and $\hat{\omega}_{g'}$ may yield a sum of processes $\hat{\omega}_k$. Note, that in principle the two fusing diagrams may be the same, resulting in a combinatorial fusion factor due to indistinguishable diagrams (compare 5.24 with 5.29). We shall here assume, that all diagrams are different, which yields a factor of one in front of every fused diagram. In order to build $\hat{\omega}_k$, we may then take $\hat{\omega}_g$ from $\hat{\mathcal{X}}$ or from $\hat{\mathcal{Y}}$, and therefore have two possibilities. If $\hat{\omega}_g$ and $\hat{\omega}_{g'}$ happen to be identical, then we will accidentally double count them, producing the right combinatorial factor.

Equating the last two equations, we find

$$d_k - c_k = \sum_g c_g d_{\bar{g}}, \tag{5.72}$$

where $\hat{\omega}_{\bar{g}}$ denotes the complementary diagram to $\hat{\omega}_g$, in order to form $\hat{\omega}_k$. The last sum therefore simply considers all ways to fuse two diagrams to $\hat{\omega}_k$. For connected processes $\hat{\omega}_k$ there is no way of formation at lowest order, and we obtain $c_k = d_k$. Considering a disconnected diagram $\hat{\omega}_{12}$ consisting of two connected pieces $\hat{\omega}_1 = \hat{\omega}_{\bar{2}}$ and $\hat{\omega}_2 = \hat{\omega}_{\bar{1}}$, there are two ways of formation. We can take $\hat{\omega}_1$ from $\hat{\mathcal{X}}$ and its complement $\hat{\omega}_{\bar{1}}$ from $\hat{\mathcal{Y}}$ and the other way round. Thus Eq. (5.72) becomes

$$\begin{aligned} d_{12} - c_{12} &= c_1 d_2 + c_2 d_1 && (5.73)\\ &= 2 d_1 d_2 && (5.74)\\ &= 2 d_{12}. && (5.75) \end{aligned}$$

Here, we used the fact $\hat{\omega}_1$ and $\hat{\omega}_2$ are connected processes, and order additivity requires $d_{12} = d_1 d_2$, hence $c_{12} = -d_{12}$. In general, order and energy additivity can be expressed as

$$d_{12\cdots n} = d_1 d_2 \cdots d_n, \tag{5.76}$$

and we guess the general relation between c_k and d_k to be of the form

$$c_{12\cdots n} = (-1)^{n+1} d_{12\cdots n}, \tag{5.77}$$

which is the relation we were looking for in this section. It can be proved by mathematical induction. To prepare this it is helpful to write down partitions G_n for different n. The fact that connected diagrams cannot be obtained by fusions at lowest order shall be translated into $G_1 = \emptyset$. The diagram $\hat{\omega}_{12}$ consists of $\hat{\omega}_1$ and $\hat{\omega}_2$, which shall be expressed as $G_2 = \{1, 2\}$. For $n = 3$, we can for example split the disconnected diagram $\hat{\omega}_{123}$, into the two pieces $\hat{\omega}_{12}$ and its compliment $\hat{\omega}_3$.

The partitions up to $n = 4$ read

$$\begin{aligned} G_1 &= \emptyset && (5.78)\\ G_2 &= \{1, 2\} && (5.79)\\ G_3 &= \{1, 2, 3, 12, 13, 23\} && (5.80)\\ G_4 &= \{1, 2, 3, 4, 12, 13, 14, 23, 24, 34, 234, 134, 124, 123\} && (5.81) \end{aligned}$$

and we have $g, \bar{g} \in G_n$ for a given n. Notice, that for $n = 2$ we immediately recover equation (5.73).

We now suppose, that equation (5.77) may hold up to some $n-1$. By inserting this relation into Eq. (5.72), we show that it also holds for n and thus for any value. We furthermore have to use order additivity (Eq. 5.76), hence

$$d_{12\cdots n} - c_{12\cdots n} = \sum_{g\in G_n} c_g d_{\bar{g}} \tag{5.82}$$

$$= \sum_{k=1}^{n-1} \binom{n}{k} (-1)^{k+1} d_{12\cdots n} \tag{5.83}$$

$$= d_{12\cdots n}\Bigg((-1)^n + 1 - \underbrace{\sum_{k=0}^{n} \binom{n}{k} (-1)^k}_{=0}\Bigg). \tag{5.84}$$

Therefore, we obtain the desired result,

$$c_{12\cdots n} = \begin{cases} -d_{12\cdots n} & n \text{ even} \\ d_{12\cdots n} & n \text{ odd} \end{cases}, \tag{5.85}$$

which is equivalent to equation (5.77).

Proof (part II)

Now we can do the same kind of manipulation for expression (5.66), proving the cancelation of non–connected terms. In analogy to the case before, we obtain

$$\partial_\mu \hat{\mathcal{X}} = \sum_g h_g d_g \hat{\omega}_g, \tag{5.86}$$

$$\frac{1}{2}\left\{\partial_\mu \hat{\mathcal{X}}, \hat{\mathcal{Y}}\right\} = \sum_{g,g'} h_g d_g c_{g'} \frac{1}{2}\left\{\hat{\omega}_g, \hat{\omega}_{g'}\right\}, \tag{5.87}$$

which, with the same reasoning as in (5.72), yields the weight

$$w_k = d_k h_k - \sum_g c_g d_{\bar{g}} h_{\bar{g}} \tag{5.88}$$

for the diagram $\hat{\omega}_k$. Here again, we will first consider connected diagrams, which cannot be split into any connected pieces. Therefore, the sum over the empty set G_1 is zero and we obtain $w_k = d_k h_k$. Similarly, we can consider the disconnected process $\hat{\omega}_{12}$ and we find

$$w_{12} = d_{12}h_{12} - c_1 d_2 h_2 - c_2 d_1 h_1 \tag{5.89}$$

$$= d_{12}h_{12} - d_{12}(h_1 + h_2). \tag{5.90}$$

Here, we have used $c_k = d_k$ for connected processes and order and energy additivity (Eq. 5.76). Energy additivity actually also requires $h_1 + h_2 = h_{12}$, hence we obtain $w_{12} = 0$. Therefore, the non–connected process $\hat{\omega}_{12}$ is not contained in expression (5.66), whereas the connected process $\hat{\omega}_1$ does contribute.

Using the additivity of energies for general n, which can be quantified as $h_{12\cdots n} = h_1 + h_2 + \cdots + h_n$, we obtain

$$w_{12\cdots n} = d_{12\cdots n} h_{12\cdots n} - \sum_{g \in G_n} c_g d_{\bar{g}} h_{\bar{g}} \tag{5.91}$$

$$= d_{12\cdots n} h_{12\cdots n} - \sum_{k=1}^{n-1} \frac{n-k}{n} \binom{n}{n-k} (-1)^{k+1} d_{12\cdots n} h_{12\cdots n} \tag{5.92}$$

$$= d_{12\cdots n} h_{12\cdots n} \Bigg(\underbrace{\sum_{k=0}^{n-1} \binom{n-1}{k} (-1)^k}_{=0} \Bigg). \tag{5.93}$$

Here, the factor $\frac{n-k}{n}\binom{n}{n-k}$ counts precisely the number of ways to obtain the energy $h_{12\cdots n}$ when fusing diagrams at constant k. As a result, we obtain $w_{12\cdots n} = 0$ for $n \geq 2$, proving that disconnected diagrams cannot appear in expression (5.66). Actually, we have only proved this for disconnected diagrams in the overlap expansion of $\hat{\mathcal{X}}$ and $\partial_\mu \hat{\mathcal{X}}$. We still have to consider disconnected processes in $\hat{\mathcal{Y}}$, which could in principle appear in (5.66). However, we may rewrite Eq. (5.66) as

$$\partial_\mu \hat{\mathcal{Y}} + \frac{1}{2} \left\{ \hat{\mathcal{X}}, \partial_\mu \hat{\mathcal{Y}} \right\} \tag{5.94}$$

and observe that the present proof can be imitated, showing the absence of disconnected processes appearing in the overlap expansion of $\hat{\mathcal{Y}}$ and $\partial_\mu \hat{\mathcal{Y}}$. Finally, there are no other disconnected processes, than those in $\hat{\mathcal{X}}$ and $\hat{\mathcal{Y}}$, and hence expression (5.64) and $\hat{\mathcal{H}}_{\text{eff}}$ must be local, containing only connected diagrams.

5.2. Partial Conclusion

In summary, we have generalized the overlap expansion scheme, invented by Rokhsar and Kivelson [6], permitting the consideration of processes of arbitrary range. A key ingredient was the establishment of a formal diagrammatic language and fusion rules, as well as the development as series in powers of the parameter α with a suitable exponent. This allows for a derivation of weights not only for original plaquette flips (kinetic process) and counting terms for flippable plaquettes (potential process), but also for assisted flips and other exotic processes.

A very important result is the absence of disconnected terms in the overlap expansion for the effective Hamiltonian, although these naturally appear in the overlap matrix $\hat{\mathcal{O}}$. This means, that the expansion scheme keeps the Heisenberg Hamiltonian local and is thus well–behaved in some sense. Furthermore, we developed a numerical way to obtain the weight of any process to arbitrary precision (see section 5.1.4). This can even be refined for the class of elementary diagrams, for which analytical expressions could be derived. These precisely correspond to the processes usually considered in pure Rokhsar–Kivelson models.

The whole derivation scheme makes a connection between models with Heisenberg interaction and quantum dimer models, which is performed in two steps. Firstly, the Hamiltonian is projected into the space spanned by nearest neighbor valence bond (NNVB) states, resulting in a generalized eigenvalue problem due to the non–orthogonality of VB states. Secondly, the problem is transformed into an orthogonal eigenvalue problem by means of a similarity transformation and the consideration of the dual NNVB basis. This second step is performed diagrammatically in form of an overlap expansion. Finally, we end up with generalized quantum dimer models, which approximate the NNVB–projected Heisenberg Hamiltonian.

Notice, that the projection relies on the linear independence of NNVB states. In principle, one could project into a larger basis, taking for example into account second nearest neighbor valence bond states. An obstacle of such an approach is however, that the linear independence may not be guaranteed anymore, rendering the expansion scheme impossible. This would probably be witnessed by a very bad convergence behavior with important contributions even from very long loops.

6. Application to the Kagomé and Honeycomb Antiferromagnet

Having presented how to derive generalized quantum dimer models (GQDM) from Heisenberg spin models in the previous chapter, we will now apply this approach to specific problems. Historically, GQDM have first been derived and tested for the J_1–J_2–J_3 Heisenberg model on the square lattice. By that time the approximation scheme was only understood to very low orders, i.e. one could not yet calculate the exact weight of any process [137]. Later, the scheme was applied to the kagomé antiferromagnet [18], and the possibility to obtain the analytical (accumulated) weight of elementary processes was recognized [15]. However, non–elementary processes could still only be treated up to *relatively* low order α^{14}, i.e. a summation scheme was not known for such diagrams by that time.

When the method was applied to the J_1–J_2–J_3 Heisenberg model on the honeycomb lattice, one was already able to obtain the amplitude of any process exactly at a numerical level, with negligible computational cost. This allowed for thoroughly comparing the convergence of GQDM when refining the model and with respect to the NNVB approach [19]. Indeed, at the moment one is able to imitate the nearest neighbor valence bond physics to very high precision, by calculating the numerical exact amplitude of any targeted diagram. The fact that such an agreement is possible already at relatively low truncation orders demonstrates the fast convergence to the conceptual NNVB limit.

Applying these techniques to bi–dimensional frustrated Heisenberg antiferromagnets (2D HAF) has different reasons. Firstly, 2D HAF are believed to give rise to rather exotic phases, such as valence bond crystals [139], or spin liquids [20, 21, 140]. However, especially spin liquids seem to remain very exotic for a pure Heisenberg model. Whereas they could be ruled out for the triangular lattice [36], their existence is still debated in the case of the kagomé lattice [141]. Secondly, solving the frustrated Heisenberg model is particularly difficult, as not only analytical (e.g. perturbative) methods are conceptually challenging, but also large scale numerical (i.e. QMC) techniques are basically unaccessible. On the other side, exact diagonalizations are not able to give a complete picture due to only small accessible cluster sizes [142, 143, 41].

The situation for quantum dimer models is very different. Here, it is possible to construct simple models obeying a spin liquid phase [7, 8], but also valence bond crystals are very common [144, 9]. Indeed, QDM seem to be particularly well suited and simple systems to form these exotic phases. Furthermore, the smaller Hilbert space allows for simulating larger clusters, enabling a more reliable finite size scaling analysis. Therefore, it seems to be more than natural to establish a connection between 2D HAF and QDM through our generalized quantum dimer models approach.

6.1. Heisenberg Antiferromagnet on the Kagomé Lattice

The kagomé spin 1/2 antiferromagnet has very exotic properties, such as an exponential number of singlet states below the first triplet excitation [142, 143], reminiscent of the classical finite ground state entropy [145]. Furthermore, dimer–dimer correlations have found to be short ranged [146], pointing in favor to a spin liquid. However, the exact diagonalization spectra remain difficult to interpret for small samples [142, 143].

On the other side, different valence bond crystals have been proposed by singlet subspace effective Hamiltonians [147, 148, 149] or a large–N approach [16], enriching the amount of possible scenarios. One of them has recently gained more evidence through series expansion techniques [150, 17]. Despite this, the situation is still very puzzling and it has therefore been proposed, that the kagomé antiferromagnet may be close to a spin liquid phase [151].

The interest in the kagomé antiferromagnet was reinforced after the discovery of *herbertsmithite* [152], one of the few compounds with the kagomé structure, where spins 1/2 are interacting anti–ferromagnetically. In such materials the absence of magnetic order can be measured down to very low temperatures [153], reviving the spin liquid scenario. It should however be noticed, that in this compound not only isotropic Heisenberg interactions, but also non–isotropic Dzyaloshinksii–Moriya interactions are believed to be of importance [154].

6.1.1. Quantum Dimer Model

The reduction of the kagomé antiferromagnet to the nearest neighbor valence bond space seems to be justified by short range dimer–dimer correlations [146] and has turned out to be fruitful in the past [44]. However, the generalized eigenvalue problem is still a non–trivial one, suggesting a mapping onto an effective ordinary eigenvalue problem. This has already been carried out in previous works [138], but was only done to lowest order.

Therefore, we suggest to perform a similar approach within our GQDM formalism, presented in chapter (5). According to this, we first have to expand the overlap matrix $\hat{\mathcal{O}}$ and the Hamiltonian $\hat{\mathcal{H}}$, the details of which can be found in appendix (A). Considering only processes with one hexagon and setting $\alpha = i/\sqrt{2}$ (fermionic convention, see section 2.3.5), we obtain the effective Hamiltonian

$$\frac{\hat{\mathcal{H}}_{\text{eff}}}{J} = -\frac{4}{5}$$ $$+\frac{1}{5}$$ $$+\frac{16}{63}\Big($$ 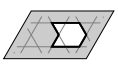 $$+\frac{2}{63}\Big($$ 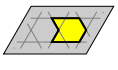 $$-\frac{16}{255}\Big($$ 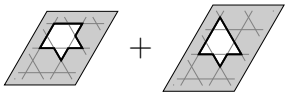 $$+\frac{1}{255}\Big($$ 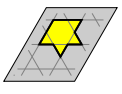 $$+0\Big($$ 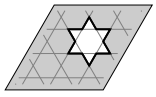 $$. \tag{6.1}$$

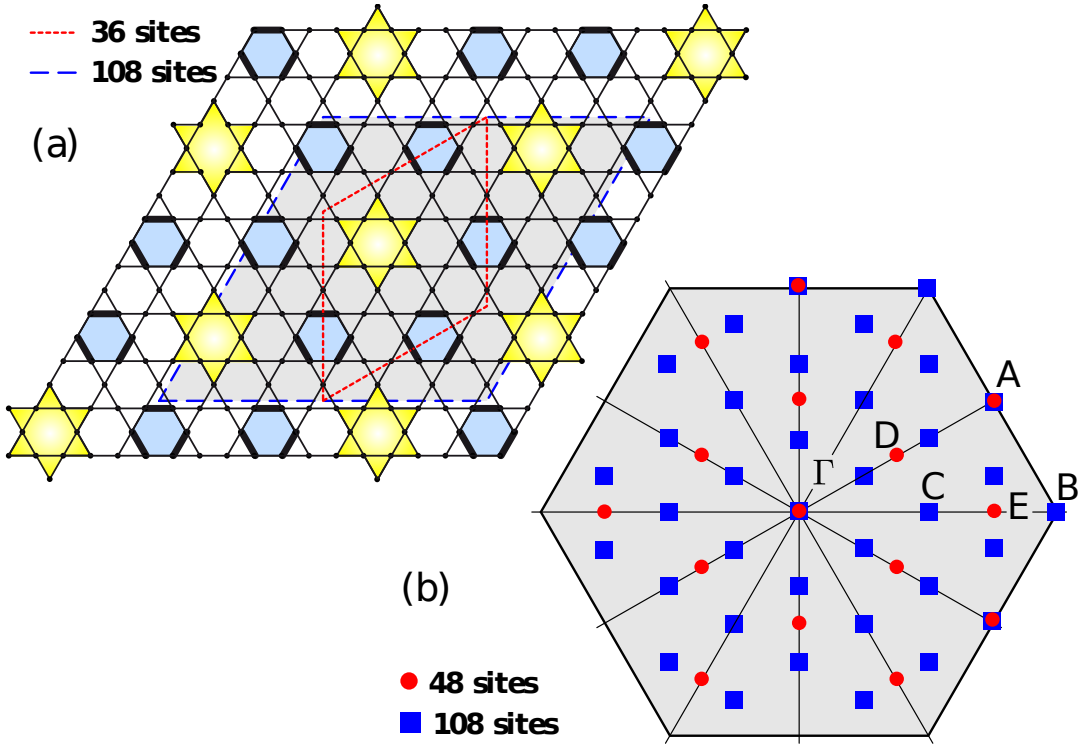

Fig. 6.1.: (a) Illustration of a VBC [16, 149, 17] with a 36–site unit cell (red frame), fitting three times into a 108–site cluster (blue frame). This valence bond crystal consists of a honeycomb lattice of perfect hexagons (blue), enclosing pinwheels (yellow). (b) Brillouin zone of the kagomé lattice with the different allowed momenta on a 48–site (108–site) cluster, represented in red (blue), respectively. The figure was taken from [18].

These are precisely the elementary processes on the kagomé lattice, for which the exact amplitude is accessible, and which arise at lowest order in the expansion scheme. Indeed, there are terms containing two hexagons, which are of order α^{10}, as shown in appendix (A). These are not considered here for numerical reasons.

First of all we notice, that this Hamiltonian is quite close to the one studied in Ref. [138]. Especially, the amplitudes for the kinetic processes are almost the same, with the difference coming basically from the summation in the present scheme. However, in [138] there were no potential terms in the Hamiltonian, leading to a subtle gap in the energy spectrum (see Fig. 3 in [138]), but absent in the Heisenberg model [142, 143]. Interestingly, this gap has a magnitude of about $36 \times 0.0055J \approx J/5$, which is precisely the amplitude of the potential process of lowest order in our Hamiltonian (6.1). This is consistent with the observation that the gap separates eigenstates with about two flippable hexagons from states with only one flippable hexagon in average (see Fig. 4 in [138]). Hence, one might expect the gap to be closed with our Hamiltonian and therefore producing a low–energy spectrum potentially closer to the one of the Heisenberg model.

Secondly, the amplitude of the kinetic and potential pinwheel process is exactly zero at all orders. This is only the case for pure nearest neighbor interactions and would

not be true anymore when for example including a second nearest neighbor interaction in our model. The numerical simulations of (6.1) actually reveal a degeneracy in the ground state, which can be lifted by introducing some finite amplitude J_{12} for the kinetic pinwheel process [18].

The simulation of the effective Hamiltonian (Eq. 6.1) is a rather challenging task, if one wants to reach sufficiently large cluster sizes. In order to perform Lanczos ED, a full consideration of the space group is required. In case of the kagomé lattice, this breaks down into the translational invariance of the lattice on a torus and the point group C_{6v}. Furthermore, for quantum dimer models one also encounters different topological sectors (TS), by considering the boundaries at which the plane lattice is glued to form a torus. Indeed, one can define a reference state $|\varphi_0\rangle$ and apply the Hamiltonian on it. Repeatedly doing this will form a family of states, which belong all to the same topological sector. However, there are states that cannot be connected to $|\varphi_0\rangle$ by a simple application of the Hamiltonian. These states belong to another topological sector and there are no local dimer flips that connect configurations between different such sectors. Two states of distinct topological sectors form an overlap graph that contains loops winding around the boundary of the torus. For the kagomé lattice, four topological sectors are observed [8], depending on the parity of boundary crossing loops with respect to the two possible boundaries, that can be defined on the torus.

The effective model (6.1) was studied by D. Poilblanc [18] for clusters that have all the relevant space group symmetries, i.e. samples with $N = 3n^2$ or $N = 9n^2$. A singlet ground state can only be obtained for an even number of sites, hence possible values for the cluster sizes are among $\{12, 36, 48, 108, 144\}$. The biggest of these samples cannot currently be simulated, whereas the others are numerically accessible. The two smallest samples can be simulated with Lanczos ED in the $\hat{S}^z$ basis [142], thus we concentrate on the $N = 48$ and $N = 108$ clusters and try to find evidence for the different proposed scenarios in literature, summarized in Tab. (6.1).

VBC	Γ	A	B	C	D	E
$3 \times 2 \times 2$ [147]	$(+,+,\pm)$	$(\times,+,\pm)$				
$3 \times 2\sqrt{3} \times 2\sqrt{3}$ [16, 149, 17]	$(+,+,\pm)$	$(\times,+,\pm)$	$(+,\times,\pm)$	$(\times,\times,\pm)$		
$3 \times 4 \times 4$ [148]	$(+,+,\pm)$	$(\times,+,\pm)$			$(\times,\times,\pm)$	$(\times,\times,\pm)$
$\mathbb{Z}_2$ dimer liquid [8]	$(+,+,+)$					

Tab. 6.1.: Quantum numbers of the different candidate VBC states and the $\mathbb{Z}_2$ dimer liquid, as presented in [18, 38]. The momenta are illustrated in Fig. (6.1) and are consistent with [38]. The point group symmetry is denoted as (R_3, R_2, σ), where $R_3 = +$ denotes the invariance under a rotation of $2\pi/3$ around the center of a hexagon and $R_2 = \pm$ denotes a phase factor of ± 1 under a rotation of π. $\sigma = +$ ($\sigma = -$) corresponds to an even (odd) state, which acquires a phase factor of $+1$ (-1) under reflexion about the momentum direction. $\times$ denotes that any quantum number is consistent with the considered state. Note, that the dimer liquid state is degenerate with states form other topological sectors. The table is taken from [18].

In this table we find different valence bond crystals, which were proposed as ground states for the Heisenberg model on the kagomé lattice. Furthermore, a $\mathbb{Z}_2$ dimer liquid is listed, which is the exact ground state for the following exactly solvable quantum dimer model [8],

$$\frac{\hat{\mathcal{H}}_{RK}}{\Gamma} = -$$

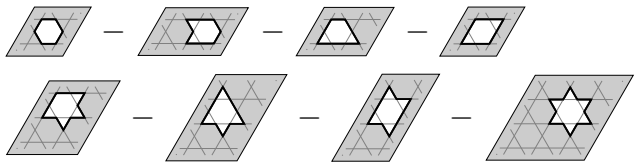

$$. \qquad (6.2)$$

Notice, that the overall sign of this Hamiltonian does not matter. The lowest excitations (called visons) are non–local with a gap $\Delta = 4\Gamma$ above the ground state, as shown in [8].

The actual effective Hamiltonian (6.1) to implement has no parameter, making it tempting to introduce an artificial one. As mentioned before, one can study the influence of a finite pinwheel amplitude J_{12}. On the other side, the availability of an exactly solvable quantum dimer model suggests to study the following interpolated Hamiltonian

$$\hat{\mathcal{H}}_{\text{interp.}}(\gamma, J_{12}) = \gamma\hat{\mathcal{H}}_{\text{eff}} + (1-\gamma)\hat{\mathcal{H}}_{\text{RK}} + \left(J_{12} + \frac{1}{4}(\gamma - 1)\right)$$

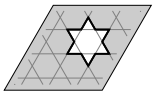

$$, \qquad (6.3)$$

where $J = 1$ is chosen in (6.1) and for $\hat{\mathcal{H}}_{\text{RK}}$ in 6.2 one takes $\Gamma = -1/4$.

Results and Discussion

Firstly, we present the results of the interpolation $\hat{\mathcal{H}}_{\text{interp.}}(\gamma = \lambda, J_{12} = (1-\lambda)/4)$ between $\hat{\mathcal{H}}_{\text{eff}}$ and $\hat{\mathcal{H}}_{\text{RK}}$, as obtained in [18]. The low–energy spectrum of this Hamiltonian is illustrated in Fig. (6.2).

Inspecting this spectrum, a quantum critical point near the Heisenberg point is observed, manifested through two different features. Firstly, the excited states of the solvable $\hat{\mathcal{H}}_{\text{RK}}$ collapse to the absolute ground state. Secondly, the energy susceptibility $\chi_E = -\partial^2 E/(N\partial\lambda^2)$, mentioned in section (4.1), shows a sharp peak similarly to the behavior expected for the fidelity susceptibility χ_F [110]. This allows for locating the quantum critical point at $\lambda_c \sim 0.9357$ [18], and is another example for the power of the fidelity approach. Indeed, the signal of χ_F is expected to be even sharper than the one of χ_E [110].

However, the symmetry sectors with even and odd parity σ are merged in the spectrum, a feature that will be resolved by considering a finite pinwheel amplitude. Therefore, we consider the Hamiltonian $\hat{\mathcal{H}}_{\text{interp.}}(0, J_{12})$, which artificially adds an amplitude to the kinetic pinwheel process. The spectrum of this Hamiltonian is illustrated in Fig. (6.3) for the $N = 48$ cluster. We observe a level crossing between different eigenstates characteristic for a valence bond crystal with a 48–site supercell [148] and odd parity ($J_{12} < 0$) and another VBC with a 12–site cell [147] and even parity ($J_{12} > 0$). Interestingly, both VBC seem to be degenerate almost exactly for the effective QDM ($J_{12} = 0$).

It should however be noted, that among the three different candidates for a VBC (Tab. 6.1), the $\mathcal{N} = 36$ site supercell crystal does not fit on the 48–site cluster, but on

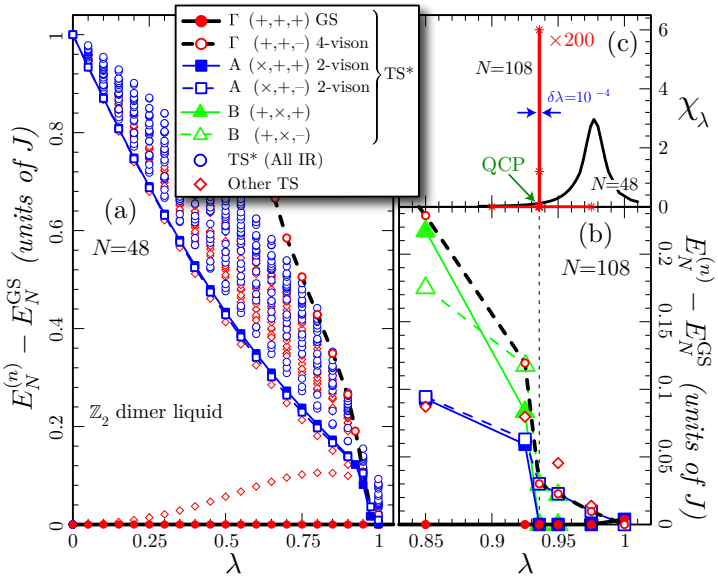

Fig. 6.2.: (a) Low–energy spectrum of the interpolated Hamiltonian on the 48–site cluster. The excited states of $\hat{\mathcal{H}}_{\mathrm{RK}}$ (visons [8]) at $\lambda = 0$ collapse when approaching the Heisenberg point ($\lambda = 1$). (b–c) Interestingly, when inspecting the spectrum of the 108–site cluster, this collapse coincides with a sharp peak in χ_E (here denoted as χ_λ). The data were produced by D. Poilblanc and the figure is taken from [18].

the larger 108–site sample. The spectrum on this cluster is illustrated in Fig. (6.4), and underlines the degeneracy between even and odd parity crystals for the effective model. Nevertheless, the favored ground state levels are here rather consistent with the $\mathcal{N} = 36$ site VBC, in agreement with [150, 17].

In summary, we propose the following picture. Apparently, our effective Hamiltonian describes a valence bond crystal phase with a hidden degeneracy between ground states of even and odd parity, as found for both studied clusters (Figs. 6.3 and 6.4). Furthermore, a $\mathbb{Z}_2$ dimer liquid [8] seems to be nearby the model, therefore suggesting a multi critical point in the vicinity. A schematic phase diagram of this picture can be found in Fig. (6.5).

The answer to the question of which VBC crystals are separated by the $J_{12} = 0$ line is still a bit less obvious. The main problem are the relatively large unit cells of the candidates, which make it difficult to find a cluster that can accommodate all of them. Indeed, only on the $N = 144$ sample all VBC listed in Tab. (6.1) would fit and thus a definite decision could be made by studying such a sample. This is however still beyond the capacities of present computers. Regarding the ground state energy per site (Fig. 6.4 a), we have however the impression, that the $\mathcal{N} = 36$ site cluster is energetically favored. This seems to be confirmed by the fact, that the $\mathcal{N} = 12$ site VBC, which fits on both clusters, is energetically favored for $J_{12} > 0$ on the $N = 48$ sample, but can be ruled out on the $N = 108$ cluster. Two arguments support this: firstly the appearance of a level with momentum $K = B$ within the quasi degenerate ground state manifold is not consistent with the $\mathcal{N} = 12$ VBC. Secondly, the number of flippable loops on

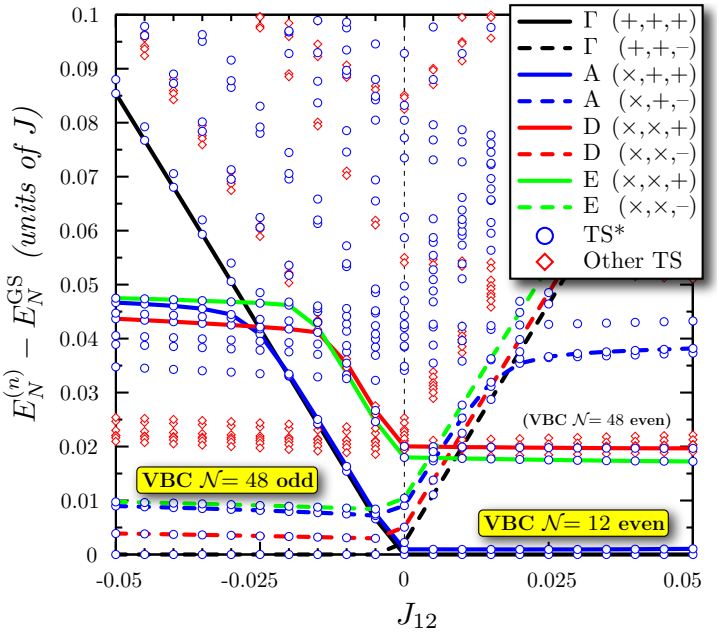

Fig. 6.3.: Low–energy spectrum of the $N = 48$ cluster. The lowest levels for $J_{12} < 0$ correspond to those of the VBC with 48 site supercell and odd parity, whereas for $J_{12} > 0$ we observe the levels of the 12 site VBC with even parity (see Tab. 6.1). The levels of both VBC seem to become degenerate at $J_{12} \approx 0$. The data were produced by D. Poilblanc and the figure is taken from [18].

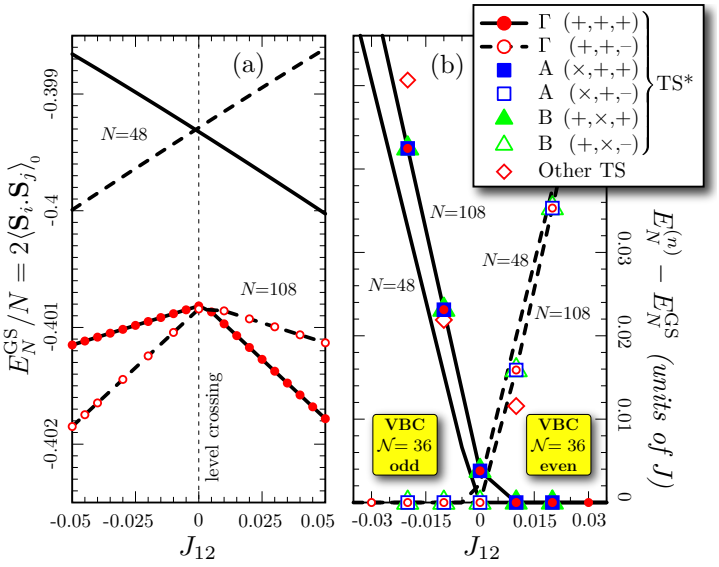

Fig. 6.4.: (a) Ground state energy per site vs. J_{12} for the two studied clusters. In both cases a level crossing indicates a first order phase transition. (b) Low–energy levels vs. J_{12} for both clusters. The levels for the $N = 108$ sample are consistent with the odd (even) 36–site supercell VBC [16, 149, 17] for $J_{12} < 0$ ($J_{12} > 0$). The data were produced by D. Poilblanc and the figure is taken from [18].

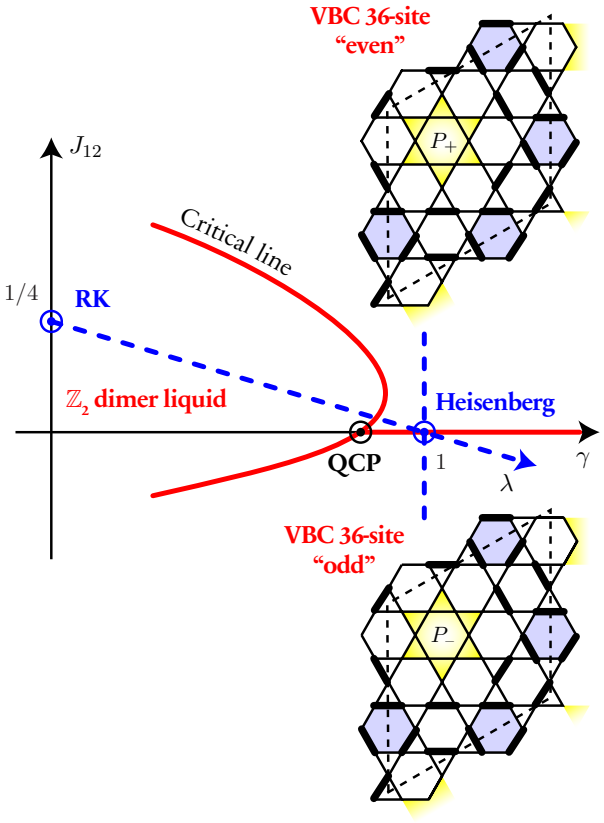

Fig. 6.5.: Sketch of the phase diagram of $\hat{\mathcal{H}}_{\text{interp.}}$, taken from [15]. The dashed blue lines represent the parameter space that was studied within the present approach. Whereas varying λ connects our effective Hamiltonian to the $\mathbb{Z}_2$ dimer liquid [8], with a quantum critical point in the vicinity of our model, the pinwheel amplitude J_{12} separates an even from an odd 36–site VBC. Hence, the effective model seems to be close to a multi critical point.

the $N = 108$ sample, corresponds almost precisely to the one expected for the $\mathcal{N} = 36$ VBC [18].

Regarding the antiferromagnetic Heisenberg model on the kagomé lattice, it is rather intriguing that the effective Hamiltonian is found to be in the close vicinity of a multi–critical point, especially because its derivation is not biased in any sense. The GQDM approach is non–perturbative and does not have any free parameter, hence pointing towards a relevant feature of the original model. Indeed, such a behavior might explain the many different suggested ground states and the difficulty to interpret exact diagonalization spectra. One can also imagine, that refining the effective quantum dimer model may push the ground state away from the valence bond crystal phase into the nearby dimer liquid. This is further stirred up by recent DMRG simulations, which are in favor of a spin liquid phase [155].

6.2. Honeycomb Lattice

The honeycomb structure, met for example in graphene, seems to have very peculiar properties, when studying electrons with charge and spin degrees of freedom. Within the tight binding approximation, which corresponds to a Hubbard model without Coulomb repulsion, a linear energy dispersion is observed [156], interpreted as the emergence of massless Dirac electrons in graphene [157]. This model undergoes a phase transition into a spin liquid phase when increasing the Coulomb repulsion between the electrons [158], before exhibiting an insulating phase upon further increase of the repulsion term. The finding of a spin liquid phase was quite unexpected for a non–frustrated system, as the honeycomb lattice [2].

A very natural question to ask is whether such a behavior could also be observed in a Heisenberg model, emerging from the Hubbard model for large Coulomb repulsion at half filling. We therefore propose to study the J_1–J_2–J_3 Heisenberg model on the honeycomb lattice, where we added the third neighbor interaction for completeness. This model, the lattice of which being depicted in Fig. (6.6), has already been studied earlier within Lanczos ED in the spin basis [41].

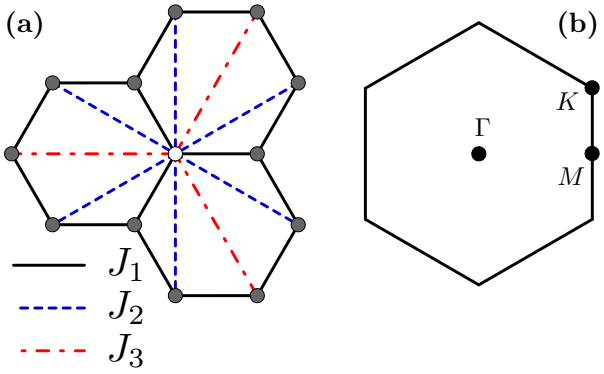

Fig. 6.6.: (a) Illustration of the honeycomb lattice with first (J_1), second (J_2) and third neighbor (J_3) interactions. (b) First Brillouin zone with the different momenta Γ, M and the Dirac point K. The figure is taken from [19].

A first impression about phase boundaries within the domain $J_2, J_3 \in [0, 1]$ for antiferromagnetic nearest neighbor coupling ($J_1 = 1$) can be obtained via the fidelity approach, as described in chapter (4). Basically, one calculates the overlap between ground states of neighboring points in the phase space (Fig. 6.7), which displays minima in J_2 and J_3 direction [19]. These fidelity dips, obtained for rather small clusters though, can be used to roughly localize quantum phase transitions. In order to characterize the different phases and nail down their boundaries, other approaches have however to be used.

The pure Heisenberg model is known to display Néel long range order (LRO), which persists even for slight frustration. In exact diagonalization this is signaled by the typical tower of states (TOS) structure [36], where even spin sectors appear in the A_1 representation with Γ momentum and odd spin sectors belong to B_2 with the same momentum [41, 19]. The corresponding order parameter is the staggered magnetization,

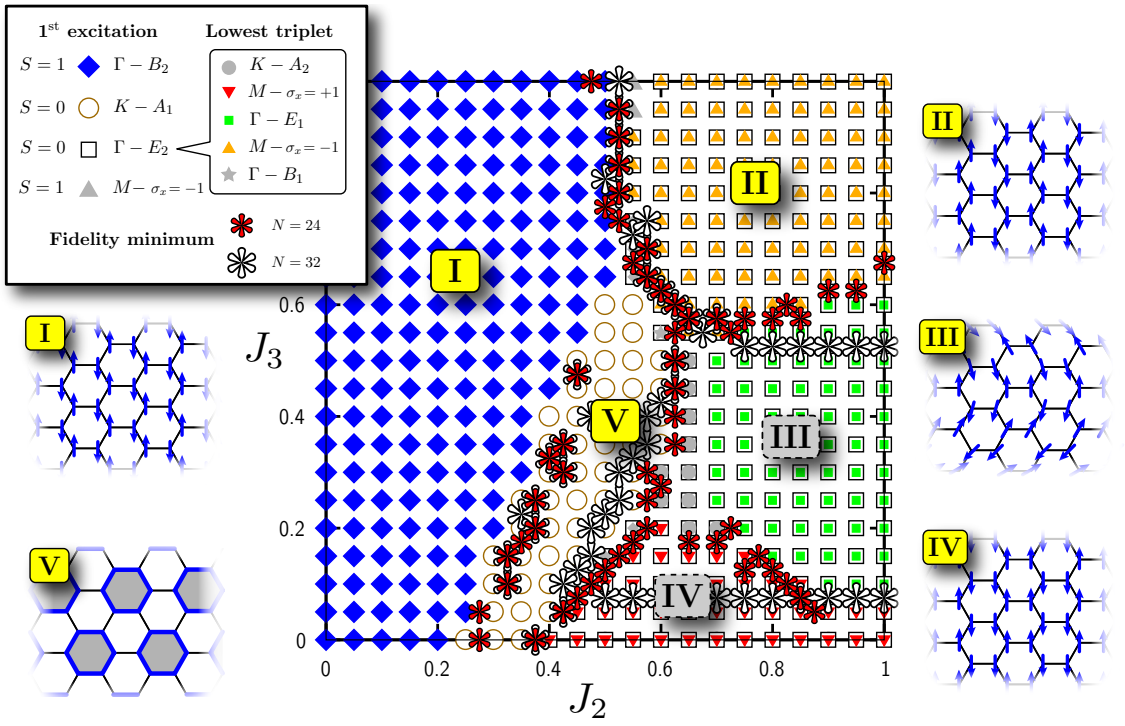

Fig. 6.7.: Illustration of the phase diagram for the Heisenberg model on the honeycomb lattice, obtained with ED by A. Läuchli and S. Capponi [19]. The absolute ground state is always a singlet with momentum Γ, whereas the quantum numbers for the lowest excitations on a cluster with $N = 24$ sites are indicated in the legend. The red (white) boundaries display fidelity minima, obtained with ED on $N = 24$ ($N = 32$) clusters. Region (I) corresponds to a Néel phase with staggered magnetization, whereas phase (II) is a magnetically ordered collinear state. Phases (III) and (IV) cannot be identified unambiguously with exact diagonalization due to strong finite size effects. There is some evidence for region (III) to be in a spiral phase [159], whereas region (IV) represents another collinear magnetically (dis-)ordered phase [19]. Phase (V) is shown to be a plaquette VBC. The figure is taken from [19].

which vanishes at $J_2 = 0.17 \sim 0.22$ for $J_3 = 0$, indicating the disappearance of Néel LRO [19]. In Fig. (6.7) the Néel phase is denoted by phase (I).

Around the point $J_2 = J_3 = 1$ one observes a collinear magnetically ordered phase [19, 160, 159], which is also present in the classical Heisenberg model [41]. This phase can also be characterized by the appearance of specific low–energy levels in finite size diagonalization spectra [19] and is denoted as phase (II) in Fig. (6.7).

Phases (III) and (IV) cannot be determined precisely through exact diagonalization studies due to strong finite size effects. Recently it was however proposed, that region (III) might correspond to a spiral phase [159], whereas phase (IV) might be either staggered (see Fig. 6.8) [19, 159], or a collinear magnetically ordered one [19, 41].

Phase (V) has found to be magnetically disordered, within self–consistent cluster mean field theory [19], exact diagonalization [19, 41], Schwinger–Boson mean field the-

ory [160] and pseudo–fermion functional renormalization group techniques [159]. In order to characterize this phase, dimer–dimer correlations can be calculated within Lanczos ED, giving evidence for columnar or plaquette physics (see Fig. 6.8) [19]. However, neither the correlation patterns, nor the symmetry breaking low–energy levels allow for a discrimination between both candidates. Indeed, both, the columnar and the plaquette VBC require the collapse of three levels with momentum Γ, K and K' respectively, and the A_1 representation for the corresponding point group in each momentum sector [19].

Fortunately, the open gap above the VBC phase suggests to restrict ourselves to the NNVB subspace. Such an approach is expected to describe plaquette physics as well as a columnar phase correctly, as both are also present in a previously studied quantum dimer model [9]. Nevertheless, the ansatz to work within the nearest neighbor valence bond basis has to be validated by comparing the obtained results with unbiased exact diagonalization data. This has been carried out by F. Albuquerque [19] and shall be summarized in section (6.2.1). We will see, that the NNVB approach is indeed justified and one may therefore derive a corresponding effective quantum dimer model, which will be presented in section (6.2.2). A very important step at that stage will be to justify the truncation scheme, that has to be applied to keep the quantum dimer model simple. This has not been studied before and shall here be performed in section (6.2.3), by comparing different GQDM, that have been truncated in a different way. Furthermore, we will compare the most accurate effective Hamiltonian among them with previously obtained NNVB data (section 6.2.4).

After having justified the nearest neighbor valence bond approach and a corresponding effective quantum dimer model, we may finally address the problem to identify phase (V). The two possible candidates, a plaquette VBC and a columnar one, which are consistent with finite size exact diagonalization data [19] are illustrated in Fig. (6.8). We will see in section (6.2.5), that with the effective Hamiltonian one can discriminate between the two possible VBC. This has two major reasons: firstly, one is able to simulate rather large clusters with $N = 126$ sites, compared to $N = 96$ within NNVB and $N = 42$ for exact diagonalization in the spin basis. Furthermore, the effective quantum dimer model shows much less finite size effects, rendering the interpretation of the data much easier. Secondly, it is very simple to define dimer vector histograms, which allow to visualize the difference between a plaquette and a columnar VBC in a more obvious way than this is possible with correlation functions.

6.2.1. Comparison between Exact Diagonalization and the NNVB Approach

In order to justify an effective quantum dimer model, we need to compare it with the original model. Remember that the derivation of a GQDM is done in two steps: firstly, we project the Heisenberg Hamiltonian into the nearest neighbor valence bond basis, which represents a variational ansatz. Secondly, we transform the generalized eigenvalue problem back into an orthogonal one, using a diagrammatic approximation series (see chapter 5).

Certainly, we will miss some information through the different derivation steps. A

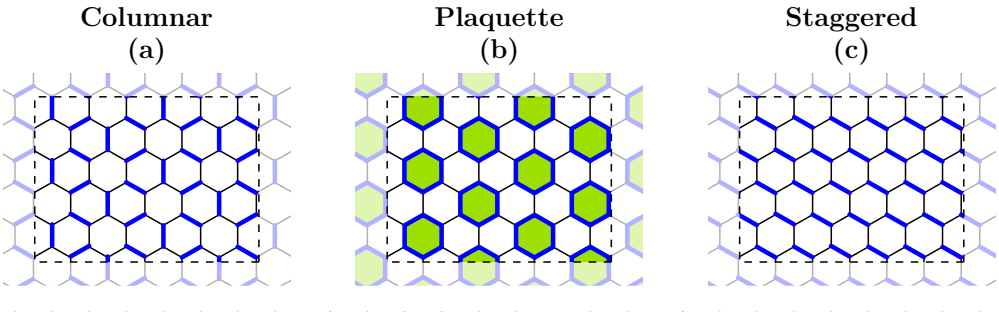

Fig. 6.8.: Illustration of the (a) columnar, (b) plaquette and (c) staggered valence bond crystal on the honeycomb lattice. The figure is taken from [19].

very natural question is at which point the loss occurs and how we can improve on this. The first part of the question will be addressed in the following, by comparing exact diagonalizations of the Heisenberg model with results from the NNVB approach.

For a variational approach, we may first compare the obtained energies, which are illustrated in Fig. (6.9). We plot the relative deviation $(E_0^{\text{NN–VB}} - E_0^{\text{ED}})/E_0^{\text{ED}}$ of the ground state energy within the NNVB approach from the ED energy. Interestingly, this deviation is minimal within a region that roughly corresponds to Phase (V) in Fig. (6.7). Notice, that the data was obtained for a $N = 24$ sites cluster, which is relatively small. Similar results are obtained, when studying a $N = 30$ sample [19]. These clusters allow for a thorough scan within ED in the $\hat{S}^z$ basis, but display rather strong finite size effects. Indeed, first neighbor singlets on a $N = 24$ cluster span already a relatively long distance, compared to the characteristic length of the sample, as loops of length 8 suffice to surround the cluster across its boundaries. Naturally, going beyond NNVB would require involving longer singlets in the variational basis. One therefore somehow expects, that the relative length of the longest considered valence bond may be some kind of measure for the quality of the basis. This basically means, that ground state energies are particularly good for the small $N = 24$ cluster, as can also be seen in Fig. (6.13). However, the principle behavior of a best agreement within phase (V) is also valid on larger clusters.

Another possible comparison can be based on the four–spin correlations, as shown in Fig. (6.10). These correlations have also been obtained for $N = 24$ for the point $(J_2, J_3) = (0.5, 0.3)$ within phase (V) and show a behavior, which is consistent with plaquette and columnar physics. The fact that correlations are relatively close, when comparing the NNVB approach with the results from exact diagonalization represent another validating argument for the projection into the nearest neighbor subspace. However, it should be noticed, that the correlations obtained within NNVB are slightly reduced compared to exact diagonalization. This must be due to the way the NNVB projection is performed, by simply expressing the Hamiltonian in some variational basis and therefore splitting it into four different blocks. The NNVB approach explicitly works in the block representing the nearest neighbor valence bond subspace, neglecting the other three. As we can see in Fig. (6.10), it captures however the physics correctly. This now allows us to describe phase (V) with the GQDM approach.

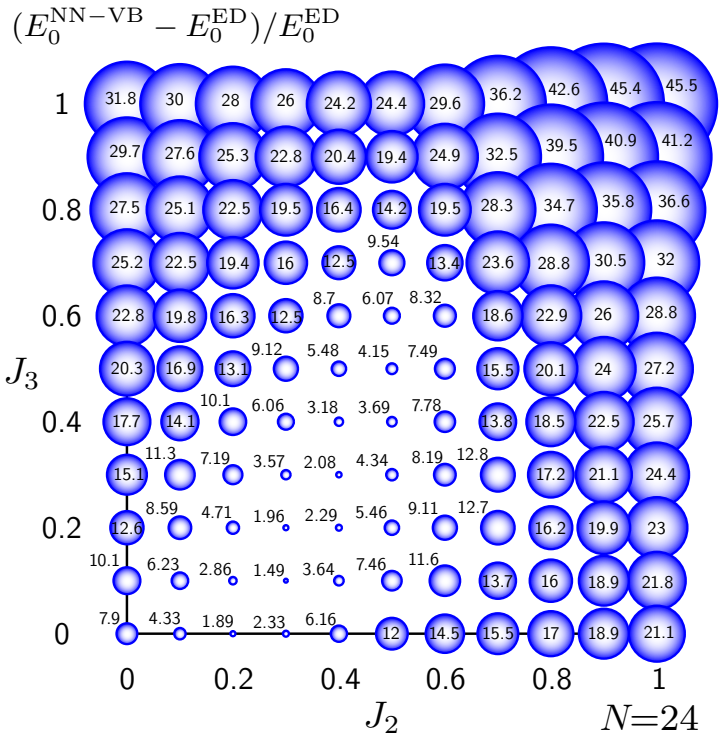

Fig. 6.9.: Relative difference between the ground state energies obtained by the NNVB approach and those obtained in the $\hat{S}^z$ basis. The data were obtained by F. Albuquerque for a $N = 24$ cluster and are indicated in percent. The radius of the circles is proportional to the relative deviation of the NNVB approach. The figure is taken from [19].

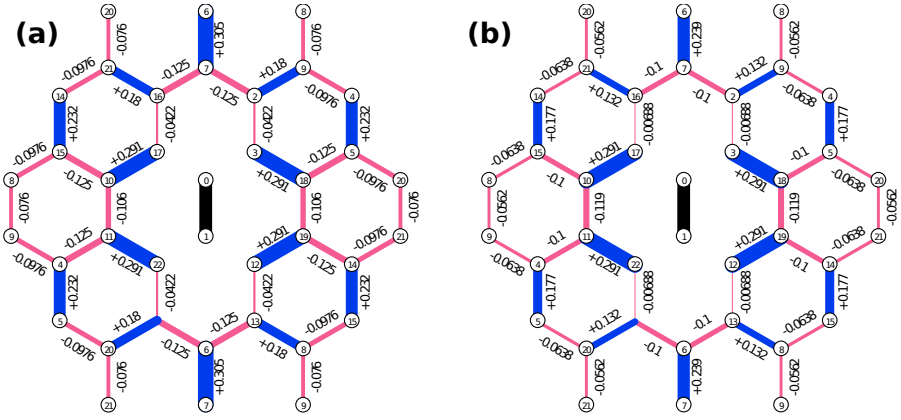

Fig. 6.10.: Four spin correlations $C_{ijkl} \sim \langle(\hat{\boldsymbol{S}}_i \cdot \hat{\boldsymbol{S}}_j)(\hat{\boldsymbol{S}}_k \cdot \hat{\boldsymbol{S}}_l)\rangle - \langle \hat{\boldsymbol{S}}_i \cdot \hat{\boldsymbol{S}}_j\rangle^2$ for a $N = 24$ sample, obtained by (a) exact diagonalization in the $\hat{S}^z$ basis and (b) through the NNVB approach. The width of the bonds is proportional to the correlations, while the color indicates the sign and the reference bond is illustrated in black. The correlations were obtained by F. Albuquerque, S. Capponi and A. Läuchli for $(J_2, J_3) = (0.5, 0.3)$ and have been published in [19].

6.2.2. Effective Quantum Dimer Model

Following the explanations in chapter (5), we derive a quantum dimer model with terms comprising one and two hexagons. The required fusion rules are to be found in appendix (B). As illustrated in Fig. (6.11), there are two different dimer configurations on a single hexagon, which can be connected by two processes. Similarly, on two hexagons we find three dimer configurations being described by four different terms in the GQDM.

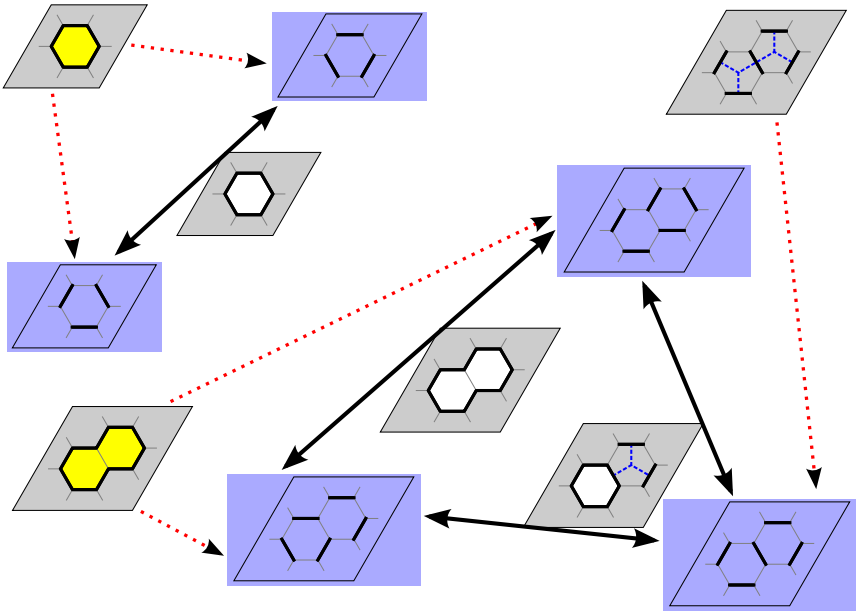

Fig. 6.11.: Illustration of the six possible processes on the honeycomb lattice, containing up to two hexagons. The blue frames show the five different dimer configurations, and black strong arrows indicate possible kinetic processes resonating between them. Potential terms for every configuration are associated through red dotted arrows.

Therefore, we arrive at an effective quantum dimer model, which is given by

$$\mathcal{H}_{\text{eff}} = -t_6 \; - t_{10} \; + \frac{t_{10}}{8} \; + \frac{t_6}{4} \; + v_{10} \; - \frac{v_{10}}{2} \; , \tag{6.4}$$

and choosing the bipartite ($\alpha = 1/\sqrt{2}$) or the fermionic convention ($\alpha = i/\sqrt{2}$), the different amplitudes turn out to be

1 hexagon	2 hexagons	
$t_6 = -\frac{4}{5}\left(2J_2^{\text{eff}} - 1\right)$	$t_{10} = -\frac{4}{3}\tau_{10}\left(8J_2^{\text{eff}} - 3\right)$	$\tau_{10} = 0.049218(5)$
	$v_{10} = \frac{4}{3}\nu_{10}\left(8J_2^{\text{eff}} - 3\right)$	$\nu_{10} = 0.001562(9)$

Notice, that on the honeycomb lattice all diagrams appear at orders which are multiples of α^4, thus rendering the two different conventions equivalent. Note furthermore, that the terms on a single hexagon are precisely the elementary processes on the honeycomb lattice, and are thus known analytically, whereas two–hexagon amplitudes are exact numerical values, as explained in section (5.1.4). It is very interesting to observe, that the whole model depends only on one parameter, $J_2^{\text{eff}} = J_2/(J_1 + J_3)$. Even though this is only true for diagrams containing up to two hexagons, it very nicely matches the form of phase (V) in figure (6.7), when leaving the line $J_3 = 0$ up to intermediate values. Effectively, we will only study the quantum dimer model along $J_3 = 0$ and obtain the rest of the phase diagram through

$$\mathcal{H}_{\text{eff}}(J_1, J_2, J_3) = (J_1 + J_3)\mathcal{H}_{\text{eff}}\left(1, J_2^{\text{eff}} = \frac{J_2}{J_1 + J_3}, 0\right). \tag{6.5}$$

Of course, this already suggests the limitations of the QDM (6.4), which will not expected to be physical beyond a certain value of J_3, where we expect to enter the Néel phase or the collinear magnetically ordered one. It is however a very good sign, that the effective model captures some basic characteristics of phase (V).

Regarding the effective model, we moreover observe, that t_6 changes sign at $J_2^{\text{eff}} = 1/2$, while t_{10} and v_{10} change sign at $J_2^{\text{eff}} = 3/8$. The last value is particularly interesting, as our model reduces to a particular point of a Rokhsar Kivelson (RK) quantum dimer model, which has been studied previously [9]. In the notation of this reference (e.g. Eq. 5.27), the special point corresponds to a value of $V/t = t_6/(4t_6) = 1/4$, where a plaquette phase is reported, a first indication of plaquette behavior for the Heisenberg model on the honeycomb lattice. Indeed, such a connection has already been conjectured, but could not be put on firm grounds [9]. Here we explicitly see, that the point $(J_2, J_3) = (3/8, 0)$, lying in phase (V), is in the plaquette phase. Using the previous argument, this phase should also have some extend on the line $J_2 = 3/8(1 + J_3)$.

The extent of the plaquette phase into other directions is however much less clear, as the influence of two–hexagon processes may be important. This is in particular true for $J_2 = 1/2$, where both terms in t_6 vanish and the model is governed by the two–hexagon diagrams. The leading process among the latter has already been considered in the context of supersolids of hardcore bosons on the triangular lattice [161, 162]. Notice, that the ratio v_{10}/t_{10} does not depend on J_2^{eff}, although we cannot provide its analytical value. Hence, the relative amplitude of all two–hexagon processes is constant, as known to be the case for elementary diagrams [15]. Thus, there is no value of J_2^{eff}, where our model reduces to the one studied in [161, 162].

6.2.3. Effect of Truncation for the GQDM

The effective Hamiltonian (Eq. 6.4) was derived by restricting ourselves to processes containing one or two hexagons. The amplitudes of those terms were calculated exactly and not simply approximated at some low order. The natural question is however, whether this Hamiltonian is sufficient to capture the NNVB physics. In this section we will address this question by considering even more simplified quantum dimer models,

which have been obtained by truncating the GQDM scheme in a different way. Notice, that one may also have considered quantum dimer models with more terms. We will see however in the following, that this is not necessary, justifying the chosen truncation scheme.

Here we will study the following generalized quantum dimer models, obtained by truncating at some lower order,

$$\hat{\mathcal{H}}_{\text{eff}}^{\text{RK}} = -t_6 \quad + \frac{t_6}{4} \quad , \tag{6.6}$$

$$\hat{\mathcal{H}}_{\text{eff}}^{\text{LO}} = -t_6 \quad + \frac{t_6}{4} \quad + \alpha^8(8J_2^{\text{eff}} - 3) \quad , \tag{6.7}$$

where the amplitude t_6 is defined as in Eq. (6.4). Note, that $\hat{\mathcal{H}}_{\text{eff}}^{\text{RK}}$ is simply the effective QDM (6.4) without two–hexagon processes, whereas $\hat{\mathcal{H}}_{\text{eff}}^{\text{LO}}$ includes the most important two–hexagon process at lowest order α^8, but not with its full weight.

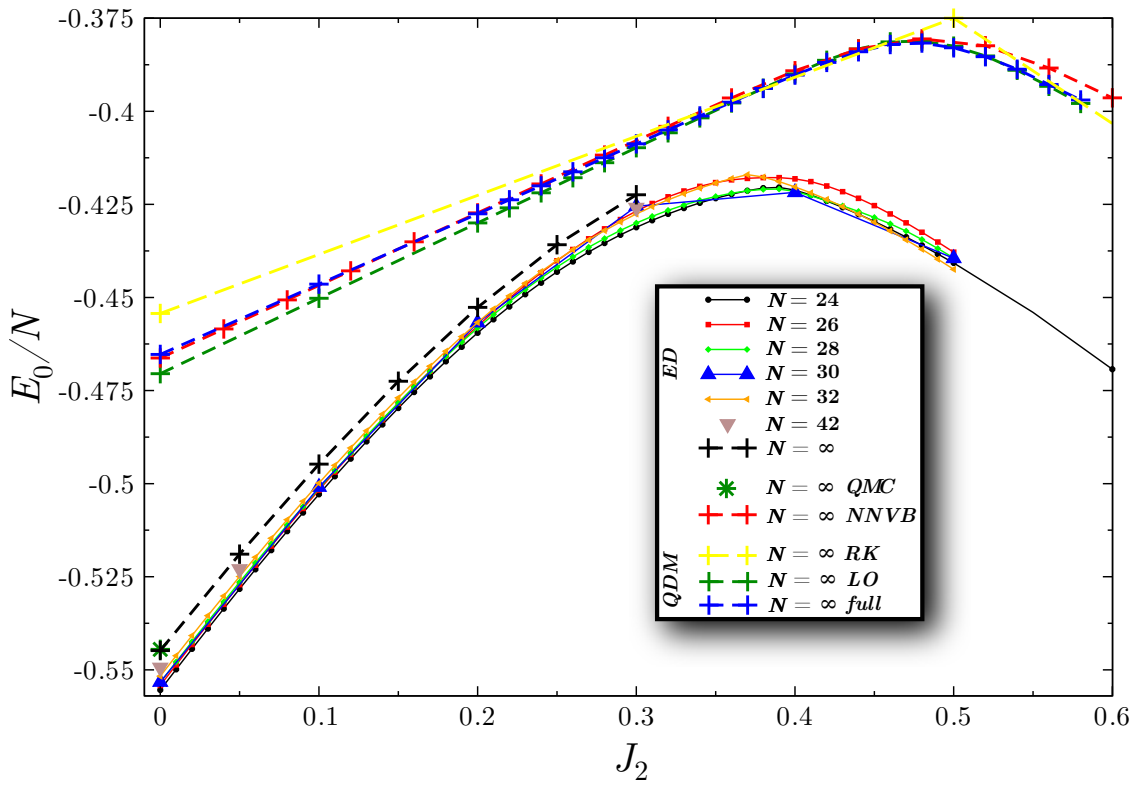

Fig. 6.12.: Ground state energies for different quantum dimer models, compared to exact diagonalization in the spin basis and NNVB data for $J_3 = 0$. "RK QDM" refers to $\hat{\mathcal{H}}_{\text{eff}}^{\text{RK}}$, "LO QDM" refers to $\hat{\mathcal{H}}_{\text{eff}}^{\text{LO}}$ and "full QDM" refers to equation (6.4). Refining the quantum dimer model converges the ground state energy to its conceptual limit, the nearest neighbor valence bond approach. The ED and QMC data were obtained by A. Läuchli [19], while the NNVB data were produced by F. Albuquerque [19].

In figure (6.12) we compare the ground state energies with the previous obtained results for $J_3 = 0$. Notice, that $\hat{\mathcal{H}}_{\text{eff}}^{\text{RK}}$ describes basically a Hamiltonian, which scales with an overall factor t_6. Therefore, the physics of this Hamiltonian depends only on the sign of t_6, which changes at $J_2 = 0.5$, as can be seen in Eq. (6.4). At $J_2 = 0$ the ground state energy is simply $-3/8$, which is basically the shift defined in Eq. (5.5). The ground state energy deviates most from the NNVB approach at small J_2 and around $J_2 \sim 0.5$.

Adding a two–hexagon process ($\hat{\mathcal{H}}_{\text{eff}}^{\text{LO}}$) at lowest order improves on the ground state energy in both major deviation zones. However, at low J_2 one only converges at a satisfactory scale, when the "full" effective quantum dimer model is used (Eq. 6.4). Of course, building a more complicated QDM would further improve on the energy. Notice however, that the finite size scaling within the NNVB approach is not as smooth as for the quantum dimer model, as can be seen in Fig. (6.13). This is true especially for $J_2 \gtrsim 0.5$, where we observe significant deviations for the finite size extrapolated NNVB data (see Fig. 6.12). Therefore a comparison between more accurate QDMs and the NNVB data would not make much sense.

One interesting feature can nevertheless be seen for small J_2. When expressing the Hamiltonian in a basis of diagrams, as described in section (5.1.4), the ground state energy seems to be larger than the one obtained by NNVB. This is the case for $\hat{\mathcal{H}}_{\text{eff}}^{\text{RK}}$ and the "full" effective QDM. When on the other side deriving the quantum dimer model at a certain order, rather than calculating the exact (accumulated) weights of processes, the energy of the QDM can also be lower than for the NNVB approach. This is the case for $\hat{\mathcal{H}}_{\text{eff}}^{\text{LO}}$ and suggests some kind of variational behavior when doing the overlap expansion appropriately.

6.2.4. Comparison of the Effective Quantum Dimer Model with the NNVB Approach

The next step in gauging the effective quantum dimer model (Eq. 6.4) is to explicitly compare it with the data obtained within the nearest neighbor valence bond approach. Both methods are based on the nearest neighbor valence bond basis, but whereas the NNVB technique treats the effect of the overlap matrix correctly, this is not the case for the QDM. Indeed, the loop expansion is performed hierarchically and has to be truncated at some order, which necessarily introduces a systematic error. However, as we have seen in section (6.2.3), this is rather well controlled and one can in principle push the scheme to arbitrary precision.

As in Fig. (6.12), we can compare the ground state energies for both approaches. Here, we do this for a different value of $J_3 = 0.3$ and also include finite size data. Actually, the finite size extrapolation to obtain the ground state energy in the thermodynamic limit can be based on the one valid within the Néel phase, which reads at lowest order [41]

$$\frac{E_0}{N} = e_\infty - \frac{\alpha'}{N^{3/2}}, \tag{6.8}$$

where α' is some coefficient and e_∞ the finite size extrapolated ground state energy per site. This scaling shall be assumed for the NNVB approach and the quantum

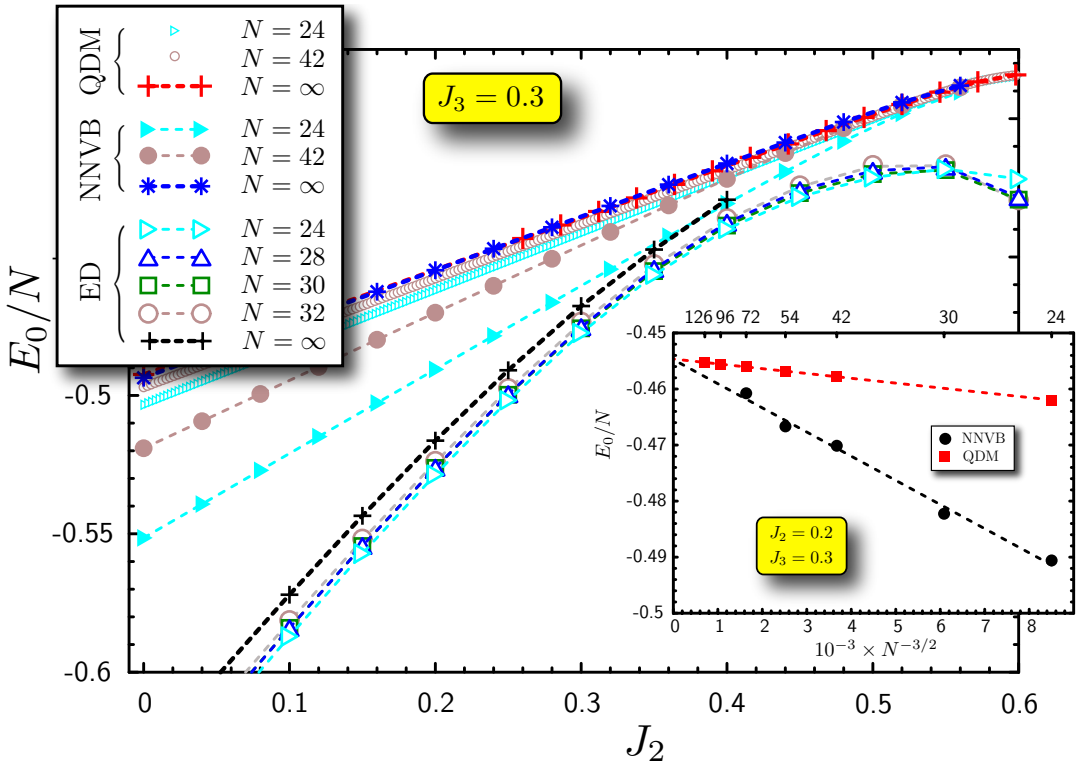

Fig. 6.13.: Illustration of the ground state energies vs. J_2 for different system size and the extrapolated thermodynamical limit. The data are compared for different techniques at $J_3 = 0.3$. In the inset we show the finite size extrapolation within NNVB and for the QDM for the arbitrarily chosen point $(J_2, J_3) = (0.2, 0.3)$. NNVB and ED data were obtained by F. Albuquerque, S. Capponi and A. Läuchli and the figure is taken from [19].

dimer model for any J_2, which seems to be justified. Comparing ground state energies, obtained within the NNVB approach with the one from the effective quantum dimer model (see Fig. 6.13), we here observe an improved finite size scaling behavior of the QDM. This is manifested in two aspects: firstly, the finite size samples produce energies that are less deviated from the assumed scaling extrapolation. Secondly, the energies from finite size samples are also closer to the extrapolated one. Nevertheless, we observe very good agreement between both models in the thermodynamic limit, indicating that the effective quantum dimer model can indeed capture the physics within the nearest neighbor valence bond space, even though it is only an approximate model.

In addition to the ground state energies, one may also consider the entire low–energy spectrum. In figure (6.14) we compare the spectra for both approaches for a cluster of $N = 54$ sites at $J_3 = 0.3$. Interestingly, these spectra are rather similar regarding the main features. However, one difference concerns the quantum numbers of the corresponding levels, a fact that can be explained through the symmetry properties of the basis states. Whereas singlets are antisymmetric with respect to a site permutation, quantum dimers are rather symmetric. This difference is somehow mediated by the

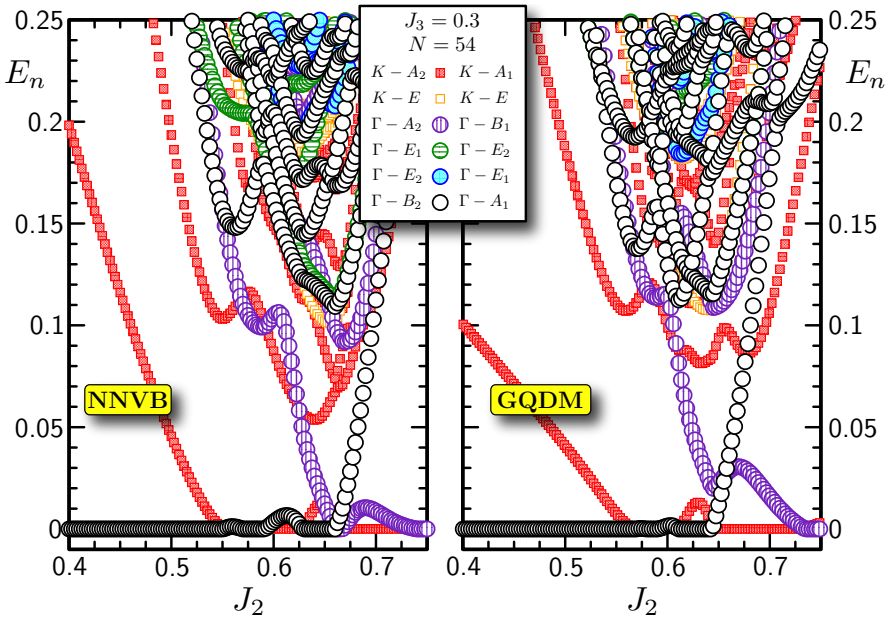

Fig. 6.14.: Low energy spectrum of the Heisenberg model projected into the NNVB subspace (left panel) and the corresponding spectrum of the effective quantum dimer model (right panel) for $N = 54$ sites. We plot the difference with the absolute ground state vs. J_2 at $J_3 = 0.3$. Notice, that the quantum numbers for corresponding levels are not the same, as for the NNVB approach we consider (directed) singlets, whereas the dimers within the QDM are symmetric (undirected). Apart from this issue the spectra are qualitatively similar. The NNVB data were produced by F. Albuquerque and the figure is taken from [19].

similarity transformation, which relates the two approaches (see chapter 5).

Another feature can immediately be seen by comparing the lowest levels with K momentum. Whereas the lowest level of the A_1 representation in the QDM decreases almost linearly with J_2, the corresponding level obtained within the NNVB approach does not show a linear behavior. A deeper understanding of this effect can be achieved when looking at the finite size scaling of the gap between the total ground state and the lowest excitation with momentum K. This is illustrated in figure (6.15) for the particular choice of $J_2 = 0.5$ and shows, that this gap will close in the thermodynamic limit. Going back to Fig. (6.14), this indicates that the quantum dimer model converges faster to the thermodynamic limit. In other words, the collapse of the gap seems to be much more progressed in the QDM, compared to the NNVB approach, although we compare clusters of the same size.

The collapse of the finite size gap for the lowest K (and K') excitation, shown in Fig. (6.15), will form the three quasi–degenerated ground states, required to build the plaquette VBC, which will be detected independently in section (6.2.5). It can be nicely seen, that this collapse is visible in all used techniques, the exact diagonalization in the $\hat{S}^z$ basis, the NNVB approach and the effective quantum dimer model. However, the attainable sample sizes strongly depend on the used method. Whereas for ED in the

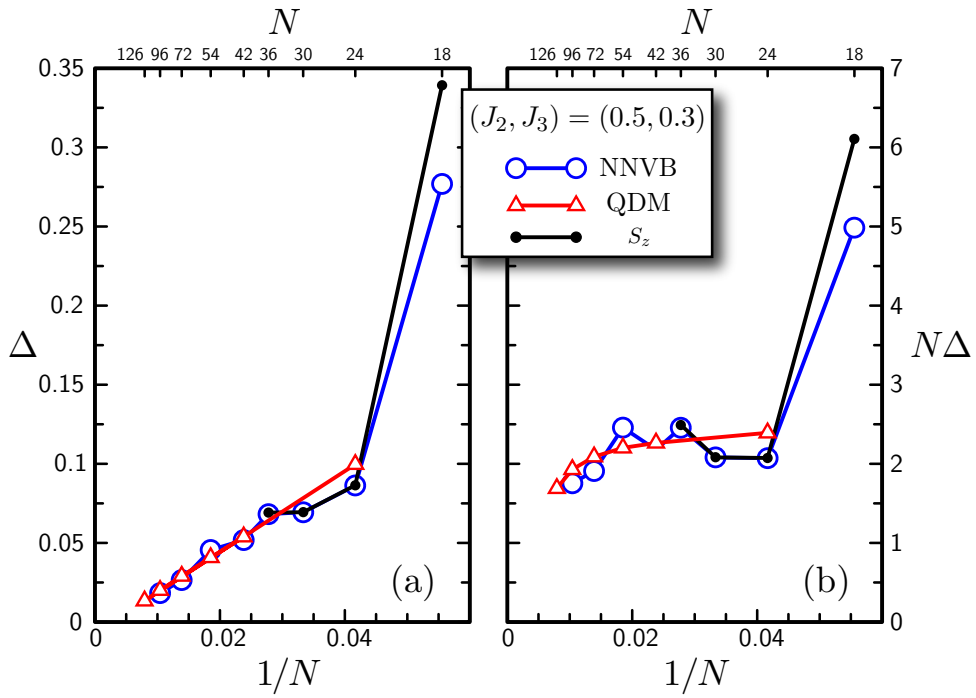

Fig. 6.15.: Finite size scaling of the gap between the ground state and the lowest excitation with momentum K, for the point $(J_2, J_3) = (0.5, 0.3)$. Notice, that this point displays particularly strong plaquette/columnar correlations within ED in the spin basis [19]. The data were obtained with exact diagonalization in the $\hat{S}^z$ basis by S. Capponi and A. Läuchli, the NNVB approach (F. Albuquerque) and for the effective quantum dimer model. Notice, that although the ground state energy does not seem to be optimal for the NNVB approach and the QDM (see Fig. 6.13), the gap matches rather well with the results of the original spin model. The figure is taken from [19].

spin basis one observes rather large finite size effects and one only merely recognizes a collapse as N^{-1} for the gap, for the NNVB approach a decay faster than N^{-1} is suggested (see right panel in Fig. (6.15)). This behavior is even more pronounced for the QDM, as finite size effects are substantially reduced and bigger clusters are available. Notice, that due to the finite correlation length in the VBC one would indeed expect an exponential collapse of the finite size gap for large enough system sizes.

Therefore, the effective quantum dimer model seems to capture the physics of the nearest neighbor valence bond approach very accurately. Indeed, the ground state energies match, as well as the finite size gap in the zone where we expect the disordered phase (V), when comparing with Fig. (6.7). Furthermore, the low–energy spectrum looks very similar to the one obtained by NNVB. Furthermore, the effective quantum dimer model shows much less finite size effects and allows for simulating larger clusters. This allows to clarify the picture about the collapsing finite size gap to the K A_1 level (Fig. 6.15), which was not clear at all from exact diagonalization data. The agreement between the different methods is indeed very striking, despite the less accurate ground state energy.

6.2.5. Dimer Vector Histograms

There are two basic advantages for studying quantum dimer models. Firstly, one can simulate much larger clusters, due to the less complex NNVB space and the presence of an orthogonal eigenvalue problem, which can be treated with efficient numerical techniques, such as Lanczos ED. Secondly, one has access to observables, that would be much more difficult to compute in the $\hat{S}^z$ basis or the non–orthogonal NNVB approach. This is rather valuable, as there are indeed quantities [78, 163, 164, 165, 77], which can discriminate between plaquette and columnar physics, in contrast to correlation functions or low–energy level quantum numbers. The basic insight is to associate a two–dimensional vector to every dimer and to study the distribution of such vectors, rather than the entire state. The result are the so–called *dimer vector histograms*, which can be introduced as follows.

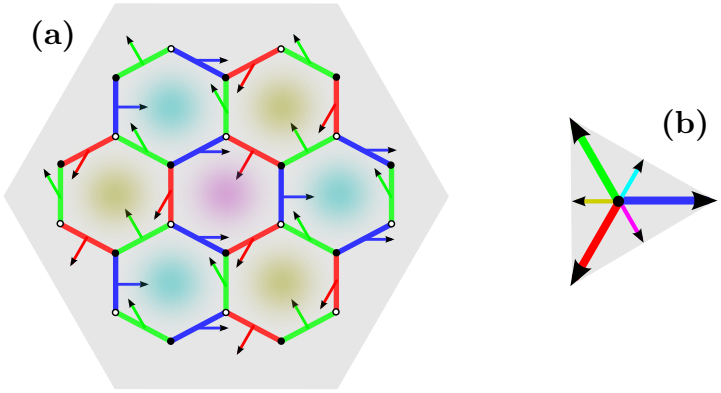

Fig. 6.16.: (a) Definition of the dimer vectors for a discrimination between *columnar* and *plaquette* physics, as presented in [19]. Dimers of the same color have the same dimer vector associated and belong to the same of three degenerated *columnar* states. In order to form a resonating *plaquette*, two different dimer vectors have to be considered, contributing equally to the *plaquette* state. (b) Allowed dimer vectors form an equilateral triangle as phase space, with the corners corresponding to a *columnar* state. A *plaquette* state is signaled by a binomial distribution on the edges, while a *staggered* state corresponds to a signal in the center.

Writing the QDM ground state $|\psi_0\rangle = \sum_i a_i |\varphi_i\rangle$ as superposition of dimer configurations $|\varphi_i\rangle$, one defines the appropriate histogram as

$$P(N_x, N_y) = \sum_{i \in \mathcal{C}_{N_x,N_y}} |a_i|^2 , \tag{6.9}$$

where $\mathcal{C}_{N_x,N_y}$ is indexing all dimer states $|\varphi_i\rangle$ that have a total dimer vector

$$(N_x, N_y) = \sum_{[i,j] \in |\varphi\rangle} \mathbf{v}_{[i,j]}. \tag{6.10}$$

For our purpose, we will choose dimer vectors as illustrated in Fig. (6.16), and the resulting histogram signals a *columnar* (Read–Sachdev [139]) state in the corners of an

equilateral triangle. A *plaquette* state is signaled on the edges of the triangle, while a *staggered* (lattice–nematic) state would produce a signal in the center.

The dimer histograms, obtained with the effective quantum dimer model (Eq. 6.4) are shown in figure (6.17) for the three largest simulated samples, $N \in \{72, 96, 126\}$. As we will see in section (6.2.1), the region with white background is expected to describe the Heisenberg model on the honeycomb lattice and displays a rather pronounced *plaquette* signal. This indeed underlines the preliminary observation, that around the point $(J_2, J_3) = (3/8, 0)$ the effective Hamiltonian reduces to a Rokhsar Kivelson model within the plaquette phase [9]. Whereas the plaquette signal is even amplified when moving to larger J_2, we observe that the dimer histograms become rather round when approaching the transition region to the Néel phase at smaller J_2. This actually reminds of the $U(1)$–like behavior, observed at different Néel to VBC transitions [78, 165, 77, 100].

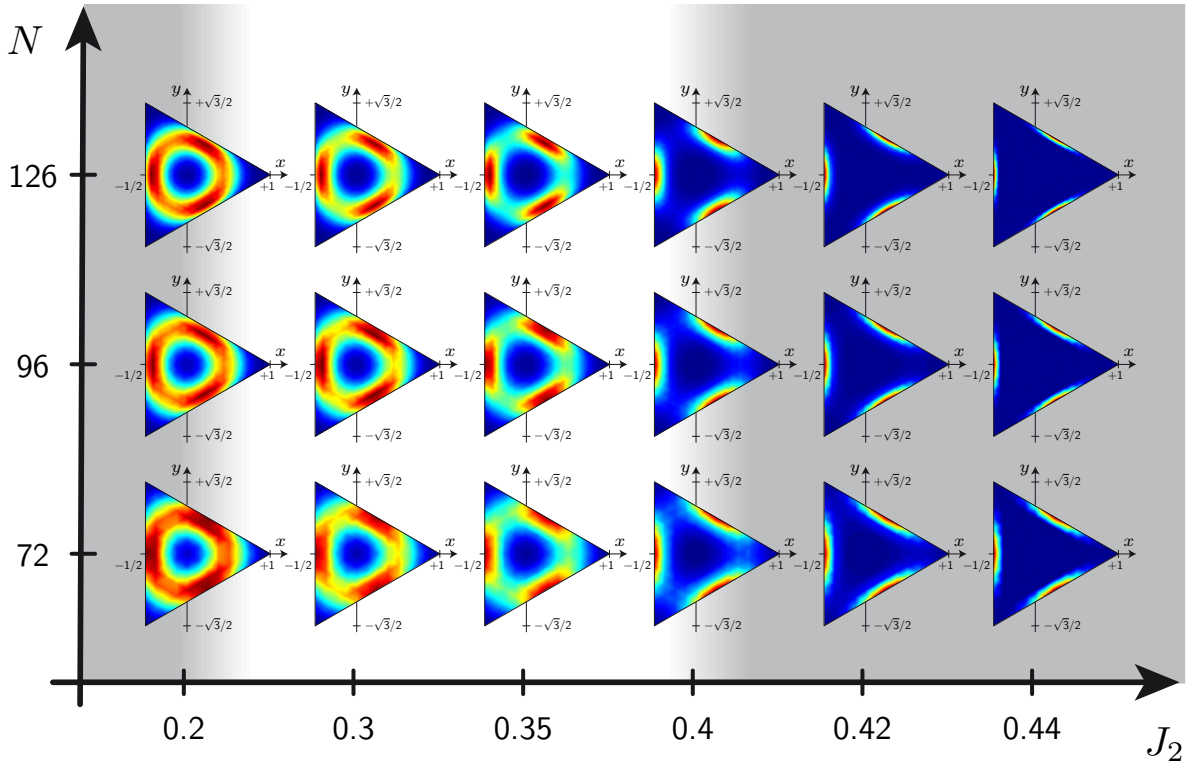

Fig. 6.17.: Normalized dimer histograms $P(N_x, N_y)$, as defined by Eq. (6.9), for different system sizes. The histograms were computed for different J_2 at $J_3 = 0$. At small J_2, the histograms display rather U(1) like behavior, whereas at larger J_2 a clear plaquette signal is observed. The gray shaded region is not expected to describe the physics of Heisenberg model, described in section (6.2.1). The figure is taken from [19].

Notice however, that our quantum dimer model cannot capture the physics of the Néel phase, as this would involve arbitrary ranged valence bonds in the singlet sector. This is beyond the NNVB approach and therefore also beyond the model described in

Eq. (6.4). In the dimer histograms this is indicated by a non–vanishing radius of the distribution, when approaching $J_2 = 0$. Therefore, it is not clear whether the observed $U(1)$–like regime is also present in the original Heisenberg model. A similar statement can be made about the parameter region $J_2 \gtrsim 0.4$, where the plaquette signal is most developed in the QDM. Comparing with correlations in the original model [19], the plaquette signal for larger J_2 in the QDM cannot be related to the Heisenberg model.

6.3. Partial Conclusion

We have seen, that using the generalized quantum dimer approach, described in chapter (5), we can reproduce the results obtained within the NNVB basis basically to arbitrary precision, by deriving a sufficiently complicated effective model. There are two main advantages of solving quantum dimer models. Firstly, we have an orthogonal eigenvalue problem, which can be solved with less numerical effort than the generalized eigenvalue problem obtained within NNVB. This allows for the simulation of larger clusters, enabling more reliable finite size scaling. This is further improved by the fact, that both the ground state energy and the lowest excitation gap (and possibly even more parts of the spectrum) show much smaller finite size effects, resulting in a much more well–behaved finite size analysis.

This last point might be surprising at first glance, but has a very simple explanation. The derivation scheme of the general quantum dimer models and especially the required fusion rules are implemented on the infinite lattice. This is primarily for technical reasons as it seems relatively non–trivial to derive fusion rules, which are suitable to describe a finite lattice. Indeed, this would set a limit on the loop lengths and possibly alter some pre–factors in the fusion rules, and thus primarily complicate the whole scheme. Fortunately, however simulating the infinite QDM on finite clusters increases the convergence properties with respect to the NNVB approach, a quite remarkable property of the GQDM.

Using this technique we have found evidence for valence bond crystals on both, the kagomé and the honeycomb lattice. In the first case we find that the effective model lies rather close to a multi–critical point, which might possibly explain the much debated different findings of VBCs and spin liquids. However, recently new evidence was found for the kagomé Heisenberg model to be in a spin liquid phase [155]. This seems to indicate that the NNVB approach, as it is implemented here, is not enough to describe the physics of the kagomé lattice, even though spin liquids could in principle be described with nearest neighbor valence bonds.

On the honeycomb lattice we found very strong evidence for a plaquette VBC phase. A very intriguing property of the effective model is the fact that dimer–dimer correlations are smaller than expected in the plaquette, although this phase should be contained within NNVB. The same is true for a possible staggered phase at large J_2 [159], for which we find no evidence at all within the NNVB or the QDM approach. Here as well a staggered VBC could in principle be described with nearest neighbor valence bonds.

Both previous examples may be explained by the following argument. When expressing the Heisenberg Hamiltonian within the nearest neighbor valence bonds we actually

divide the Hamiltonian into four blocks [136]: two diagonal blocks which correspond to the NNVB space and its orthogonal space respectively, and two off–diagonal blocks that connect the different spaces. The way the NNVB approach is used here, we simply diagonalize the block corresponding to the NNVB subspace, neglecting the off–diagonal blocks.

A crucial insight here is that it seems possible to go beyond this simple NNVB projection scheme by including longer dimers into the GQDM derivation. Consider the following reduced fusion rule,

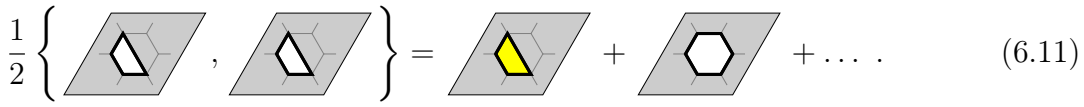

(6.11)

This means that there are fusion rules, which build terms within NNVB from other processes, also containing longer dimers. Therefore it seems that one can precisely imitate the inter–block terms and derive a quantum dimer model diagrammatically, that goes beyond the simple NNVB projection procedure. The aim at the end would however be to only improve on processes within NNVB, i.e. derive corrections to the existing amplitudes t_6, t_{10} and so on. We need to exclude longer valence bonds for two reasons: firstly, they are expected to contribute less to the actual ground state, as has been shown in the case of the square lattice [43]. Secondly, taking into account third neighbor valence bonds, as in Eq. (6.11), would enlarge the basis and thus annihilate the advantage of working with effective quantum dimer models.

For this reason one should concentrate on improving the projection into the nearest neighbor valence bond basis. It seems to be rather likely, that a staggered VBC, if present for the honeycomb lattice may be detected within such an approach. The same argument should hold for spin liquid behavior on the kagomé lattice. It might be imaginable, that an improved NNVB projection pushes the parameters into the $\mathbb{Z}_2$ spin liquid phase [8], if it is the ground state of the kagomé antiferromagnet.

Of course, this is very speculative and will have to be tested. However, such an *extended* quantum dimer model derivation scheme seems to be a very appealing route for future studies. The question is however whether the linear dependence of second nearest neighbors may spoil such an approach or not. Nevertheless, in the case of a successful implementation one might expect to benefit from the nice finite size scaling behavior of the generalized quantum dimer models.

7. Conclusion

In this thesis I showed how studying the singlet subspace, in terms of valence bonds, can contribute to answer questions in condensed matter systems. Although working in a non–orthogonal basis is rather non–trivial, as a result of a reduced number of efficient analytical and numerical techniques, it is possible to apply this approach to problems of actual research.

For bipartite systems one can use quantum Monte Carlo simulations [12], which allow to access rather large system sizes within bipartite valence bond states. It was shown how fidelity can be measured in large scale QMC simulations, providing complementary information to standard approaches, based on order parameters. This method was previously only used with analytical techniques or Lanczos exact diagonalization. Interestingly, the fidelity approach played a role in all studied problems: the CaV_4O_9 compound, the kagomé lattice and the honeycomb lattice, showing to which extent this interdisciplinary approach can serve in numerical studies.

On the technical side, one might wonder whether projector QMC schemes, carried out in the spin basis, can be used for fidelity measurements, as this would potentially reduce fluctuations, induced by the valence bond approach. It remains however to be tested, whether such a scheme can be similarly efficient, especially as a small finite size singlet triplet gap might spoil such a method, due to relatively long projection lengths.

For frustrated systems, quantum Monte Carlo suffers from the famous sign problem, making it necessary to use other techniques. One of the most celebrate numerical approaches is Lanczos exact diagonalization. However, studying large clusters is rather demanding. A possible way out of this is to derive effective Hamiltonians, acting on a subset of the configuration space. It was shown in the present work, how this can be carried in the valence bond basis, being reduced to nearest neighbor singlets. This method allowed to systematically relate quantum dimer models to problems formulated with valence bonds, an approach which was initiated by Rokhsar and Kivelson [6]. Using this generalized quantum dimer model approach, we have seen that basically larger accessible cluster sizes and a smoother finite size scaling allowed for a significant improvement on the interpretation of finite size data. In the case of the kagomé lattice, one could confirm the presence of a 36–site VBC, although a nearby $\mathbb{Z}_2$ spin liquid may play a role when further corrections are considered. On the other side, a plaquette VBC was identified on the honeycomb lattice, basically through results from the GQDM approach. This was also possible by exploiting dimer histograms, which are easily defined for a quantum dimer model, and represent a rather visual tool to recognize different phases.

One may also be interested in also regarding spin correlation functions in quantum dimer models. Indeed, similarly to the Hamiltonian, all observables would have to be transformed by an overlap expansion, in order to allow a measurement of such quantities. This has not been studied yet, but might be a possible direction for the future, rendering

observables accessible for general quantum dimer models.

Another possible direction is the inclusion of longer valence bonds in the derivation scheme, in order to go beyond NNVB. One might also try to develop effective models for higher spin sectors, as for example for the triplet excitations. Both techniques would allow to clarify the situation on the kagomé lattice, regarding the presence of a true spin liquid, or the honeycomb lattice, regarding magnetic or non–magnetic phases at larger J_2. Indeed, it is rather intriguing, that a staggered VBC could not be signaled with the present effective Hamiltonian, although it is suggested by complementary studies [159] and despite the fact that an ordinary Rokhsar Kivelson model can contain such a phase [9].

Finally, the studied problems were concentrated in frustrated and non–frustrated magnetism, some of which are very old, like the kagomé antiferromagnet. One of the major problems in this context is the practical realization of spin liquids and their theoretical description with spin models. A solution to this problem may be of importance for high–temperature superconductivity [21]. Detecting spin liquids may require some non–traditional probes, such as the fidelity approach or entanglement scaling, which were presented in this thesis.

On the other side, working with effective models is one of the few approaches for systems that suffer from a sign problem. The derivation of such models almost always requires to perform some series expansion. Understanding how to carry this out within a diagrammatic language may be helpful in establishing such a expansion, as well as for the convergence of the series.

Part IV.

Supplementary Material

A. Overlap Expansion for the Kagomé Lattice

In this appendix we present the overlap expansion scheme for the kagomé lattice, as shown in [15]. In particular, we display the fusion rules up to order α^{14}, the overlap expansion of $\hat{\mathcal{O}}$ and $\hat{\mathcal{H}}$, and the expansion scheme for the resulting effective Hamiltonian $\hat{\mathcal{H}}_{\text{eff}}$.

Fusion rules at order 8

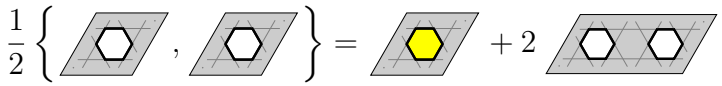

Fusion rules at order 10

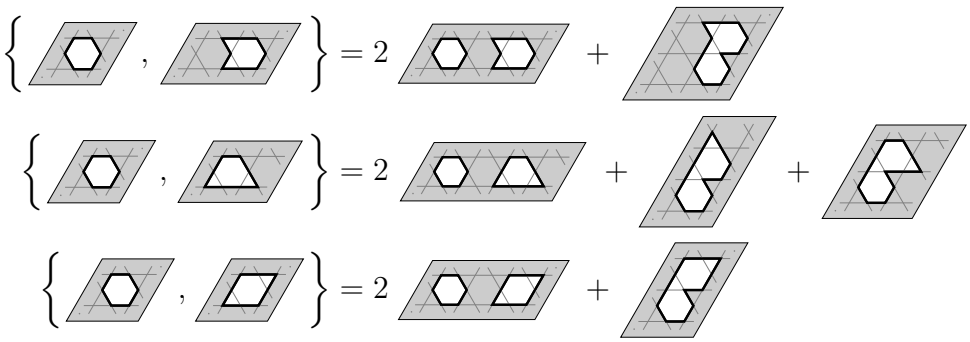

Fusion rules at order 12

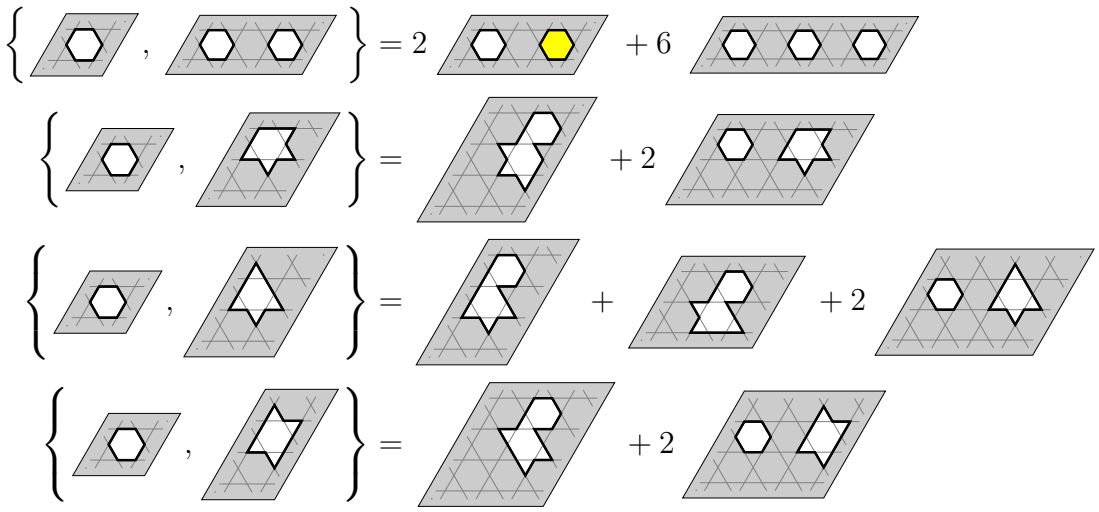

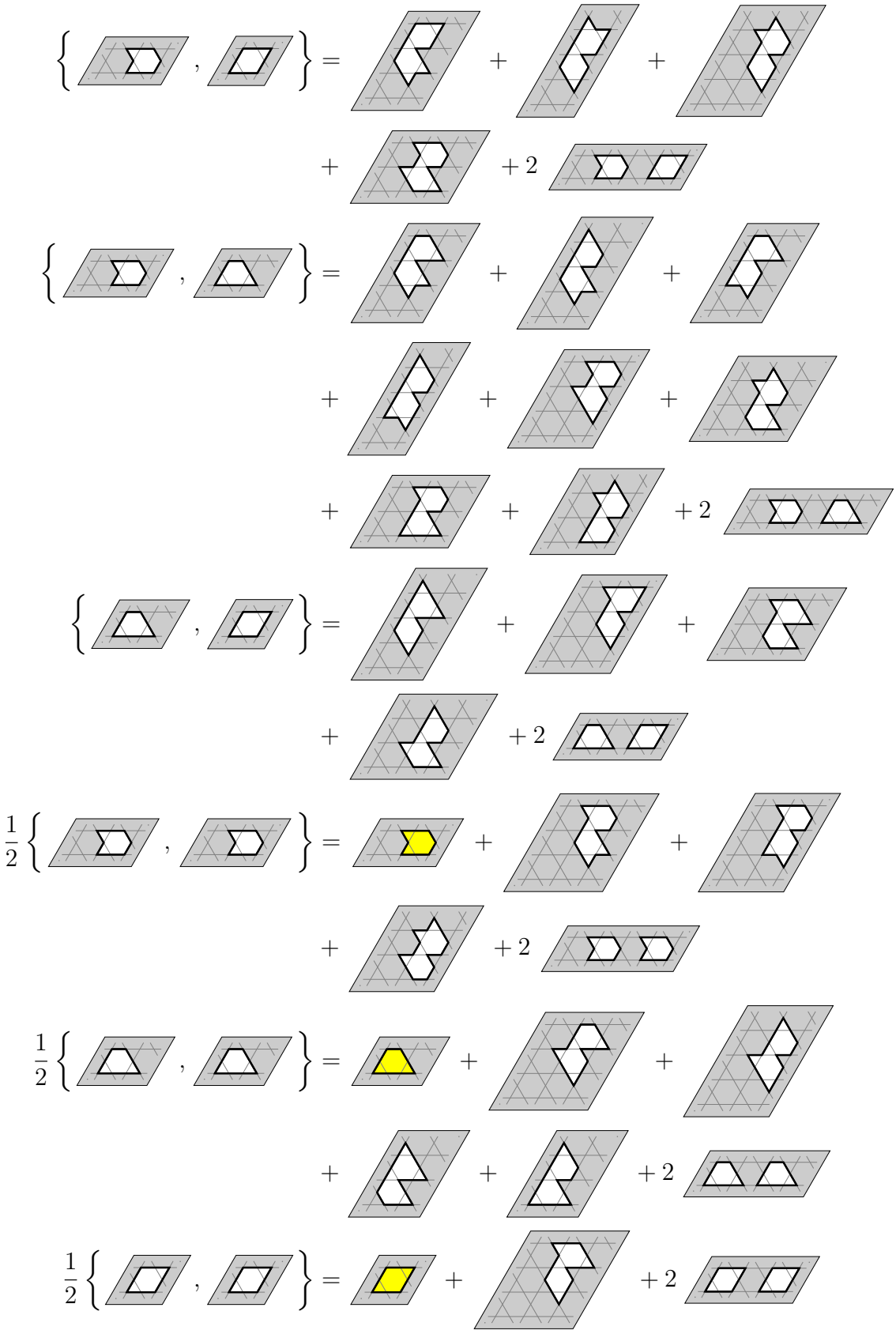

Fusion rules at order 14

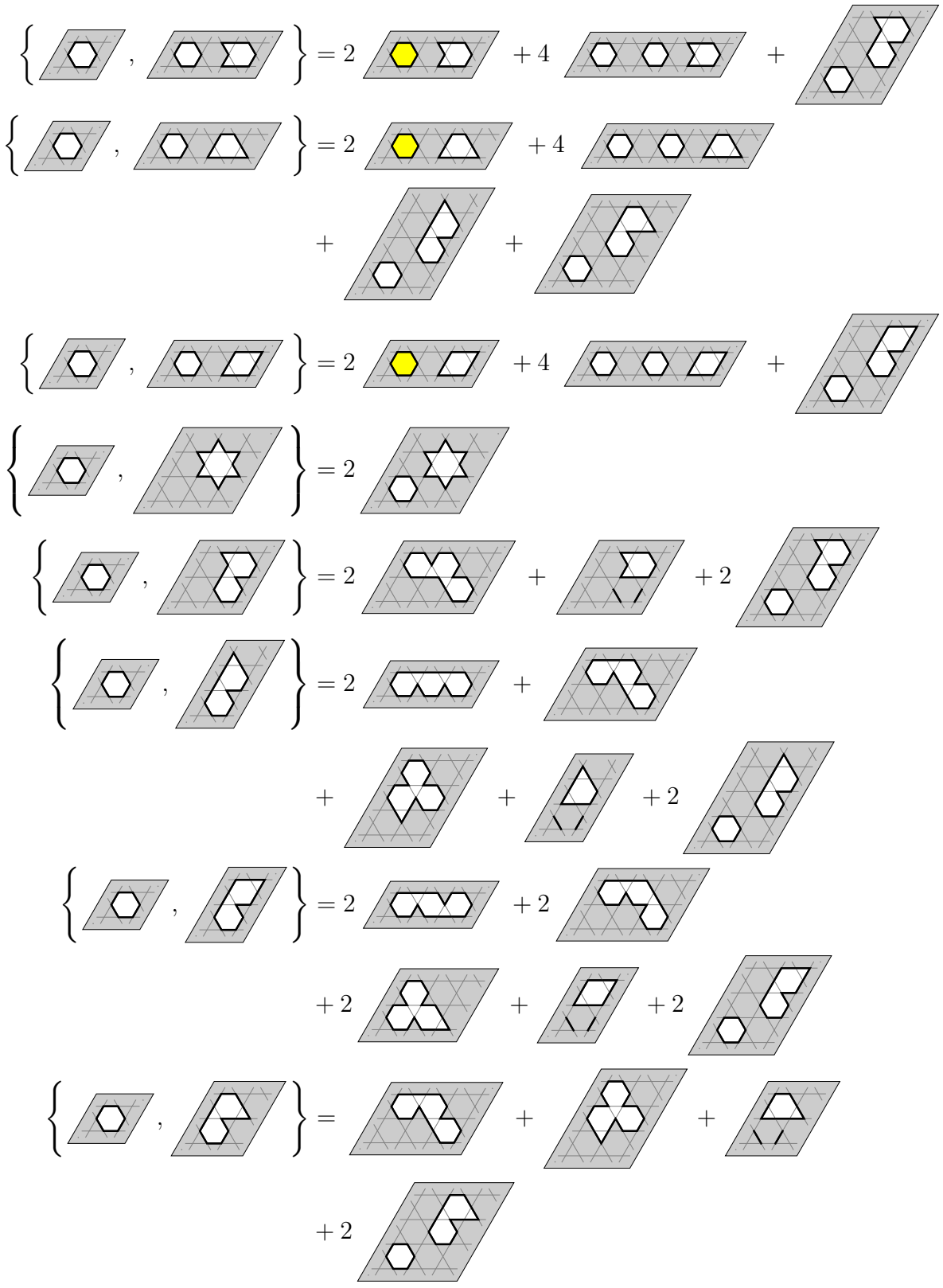

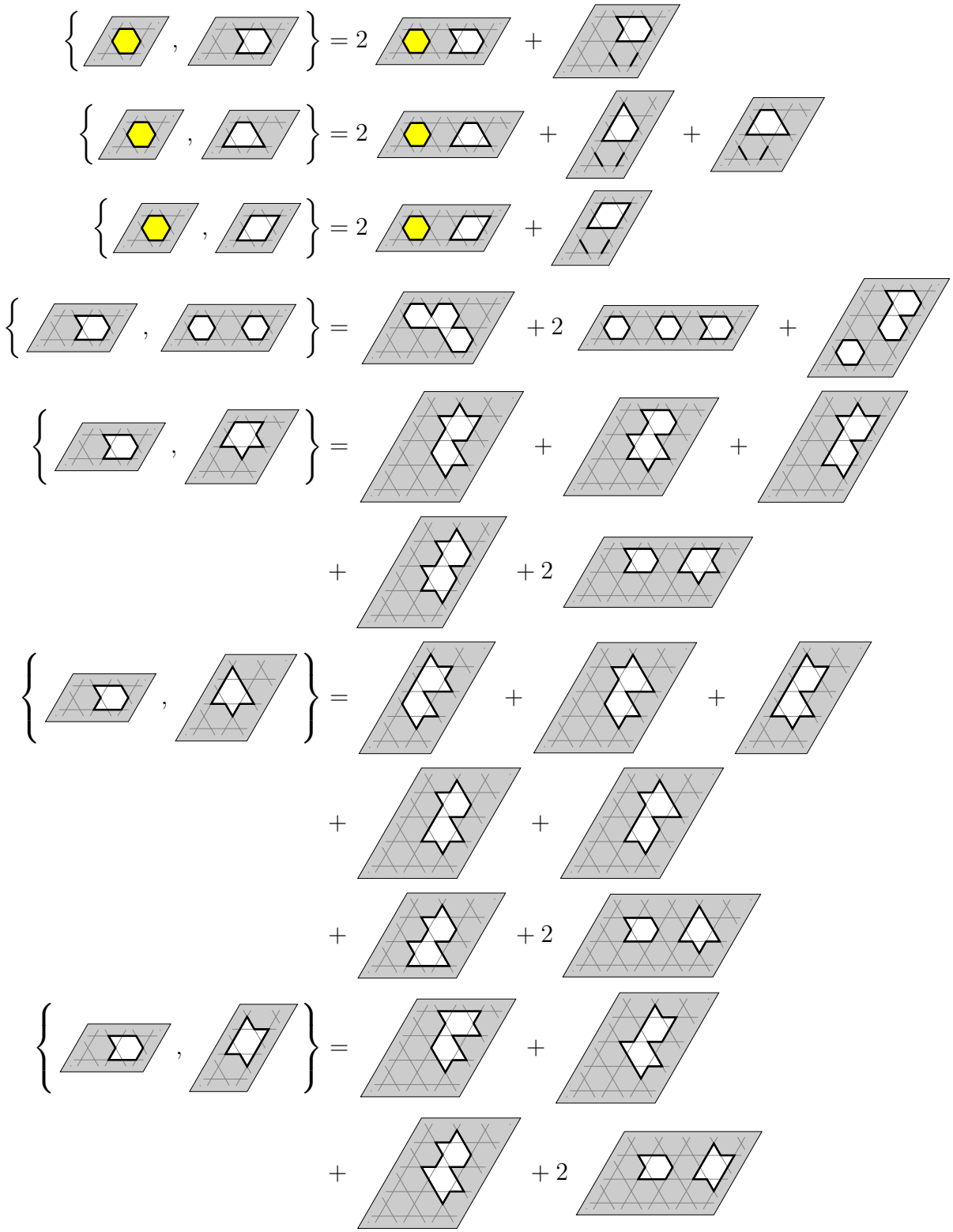

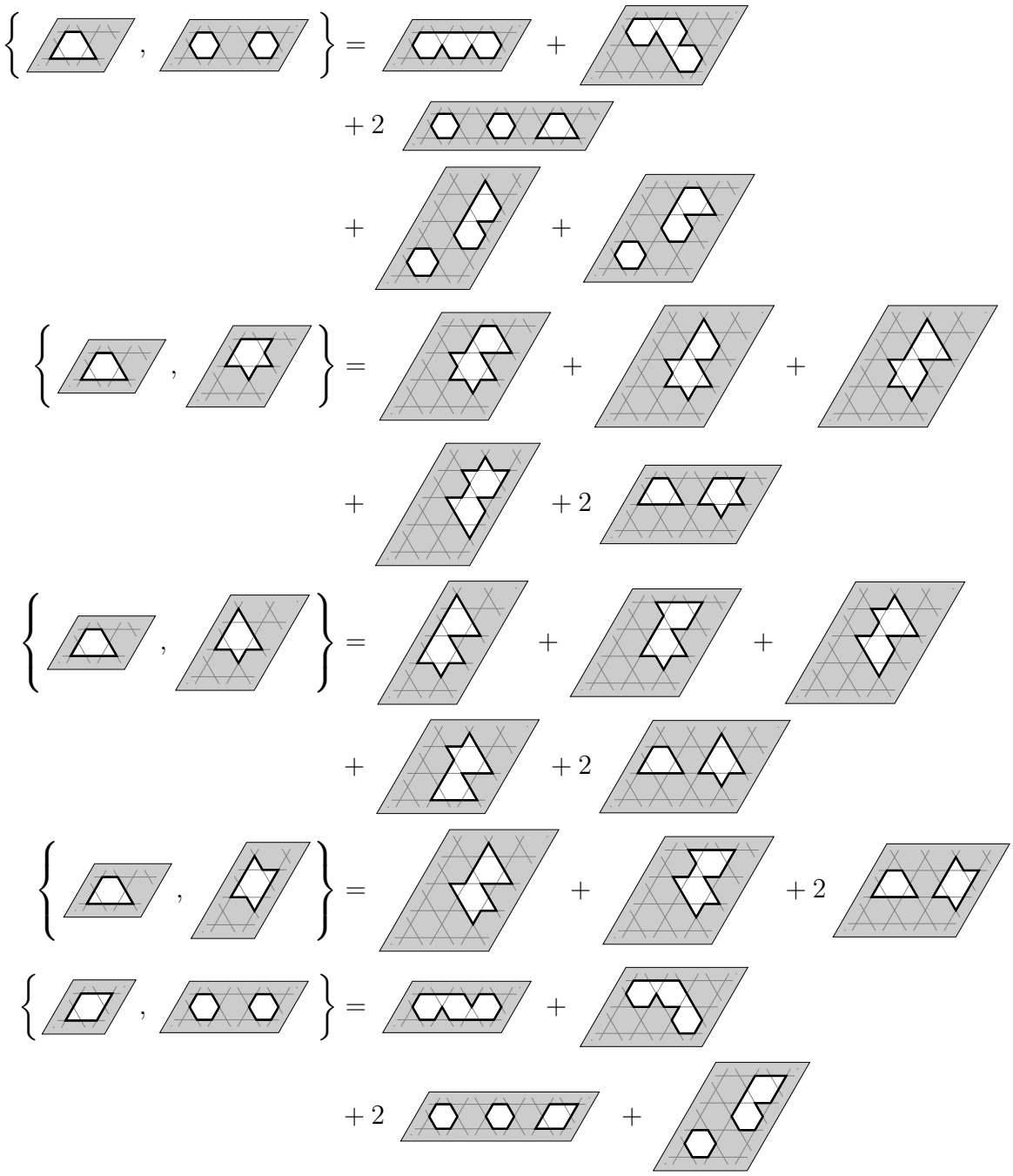

Processes $\hat{\omega}_g$ and their energies h_g up to orders $\alpha^{2\mathrm{n}_g} = \alpha^{14}$

$\hat{\omega}_g$	$2\mathrm{n}_g$	h_g	$\hat{\omega}_g$	$2\mathrm{n}_g$	h_g	$\hat{\omega}_g$	$2\mathrm{n}_g$	h_g	$\hat{\omega}_g$	$2\mathrm{n}_g$	h_g
	4	$-3J$		12	$-3J$	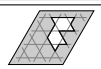	14	$-2J$		14	$-2J$
	6	$-2J$		12	$-3J$		14	$-2J$		14	$-6J$
	6	$-2J$		12	$-3J$		14	$-2J$		14	$-6J$
	6	$-2J$		12	$-3J$		14	$-2J$		14	$-6J$
	8	$-6J$		12	$-3J$		14	$-2J$		14	$-6J$
	8	$-J$		12	$-3J$		14	$-2J$		14	$-6J$
	8	$-J$		12	$-3J$		14	$-2J$		14	$-5J$
	8	$-J$		12	$-3J$		14	$-2J$		14	$-5J$
	10	$-5J$		12	$-3J$		14	$-2J$		14	$-8J$
	10	$-5J$		12	$-3J$		14	$-2J$	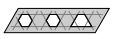	14	$-8J$
	10	$-5J$		12	$-3J$		14	$-2J$		14	$-8J$
	10	0		12	$-3J$		14	$-2J$		14	$-3J$
	10	$-4J$		12	$-3J$		14	$-2J$		14	$-7J$
	10	$-4J$		12	$-3J$		14	$-2J$		14	$-7J$
	10	$-4J$		12	$-3J$		14	$-2J$		14	$-7J$
	10	$-4J$		12	$-3J$		14	$-2J$		14	$-7J$
	10	$-4J$		12	$-3J$		14	$-2J$		14	$-7J$
	12	$-3J$		12	$-3J$		14	$-2J$		14	$-3J$
	12	$-3J$		12	$-3J$		14	$-2J$		14	$-3J$
	12	$-3J$		12	$-9J$		14	$-2J$		14	$-3J$
	12	$-3J$		12	$-4J$		14	$-2J$		14	$-3J$
	12	$-3J$		12	$-4J$		14	$-2J$		14	$-3J$
	12	$-3J$		12	$-4J$		14	$-2J$		14	$-3J$
	12	$-3J$		12	$-4J$		14	$-2J$		14	$-3J$
	12	$-3J$		12	$-4J$		14	$-2J$		14	$-3J$
	12	$-3J$		12	$-4J$		14	$-2J$		14	$-3J$
	12	$-3J$		12	$-4J$		14	$-2J$		14	$-3J$
	12	$-3J$		14	$-2J$		14	$-2J$			

Expansion of $\hat{\mathcal{H}}_{\text{eff}}$ up to order α^{14} and accumulated amplitudes

Processes $\hat{\omega}_g$ that appear in the expansion of the effective Hamiltonian $\hat{\mathcal{H}}_{\text{eff}}$. We indicate their amplitudes at lowest order (LO) and the accumulated weight (∞), if applicable.

$\hat{\omega}_g$	LO	∞	$\hat{\omega}_g$	LO	$\hat{\omega}_g$	LO	$\hat{\omega}_g$	LO
	$-3J\alpha^4$	$\frac{3J\alpha^4}{\alpha^8-1}$		$\frac{7J\alpha^{14}}{8}$		$-J\alpha^{12}$	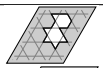	$-\frac{J\alpha^{14}}{2}$
	$3J\alpha^8$	$-\frac{3J\alpha^8}{\alpha^8-1}$		$-J\alpha^{12}$		$-J\alpha^{12}$	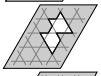	$-\frac{J\alpha^{14}}{2}$
	$-2J\alpha^6$	$\frac{2J\alpha^6}{\alpha^{12}-1}$		$-J\alpha^{12}$		$-J\alpha^{12}$	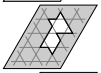	$-\frac{J\alpha^{14}}{2}$
	$-2J\alpha^6$	$\frac{2J\alpha^6}{\alpha^{12}-1}$		$-J\alpha^{12}$		$-J\alpha^{12}$	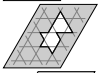	$-\frac{J\alpha^{14}}{2}$
	$-2J\alpha^6$	$\frac{2J\alpha^6}{\alpha^{12}-1}$		$-J\alpha^{12}$		$-J\alpha^{12}$		$-\frac{J\alpha^{14}}{2}$
	$2J\alpha^{12}$	$-\frac{2J\alpha^{12}}{\alpha^{12}-1}$		$-J\alpha^{12}$		$-J\alpha^{12}$		$-\frac{J\alpha^{14}}{2}$
	$2J\alpha^{12}$	$-\frac{2J\alpha^{12}}{\alpha^{12}-1}$		$-J\alpha^{12}$		$-\frac{J\alpha^{14}}{2}$	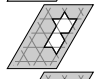	$-\frac{J\alpha^{14}}{2}$
	$2J\alpha^{12}$	$-\frac{2J\alpha^{12}}{\alpha^{12}-1}$		$-J\alpha^{12}$		$-\frac{J\alpha^{14}}{2}$	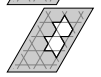	$-\frac{J\alpha^{14}}{2}$
	$-J\alpha^8$	$\frac{J\alpha^8}{\alpha^{16}-1}$		$-J\alpha^{12}$		$-\frac{J\alpha^{14}}{2}$	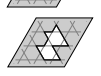	$-\frac{J\alpha^{14}}{2}$
	$-J\alpha^8$	$\frac{J\alpha^8}{\alpha^{16}-1}$		$-J\alpha^{12}$		$-\frac{J\alpha^{14}}{2}$	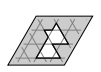	$-\frac{J\alpha^{14}}{2}$
	$-J\alpha^8$	$\frac{J\alpha^8}{\alpha^{16}-1}$		$-J\alpha^{12}$	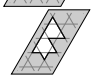	$-\frac{J\alpha^{14}}{2}$	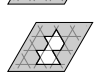	$-\frac{J\alpha^{14}}{2}$
	$J\alpha^{16}$	$-\frac{J\alpha^{16}}{\alpha^{16}-1}$		$-J\alpha^{12}$		$-\frac{J\alpha^{14}}{2}$	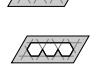	$-\frac{J\alpha^{14}}{2}$
	$J\alpha^{16}$	$-\frac{J\alpha^{16}}{\alpha^{16}-1}$		$-J\alpha^{12}$		$-\frac{J\alpha^{14}}{2}$	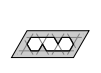	$-\frac{J\alpha^{14}}{2}$
	$J\alpha^{16}$	$-\frac{J\alpha^{16}}{\alpha^{16}-1}$		$-J\alpha^{12}$		$-\frac{J\alpha^{14}}{2}$	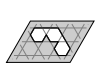	$-\frac{J\alpha^{14}}{2}$
	0	0		$-J\alpha^{12}$		$-\frac{J\alpha^{14}}{2}$	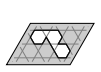	$-\frac{J\alpha^{14}}{2}$
	0	0		$-J\alpha^{12}$	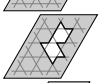	$-\frac{J\alpha^{14}}{2}$	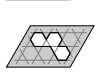	$-\frac{J\alpha^{14}}{2}$
	$-\frac{3J\alpha^{10}}{2}$			$-J\alpha^{12}$	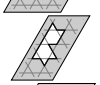	$-\frac{J\alpha^{14}}{2}$	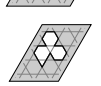	$-\frac{3J\alpha^{14}}{4}$
	$-\frac{3J\alpha^{10}}{2}$			$-J\alpha^{12}$		$-\frac{J\alpha^{14}}{2}$		$-\frac{3J\alpha^{14}}{4}$
	$-\frac{3J\alpha^{10}}{2}$			$-J\alpha^{12}$		$-\frac{J\alpha^{14}}{2}$		
	$-\frac{3J\alpha^{10}}{2}$			$-J\alpha^{12}$		$-\frac{J\alpha^{14}}{2}$		
	$\frac{7J\alpha^{14}}{8}$			$-J\alpha^{12}$	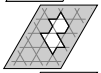	$-\frac{J\alpha^{14}}{2}$		
	$\frac{7J\alpha^{14}}{8}$			$-J\alpha^{12}$	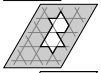	$-\frac{J\alpha^{14}}{2}$		
	$\frac{7J\alpha^{14}}{8}$			$-J\alpha^{12}$	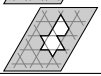	$-\frac{J\alpha^{14}}{2}$		

B. Overlap Expansion for the Honeycomb Lattice

In this appendix we present the overlap expansion scheme for the honeycomb lattice. In contrast to appendix (A) we here derive *reduced* fusion rules, involving only terms with one or two hexagons. The corresponding basis is thus represented by the following set of diagrams

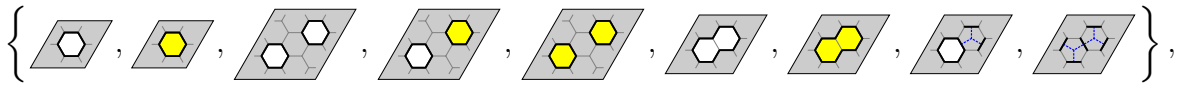

and we can therefore express the overlap matrix $\hat{\mathcal{O}} = \hat{1} + \hat{\mathcal{X}}$ and the Hamiltonian $\hat{\mathcal{H}}$ as vectors

$$\hat{\mathcal{X}} = \begin{pmatrix} \alpha^4 \\ 0 \\ \alpha^8 \\ 0 \\ 0 \\ \alpha^8 \\ 0 \\ 0 \\ 0 \end{pmatrix}, \qquad \hat{\mathcal{H}} = \begin{pmatrix} 6\alpha^4 J_2 - 3\alpha^4(J_1 + J_3) \\ 0 \\ 12\alpha^8 J_2 - 6\alpha^8(J_1 + J_3) \\ 0 \\ 0 \\ 14\alpha^8 J_2 - 6\alpha^8(J_1 + J_3) \\ 0 \\ 0 \\ 0 \end{pmatrix}.$$

Equivalently, this can be expressed in the following table, showing the orders and energies of all purely kinetic diagrams, that is all processes, which appear in the overlap expansion of $\hat{\mathcal{O}}$ and $\hat{\mathcal{H}}$.

$\hat{\omega}_g$	2n(g)	h$_g$	$\hat{\mathcal{H}}_{\text{eff}}$
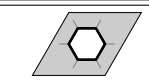	4	$6J_2 - 3(J_1 + J_3)$	$\frac{4}{5}\Big(2J_2 - (J_1 + J_3)\Big)$
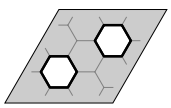	8	$12J_2 - 6(J_1 + J_3)$	0
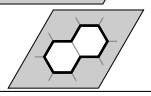	8	$14J_2 - 6(J_1 + J_3)$	$\frac{4}{3}\tau_{10}\Big(8J_2 - 3(J_1 + J_3)\Big)$

Using the reduced fusion rules, which are represented in detail at the end of this appendix, we find the fusion operator for the overlap matrix $\hat{\mathcal{O}}$ as

$$\frac{1}{2}\left\{\hat{\mathcal{X}},\bullet\right\} = \begin{pmatrix} 0 & \alpha^4 & 0 & 0 & 0 & 0 & 0 & 0 & 0 \\ \alpha^4 & 0 & 0 & 0 & 0 & 0 & 0 & 0 & 0 \\ 2\alpha^4 & 2\alpha^8 & 0 & 2\alpha^4 & \alpha^8 & 0 & 0 & 0 & 0 \\ \alpha^8 & \alpha^4 & \alpha^4 & \alpha^8 & \alpha^4 & 0 & 0 & 0 & 0 \\ 0 & 0 & \alpha^8 & 2\alpha^4 & 0 & 0 & 0 & 0 & 0 \\ \alpha^4 & \alpha^8 & 0 & 0 & 0 & 0 & \alpha^8 & \alpha^4 & 0 \\ 0 & 0 & 0 & 0 & 0 & \alpha^8 & 0 & \alpha^4 & 0 \\ \frac{\alpha^8}{2} & \frac{\alpha^4}{2} & 0 & 0 & 0 & \frac{\alpha^4}{2} & \frac{\alpha^4}{2} & \frac{\alpha^8}{2} & \frac{\alpha^4}{2} \\ 0 & 0 & 0 & 0 & 0 & 0 & 0 & 2\alpha^4 & 0 \end{pmatrix}.$$

This is now sufficient to apply equations (5.42), (5.43) and (5.44), and we obtain the effective Hamiltonian $\hat{\mathcal{H}}_{\text{eff}}$ with the following amplitudes

$\hat{\omega}_g$	$\hat{\mathcal{H}}_{\text{eff}}$	$\hat{\omega}_g$	$\hat{\mathcal{H}}_{\text{eff}}$
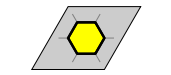	$-\frac{1}{5}\Big(2J_2-(J_1+J_3)\Big)$	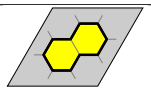	$-\frac{2}{3}\nu_{10}\Big(8J_2-3(J_1+J_3)\Big)$
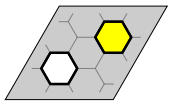	0	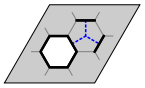	$-\frac{1}{6}\tau_{10}\Big(8J_2-3(J_1+J_3)\Big)$
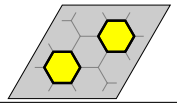	0	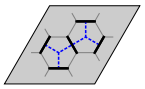	$\frac{4}{3}\nu_{10}\Big(8J_2-3(J_1+J_3)\Big)$

where $\tau_{10} = 0.049218(5)$ and $\nu_{10} = 0.001562(9)$, as in section (6.2.2).

Reduced fusion rules on the honeycomb lattice

Here, the fusion rules are explicitly not presented at certain orders, but rather describe all $9 \cdot 10/2 = 45$ possible fusions of the 9 different participating processes. This also involves the appearance of (two–hexagon) processes at rather high order, while others (i.e. three–hexagon terms) at lower orders are neglected.

Notice, that we also consider non–connected processes for completeness, even though this is not necessary. Indeed, within the reduced fusion rules, connected and disconnected two–hexagon processes form two independent branches, as fusions between them typically vanish, an effect that does usually not occur for general fusion rules.

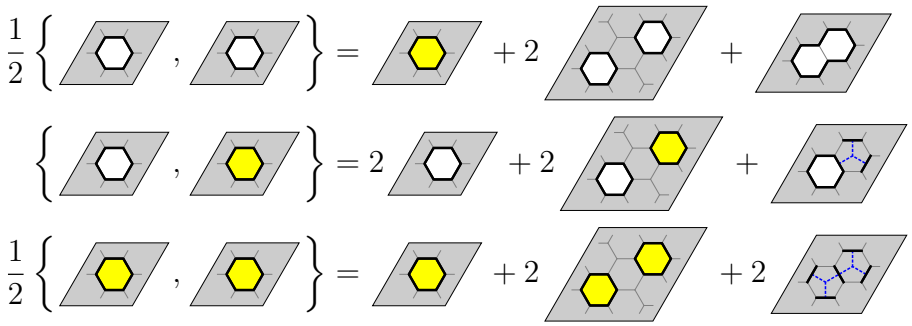

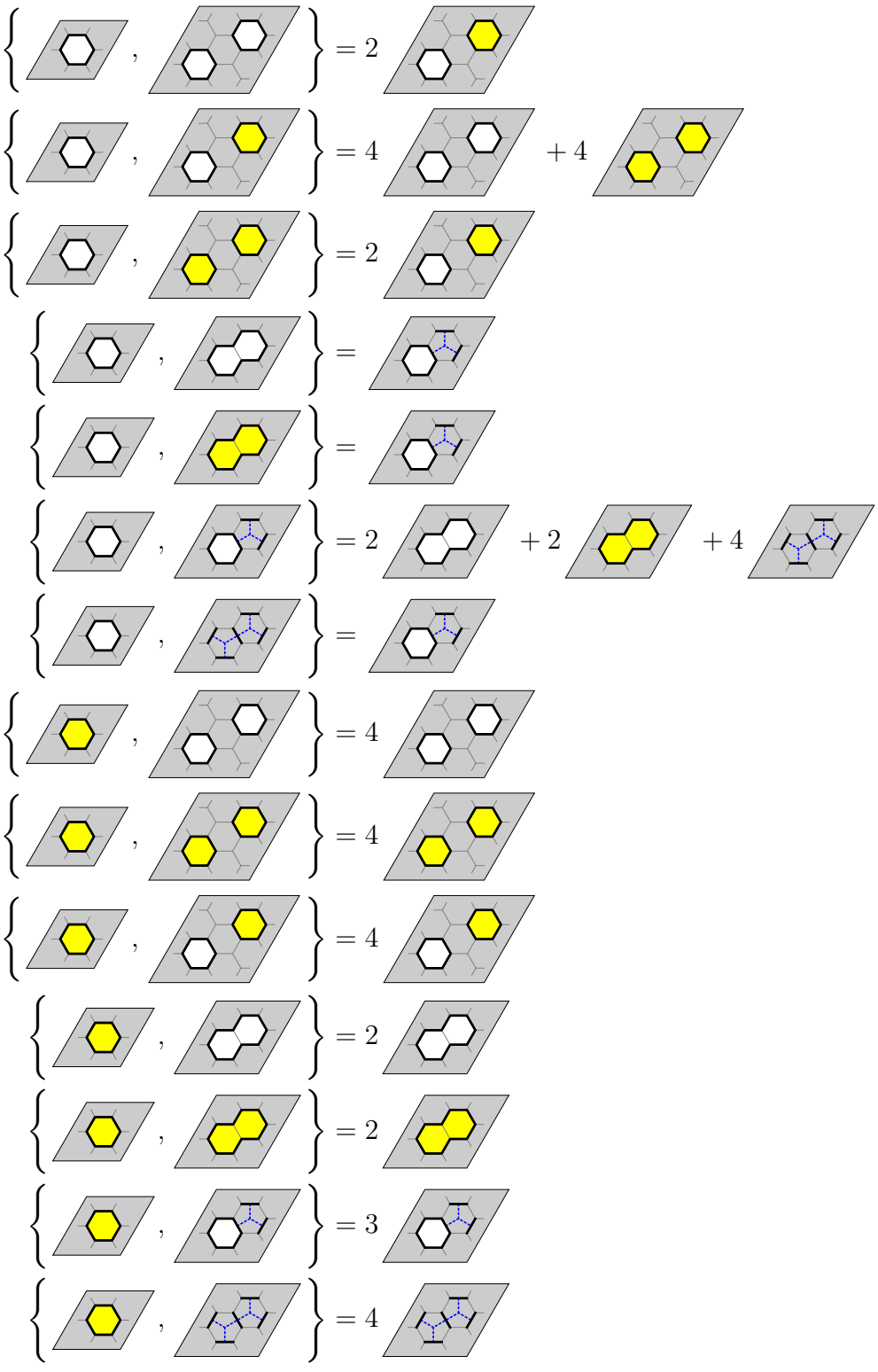

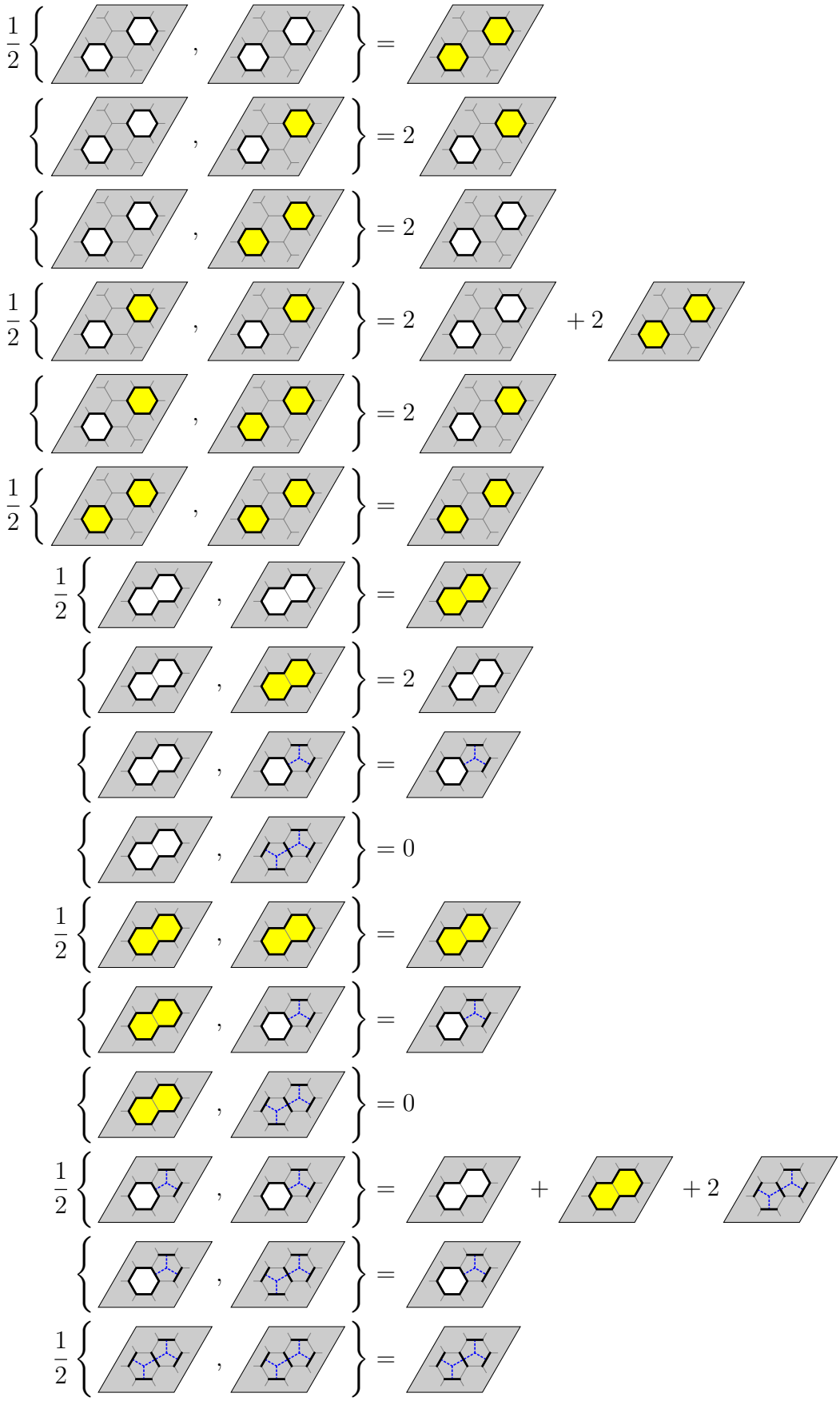

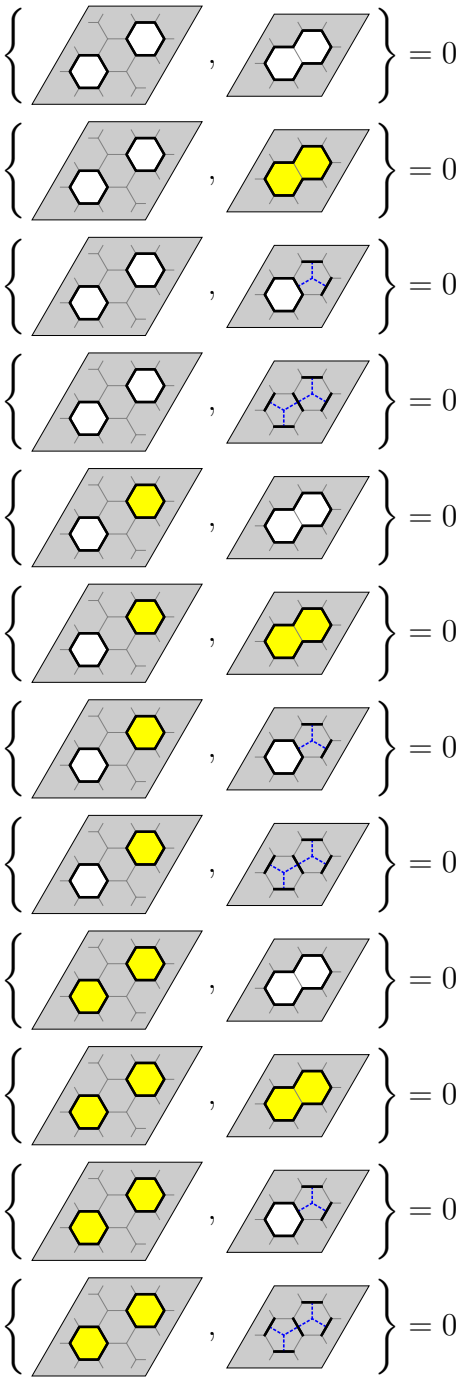

List of Publications

1. D. Schwandt, F. Alet & S. Capponi, "*Quantum Monte Carlo Simulations of Fidelity at Magnetic Quantum Phase Transitions*", Phys. Rev. Lett. **103**, 170501 (2009), DOI: 10.1103/PhysRevLett.103.170501, arXiv:0907.0191v3 [cond-mat.str-el].

2. D. Poilblanc, M. Mambrini & D. Schwandt, "*Effective quantum dimer model for the kagome Heisenberg antiferromagnet: Nearby quantum critical point and hidden degeneracy*", Phys. Rev. B **81**, 180402(R) (2010), DOI: 10.1103/PhysRevB.81.180402, arXiv:0912.0724v2 [cond-mat.str-el].

3. D. Schwandt, M. Mambrini & D. Poilblanc, "*Generalized hard-core dimer model approach to low-energy Heisenberg frustrated antiferromagnets: General properties and application to the kagome antiferromagnet*", Phys. Rev. B **81**, 214413 (2010), DOI: 10.1103/PhysRevB.81.214413, arXiv:1002.0774v2 [cond-mat.str-el].

4. A. F. Albuquerque, D. Schwandt, B. Hetényi, S. Capponi, M. Mambrini & A. M. Läuchli, "*Phase diagram of a frustrated quantum antiferromagnet on the honeycomb lattice: Magnetic order versus valence-bond crystal formation*", Phys. Rev. B **84**, 024406 (2011), DOI: 10.1103/PhysRevB.84.024406, arXiv:1102.5325v3 [cond-mat.str-el].

Bibliography

[1] N. W. Ashcroft & D. N. Mermin, "*Solid State Physics*" (Thomson Learning, ed. 1, 1976), ISBN: 0030839939.

[2] L. Balents, "*Spin liquids in frustrated magnets*", Nature **464**, 199 (2010), DOI: 10.1038/nature08917.

[3] G. Rumer, "*Zur Theorie der Spinvalenz*", Nachr. v. d. Ges. d. Wiss. zu Göttingen, Math.–Phys. Klasse **1932**, 337 (1932), http://resolver.sub.uni-goettingen.de/purl?GDZPPN002508877.

[4] G. Rumer, E. Teller & H. Weyl, "*Eine für die Valenztheorie geeignete Basis der binären Vektorinvarianten*", Nachr. v. d. Ges. d. Wiss. zu Göttingen, Math.–Phys. Klasse **1932**, 499 (1932), http://resolver.sub.uni-goettingen.de/purl?GDZPPN002508982.

[5] L. Pauling, "*The Calculation of Matrix Elements for Lewis Electronic Structures of Molecules*", J. Chem. Phys. **1**, 280 (1933), DOI: 10.1063/1.1749284.

[6] D. S. Rokhsar & S. A. Kivelson, "*Superconductivity and the Quantum Hard-Core Dimer Gas*", Phys. Rev. Lett. **61**, 2376 (1988), DOI: 10.1103/PhysRevLett.61.2376.

[7] R. Moessner & S. L. Sondhi, "*Resonating Valence Bond Phase in the Triangular Lattice Quantum Dimer Model*", Phys. Rev. Lett. **86**, 1881 (2001), DOI: 10.1103/PhysRevLett.86.1881, arXiv:cond-mat/0007378v1 [cond-mat.str-el].

[8] G. Misguich, D. Serban & V. Pasquier, "*Quantum Dimer Model on the Kagome Lattice: Solvable Dimer-Liquid and Ising Gauge Theory*", Phys. Rev. Lett. **89**, 137202 (2002), DOI: 10.1103/PhysRevLett.89.137202, arXiv:cond-mat/0204428v2 [cond-mat.str-el].

[9] R. Moessner, S. L. Sondhi & P. Chandra, "*Phase diagram of the hexagonal lattice quantum dimer model*", Phys. Rev. B **64**, 144416 (2001), DOI: 10.1103/PhysRevB.64.144416, arXiv:cond-mat/0106288v1 [cond-mat.stat-mech].

[10] P. Zanardi & N. Paunković, "*Ground state overlap and quantum phase transitions*", Phys. Rev. E **74**, 031123 (2006), DOI: 10.1103/PhysRevE.74.031123, arXiv:quant-ph/0512249v2.

[11] B. Sutherland, "*Systems with resonating-valence-bond ground states: Correlations and excitations*", Phys. Rev. B **37**, 3786 (1988), DOI: 10.1103/PhysRevB.37.3786.

[12] A. W. Sandvik, "*Ground State Projection of Quantum Spin Systems in the Valence-Bond Basis*", Phys. Rev. Lett. **95**, 207203 (2005), DOI: 10.1103/PhysRevLett.95.207203, arXiv:cond-mat/0509558v1 [cond-mat.str-el].

[13] A. W. Sandvik & H. G. Evertz, "*Loop updates for variational and projector quantum Monte Carlo simulations in the valence-bond basis*", Phys. Rev. B **82**, 024407 (2010), DOI: 10.1103/PhysRevB.82.024407, arXiv:0807.0682v2 [cond-mat.str-el].

[14] D. Schwandt, F. Alet & S. Capponi, "*Quantum Monte Carlo Simulations of Fidelity at Magnetic Quantum Phase Transitions*", Phys. Rev. Lett. **103**, 170501 (2009), DOI: 10.1103/PhysRevLett.103.170501, arXiv:0907.0191v3 [cond-mat.str-el].

[15] D. Schwandt, M. Mambrini & D. Poilblanc, "*Generalized hard-core dimer model approach to low-energy Heisenberg frustrated antiferromagnets: General properties and application to the kagome antiferromagnet*", Phys. Rev. B **81**, 214413 (2010), DOI: 10.1103/PhysRevB.81.214413, arXiv:1002.0774v2 [cond-mat.str-el].

[16] J. B. Marston & C. Zeng, "*Spin-Peierls and spin-liquid phases of Kagomé quantum antiferromagnets*", J. Appl. Phys. **69**, 5962 (1991), DOI: 10.1063/1.347830.

[17] R. R. P. Singh & D. A. Huse, "*Triplet and singlet excitations in the valence bond crystal phase of the kagome lattice Heisenberg model*", Phys. Rev. B **77**, 144415 (2008), DOI: 10.1103/PhysRevB.77.144415, arXiv:0801.2735v1 [cond-mat.str-el].

[18] D. Poilblanc, M. Mambrini & D. Schwandt, "*Effective quantum dimer model for the kagome Heisenberg antiferromagnet: Nearby quantum critical point and hidden degeneracy*", Phys. Rev. B **81**, 180402(R) (2010), DOI: 10.1103/PhysRevB.81.180402, arXiv:0912.0724v2 [cond-mat.str-el].

[19] A. F. Albuquerque, D. Schwandt, et al., "*Phase diagram of a frustrated quantum antiferromagnet on the honeycomb lattice: Magnetic order versus valence-bond crystal formation*", Phys. Rev. B **84**, 024406 (2011), DOI: 10.1103/PhysRevB.84.024406, arXiv:1102.5325v3 [cond-mat.str-el].

[20] P. W. Anderson, "*Resonating valence bonds: A new kind of insulator?*", Mater. Res. Bull. **8**, 153 (1973), DOI: 10.1016/0025-5408(73)90167-0.

[21] P. W. Anderson, "*The Resonating Valence Bond State in La_2CuO_4 and Superconductivity*", Science **235**, 1196 (1987), DOI: 10.1126/science.235.4793.1196.

[22] T. Oguchi & H. Kitatani, "*Theory of the Resonating Valence Bond in Quantum Spin System*", J. Phys. Soc. Jpn. **58**, 1403 (1989), DOI: 10.1143/JPSJ.58.1403.

[23] R. Saito, "*A Proof of the Completeness of the Non Crossed Diagrams in Spin 1/2 Heisenberg Model*", J. Phys. Soc. Jpn. **59**, 482 (1990), DOI: 10.1143/JPSJ.59.482.

[24] M. S. Dresselhaus, G. Dresselhaus & A. Jorio, "*Group theory : application to the physics of condensed matter*" (Springer-Verlag Berlin, 2008), ISBN: 978-3-540-32897-1.

[25] K. Gottfried & T.-M. Yan, "*Graduate Texts in Contemporary Physics*: *Quantum Mechanics: Fundamentals*" (Springer-Verlag New York Inc., ed. 2, 2004), ISBN: 978-0-387-22023-9.

[26] A. Yong, "*What is a Young tableau?*", Notices of the AMS, February 2007, Vol. 54, No. 2 (2006), arXiv:math/0611030v1 [math.CO].

[27] Z. Yu & N. Lin, "*Applications of permutation group theory to Heisenberg spin-1/2 chain*", J. Phys. A: Math. Gen. **26**, L881 (1993), DOI: 10.1088/0305-4470/26/17/022.

[28] J. Nachamkin, "*Direct use of Young tableau algebra to generate the Clebsch–Gordan coefficients of SU(2)*", J. Math. Phys. **16**, 2391 (1975), DOI: 10.1063/1.522504.

[29] A. Auerbach, "*Graduate Texts in Contemporary Physics*: *Interacting Electrons and Quantum Magnetism*" (Springer-Verlag New York Inc., 1994), ISBN: 0-387-94286-6.

[30] W. Nolting, "*Grundkurs theoretische Physik*: *Viel–Teilchen–Theorie*" (Springer Verlag Berlin, 2009), ISBN: 978-3-642-01605-9.

[31] H. T. Diep, Ed., "*Frustrated Spin Systems*" (World Scientific Publishing Company, 2004), ISBN: 978-9812560919.

[32] W. Marshall, "*Antiferromagnetism*", Proc. R. Soc. A **232**, 48 (1955), DOI: 10.1098/rspa.1955.0200.

[33] E. Lieb & D. Mattis, "*Ordering Energy Levels of Interacting Spin Systems*", J. Math. Phys. **3**, 749 (1962), DOI: 10.1063/1.1724276.

[34] C. Lhuillier, "*Frustrated Quantum Magnets*" (2005), arXiv:cond-mat/0502464v1 [cond-mat.str-el].

[35] P. W. Anderson, "*An Approximate Quantum Theory of the Antiferromagnetic Ground State*", Phys. Rev. **86**, 694 (1952), DOI: 10.1103/PhysRev.86.694.

[36] B. Bernu, C. Lhuillier & L. Pierre, "*Signature of Néel order in exact spectra of quantum antiferromagnets on finite lattices*", Phys. Rev. Lett. **69**, 2590 (1992), DOI: 10.1103/PhysRevLett.69.2590.

[37] B. Bernu, P. Lecheminant, et al., "*Exact spectra, spin susceptibilities, and order parameter of the quantum Heisenberg antiferromagnet on the triangular lattice*", Phys. Rev. B **50**, 10048 (1994), DOI: 10.1103/PhysRevB.50.10048, arXiv:cond-mat/9407028v1.

[38] G. Misguich & P. Sindzingre, "*Detecting spontaneous symmetry breaking in finite-size spectra of frustrated quantum antiferromagnets*", J. Phys.: Cond. Mat. **19**, 145202 (2007), DOI: 10.1088/0953-8984/19/14/145202, arXiv:cond-mat/0607764v3 [cond-mat.str-el].

[39] H. J. Schulz & T. A. L. Ziman, "*Finite-Size Scaling for the Two-Dimensional Frustrated Quantum Heisenberg Antiferromagnet*", Europhys. Lett. **18**, 355 (1992), DOI: 10.1209/0295-5075/18/4/013.

[40] A. W. Sandvik, "*Finite-size scaling of the ground-state parameters of the two-dimensional Heisenberg model*", Phys. Rev. B **56**, 11678 (1997), DOI: 10.1103/PhysRevB.56.11678, arXiv:cond-mat/9707123v1 [cond-mat.str-el].

[41] J.-B. Fouet, P. Sindzingre & C. Lhuillier, "*An investigation of the quantum J_1-J_2-J_3 model on the honeycomb lattice*", Eur. Phys. J. B **20**, 241 (2001), DOI: 10.1007/s100510170273, arXiv:cond-mat/0101421v1 [cond-mat.str-el].

[42] P. Sindzingre, C. Lhuillier & J.-B. Fouet, "*Quantum phases in two-dimensional frustrated spin-1/2 antiferromagnets*" (2001), arXiv:cond - mat / 0110283v1 [cond-mat.str-el].

[43] S. Liang, B. Douçot & P. W. Anderson, "*Some New Variational Resonating-Valence-Bond-Type Wave Functions for the Spin-$\frac{1}{2}$ Antiferromagnetic Heisenberg Model on a Square Lattice*", Phys. Rev. Lett. **61**, 365 (1988), DOI: 10.1103/PhysRevLett.61.365.

[44] M. Mambrini & F. Mila, "*RVB description of the low-energy singlets of the spin 1/2 kagomé antiferromagnet*", Eur. Phys. J. B **17**, 651 (2000), DOI: 10.1007/PL00011071, arXiv:cond-mat/0003080v1 [cond-mat.str-el].

[45] M. Mambrini, A. Läuchli, et al., "*Plaquette valence-bond crystal in the frustrated Heisenberg quantum antiferromagnet on the square lattice*", Phys. Rev. B **74**, 144422 (2006), DOI: 10.1103/PhysRevB.74.144422, arXiv:cond-mat/0606776v2 [cond-mat.str-el].

[46] A. Seidel, "*Linear independence of nearest-neighbor valence-bond states on the kagome lattice and construction of $SU(2)$-invariant spin-1/2 Hamiltonian with a Sutherland-Rokhsar-Kivelson quantum liquid ground state*", Phys. Rev. B **80**, 165131 (2009), DOI: 10.1103/PhysRevB.80.165131, arXiv:0906.0357v2 [cond-mat.str-el].

[47] J. Wildeboer & A. Seidel, "*Linear independence of nearest-neighbor valence bond states in several two-dimensional lattices*", Phys. Rev. B **83**, 184430 (2011), DOI: 10.1103/PhysRevB.83.184430, arXiv:1101.1621v3 [cond-mat.str-el].

[48] V. Elser, "*Nuclear antiferromagnetism in a registered ^3He solid*", Phys. Rev. Lett. **62**, 2405 (1989), DOI: 10.1103/PhysRevLett.62.2405.

[49] V. Elser & C. Zeng, "*Kagomé spin-1/2 antiferromagnets in the hyperbolic plane*", Phys. Rev. B **48**, 13647 (1993), DOI: 10.1103/PhysRevB.48.13647.

[50] M. E. Fisher, "*Statistical Mechanics of Dimers on a Plane Lattice*", Phys. Rev. **124**, 1664 (1961), DOI: 10.1103/PhysRev.124.1664.

[51] H. N. V. Temperley & M. E. Fisher, "*Dimer problem in statistical mechanics-an exact result*", Philosophical Magazine **6**, 1061 (1961), DOI: 10.1080/14786436108243366.

[52] P. W. Kasteleyn, "*The statistics of dimers on a lattice: I. The number of dimer arrangements on a quadratic lattice*", Physica **27**, 1209 (1961), DOI: 10.1016/0031-8914(61)90063-5.

[53] P. W. Kasteleyn, "*Dimer Statistics and Phase Transitions*", J. Math. Phys. **4**, 287 (1963), DOI: 10.1063/1.1703953.

[54] K. S. D. Beach & A. W. Sandvik, "*Some formal results for the valence bond basis*", Nucl. Phys. B **750**, 142 (2006), DOI: 10.1016/j.nuclphysb.2006.05.032, arXiv:cond-mat/0605103v1 [cond-mat.str-el].

[55] N. Read & B. Chakraborty, "*Statistics of the excitations of the resonating-valence-bond state*", Phys. Rev. B **40**, 7133 (1989), DOI: 10.1103/PhysRevB.40.7133.

[56] A. W. Sandvik & K. S. D. Beach, "*Monte Carlo Simulations of Quantum Spin Systems in the Valence Bond Basis*" (2007), arXiv:0704.1469v1 [cond-mat.str-el].

[57] B. A. Cipra, "*The Best of the 20th Century: Editors Name Top 10 Algorithms*", SIAM News **33** (2000), http://www.siam.org/pdf/news/637.pdf.

[58] http://www.netlib.org/lapack/.

[59] N. Metropolis, A. W. Rosenbluth, et al., "*Equation of State Calculations by Fast Computing Machines*", J. Chem. Phys. **21**, 1087 (1953), DOI: 10.1063/1.1699114.

[60] C. Lanczos, "*An Iteration Method for the Solution of the Eigenvalue Problem of Linear Differential and Integral Operators*", J. Res. Natl. Bur. Stand. **45**, 255 (1950), http://nvlpubs.nist.gov/nistpubs/jres/045/4/V45.N04.A01.pdf.

[61] C. Lanczos, "*Solution of Systems of Linear Equations by Minimized Iterations*", J. Res. Natl. Bur. Stand. **49**, 33 (1952), http://nvlpubs.nist.gov/nistpubs/jres/049/1/V49.N01.A06.pdf.

[62] R. Assaraf & M. Caffarel, "*Zero-Variance Principle for Monte Carlo Algorithms*", Phys. Rev. Lett. **83**, 4682 (1999), DOI: 10.1103/PhysRevLett.83.4682, arXiv:cond-mat/9911396v1 [cond-mat.stat-mech].

[63] B. Efron, "*Bootstrap Methods: Another Look at the Jackknife*", Ann. Stat. **7**, 1 (1979), DOI: 10.1214/aos/1176344552.

[64] M. H. Quenouille, "*Notes on bias in estimation*", Biometrika **43**, 353 (1956), DOI: 10.1093/biomet/43.3-4.353.

[65] J. W. Tukey, "*Bias and confidence in not quite large samples*", Ann. Math. Stat. **29**, 614 (1958), DOI: 10.1214/aoms/1177706647.

[66] M. Matsumoto & T. Nishimura, "*Mersenne twister: a 623-dimensionally equidistributed uniform pseudo-random number generator*", ACM Trans. Model. Comput. Simul. **8**, 3 (1998), DOI: 10.1145/272991.272995.

[67] A. Albuquerque, F. Alet, et al., "*The ALPS project release 1.3: Open-source software for strongly correlated systems*", J. Magn. Magn. Mater. **310**, 1187 (2007), DOI: 10.1016/j.jmmm.2006.10.304, arXiv:0801.1765v1 [cond-mat.str-el].

[68] http://alps.comp-phys.org/.

[69] W. K. Hastings, "*Monte Carlo sampling methods using Markov chains and their applications*", Biometrika **57**, 97 (1970), DOI: 10.1093/biomet/57.1.97.

[70] W. Krauth, "*Statistical Mechanics*: *Algorithms and Computations*" (Oxford University Press, 2006), ISBN: 978-0-19-851536-4.

[71] H. G. Evertz, G. Lana & M. Marcu, "*Cluster algorithm for vertex models*", Phys. Rev. Lett. **70**, 875 (1993), DOI: 10.1103/PhysRevLett.70.875, arXiv:cond-mat/9211006v1.

[72] H. G. Evertz, "*The loop algorithm*", Adv. Phys. **52**, 1 (2003), DOI: 10.1080/0001873021000049195, arXiv:cond-mat/9707221v3 [cond-mat.str-el].

[73] A. W. Sandvik, "*Stochastic series expansion method with operator-loop update*", Phys. Rev. B **59**, 14157(R) (1999), DOI: 10.1103/PhysRevB.59.R14157, arXiv:cond-mat/9902226v1 [cond-mat.str-el].

[74] O. F. Syljuåsen & A. W. Sandvik, "*Quantum Monte Carlo with directed loops*", Phys. Rev. E **66**, 046701 (2002), DOI: 10.1103/PhysRevE.66.046701, arXiv:cond-mat/0202316v2 [cond-mat.str-el].

[75] H. Suwa & S. Todo, "*Markov Chain Monte Carlo Method without Detailed Balance*", Phys. Rev. Lett. **105**, 120603 (2010), DOI: 10.1103/PhysRevLett.105.120603, arXiv:1007.2262v2 [cond-mat.stat-mech].

[76] J. Lou & A. W. Sandvik, "*Variational ground states of two-dimensional antiferromagnets in the valence bond basis*", Phys. Rev. B **76**, 104432 (2007), DOI: 10.1103/PhysRevB.76.104432, arXiv:cond-mat/0605034v3 [cond-mat.str-el].

[77] K. S. D. Beach, F. Alet, et al., "*$SU(N)$ Heisenberg model on the square lattice: A continuous-N quantum Monte Carlo study*", Phys. Rev. B **80**, 184401 (2009), DOI: 10.1103/PhysRevB.80.184401, arXiv:0812.3657v2 [cond-mat.str-el].

[78] A. W. Sandvik, "*Evidence for Deconfined Quantum Criticality in a Two-Dimensional Heisenberg Model with Four-Spin Interactions*", Phys. Rev. Lett. **98**, 227202 (2007), DOI: 10.1103/PhysRevLett.98.227202, arXiv:cond-mat/0611343v3 [cond-mat.str-el].

[79] A. Sen & A. W. Sandvik, "*Example of a first-order Néel to valence-bond-solid transition in two dimensions*", Phys. Rev. B **82**, 174428 (2010), DOI: 10.1103/PhysRevB.82.174428, arXiv:1009.0691v1 [cond-mat.str-el].

[80] Y. Saad, "*Algorithms and architectures for advanced scientific computing*: *Numerical Methods for Large Eigenvalue Problems*" (Manchester University Press, 1992), ISBN: 978-0470218204.

[81] J. G. F. Francis, "*The QR Transformation A Unitary Analogue to the LR Transformation - Part 1*", The Computer Journal **4**, 265 (1961), DOI: 10.1093/comjnl/4.3.265.

[82] N. Laflorencie & D. Poilblanc, "*Simulations of pure and doped low-dimensional spin-1/2 gapped systems*" **645**, 227 (2004), DOI: 10.1007/BFb0119595, arXiv:cond-mat/0408363v1 [cond-mat.str-el].

[83] A. W. Sandvik & J. Kurkijärvi, "*Quantum Monte Carlo simulation method for spin systems*", Phys. Rev. B **43**, 5950 (1991), DOI: 10.1103/PhysRevB.43.5950.

[84] A. W. Sandvik, "*A generalization of Handscomb's quantum Monte Carlo scheme-application to the 1D Hubbard model*", J. Phys. A: Math. Gen. **25**, 3667 (1992), DOI: 10.1088/0305-4470/25/13/017.

[85] M. Suzuki, "*Relationship between d-Dimensional Quantal Spin Systems and (d + 1)-Dimensional Ising Systems*", Prog. Theor. Phys. **56**, 1454 (1976), DOI: 10.1143/PTP.56.1454.

[86] H. F. Trotter, "*On the product of semi-groups of operators*", Proc. Amer. Math. Soc. **10**, 545 (1959), DOI: 10.1090/S0002-9939-1959-0108732-6.

[87] S. R. White, "*Density matrix formulation for quantum renormalization groups*", Phys. Rev. Lett. **69**, 2863 (1992), DOI: 10.1103/PhysRevLett.69.2863.

[88] S. R. White, "*Density-matrix algorithms for quantum renormalization groups*", Phys. Rev. B **48**, 10345 (1993), DOI: 10.1103/PhysRevB.48.10345.

[89] U. Schollwöck, "*The density-matrix renormalization group in the age of matrix product states*", Annals of Physics **326**, 96 (2011), DOI: 10.1016/j.aop.2010.09.012, arXiv:1008.3477v2 [cond-mat.str-el].

[90] E. M. Stoudenmire & S. R. White, "*Studying Two-Dimensional Systems with the Density Matrix Renormalization Group*", Ann. Rev. Cond. Mat. Phys. **3** (2012), DOI: 10.1146/annurev-conmatphys-020911-125018, arXiv:1105.1374v2 [cond-mat.str-el].

[91] W. L. McMillan, "*Ground State of Liquid He^4*", Phys. Rev. **138**, A442 (1965), DOI: 10.1103/PhysRev.138.A442.

[92] D. Ceperley, G. V. Chester & M. H. Kalos, "*Monte Carlo simulation of a many-fermion study*", Phys. Rev. B **16**, 3081 (1977), DOI: 10.1103/PhysRevB.16.3081.

[93] S. Sachdev, "*Quantum Phase Transitions*" (Cambridge University Press, 1999), ISBN: 0-521-58254-7.

[94] P. C. Hohenberg, "*Existence of Long-Range Order in One and Two Dimensions*", Phys. Rev. **158**, 383 (1967), DOI: 10.1103/PhysRev.158.383.

[95] N. D. Mermin & H. Wagner, "*Absence of Ferromagnetism or Antiferromagnetism in One- or Two-Dimensional Isotropic Heisenberg Models*", Phys. Rev. Lett. **17**, 1133 (1966), DOI: 10.1103/PhysRevLett.17.1133.

[96] S. Coleman, "*There are no Goldstone bosons in two dimensions*", Comm. Math. Phys. **31**, 259 (1973), http://projecteuclid.org/euclid.cmp/1103859034.

[97] L. D. Landau, E. M. Lifshitz & E. M. Pitaevskii, "*Course of Theoretical Physics*: *Statistical Physics*" (Butterworth-Heinemann, 1999), ISBN: 978-0750633727.

[98] S. Sachdev, "*Quantum magnetism and criticality*", Nat. Phys. **4**, 173 (2008), DOI: 10.1038/nphys894, arXiv:0711.3015v4 [cond-mat.str-el].

[99] H. Kronmüller & S. Parkin, Eds., "*Handbook of Magnetism and Advanced Magnetic Materials*" (John Wiley and Sons, 2007), ISBN: 978-0-470-02217-7.

[100] T. Senthil, A. Vishwanath, et al., "*Deconfined Quantum Critical Points*", Science **303**, 1490 (2004), DOI: 10.1126/science.1091806, arXiv:cond-mat/0311326v1 [cond-mat.str-el].

[101] A. Osterloh, L. Amico, et al., "*Scaling of entanglement close to a quantum phase transition*", Nature **416**, 608 (2002), DOI: 10.1038/416608a, arXiv:quant-ph/0202029v2.

[102] L. Amico, R. Fazio, et al., "*Entanglement in many-body systems*", Rev. Mod. Phys. **80**, 517 (2008), DOI: 10.1103/RevModPhys.80.517, arXiv:quant-ph/0703044v3.

[103] R. Augusiak, F. M Cucchietti & M. Lewenstein, "*Many body physics from a quantum information perspective*" (2010), arXiv:1003.3153v2 [quant-ph].

[104] P. Zanardi, P. Giorda & M. Cozzini, "*Information-Theoretic Differential Geometry of Quantum Phase Transitions*", Phys. Rev. Lett. **99**, 100603 (2007), DOI: 10.1103/PhysRevLett.99.100603, arXiv:quant-ph/0701061v1.

[105] M. A. Nielsen & I. L. Chuang, "*Quantum Computation and Quantum Information*" (Cambridge University Press, ed. 1, 2000), ISBN: 0-521-63503-9.

[106] S.-J. Gu, "*Fidelity approach to quantum phase transitions*", Intl. J. Mod. Phys. B **24**, 4371 (2010), DOI: 10.1142/S0217979210056335, arXiv:0811.3127v1 [quant-ph].

[107] P. W. Anderson, "*Infrared Catastrophe in Fermi Gases with Local Scattering Potentials*", Phys. Rev. Lett. **18**, 1049 (1967), DOI: 10.1103/PhysRevLett.18.1049.

[108] H.-Q. Zhou & J. P. Barjaktarevič, "*Fidelity and quantum phase transitions*", J. Phys. A: Math. Theor. **41**, 412001 (2008), DOI: 10.1088/1751-8113/41/41/412001, arXiv:cond-mat/0701608v1 [cond-mat.stat-mech].

[109] W.-L. You, Y.-W. Li & S.-J. Gu, "*Fidelity, dynamic structure factor, and susceptibility in critical phenomena*", Phys. Rev. E **76**, 022101 (2007), DOI: 10.1103/PhysRevE.76.022101, arXiv:quant-ph/0701077v2.

[110] S. Chen, L. Wang, et al., "*Intrinsic relation between ground-state fidelity and the characterization of a quantum phase transition*", Phys. Rev. A **77**, 032111 (2008), DOI: 10.1103/PhysRevA.77.032111, arXiv:0801.0020v2 [cond-mat.other].

[111] L. Campos Venuti & P. Zanardi, "*Quantum Critical Scaling of the Geometric Tensors*", Phys. Rev. Lett. **99**, 095701 (2007), DOI: 10.1103/PhysRevLett.99.095701, arXiv:0705.2211v2 [quant-ph].

[112] C. De Grandi, V. Gritsev & A. Polkovnikov, "*Quench dynamics near a quantum critical point*", Phys. Rev. B **81**, 012303 (2010), DOI: 10.1103/PhysRevB.81.012303, arXiv:0909.5181v3 [cond-mat.stat-mech].

[113] A. F. Albuquerque, F. Alet, et al., "*Quantum critical scaling of fidelity susceptibility*", Phys. Rev. B **81**, 064418 (2010), DOI: 10.1103/PhysRevB.81.064418, arXiv:0912.2689v2 [cond-mat.str-el].

[114] M. M. Rams & B. Damski, "*Quantum Fidelity in the Thermodynamic Limit*", Phys. Rev. Lett. **106**, 055701 (2011), DOI: 10.1103/PhysRevLett.106.055701, arXiv:1010.1048v2 [quant-ph].

[115] M. M. Rams & B. Damski, "*Scaling of ground-state fidelity in the thermodynamic limit: XY model and beyond*", Phys. Rev. A **84**, 032324 (2011), DOI: 10.1103/PhysRevA.84.032324, arXiv:1104.4104v3 [quant-ph].

[116] F. Verstraete, V. Murg & J. I. Cirac, "*Matrix product states, projected entangled pair states, and variational renormalization group methods for quantum spin systems*", Adv. Phys. **57**, 143 (2008), DOI: 10.1080/14789940801912366, arXiv:0907.2796v1 [quant-ph].

[117] M. B. Hastings, I. González, et al., "*Measuring Renyi Entanglement Entropy in Quantum Monte Carlo Simulations*", Phys. Rev. Lett. **104**, 157201 (2010), DOI: 10.1103/PhysRevLett.104.157201, arXiv:1001.2335v2 [cond-mat.str-el].

[118] M. Troyer, H. Kontani & K. Ueda, "*Phase Diagram of Depleted Heisenberg Model for CaV_4O_9*", Phys. Rev. Lett. **76**, 3822 (1996), DOI: 10.1103/PhysRevLett.76.3822.

[119] M. Troyer, M. Imada & K. Ueda, "*Critical Exponents of the Quantum Phase Transition in a Planar Antiferromagnet*", J. Phys. Soc. Jpn. **66**, 2957 (1997), DOI: 10.1143/JPSJ.66.2957.

[120] P. Zanardi, L. Campos Venuti & P. Giorda, "*Bures metric over thermal state manifolds and quantum criticality*", Phys. Rev. A **76**, 062318 (2007), DOI: 10.1103/PhysRevA.76.062318, arXiv:0707.2772v2 [quant-ph].

[121] M. Campostrini, M. Hasenbusch, et al., "*Critical exponents and equation of state of the three-dimensional Heisenberg universality class*", Phys. Rev. B **65**, 144520 (2002), DOI: 10.1103/PhysRevB.65.144520, arXiv:cond-mat/0110336v2 [cond-mat.stat-mech].

[122] C. H. Bennett, H. J. Bernstein, et al., "*Concentrating partial entanglement by local operations*", Phys. Rev. A **53**, 2046 (1996), DOI: 10.1103/PhysRevA.53.2046.

[123] P. Calabrese, M. Campostrini, et al., "*Parity Effects in the Scaling of Block Entanglement in Gapless Spin Chains*", Phys. Rev. Lett. **104**, 095701 (2010), DOI: 10.1103/PhysRevLett.104.095701, arXiv:0911.4660v2 [cond-mat.stat-mech].

[124] P. Calabrese & J. Cardy, "*Entanglement entropy and quantum field theory*", J. Stat. Mech.: Theor. Exp. **2004**, P06002 (2004), DOI: 10.1088/1742-5468/2004/06/P06002, arXiv:hep-th/0405152v3.

[125] F. Alet, S. Capponi, et al., "*Valence Bond Entanglement Entropy*", Phys. Rev. Lett. **99**, 117204 (2007), DOI: 10.1103/PhysRevLett.99.117204, arXiv:cond-mat/0703027v2 [cond-mat.str-el].

[126] R. W. Chhajlany, P. Tomczak & A. Wójcik, "*Topological Estimator of Block Entanglement for Heisenberg Antiferromagnets*", Phys. Rev. Lett. **99**, 167204 (2007), DOI: 10.1103/PhysRevLett.99.167204.

[127] Y.-C. Lin & A. W. Sandvik, "*Definitions of entanglement entropy of spin systems in the valence-bond basis*", Phys. Rev. B **82**, 224414 (2010), DOI: 10.1103/PhysRevB.82.224414, arXiv:1005.0821v2 [cond-mat.str-el].

[128] J. L. Jacobsen & H. Saleur, "*Exact Valence Bond Entanglement Entropy and Probability Distribution in the XXX Spin Chain and the Potts Model*", Phys. Rev. Lett. **100**, 087205 (2008), DOI: 10.1103/PhysRevLett.100.087205, arXiv:0711.3391v1 [cond-mat.stat-mech].

[129] J. Eisert, M. Cramer & M. B. Plenio, "*Colloquium: Area laws for the entanglement entropy*", Rev. Mod. Phys. **82**, 277 (2010), DOI: 10.1103/RevModPhys.82.277, arXiv:0808.3773v4 [quant-ph].

[130] C. K. Majumdar & D. K. Ghosh, "*On Next-Nearest-Neighbor Interaction in Linear Chain. I*", J. Math. Phys. **10**, 1388 (1969), DOI: 10.1063/1.1664978.

[131] D. J. Klein, "*Exact ground states for a class of antiferromagnetic Heisenberg models with short-range interactions*", J. Phys. A: Math. Gen. **15**, 661 (1982), DOI: 10.1088/0305-4470/15/2/032.

[132] J. T. Chayes, L. Chayes & S. A. Kivelson, "*Valence bond ground states in a frustrated two-dimensional spin-1/2 Heisenberg antiferromagnet*", Comm. Math. Phys. **123**, 53 (1989), DOI: 10.1007/BF01244017.

[133] K. S. Raman, R. Moessner & S. L. Sondhi, "*SU(2)-invariant spin- $\frac{1}{2}$ Hamiltonians with resonating and other valence bond phases*", Phys. Rev. B **72**, 064413 (2005), DOI: 10.1103/PhysRevB.72.064413, arXiv:cond-mat/0502146v2 [cond-mat.str-el].

[134] J. Cano & P. Fendley, "*Spin Hamiltonians with Resonating-Valence-Bond Ground States*", Phys. Rev. Lett. **105**, 067205 (2010), DOI: 10.1103/PhysRevLett.105.067205, arXiv:0910.5708v3 [cond-mat.str-el].

[135] S. Dommange, M. Mambrini, et al., "*Static impurities in the $S = 1/2$ kagome lattice: Dimer freezing and mutual repulsion*", Phys. Rev. B **68**, 224416 (2003), DOI: 10.1103/PhysRevB.68.224416, arXiv:cond-mat/0306299v1 [cond-mat.str-el].

[136] P. Durand, "*Direct determination of effective Hamiltonians by wave-operator methods. I. General formalism*", Phys. Rev. A **28**, 3184 (1983), DOI: 10.1103/PhysRevA.28.3184.

[137] A. Ralko, M. Mambrini & D. Poilblanc, "*Generalized quantum dimer model applied to the frustrated Heisenberg model on the square lattice: Emergence of a mixed columnar-plaquette phase*", Phys. Rev. B **80**, 184427 (2009), DOI: 10.1103/PhysRevB.80.184427, arXiv:0905.2039v1 [cond-mat.str-el].

[138] C. Zeng & V. Elser, "*Quantum dimer calculations on the spin-1/2 kagomé Heisenberg antiferromagnet*", Phys. Rev. B **51**, 8318 (1995), DOI: 10.1103/PhysRevB.51.8318.

[139] N. Read & S. Sachdev, "*Spin-Peierls, valence-bond solid, and Néel ground states of low-dimensional quantum antiferromagnets*", Phys. Rev. B **42**, 4568 (1990), DOI: 10.1103/PhysRevB.42.4568.

[140] M. Hermele, Y. Ran, et al., "*Properties of an algebraic spin liquid on the kagome lattice*", Phys. Rev. B **77**, 224413 (2008), DOI: 10.1103/PhysRevB.77.224413, arXiv:0803.1150v3 [cond-mat.str-el].

[141] H. C. Jiang, Z. Y. Weng & D. N. Sheng, "*Density Matrix Renormalization Group Numerical Study of the Kagome Antiferromagnet*", Phys. Rev. Lett. **101**, 117203 (2008), DOI: 10.1103/PhysRevLett.101.117203, arXiv:0804.1616v1 [cond-mat.str-el].

[142] P. Lecheminant, B. Bernu, et al., "*Order versus disorder in the quantum Heisenberg antiferromagnet on the kagomé lattice using exact spectra analysis*", Phys. Rev. B **56**, 2521 (1997), DOI: 10.1103/PhysRevB.56.2521, arXiv:cond-mat/9706167v1 [cond-mat.str-el].

[143] P. Sindzingre, G. Misguich, et al., "*Magnetothermodynamics of the Spin- $\frac{1}{2}$ Kagomé Antiferromagnet*", Phys. Rev. Lett. **84**, 2953 (2000), DOI: 10.1103/PhysRevLett.84.2953, arXiv:cond-mat/9907220v3 [cond-mat.str-el].

[144] P. W. Leung, K. C. Chiu & K. J. Runge, "*Columnar dimer and plaquette resonating-valence-bond orders in the quantum dimer model*", Phys. Rev. B **54**, 12938 (1996), DOI: 10.1103/PhysRevB.54.12938.

[145] J. T. Chalker, P. C. W. Holdsworth & E. F. Shender, "*Hidden order in a frustrated system: Properties of the Heisenberg Kagomé antiferromagnet*", Phys. Rev. Lett. **68**, 855 (1992), DOI: 10.1103/PhysRevLett.68.855.

[146] P. W. Leung & V. Elser, "*Numerical studies of a 36-site kagomé antiferromagnet*", Phys. Rev. B **47**, 5459 (1993), DOI: 10.1103/PhysRevB.47.5459.

[147] A. V. Syromyatnikov & S. V. Maleyev, "*Hidden long-range order in kagomé Heisenberg antiferromagnets*", Phys. Rev. B **66**, 132408 (2002), DOI: 10.1103/PhysRevB.66.132408, arXiv:cond-mat/0202117v3 [cond-mat.str-el].

[148] R. Budnik & A. Auerbach, "*Low-Energy Singlets in the Heisenberg Antiferromagnet on the Kagome Lattice*", Phys. Rev. Lett. **93**, 187205 (2004), DOI: 10.1103/PhysRevLett.93.187205, arXiv:cond-mat/0406651v1 [cond-mat.str-el].

[149] P. Nikolic & T. Senthil, "*Physics of low-energy singlet states of the Kagome lattice quantum Heisenberg antiferromagnet*", Phys. Rev. B **68**, 214415 (2003), DOI: 10.1103/PhysRevB.68.214415, arXiv:cond-mat/0305189v1 [cond-mat.str-el].

[150] R. R. P. Singh & D. A. Huse, "*Ground state of the spin-1/2 kagome-lattice Heisenberg antiferromagnet*", Phys. Rev. B **76**, 180407(R) (2007), DOI: 10.1103/PhysRevB.76.180407, arXiv:0707.0892v3 [cond-mat.str-el].

[151] P. Sindzingre & C. Lhuillier, "*Low-energy excitations of the kagomé antiferromagnet and the spin-gap issue*", Eur. Phys. Lett. **88**, 27009 (2009), DOI: 10.1209/0295-5075/88/27009, arXiv:0907.4164v2 [cond-mat.str-el].

[152] M. P. Shores, E. A. Nytko, et al., "*A Structurally Perfect S = 1/2 Kagomé Antiferromagnet*", J. Am. Chem. Soc. **127**, 13462 (2005), DOI: 10.1021/ja053891p.

[153] P. Mendels, F. Bert, et al., "*Quantum Magnetism in the Paratacamite Family: Towards an Ideal Kagomé Lattice*", Phys. Rev. Lett. **98**, 077204 (2007), DOI: 10.1103/PhysRevLett.98.077204, arXiv:cond-mat/0610565v2 [cond-mat.str-el].

[154] M. Rigol & R. R. P. Singh, "*Magnetic Susceptibility of the Kagome Antiferromagnet $ZnCu_3(OH)_6Cl_2$*", Phys. Rev. Lett. **98**, 207204 (2007), DOI: 10.1103/PhysRevLett.98.207204, arXiv:cond-mat/0701087v3 [cond-mat.str-el].

[155] S. Yan, D. A. Huse & S. R. White, "*Spin Liquid Ground State of the $S = 1/2$ Kagome Heisenberg Model*", Science **332**, 1173 (2011), DOI: 10.1126/science.1201080, arXiv:1011.6114v1 [cond-mat.str-el].

[156] P. R. Wallace, "*The Band Theory of Graphite*", Phys. Rev. **71**, 622 (1947), DOI: 10.1103/PhysRev.71.622.

[157] A. H. Castro Neto, F. Guinea, et al., "*The electronic properties of graphene*", Rev. Mod. Phys. **81**, 109 (2009), DOI: 10.1103/RevModPhys.81.109, arXiv:0709.1163v2 [cond-mat.other].

[158] Z. Y. Meng, T. C. Lang, et al., "*Quantum spin liquid emerging in two-dimensional correlated Dirac fermions*", Nature **464**, 847 (2010), DOI: 10.1038/nature08942, arXiv:1003.5809v1 [cond-mat.str-el].

[159] J. Reuther, D. A. Abanin & R. Thomale, "*Magnetic order and paramagnetic phases in the quantum J_1-J_2-J_3 honeycomb model*", Phys. Rev. B **84**, 014417 (2011), DOI: 10.1103/PhysRevB.84.014417, arXiv:1103.0859v1 [cond-mat.str-el].

[160] D. C. Cabra, C. A. Lamas & H. D. Rosales, "*Quantum disordered phase on the frustrated honeycomb lattice*", Phys. Rev. B **83**, 094506 (2011), DOI: 10.1103/PhysRevB.83.094506, arXiv:1003.3226v5 [cond-mat.str-el].

[161] A. Sen, P. Dutt, et al., "*Variational Wave-Function Study of the Triangular Lattice Supersolid*", Phys. Rev. Lett. **100**, 147204 (2008), DOI: 10.1103/PhysRevLett.100.147204, arXiv:0801.0791v2 [cond-mat.stat-mech].

[162] F. Wang, F. Pollmann & A. Vishwanath, "*Extended Supersolid Phase of Frustrated Hard-Core Bosons on a Triangular Lattice*", Phys. Rev. Lett. **102**, 017203 (2009), DOI: 10.1103/PhysRevLett.102.017203, arXiv:0809.1667v1 [cond-mat.stat-mech].

[163] N. Kawashima & Y. Tanabe, "*Ground States of the $SU(N)$ Heisenberg Model*", Phys. Rev. Lett. **98**, 057202 (2007), DOI: 10.1103/PhysRevLett.98.057202, arXiv:cond-mat/0702599v1 [cond-mat.stat-mech].

[164] G. Misguich, V. Pasquier & F. Alet, "*Correlations and order parameter at a Coulomb-crystal phase transition in a three-dimensional dimer model*", Phys. Rev. B **78**, 100402(R) (2008), DOI: 10.1103/PhysRevB.78.100402, arXiv:0803.2196v2 [cond-mat.stat-mech].

[165] J. Lou, A. W. Sandvik & N. Kawashima, "*Antiferromagnetic to valence-bond-solid transitions in two-dimensional $SU(N)$ Heisenberg models with multispin interactions*", Phys. Rev. B **80**, 180414(R) (2009), DOI: 10.1103/PhysRevB.80.180414, arXiv:0908.0740v1 [cond-mat.str-el].

List of Figures

2.1. Possible magnetizations of the spin triplet 17
2.2. Anderson tower of states for a toy model 22
2.3. Valence bond coverings for $N = 6$ sites 26
2.4. Nearest neighbor valence bond states on the kagomé lattice 29
2.5. Size of the Hilbert space for different basis sets 30
2.6. Bipartite overlap graph 33
2.7. Different values of a loop estimator 35
2.8. Fermionic convention 36

3.1. Loop update on an overlap graph 48
3.2. Convergence of eigenvalues for the Lanczos algorithm 52

4.1. Fidelity for the transverse–field Ising model 59
4.2. Action of the swap operator 62
4.3. Heisenberg model on the 1/5–depleted square lattice 64
4.4. Fidelity for the 1/5–depleted square lattice 65
4.5. Fidelity susceptibility for the 1/5–depleted square lattice 66
4.6. Rényi entropy and valence bond entropy for the Heisenberg chain 68

5.1. Dimer flipping and counting processes on the honeycomb lattice 82

6.1. Valence bond crystal on the kagomé lattice 95
6.2. Low–energy spectrum of the interpolated Hamiltonian for $N = 48$ sites . 98
6.3. Effect of pinwheel perturbations on the 48–site cluster 99
6.4. Pinwheel perturbations on different clusters on the kagomé lattice 99
6.5. Phase diagram of the interpolated Hamiltonian on the kagomé lattice . . 100
6.6. Heisenberg model on the honeycomb lattice 101
6.7. Phase diagram of the J_1–J_2–J_3 honeycomb lattice Heisenberg model . . . 102
6.8. Different valence bond crystals on the honeycomb lattice 104
6.9. Ground state energy for the NNVB approach 105
6.10. Dimer–dimer correlations for the NNVB approach vs. ED 105
6.11. Quantum dimer model on the honeycomb lattice 106
6.12. Comparison of the GS energy for different techniques 108
6.13. FS scaling of the GS energy for the NNVB approach and the QDM . . . 110
6.14. Low–energy spectrum of the QDM vs. the NNVB approach 111
6.15. Finite size gap for the honeycomb lattice Heisenberg model 112
6.16. Definition of dimer vectors for the honeycomb lattice 113
6.17. Dimer vector histograms for the honeycomb lattice QDM 114

List of Tables

2.1. Angular momentum coupling of up to $N = 4$ spins 19
2.2. NNVB coverings on the square and honeycomb lattices 30

6.1. Quantum numbers of different VBC on the honeycomb lattice 96

Table of Contents

1. Introduction **9**

I. Preliminaries 13

2. Elements of Valence Bond Theory **15**
2.1. Spin . . . 15
2.1.1. Angular Momentum Coupling . . . 17
2.2. Heisenberg Model . . . 20
2.3. Valence Bond Basis . . . 24
2.3.1. Non–crossing Valence Bond Basis . . . 25
2.3.2. Bipartite Valence Bonds . . . 27
2.3.3. Nearest Neighbor Valence Bonds . . . 28
2.3.4. Bipartite Overlap Graphs . . . 31
2.3.5. Generic Overlap Graphs . . . 34
2.4. Partial Conclusion . . . 37

3. Numerical Methods **39**
3.1. Monte Carlo Algorithm . . . 39
3.1.1. Metropolis–Hastings Algorithm . . . 41
3.1.2. Valence Bond Monte Carlo . . . 45
3.2. Lanczos Exact Diagonalization . . . 49
3.3. Partial Conclusion . . . 53

II. Quantum Information 55

4. Fidelity Approach to Quantum Phase Transitions **57**
4.1. Fidelity . . . 58
4.1.1. Universal Behavior . . . 60
4.1.2. Valence Bond QMC Approach . . . 61
4.1.3. 1/5–depleted Square Lattice . . . 64
4.2. Bipartite Entanglement . . . 66
4.3. Partial Conclusion . . . 69

III. Quantum Dimer Models 71

5. Generalized Quantum Dimer Models 73
5.1. Overlap Expansion Scheme . . . 74
5.1.1. Dual Basis and Effective Hamiltonian . . . 74
5.1.2. Overlap Matrix Expansion and Fusion Rules . . . 76
5.1.3. Hamiltonian Expansion . . . 80
5.1.4. Effective Hamiltonian Expansion . . . 81
5.1.5. Elementary Processes . . . 84
5.1.6. Locality of the Effective Hamiltonian . . . 86
5.2. Partial Conclusion . . . 91

6. Application to the Kagomé and Honeycomb Antiferromagnet 93
6.1. Heisenberg Antiferromagnet on the Kagomé Lattice . . . 94
6.1.1. Quantum Dimer Model . . . 94
6.2. Honeycomb Lattice . . . 101
6.2.1. Comparison between Exact Diagonalization and the NNVB Approach . . . 103
6.2.2. Effective Quantum Dimer Model . . . 106
6.2.3. Effect of Truncation for the GQDM . . . 107
6.2.4. Comparison of the Effective Quantum Dimer Model with the NNVB Approach . . . 109
6.2.5. Dimer Vector Histograms . . . 113
6.3. Partial Conclusion . . . 115

7. Conclusion 117

IV. Supplementary Material 119

A. Overlap Expansion for the Kagomé Lattice 121

B. Overlap Expansion for the Honeycomb Lattice 129

List of Publications 135

Bibliography 137

List of Figures 149

List of Tables 151

AUTHOR: David SCHWANDT

TITLE: *Valence bond* approach to the low–energy physics of antiferromagnets

ADVISOR: Fabien ALET

CO–ADVISOR: Matthieu MAMBRINI

PLACE AND DATE OF DEFENSE: Toulouse, 13 July 2011

ABSTRACT: The purpose of this thesis is the treatment of the antiferromagnetic Heisenberg model within the valence bond basis, allowing for the description of its low–energy physics. The manuscript is organized in two parts: In the first part we utilize the fidelity concept in order to detect quantum phase transitions. It is notably shown, that this quantity is accessible in a valence bond projector quantum Monte Carlo algorithm, making available the fidelity approach to large scale simulations. The second part is devoted to the generalization of an idea going back to Rokhsar and Kivelson, which aims to map a Heisenberg model onto a numerically less demanding quantum dimer model. Starting from a rigourous derivation, the method is then applied to the kagomé lattice and allows to establish the existence of a tricritical point in the vicinity of the original model. The same technique is also used to treat the J_1–J_2–J_3 Heisenberg model on the honeycomb lattice, showing the existence of a plaquette phase in a determined parameter regime.

KEYWORDS: Condensed matter physics, Heisenberg model, Valence bond theory, Fidelity approach to quantum phase transitions, Quantum Monte Carlo, Generalized quantum dimer models

AUTEUR : David SCHWANDT

TITRE : Approche *liens de valence* de la physique de basse énergie des systèmes antiferromagnétiques

DIRECTEUR DE THÈSE : Fabien ALET

CO–DIRECTEUR DE THÈSE : Matthieu MAMBRINI

LIEU ET DATE DE SOUTENANCE : Toulouse, le 13 Juillet 2011

RÉSUMÉ : L'objet de cette thèse est le traitement du modèle de Heisenberg antiferromagnétique dans la base de liens de valence, qui permet d'en décrire la physique de basse énergie. Le manuscrit est organisé en deux parties : dans la première nous utilisons le concept de fidélité afin de détecter les transitions de phases quantiques. Nous démontrons notamment que cette quantité est accessible dans un algorithme de Monte Carlo quantique, formulé dans la base de liens de valence, permettant ainsi de calculer la fidélité sur des systèmes de grande taille. La deuxième partie vise à développer l'idée initiale de Rokhsar et Kivelson, qui a pour but de transformer un modèle de Heisenberg en un modèle de dimères quantiques, généralement moins complexe d'un point de vue numérique. Après une dérivation rigoureuse, cette technique est appliquée au réseau kagomé et permet d'établir l'existence d'un point tricritique au voisinage du modèle initial. La même méthode est ensuite utilisée afin de traiter le modèle J_1–J_2–J_3 sur le réseau hexagonal et démontre l'existence d'une phase plaquette dans un domaine de paramètres déterminé.

MOTS–CLÉS : Physique de la matière condensée, Modèle de Heisenberg, Théorie de liens de valence, Fidélité et transitions de phases quantiques, Monte Carlo quantique, Modèles de dimères quantiques généralisés

---

SPÉCIALITÉ : Physique de la matière

UNITÉ DE RECHERCHE : Laboratoire de Physique Théorique – IRSAMC
Université Paul Sabatier
Bât. 3R1B4
118, route de Narbonne
31062 Toulouse Cedex 04, France